Title	Aplanatic lens correctors for imaging optics
Author(s)	Rocha, Michelle Cristine
Publication Date	2022-09-05
Publisher	NUI Galway
Item record	http://hdl.handle.net/10379/17344

NATIONAL UNIVERSITY OF IRELAND GALWAY

DOCTORAL THESIS

Aplanatic lens correctors for imaging optics

Author:
Michelle C. ROCHA

Supervisor:
Dr. Alexander V.
GONCHAROV

A thesis submitted in fulfillment of the requirements
for the degree of Doctor of Philosophy

in the

Applied Optics
School of Physics

An Grúpa Optaice Feidhmí

August 30, 2022

Contents

Declaration of Authorship

I, Michelle C. ROCHA, author of the thesis titled "Aplanatic lens correctors for imaging optics", declare that:

- The work presented herein is wholly my own work unless stated otherwise in the text.

- The work of this thesis has been done entirely while in her Ph.D. candidacy for a research degree in Optical Engineering at the National University of Ireland, Galway.

- The work presented in this dissertation has not been applied to any other degree.

- All of the references for this thesis have been given.

- All the major sources of support have been acknowledged.

Signed:

_____

Date:

_____

"To explain all nature is too difficult a task for any one man or even for any one age. 'Tis much better to do a little with certainty, and leave the rest for others that come after you, than to explain all things by conjecture without making sure of any thing."

Isaac Newton

NATIONAL UNIVERSITY OF IRELAND GALWAY

Abstract

College of Science and Engineering
School of Physics

Doctor of Philosophy

Aplanatic lens correctors for imaging optics

by Michelle C. ROCHA

This thesis proposes analytically developed aplanatic field correctors. To begin, an astigmatism correction method for aplanatic Gregorian telescopes was developed employing two lenses with spherical surfaces and a spherical GRIN medium. Second, to expand the field of view of RC telescopes, a meniscus lens with aspherical surfaces has been designed. This meniscus can flatten the image surface while correcting astigmatism. The meniscus, on the other hand, has lateral color. Finally, using the same principle as the meniscus, a refractive pair has also been designed to increase the FoV in RC telescopes. It does, however, correct the lateral color at the expense of introducing axial color. By adjusting the distance between the pair, this pair may function for various spectral bands individually. All of the methods mentioned above may be added to or removed from an existing aplanatic telescope without compromising image quality or changing the original telescope design. Furthermore, their employment maintains the telescope's aplanatic properties.

Acknowledgements

I would like to thank a lot of people, but I will only highlight the most essential ones here.

First and foremost, I want to express my gratitude to my family. They consistently encouraged and inspired me, as well as making sacrifices to ensure that I had the greatest education possible.

I thank my partner for constantly encouraging me.

I would like to express my appreciation to Sasha for accepting me as his PhD student, for all of his efforts to assist me in obtaining a scholarship, and for everything he has taught me over the years.

I would also like to convey my thankfulness to Prof. Christopher Dainty, who served as my second supervisor and was always willing to teach me everything about the industry career.

I appreciate my former university, UNICAMP, for having excellent teachers that helped me prepare for my PhD.

And, of course, I couldn't forget about my friends, especially those who stood by my side during my PhD journey: Fadi Nammour, Adriana Cardinot, Thaize Baroni, Conor Flynn, Ciarraí O'Toole, Conor Waldron, and Ciaran Murray (to name a few, but the best!).

I am grateful to everyone engaged in my PhD defense, Sasha, Nicholas Devaney, Rafael González-Acuña, John Sheridan, and Miriam Byrne, for being a part of this journey and for taking their time to read my thesis and participating in my viva.

List of Figures

List of Tables

List of Abbreviations

AS	**A**perture **S**top
ASC	**A**bbe **S**ine **C**condition
BFD	**B**ack **F**ocal **D**istance
CR	**C**hief **R**ay
CoC	**C**ircle **o**f least **C**onfusion
DoF	**D**epth **o**f **F**ield
EE80	**E**ncircled **E**nergy at **80**%
EFL	**E**ffective **F**ocal **L**ength
EnP	**En**trance **P**upil
ExP	**Ex**it **P**upil
FoV	**F**ield of **V**iew
FS	**F**ield **S**top
F#	**F**-Number
FWHW	**F**ull **W**idth at **H**alf **M**aximum
GRIN	**GR**adient-**IN**dex
GPL	**G**eometrical **P**ath **L**ength
MR	**M**arginal **R**ay
MTF	**M**odulation **T**ransfer **F**unction
NA	**N**umerical **A**perture
NIR	**N**ear-**I**nfra**R**ed
OPD	**O**ptical **P**ath **D**ifference
OPL	**O**ptical **P**ath **L**ength
PP	**P**rincipal **P**lane
PSF	**P**oint **S**pread **F**unction
RC	**R**itchey-**C**hrétien
RCm	**R**itchey-**C**hrétien with an aplanatic **m**eniscus
RCp	**R**itchey-**C**hrétien with an aplanatic **p**air
RMS	**R**oot **M**ean **S**quare
ROC	**R**adius **O**f **C**urvature
SA	**S**pherical **A**berration

List of Symbols

ε	Eccentricity of a conic section	
k	Conic constant	
F	First focal point	
F'	Second focal point	
k	Conic Constant	
n	Refractive index	
N	First nodal point	
N'	Second nodal point	
P	First principal point	
P'	Second principal point	
R	Radius of curvature	mm
z	Sagitta of a surface	
ε	Eccentricity of a conic section	
η	Object size	mm
η'	Image size	mm

Dissemination of Research

Journal articles

- M. C. Rocha and A. V. Goncharov, "Aplanatic meniscus lens corrector for Ritchey-Chrétien telescopes," Opt. Express 30, 6076-6089 (2022) [1] **[Published]**

- M. C. Rocha and A. V. Goncharov, "Quasi-aplanatic refractive pair corrector for Ritchey-Chrétien telescopes" **[In progress]**

Proceedings articles

- M. C. Rocha, A. V. Goncharov, and C. Dainty, "Aplanatic afocal system using two GRIN lenses with spherical surfaces," Proc. SPIE 11105, Novel Optical Systems, Methods, and Applications XXII, 111050C (9 September 2019)[2] **[Published]**

- M. C. Rocha and A. V. Goncharov, "An aplanatic meniscus lens for correcting astigmatism in Ritchey-Chrétien telescopes," Proc. SPIE 11451, Advances in Optical and Mechanical Technologies for Telescopes and Instrumentation IV, 114514E (13 December 2020)[3] **[Published]**

- M. C. Rocha and A. V. Goncharov, "A quasi-aplanatic refractive pair for correcting astigmatism in Ritchey-Chrétien telescopes," Proc. SPIE 11871, Optical Design and Engineering VIII, 1187108 (12 September 2021)[4] **[Published]**

Conferences participation

- SPIE Optical Systems Design, 2018, Frankfurt, Hesse, Germany **[Attendance]**

- SPIE Optical Engineering + Applications, 2019, San Diego, California, United States **[Oral presentation]**

- Photonics days, 2019, Jena, Thuringia, Germany **[Attendance]**

- Doctoral students conference for the discussion of optical concepts (DokDok), 2019, Eisenach, Thuringia, Germany **[Oral presentation]**

- SPIE Astronomical Telescopes + Instrumentation, 2020, Online Only **[Poster presentation]**

- SPIE Optical Systems Design, 2021, Online Only **[Oral presentation]**

Dedicated to my family.

Chapter 1

Introduction

1.1 Field correctors for telescopes

For rotationally-symmetric optical systems, spherical aberration (SA) is the only monochromatic aberration that is present on-axis. As will be seen in Chapter 2, defocus and tilt can also occur for on-axis rays, however, they are not considered as real aberrations of the system but rather misalignment of the image plane, it is only a matter of adjusting the image plane (detector tilt and position) to correct them. The off-axis aberrations are composed of coma, astigmatism, field curvature, and distortion. The chromatic aberrations are composed of longitudinal chromatic aberration for on-axis rays, and transverse chromatic aberration for off-axis rays. There are different orders of SA. However, the most impacting in image quality in an optical system is the third-order SA, which is called the primary SA. Correction of SA is fundamental as it affects the image as a whole, not only at the periphery of the lenses as other aberrations [5]. As will be seen in Chapter 2, SA depends on the aperture stop size. In contrast with all off-axis aberrations, since the path of an off-axis beam and the chief ray through the lens is affected, SA does not depend on the aperture stop position when placed in front of the system. Moreover, it does not depend on the field angle, so it does not depend on the height of the object or image [6].

Coma is one of the monochromatic aberrations that occurs off-axis. This aberration can significantly impact image quality, especially considering the asymmetry it creates in the image spot. This asymmetry does not allow one to locate the center of the image spot as with other aberrations [7].

For this reason, it is important to correct both aberrations, creating an aplanatic system. Figure 1.1 illustrates common names used for describing systems free from SA, coma, and astigmatism. A system that is only free from SA is called stigmatic, and free only from coma is called isoplanatic. If the system is free from both SA and coma, it is called aplanatic. And if the correction goes further and a system is free from SA, coma, and astigmatism, it is denominated anastigmatic. Those definitions are important for the next Chapters.

This thesis will be dealing with aplanatic and quasi-aplanatic field correctors for telescopes.

Telescopes are optical instruments used to observe far-away objects. Its origin, officially, can be traced back to 1608 in the Netherlands when Hans Lippershey filed a patent application. The patent was denied because there were several claims of this invention being utilized by others at the same time. Jacob Metius and Zacharias Jansen, for example, had been producing telescopes known as "spyglasses", with the former applying for a patent three weeks after Lippershey. The Lippershey spyglasses were not designed with astronomy in mind. It had a tiny diameter and just three times magnification, therefore it was widely employed as spectacle lenses [8].
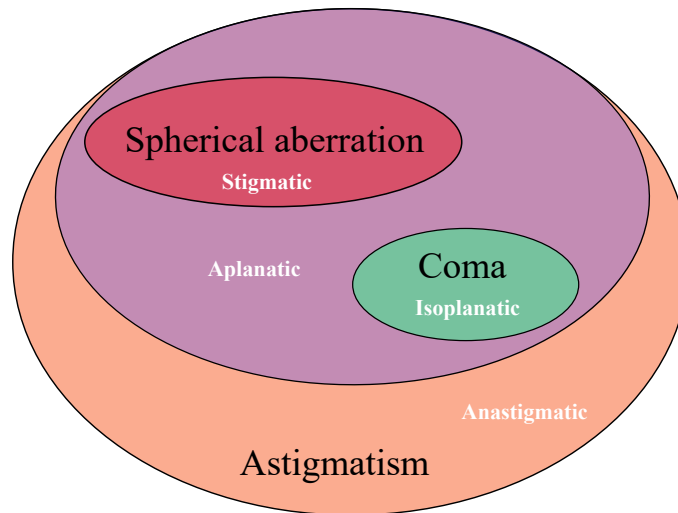
FIGURE 1.1: Common names used for describing systems free from SA, coma, and astigmatism.

Galileo Galilei was the first one to document the use of telescopes for astronomical purposes and his observations in details. He then developed theories based on his findings. Galilei's telescope consisted of a lead pipe with two lenses in the extremities, a plano-convex and a plano-concave. The eyepiece was a plano-convex lens, while the objective was a plano-concave lens. The Galilean telescope is seen in Fig. 1.2a. As can be seen, the image formed by the Galilean telescope is upright, making it more suitable for terrestrial observations [8].

The flat surface of the lenses also made it easier to manufacture them using 16th-century technology, allowing for the testing of several designs and verifying their magnification. Galileo began using the telescope for astronomical observations after a greater magnification was obtained. On-axis spherical and chromatic aberration are present due to the telescope's use of spherical refractive elements. However, because it is made up of a positive and a negative lens, the total degree of aberration is reduced [8].

The Keplerian telescope is made up of an objective and an eyepiece, both converging. In general, the entrance pupil is in the lens mount, and the exit pupil is found in the real image generated by the eyepiece. The image in this telescope is inverted. The keplerian telescope is seen in Fig. 1.2b.

Figure 1.2 illustrates the differences between the Galilean and the Keplerian telescopes. As seen, the Galilean presents an upright image while the Keplerian presents an inverted image. Moreover, the Galilean has a virtual image while the Keplerian has a real image. It is also possible to see how the Galilean is more compact compared to the Keplerian.

There are three types of telescope: refractive, reflective, and catadioptric. The catadioptric systems involve the use of both reflective and refractive elements in its composition.

The Cassegrain and the Gregorian systems are the two most commonly used two-mirror reflecting telescopes in astronomy. Their primary mirror has a concave paraboloidal surface, but their secondary mirrors, however, are different. A concave secondary mirror with an ellipsoidal surface is used in the Gregorian telescope. In this case, the secondary mirror is positioned after the prime focus, where the axial light beam is diverging, resulting in a longer telescope configuration. Furthermore,
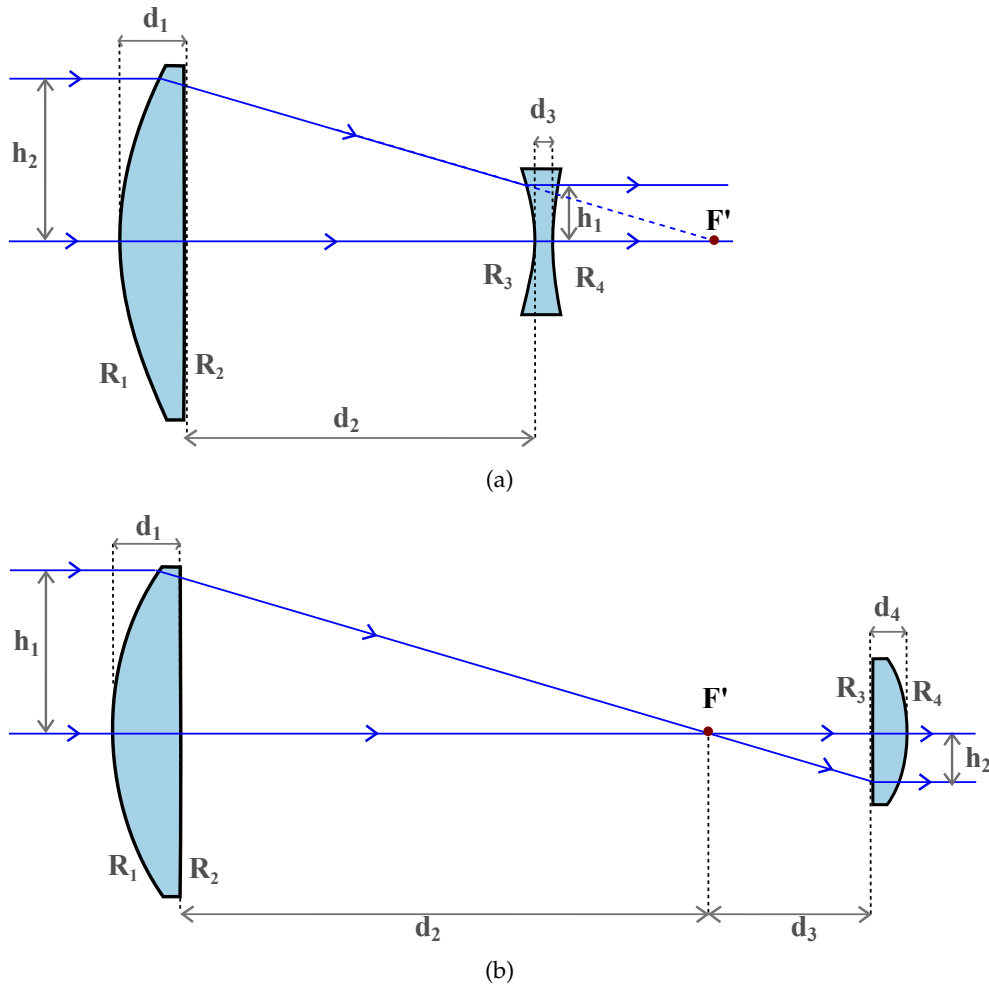
FIGURE 1.2: Layout for (*a*) a Galilean telescope, and (*b*) a Keplerian telescope.

the image generated is not inverted, which has some advantages for terrestrial ob-
servations. On the other hand, in a Cassegrain telescope, the secondary mirror being
convex hyperboloid of revolution positioned before the primary focus, where the ax-
ial light beam is converging, which leads to a shorter configuration. As a result, the
image is inverted in this case, but for large astronomical telescopes, this makes no
difference. In both configurations, all mirrors are independently free of spherical
aberration, and as a consequence, there is no spherical aberration in the system [9].

Coma is the primary aberration impacting image quality in both Cassegrain and
Gregorian telescopes. Thus, changes in the original design are necessary to correct
coma. These adjustments require converting the primary mirror's paraboloidal sur-
face into another conic of revolution and slightly adjusting the secondary mirror's
conic as well. As a result, the two-mirror system can simultaneously correct spheri-
cal aberration and coma, resulting in an aplanatic system. For the Gregorian system,
the primary mirror is transformed into an ellipsoidal surface while slightly adjusting
the conic constant of the secondary mirror. This version is known as *Aplanatic Grego-
rian*, this design is used in the Euro50 telescope, for example [10]. For the Cassegrain
system, the primary mirror is transformed into a hyperboloidal surface while adjust-
ing the secondary mirror's conic constant. This version is known as *Ritchey-Chrétien*
(RC). As a result, the unaberrated field of view is increased, but astigmatism and
field curvature become new limiting factors for such telescopes [11].
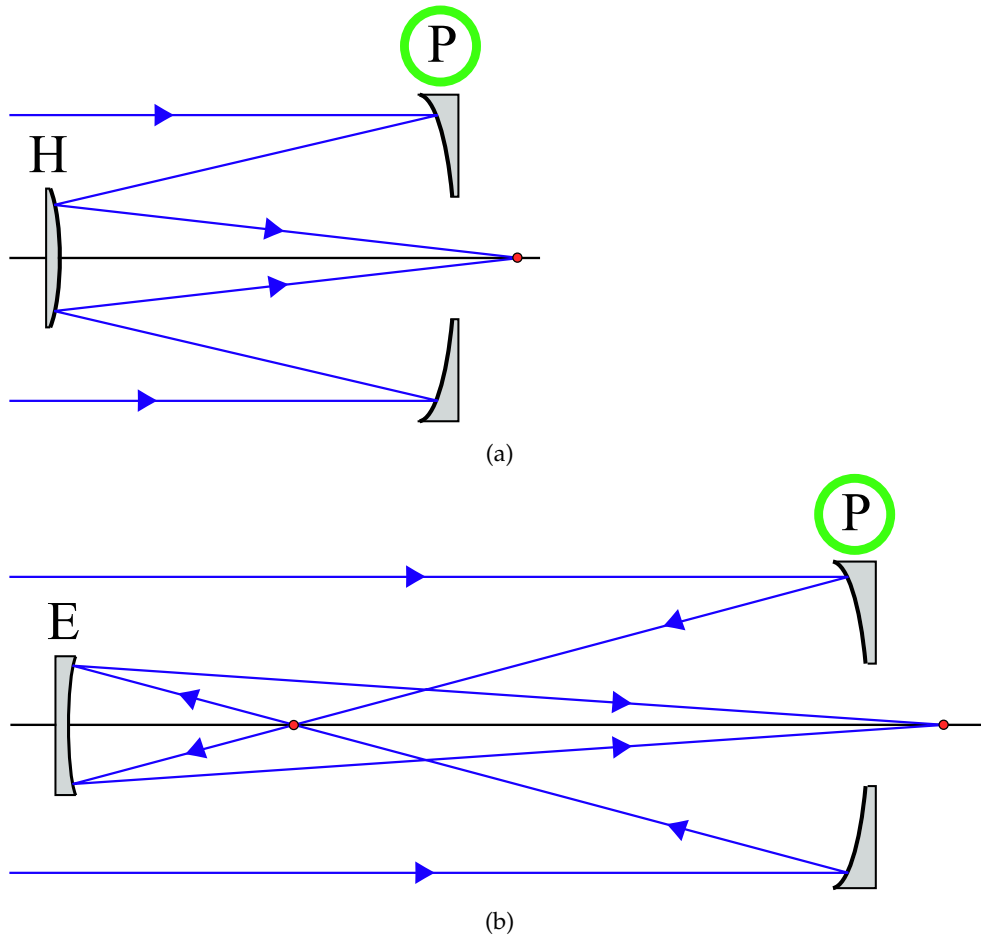
FIGURE 1.3: Layout for (*a*) a Cassegrain telescope, and (*b*) a Gregorian telescope. The hyperboloidal surface is denoted as H, the ellipsoidal as E, and the paraboloidal as P.

The RC telescope presents many advantages over the Aplanatic Gregorian, including a shorter overall length, slightly wider Field of View (FoV), and easier alignment [12]. However, as mentioned above, the aberrations that limit the RC image quality are astigmatism and field curvature. Therefore, to improve the image quality even further, the correction of those aberrations is essential. For this reason, many researchers explored different alternatives, such as using field correctors or curved sensors.

Field correctors have been introduced into telescopes so that their intrinsic aberrations can be corrected. There are different sorts of field correctors: those placed in the primary focus, those placed in the final focus, and those placed in the incoming collimated rays from the object. The first two types are known as sub-aperture correctors because they only cover the converging beam from the primary or secondary mirror of the telescope, not the entire incoming beam from the object.

R. A. Sampson suggested the first reported field correctors in the primary focus in 1913. His corrector was comprised of three lenses, each of which was spherical. The first lens, which had a silvered back for reflection in a meniscus form, named "the reverser", replaced the Cassegrain's convex mirror. The following two lenses are close to each other along the outgoing beam's path, between the large mirror and the reverser. He also focused on his solution's achromatism. It was accomplished by utilizing the same glass for all three lenses and fine-tuning their focal lengths so that the focal point and image size for any two rays at the primary focus are equal [13].
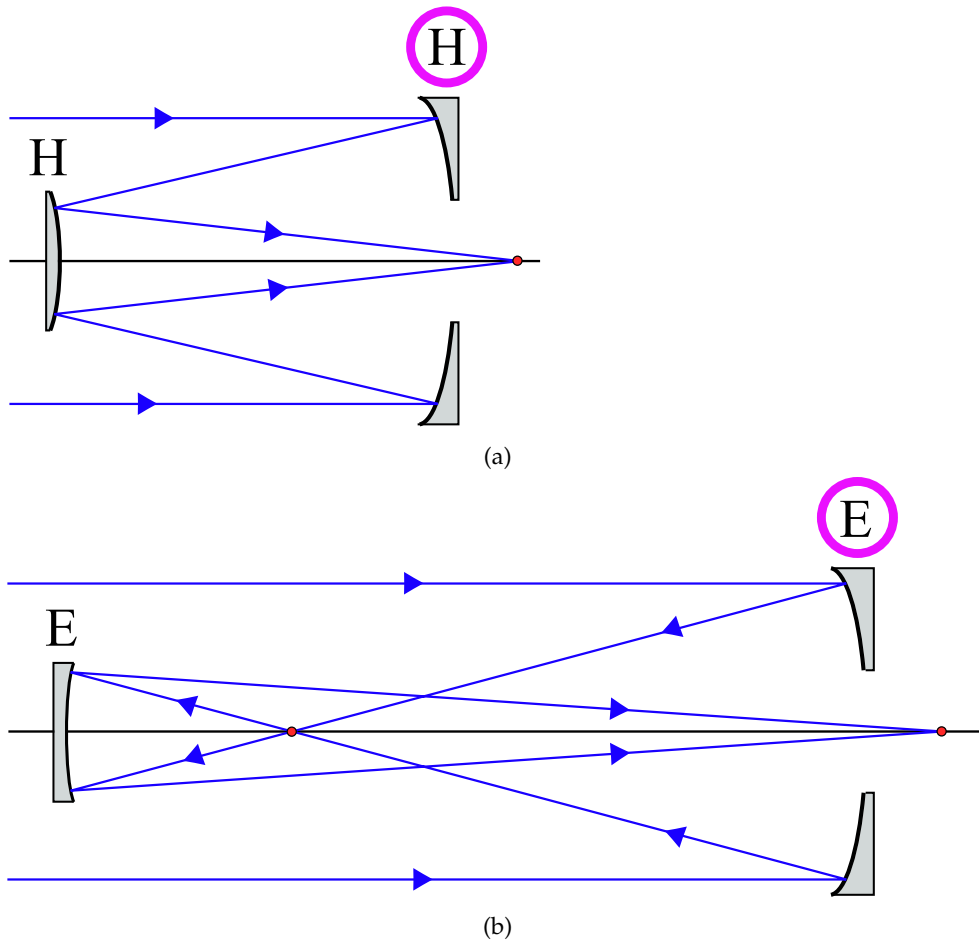
FIGURE 1.4: Layout for (*a*) a RC telescope, and (*b*) an Aplanatic Gregorian telescope. The RC is composed of two hyperboloidal mirrors, denoted as H, and the Aplanatic Gregorian is composed of two ellipsoidal mirrors, denoted as E.

In order to reduce distortion and field curvature in a parabolic mirror, F. E. Ross presented a corrector made up of two spherical lenses, a crown, and a flint in 1935. The first lens had a negative meniscus, while the second was a biconvex. SA, on the other hand, was still undercorrected. The form of the corrector lenses was determined by the distance between the lenses and the parabolic mirror's focus point, as well as the focal length. When the negative lens is placed in front of the mirror, the best results are produced. In contrast to Sampson's correctors, Ross' correctors were utilized in observatories, whereas Sampson's approach was never implemented on any telescope [14].

Based on Sampson's corrector concept, V. N. Churilovskii created a corrector for telescopes similar to Cassegrain in 1940. His solutions used afocal apochromatic lenses made of the same material. The distinction between the telescopes he employed and the Cassegrain is that all of the mirror surfaces, as well as the surfaces of the correctors, were spherical. The two lens correctors, when combined with the spherical surfaces of the mirror, corrected the system's SA and coma. He also explored combining two correctors in the convergent beam of the telescope to correct more aberrations [15].

To correct the aberrations of the spherical mirror, G. G. Slyusarev et al in 1947. presented a correction system consisting of five lenses grouped in three separate components, the first of which contains an internal reflecting surface. Doublets were

used in the first and third components. Between the first and second elements, they used parallel rays as a solution. Strong chromatic aberration afflicted this system [16].

A. B. Meinel proposed using three aspheric plates as a corrector for parabolic telescopes in 1953. Compared to Ross's corrector, Meinel's had less chromatic aberration. The distance between the plates had little effect on the correction of aberrations [17].

S. Rosin improved Ross's two-lens corrector in 1964. Both lenses in Rosin's design were replaced with fused silica to extend the spectral range into the ultraviolet and near infrared, as well as to provide undercorrected SA [18].

Ross has also created a three-lens design for the Mount Palomar observatory's 200-inch Hale telescope [19]. Despite this, he never published a scholarly article regarding his three-lens corrector. C. G. Wynne retrieved his invention in 1965. Wynne has proposed variants of the Ross corrector for Cassegrain telescopes. His variations included three-lens correctors with spherical surfaces, but with various lens shapes and thicknesses. He proposed replacing one of the three lenses with a triplet in one of his prototypes [20]. This is still one of the most popular RC telescope solutions. Undercorrected SA and coma were also evident in Wynne's solutions. Including an aspheric plate before the doublet corrector was one of Wynne's solutions for correcting the SA from Ross's corrector [21].

S. C. B. Gascoigne designed an aspheric plate at the prime focus to correct astigmatism in the RC in 1965 as well. The plate's first surface is aspheric, whereas the second is flat. However, his technique necessitated a modification of the RC system, which needed the inclusion of SA and coma to correct the aberrations caused by the aspheric plate. The plate should be adjusted to compensate for SA, coma, and astigmatism, and the aspherical parameters of the mirrors should be altered as well [22].

In 1965, P. P. Argunov suggested two new correctors for Cassegrain telescopes designs. The first corrector was comprised of two or three lenses made up of various glasses that were used to provide aplanatic and chromatic adjustments. The two-lens system, on the other hand, had a significant secondary spectrum, which was marginally reduced by adding a third lens. This three-lens corrector, however, adds to the complexity while providing little benefit in terms of image quality [23].

D. H. Schulte adapted Gascoigne's solution for RC telescopes in 1966. To begin, he employed Gascoigne's aspheric plate to create a system that was free of SA, coma, and astigmatism. A field flattener was used after the aspheric plate. The field flattener was made up of two surfaces, the first of which was spherical and the second of which was flat. The spherical surface compensates for Petzval curvature in the system. The cost of this repair is the introduction of SA into the system. When the field flattener is positioned close to the focal plane, however, the SA is reduced [24].

Rosin also introduced a new corrector in 1966, this time for RC telescopes. He employed two separated lenses in the RC's converging beam; the first and fourth surfaces of the two-lens corrector were aplanatic, therefore no SA, coma, or astigmatism was introduced. The pair's inner surfaces were concentric and did not contribute to SA, coma, or axial color. However, the system's inner surfaces introduce astigmatism, field curvature, and lateral color, whereas the outer surfaces introduce field curvature, axial color, and lateral color. The RC telescope is not affected by SA or coma while using this corrector. As a result, the aplanatic state is retained [25].

Argunov presented another corrector in 1966, which consisted of an afocal system consisting of two lenses made of the same material. The pair was positioned between the primary and secondary mirrors, causing the ray to be refracted twice

in each lens. As a result, an apochromatic system is created, which corrects spherochromatism as well. If the pair is situated at a proper distance from the secondary mirror, aplanatic results can be obtained [26].

G. M. Popov proposed a two-lens corrector design in 1966, which was comparable to Argunov's afocal system. However, with a central aperture enabling the rays from the secondary spherical mirror to pass through unaltered, this corrector only required one refraction in the lenses from the rays originating from the primary mirror. This system was able to correct astigmatism, but it was difficult to implement due to the additional complexity caused by the necessity for a long focal length for the corrector, which resulted in a large field curvature and the large size of the refractive elements. Popov also looked into a corrector design that used a meniscus near to the secondary mirror and twice refracted the rays, similar to Argunov's idea. It did not, however, achieve aplanatic or chromatic adjustments [27].

Wynne introduced a four-lens corrector for paraboloidal primary mirror telescopes in 1967. His concept consisted of two afocal systems, each with two spherical thin lenses in contact that were constructed of the same material. Each lens of the afocal systems are of the opposed optical power of each other. As a result, they are a pair with no optical power. SA and field curvature were not present in the systems. The system corrects the parabolic main mirror's coma without compromising its astigmatism. However, this was only a theoretical solution. The thickness of the lenses and their spacing must be optimized in order to execute this approach in a real-world setting, which may result in the systems losing their afocal qualities and each pair being distanced [28, 29]. SA and coma may be present in the optimized corrector.

In 1968, R. N. Wilson claimed that in the literature found by then, the aspheric constants of the RC were modified to adapt its aberrations with the corrector. The difficulty is that the corrector has to be removed for some applications, such as photographic photometry and astrometry. Even though removing the corrector had no effect on the modified RC's SA, it did cause a large degree of coma, affecting image quality and reducing the maximum FoV of the RC alone. Depending on the telescope's setup, the reduction in FoV might be as much as 50 %. In the secondary focus, he described and analyzed various correctors. H. Köhler offered a field corrector with a curved surface and another one virtually flat close to the image plane while considering single-element correctors, solution that was mentioned in the European Southern Observatory (ESO) reports [30]. The corrector is described as having good astigmatism and field curvature correction. The lens does, however, have chromatic aberrations. This field corrector may also be made by bending the virtually flat surface in such a way that the lens becomes a meniscus, with the second surface's RoC being comparable to the first. Although the meniscus with spherical surfaces has lateral color, it retains its astigmatism and field curvature correction. Because the surfaces are almost symmetric, the lens corrects for axial chromatic aberration, resulting in image quality that is superior to the prior design. The RC mirrors would need to be modified in both cases. Another way to adjust the RC parameters is to utilize three lenses, all of which are made of quartz, with two positive lenses and one negative lens. When compared to the doublet, this approach produces poorer outcomes. This occurs because chromatic aberration correction is weaker, leading to increased astigmatism and coma [31].

In 1968, I. N. Refsdal presented a two-element system for correcting aberrations in Cassegrain telescopes that used quartz positioned near to the image plane. This solution's telescope is similar to the RC's, but with stronger aspherical surfaces. The negative lens was used to correct astigmatism. The aspherical surface of the positive

lens corrects the tangential curvature and flattens the image for larger fields. There is axial chromatic aberration correction if the fourth-order term of the aspheric coefficient is optimized. The system presents lateral chromatic aberration [32].

S. Rosin and M. Amon utilized two glass plates to introduce astigmatism into an RC in 1972, while maintaining spherical and axial chromatic aberration to a minimum. The plate is positioned near the focal plane of the telescope's converging beam. They are placed at an angle to the optical axis, rotated in opposing directions. This is where the lateral aberrations adjustments are dealt with. The astigmatism created by the plates depends very little on the material's refractive index. As a result, the transmission range required for the application determines the material. The angle between the plates and the optical axis has a significant impact on the amount of astigmatism in the pair of plates. The plates are placed at a distance from the optical axis in a manner that it covers the off-axis rays. For a flat image surface, the system still presents field curvature. Therefore, they suggested the use of a field flattener after the plates [33].

Wynne suggested using a doublet to increase the FoV of large Cassegrain telescopes in 1973. He considered that using a hyperboloidal primary mirror for some applications, such as when the primary mirror's focus is to be employed alone, would be difficult due to the SA introduced by the primary mirror of an RC. As a result, he began to investigate Cassegrain telescope correctors. Each lens in the thin pair must be of opposing power, in an afocal arrangement, and in contact in order to correct for chromatic aberration. At the expense of adding SA into the system, the doublet corrects coma and astigmatism in the Cassegrain. The doublet should be placed as near to the focus point as feasible to reduce the SA. If not, modifications to the Cassegrain's settings are required. The doublet's first lens is biconvex, while the second is a meniscus. This adjustment, of course, is affected by SA, even if only in a minor manner. As a result, the system is no longer aplanatic [34].

For paraboloid mirrors, Wynne suggested a triple lens field corrector in 1974. His goal was to achieve the same good outcomes for a paraboloid as he had previously achieved for the RC. A paraboloid mirror and three lenses made of the crown glass BK7 were part of his design. Every surface was spherical. This approach minimizes SA, coma, and astigmatism while correcting for chromatic aberration and Petzval curvature [35].

In 1976, C. F. W. Harmer and Wynne presented a doublet for Cassegrain telescopes that had spherical surfaces and was nearly afocal. They revisited Wynne's 1973 doublet solution. However, this time they focused on smaller telescopes. The doublet was nearly afocal as well, although it was located farther away from the focal point of the telescope. As a result, a considerable amount of SA was introduced into the system. The secondary mirror of the Cassegrain must take on a spherical form in order to correct SA [36].

S. Ding-Qiang and W. Lan-Juan suggested a two-mirror focus reducer for Cassegrain telescopes in 1981. The reducer's primary mirror is positioned at the Cassegrain focus, allowing the diverging beam to be reflected in a convex mirror, M1, and then reflected back from a second mirror, M2, to a new focal point for the system right after M1. The system may be corrected for SA, coma, and astigmatism by carefully selecting the fourth-order aspheric terms of the elements of the reduction. High-order aberrations are also reduced as a result of this. Cassegrain, RC, and Gregorian telescopes are all compatible with their solution. The circular obscuration of each pair of mirrors in a four mirror telescope is a challenge. As a result, the beam that is transmitted is reduced. In addition, for larger fields, the system begins to suffer from vignetting. The aberration corrections do not hold if this solution is applied

in the primary focus. To address this problem, a thin aspheric plate must be used before the reducer [37].

Considering the results they obtained from those designs, they concluded that aspherical terms in the three lens system did not provide significant advantage over the original design for monochromatic corrections considering the complexity added to the system. However, it proved itself to be successful in the correction of chromatic aberrations [38].

C. Cao and N. Wilson investigated the use of aspherical surfaces for prime focus correctors in 1984. The Wynne-type triplet design was improved. The thickness of the three lenses was increased, the second, fourth, and fifth surfaces were modified from spherical to fourth power aspheres, and a field flattening lens was added. The second lens has been modified to have higher optical power than the Wynne solution, resulting in flatter surfaces on the first lens. The system, on the other hand, has a weakness in that the fourth surface is too steep and the center thickness is too thin. The high-order chromatic aberrations introduced by the correctors were reduced as a result of these improvements. They also looked at whether using the sixth aspheric term provided any benefit for the correctios of aberrations, and found that there was minimal benefit. As a result, given the additional complexity of the aspheres, this adjustment was not justified. Later in their attempt to improve the corrector, they tried using the three lenses without the field corrector, ignoring the telescope's field curvature. Given that the predominant aspherical surfaces are found in the second and third lenses, the first lens has little impact in the system. As a result, removing an aspherical surface from the first lens was a viable option. Given the complexity introduced to the system and the results obtained from those designs, they determined that aspherical terms in the three lens system did not give a substantial benefit over the original design for monochromatic adjustments. It did, however, prove to be effective in the correction of chromatic aberrations [38].

H. W. Epps and D. Faricant proposed the use of field correctors in RC telescopes used for CCD imaging in 1997, employing two components of the same material and spherical surfaces to correct astigmatism and field curvature. They opted for fused silica and employed ray-tracing tools to determine the best shape for the lenses' surfaces. The spacing between the lenses, the BFD, EFL, lens thickness, and distance between the last element and the focus were all employed as constraints in the optimization process. As a result, the first lens had a meniscus shape, whereas the second lens has a biconcave shape. Compactness was one of its benefits [39].

D. T. Puryayev and A. V. Goncharov suggested a four-mirror system to correct coma in a telescope in 1998. The first part was composed of a spherical primary and an aspherical secondary mirror, and the second part of two aspherical mirrors. The overall system is free from SA and meets the sine criterion, i.e. it is aplanatic. Not only that, but by adjusting the distance between the system's second and third mirrors, the two mirror corrector can also correct for astigmatism. The SA and coma are corrected with the use of an elegant analytical solution [114].

V. Y. Terebizh presented three primary focus corrector designs for RC telescopes in 2004, each including five fused silica lenses with spherical surfaces. The Wynne three-lens design was their starting point. He improved the design by adding two more lenses after the second and third lenses, making two doublets in total. Due to the two doublets that correct the aberrations from the hyperboloidal primary mirror, mainly coma, this new design increases the system's FoV. Because the corrector is practically afocal, the focal length of the primary mirror does not vary considerably. This method was tuned for three Blanco 4 *m* telescopes of the Cerro Tololo Inter-American Observatory (CTIO) with varying FoVs of 2.12, 2.4, and 3.0 degrees [0].

In 2004, S. A. Chuprakov proposed using a doublet with the second lens having a reflecting surface to replace the Cassegrain's secondary mirror. This method required the employment of two lenses with different materials and spherical surfaces, with the outer surfaces having the same radius of curvature and the interface being flat. The doublet operates by refracting both incoming rays from the primary mirror and incoming rays from the reflecting surface, resulting in a double ray path. The doublet's lenses are made of crown glasses, which have a minor refractive index fluctuation but a significant Abbe Number variation with wavelength. The goal of this approach was to make the system's manufacturing process as simple as possible. The image quality was impaired by chromatic aberration, and the telescope's field of view is limited by SA [40].

Yu. A. Klevtsov proposed a corrector in 2006 that consisted of a meniscus near to the secondary mirror that refracted rays from the primary mirror as well as those reflected from the secondary mirror, followed by three lenses close to the focus point. A lens having a reflecting surface on the side facing the primary mirror served as the secondary mirror. The rays from the primary mirror and the secondary reflecting surface were therefore refracted by the secondary mirror refractive element. As a result, the corrector was made up of a total of six lenses. The second one, which was positioned in front of the secondary mirror, was a quasi-afocal negative meniscus, which means that both sides of the meniscus were almost identical. A reflecting lens was the third lens. The fourth lens was a negative-power focus converter. The fifth lens was a positive-power focus converter. A concentric meniscus was the sixth and final lens. This solution corrected astigmatism and chromatic aberration, but the entire system's SA increased as the image distance between the telescope and the corrector increased [41].

Terebizh presented an aplanatic Gregorian telescope field corrector in 2007. His approach included an optical element positioned near the telescope's exit pupil (which is close to the primary focus), five lenses, and a curved detector window. The materials used for all of the elements were the same. To prevent vignetting, the first element contained a hole in the middle that allowed the primary mirror's rays to pass through without being refracted. If not, the Gregorian telescope's image quality deteriorated, diminishing its field of view [42].

A field corrector for paraboloidal primary mirrors was proposed by A. Rakich and N. J. Rumsey in 2013. Four spaced refractive elements with spherical surfaces were used in their solution. The solution focused on how to improve Wynne's four-lens corrector. In comparison to the original method, the third lens was reversed around the optical axis and positioned closer to the fourth lens, resulting in a sharper image. However, when a larger wavelength spectrum was considered, Wynne's method produced the best results. The Wynne solution, on the other hand, was more prone to coma. SA affected both systems [43].

As seen, many designs entail modifying the telescope's specifications in order to reduce aberrations with the use of correctors. In some configurations, the corrector induces SA or coma, causing the system to lose its aplanatic status. The majority of recent studies have moved away from using RC or Cassegrain original designs in favor of optimizing the entire telescope system, including lenses and mirrors.

1.2   Novel solutions of the thesis

Three correctors were analytically designed so that they can be added or removed from an aplanatic Gregorian or RC without any need to change their original design, i.e., no change in their RoC, distance between the mirrors or aspheric surfaces of the mirrors. That means that the image quality of the telescopes is maintained when the correctors are not used. As previously mentioned, R. N. Wilson described the need for an aplanatic telescope to have their corrector removed, such as for photometry or astrometry. Thus, the correctors presented here demonstrate advantages over the correctors that require modifications in the telescopes. Not only that, two of the correctors presented are aplanatic. Therefore, the overall combination of the aplanatic telescopes with the aplanatic corrects result in an aplanatic solution. One of the correctors is quasi-aplanatic, i.e., introduce a small quantity of coma into the telescope, that does not affect the image quality.

The novel correctors presented here are:

- A GRIN corrector composed of two lenses with spherical surfaces. Both lenses have a similar GRIN structure, and when combined, can either create an aplanatic afocal or an aplanatic corrector for Gregorian telescopes. The aplanatic corrector tackles the astigmatism of the Gregorian, balancing it so that the sagittal and tangential planes are at the same distance from the image plane, so that the final image of the system is circular instead of the typical oval shape of a system with astigmatism. This is important considering that symmetry may be needed for some applications. Moreover, the use of a GRIN media to correct the field in telescopes while maintaining the aplanatic conditions has not been found in literature. In fact, the use of GRIN media as a corrector with or without maintaining the aplanatic conditions has not been found. This solution is of great importance especially considering that the manufacturing process of GRIN media is a developing field, including even the 3D ink-jet printing of GRIN lenses being available. The structure of the GRIN media in this corrector is spherical, so many other techniques can also be used. Taken all that in consideration, this solution provides a theoretical approach that can also be applied in a practical manner. The challenge with this solution is possibly the costs of manufacturing the lenses, and also the limitation of the size of the lens. The size of the lens is correlated to the thickness of the lens considering that the diameter-to-thickness ratio has to be established so that the lens is not too thin, and this influences the variation in refractive index between the surfaces of the lens. The maximum variation of the refractive index possible for the lens is connected to the materials available. For example, polymers are a good alternative, but if the difference in refractive index becomes too big, it is possible that there are no polymers available to cover that refractive index, considering that a lens that is too thick would require a refractive index variation of 1 or more.

- A meniscus has been developed to increase the field-of-view (FoV) in RC telescopes. This meniscus is composed of two hyperbolic surfaces. Both surfaces have the same radius of curvature. Thus, it presents correction for spherical aberration, coma, and axial chromatic aberration. This results in an aplanatic achromat. That means that the meniscus does not change the aplanatic properties of the RC, and does not introduce axial chromatic aberration. The meniscus's overall intrinsic astigmatism is opposite to that of the RC. Therefore, the

astigmatism of the RC is corrected. As a consequence, the FoV for a diffraction limited system of the RC is increased. Moreover, this meniscus, as in the case of the GRIN corrector, can be added or removed from the RC without decreasing the image quality of the original telescope. Even though the meniscus has no field curvature, the residual high-order astigmatism in the system is also flattened. This solution has also been studied not only in a theoretical manner, but the practicality of the solution has also been investigated. The selection of materials and the diameter-to-thickness ratio for astronomical purposes have been taken into consideration. Furthermore, it works for different $F/\#$ and diameters. This meniscus, however, introduces lateral color into the system. The lateral color can be reduced by a proper choice of the distance between the meniscus and the focal point. This work brings an elegant new solution to an old problem. It has been published in Optics Express.

- A pair of lenses has been developed in order to individually optimize astigmatism correction for different spectral bands. The pair is composed of a concave-plano and a plano-convex pair, with the same configuration as the meniscus presented above. However, this solution involves the use of different materials for each lens, with a similar refractive index and different Abbe number. This results in a system that is free from spherical aberration, but that introduces a small amount of coma. The axial chromatic aberration correction presented in the meniscus does not hold. There is a residual axial chromatic aberration as a trade-off for reducing the lateral color present in the meniscus. The pair can correct astigmatism for different spectral bands individually by changing their separation. This is possible because the beam inside of the lenses is collimated, so the other aberrations are not significantly affected. The pair can be placed at a distance farther away from the focal point in order to increase the diameter-to-thickness ratio, easing the manufacturing process of the lens. One of the surfaces of the lenses being flat also helps in the manufacturing process. The solution here can also be applied for different $F/\#$ and diameters. It's practicality has also been considered with the choice of materials being restricted to existing catalogs. The solution can possibly be further improved with new materials.

1.3   Thesis Outline

This thesis is organized as follows:

Chapter 2 addresses geometrical optics and optical aberrations. These principles are utilized in the chapters that follow.

Chapter 3 covers the concepts of stigmatic and aplanatic correction in an optical system. Analytical solutions to aplanatic optical systems are discussed in the following chapters.

Chapter 4 gives an analytical solution for making a pair of GRIN lenses aplanatic. This method enables the creation of an afocal system as well as a field corrector. They are also illustrated in terms of their applications and examples.

Chapter 5 gives an analytical method for estimating an RC telescope's FoV, as well as an analytical solution for increasing it using a meniscus with aspherical surfaces.

Chapter 6 gives an analytical approach for increasing the FoV for various spectral bands in RC telescopes using a quasi-aplanatic refractive pair.

Chapter 7 concludes the thesis, which also includes an overview of future work.

Chapter 2

A review on Optical Aberrations

Image formation involves the projection of an object in three dimensions into an image on a two-dimensional surface [44]. One of the most straightforward optical systems for imaging is the *camera obscura*. A camera obscura is a dark chamber with a small hole, called a pinhole, in one of its sides. The object in front of the hole is projected onto the surface on the opposite side of the hole. Around 500 BCE, the effect of an inverted image through a pinhole was first described by the Chinese philosopher Mozi. Around 300 BCE, the same phenomenon was addressed in the collection of pseudo-Aristotelian *Problemata Physica*, describing gaps between the tree leaves working as several pinholes projecting the solar eclipse on the floor. Around 1000 CE, the Arab physicist Ibn Al-Haytham approached the topic geometrically and mentioned the correlation between the image quality and the aperture size in *On the Shape of the Eclipse* [45, 46]. His experiments demonstrated that there are certain conditions for image formation in a pinhole model. The aperture should not be too wide nor too narrow, a narrow aperture suffers diffraction, and the image is too dim. A wide aperture produces a blurred image due to more rays converging to the same point. Thus, it is crucial to balance the effects from the physical and geometric optics for good image quality by choosing a proper aperture size. The object must be bright, as only an iota of rays reaches the image plane. Therefore, dim objects need more time of exposure, resulting in a blur if the object moves. The box must be dark, as the image generated is dimmer than the object, so the image will not be seen so sharply [46].
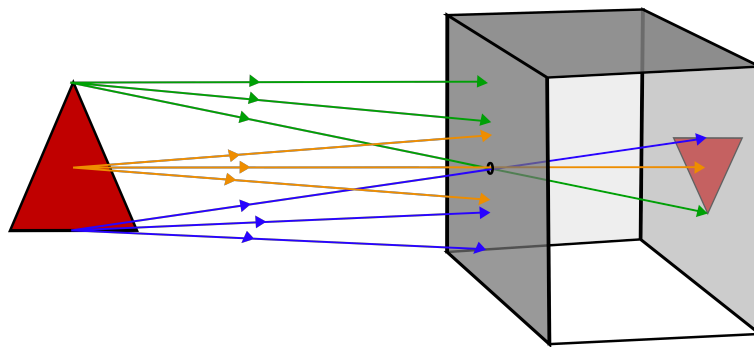
FIGURE 2.1: Representation of a camera obscura.

Figure 2.1 illustrates the layout of a camera obscura. A single ray intercepts each image point in the pinhole model representation, which is achieved by the box's surface blocking most of the rays. The final image is dimmer than the original object and inverted. The image size is dependent on the *focal length*, defined herein in an oversimplified manner as the depth of the box, so the angular magnification is constant unless the object or box position changes [47]. The depth of field (DoF) is the distance range over which the object is still in focus. That is, how much the object

can be shifted without compromising the image quality. It is inversely proportional to the aperture size [7]. Therefore, a pinhole aperture has an almost infinite DoF. The aperture should compromise between the best size for geometric and physical optics for the best image quality. Thus, the diameter of the light patch D is given by the combination of the size of the central maximum in the diffraction pattern for a small pinhole and the aperture size for a larger pinhole, as seen in Eq. (2.1) [48, 49].

$$D = 2r + \frac{f\lambda}{r} \tag{2.1}$$

where r is the radius of the pinhole, f is the *focal length*, and λ is the light wavelength.

The minimum of Eq. (2.1) gives the sharpest image. So the best aperture radius should be proportional to the square of the *focal length* and the wavelength, as seen in Eq. (2.2) [48–50].

$$r = \sqrt{\frac{f\lambda}{2}} \tag{2.2}$$

When the pinhole becomes larger, there is a possible solution for obtaining a good quality image while gathering more light into the image, using an objective lens [44]. A *lens* is an optical device that deviates the angle of a ray's path through refraction. It can either converge or diverge the light unless absorbed or scattered. Different materials refract the light into different angles due to the different refractive indices. Also, depending on their composition, the wavelength range varies as specific wavelengths are absorbed by the material [51]. Refractive index is the ratio between the speed of light in vacuum and the speed of light in a medium, seen in Eq. (2.3). The speed of light in the vacuum, c, is $3x10^8$ m/s, and the refractive index in vacuum shall be denoted as 1.0. As seen in Eq. (2.3), the RI of any other refractive medium is always greater than 1.0, as the light speed in any other material is slower than in vacuum [5], except for special cases such as metamaterials [52].

$$n = \frac{c}{v} \tag{2.3}$$

The speed the light travels in different materials is not constant. It reduces when the material is optically denser, as this density influences how much the light is slowed down. Therefore, the refractive index varies with the wavelength. There are different formulas for calculating the refractive index of a medium. The most straightforward formula is Cauchy's equation, seen in Eq. (2.4). One of the most accurate and widely used formulas is Sellmeier's Equation, seen in Eq. (2.5). The coefficients of this equation include the absorption lines. There are also external factors that might affect the refractive index of a medium, such as temperature, pressure, and impurities in the material's composition [7, 53–55].

$$n(\lambda) = A_0 + \frac{A_1}{\lambda^2} + \frac{A_2}{\lambda^4} \tag{2.4}$$

where A_0, A_1, and A_2 are constants that depend on the medium's properties.

$$n^2(\lambda) = n_0^2 + \frac{B_1\lambda^2}{\lambda^2 - C_1} + \frac{B_2\lambda^2}{\lambda^2 - C_2} + \frac{B_3\lambda^2}{\lambda^2 - C_3} \tag{2.5}$$

where B_1, B_2, B_3, C_1, C_2, and C_3 are constants that depend on the medium's properties.

According to Fermat's principle, also known as the principle of least time, a light ray traveling from one medium to another takes the path between two points, let us

say A and B, in which the optical path length (OPL) is stationary, i.e., a minimum. From all possible paths, the ray takes the one that gives the shortest OPL. The OPL is the sum of the geometrical path length traveled by the ray in a medium multiplied by its refractive index, as seen in Eq. (2.6) for isotropic homogeneous and inhomogeneous mediums. The OPL demonstrates the proportionality of the time for a light ray to propagate between two points. It is essential to notice that when traveling in a homogeneous medium, the ray travels in a straight line [55–57]. As an example, in Fig. 2.2, several possible paths for the ray are illustrated, and the ray takes the one with the least time.

$$OPL(\gamma) = \int_{\gamma} n(\lambda)ds = Min. \tag{2.6}$$

where ds is the geometrical path length, given by the GPL $ds = \sqrt{dx^2 + dy^2 + dz^2}$, and γ is the the curve between two points.
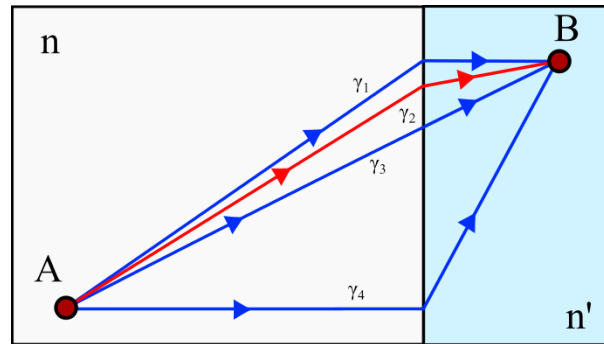
FIGURE 2.2: Illustration of the Fermat's principle. γ_1, γ_2, γ_3, and γ_4 are the possible paths. Considering that $n' > n$, the path taken by the ray that minimizes the OPL is represented in red.

From Fermat's principle, one can easily derive Snell's law. This law states that a ray's direction changes when it travels from one medium to another with different refractive indices, with the relationship between them seen in Eq. (2.7) [58]. The angle between the ray and the normal of the interface between two mediums is called incidence angle, denoted as u, and the refracted or reflected angle is called refracted/reflected angle, denoted as u'. The refractive indices before and after the surface between two mediums are denoted as n and n', respectively, and these notations shall be used for paraxial ray-tracing [56].

$$n \sin(u) = n' \sin(u') \tag{2.7}$$

Figure 2.3 demonstrates planar wavefronts and a ray, $\mathbf{r}$, being refracted or reflected by a surface. In this case in particular, the refractive index n' is higher than n. Therefore, according to Snell's law, the ray angle u' for a refracted ray, $\mathbf{r'_t}$, is smaller than the angle u. As previously mentioned, the velocity of the wavefront is slower in a high RI medium, given by $v_i = \dfrac{c}{n_i}$. And according to Fermat's principle, the OPLs of d_1 and d_2 should be equal. Therefore, the geometrical path of d_2 is smaller than d_1 [7, 54]. For reflection, the reflected angle is the same as the incidence angle, but using the sign convention, they are opposed in sign, and the ray maintains the same geometrical path length. Using Eq. (2.7), it is possible to obtain the refractive index for reflective systems using the previously mentioned relationship between the incident and reflected rays. It is trivial to notice that the refractive index of reflective
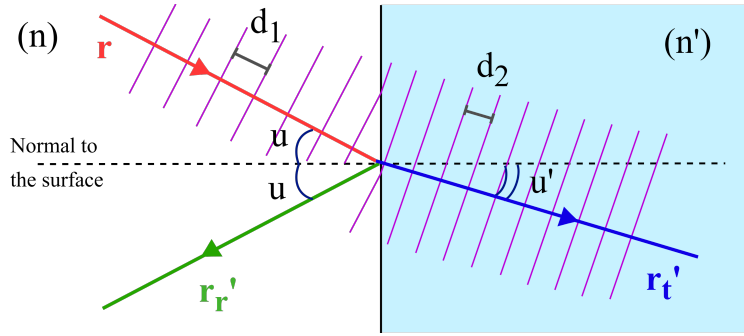
FIGURE 2.3: Representation of Snell's law. The wavefronts are represented in purple. The ray in blue represents a ray being refracted, and the ray in green represents a ray being reflected.

surfaces is given by $-n$ [56].

Not only the RI influence in the rays' deviation, but also the lens' radius of curvature. The greater the RI, and the more curved a surface, the greater the deviation of the ray. Needless to say, the shorter the wavelength, the greater the deviation. The material usually used for a lens is either glass or polymers [54]. The Abbe Number of the material gives the dispersion of a lens by expressing the relationship between the variation of the RI of a lens and the wavelength, as seen in Eq. (2.8). The Abbe number is inversely proportional to dispersion. Therefore, flint glasses present an Abbe number smaller than 50, while it is larger than 50 for crown glasses [55].

$$V = \frac{(n_m - 1)}{(n_s - n_l)} \tag{2.8}$$

where n_m is the middle, n_l is the longest, and n_s is the shortest wavelengths in a spectrum, respectively.

Figure 2.4 demonstrates the variation in refractive index with wavelength for various materials, in specific, glasses. It is possible to notice that the refractive index variation, δn, is higher for shorter wavelengths in most materials. The lenses with a high dispersion are classified as *flint glasses* while the ones with a low dispersion are classified as *crown glasses*. [55].

The simplest and most widely used shape of lenses is spherical. It can be easily manufactured by grinding a rotating glass blank against a rotating diamond tool [55]. The power of a spherical surface, ϕ, is given by the RI and radius of curvature [59].

The most straightforward representation of a lens is a thin lens in air, where the thickness of the lens is neglected, and all the optical powers are provided by the surface's radius of curvature and RI of the material, as seen in the Lensmaker's Equation, in Eq. (2.9). This representation can be helpful as a starting point for an optical lens design [54].

$$\Phi = \phi_1 + \phi_2 = \frac{(n' - n_1)}{n_1 R_1} + \frac{(n_3 - n')}{n_3 R_2} \tag{2.9}$$

where ϕ_1 and ϕ_2 are the optical power of the lens surfaces, R_1 and R_2 are the radii of curvature of the lens, n_1 and n_2 are the RI before and after the lens, and n' is the lens RI.

If a lens focuses a collimated bundle into a real point, it is classified as a convergent or positive lens. Otherwise, if the lens focuses on a virtual point, it is classified
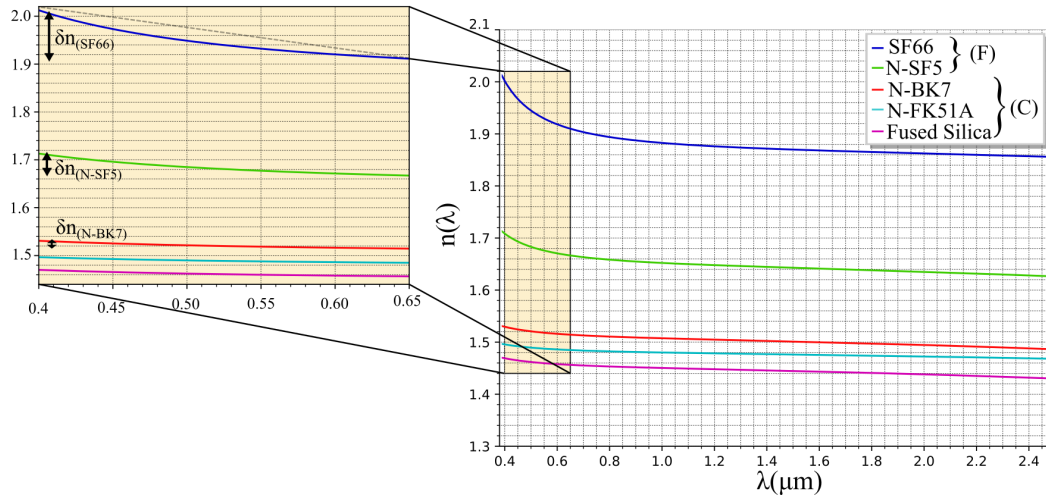
FIGURE 2.4: Refractive index for different materials. The materials with a (C) are crown, while the materials with a (F) are flint. It is noticeable that the flint glasses present a larger variation in RI than the crown glasses.

as a divergent or negative lens [55]. Figure 2.5 illustrates a positive and a negative lens. This classification shall be used in the following chapters.
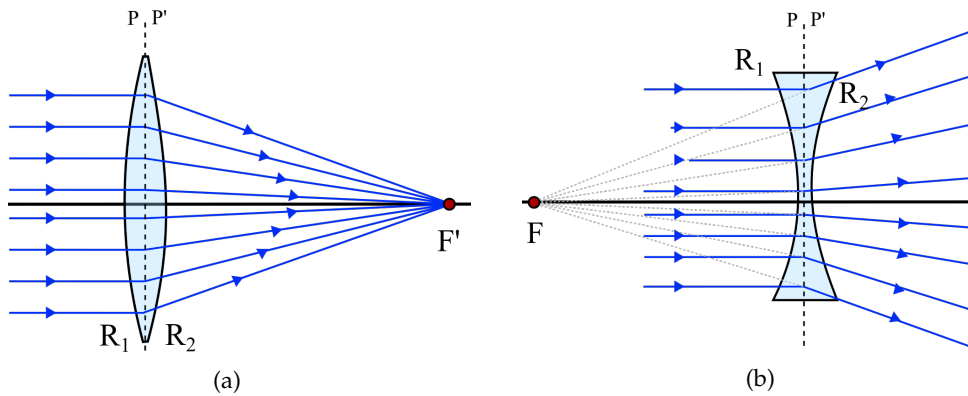
FIGURE 2.5: Ray-tracing through a thin lens that is (a) positive, and (b) negative.

A thick lens, as the name implies, takes into consideration its thickness. Therefore, the calculations are more precise, and the thickness is included in the Lensmaker's Equation, seen in Eq. (2.10) [55].

$$\Phi = \phi_1 + \phi_2 - \frac{\phi_1 \, \phi_2 \, d}{n'} = \frac{n' - n_1}{n_1 \, R_1} + \frac{n_2 - n'}{n_2 \, R_2} - \frac{(n' - n_1) \, (n_2 - n') \, d}{n_1 \, n_2 \, n' \, R_1 \, R_2} \tag{2.10}$$

In contrast to the thin lens approximation, the cardinal points of a thick lens do not coincide. The *principal planes* are not physical planes but fictitious ones. They represent the apparent position in which the rays are refracted inside of a lens. For this, incoming collimated rays from the object space, the left of a lens, and the image space, from the right of the lens are refracted and converged into the focal points F and F'. The principal point can be located by the intersection of the extended incoming and outgoing rays. The principal points define the position of the principal planes that are perpendicular to the optical axis. Not only do individual lenses have

their principal planes, but the whole optical system can also be reduced to two principal planes. Figure 2.6 shows the principal points in green. The focal lengths of a lens or optical system, f and f', are given by the distance from the principal planes to the focal points. [54, 60].

The *nodal points*, represented in yellow in Fig. 2.6, are defined such that a ray that has the same angular magnification in the object and image spaces, i.e., the incoming and outgoing angles are the same as θ, and it is given by the position in which the extrapolation of the incoming and outgoing ray intersects with the optical axis [56]. Therefore, their angular magnification is 1. If the medium before and after the lens is the same, the nodal point coincides with the principal point. Otherwise, their distance to the principal plane is $s_{PN} = s_{P'N'} = \dfrac{(n_2 - n_1)}{\Phi}$, with Φ being the optical power of the lens [54].
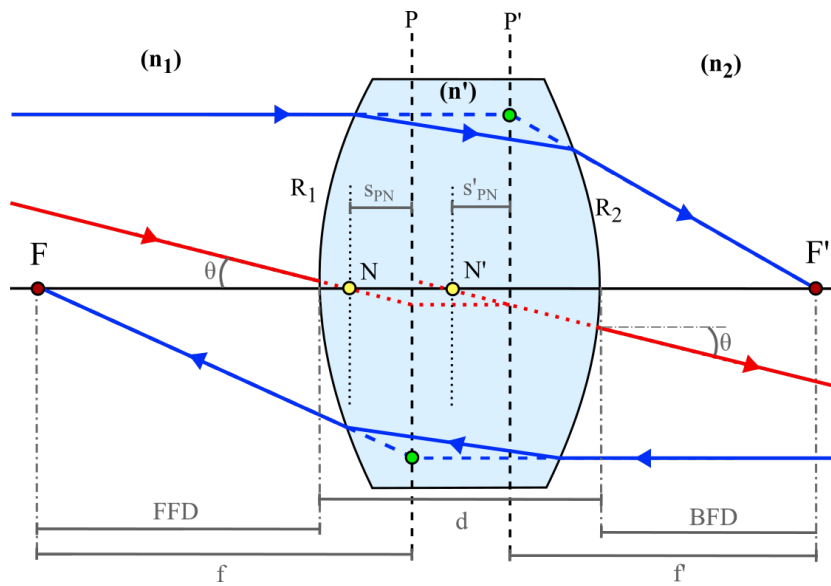
FIGURE 2.6: Ray-tracing in a thick lens showing the principal and nodal planes.

The *cardinal points*, or *Gauss points*, are special points in an optical system. They comprise the pair of focal (F,F'), principal (P,P'), and nodal (N,N') points. They are fundamental in image formation as they are used to trace a ray in an optical system. One can define the position and size of an image for a given object position and size using the cardinal elements position and Snell's law for homogeneous, or Fermat's principle for inhomogeneous mediums [54, 56, 61].

The *paraxial region*, or *Gaussian region*, is the one close to the optical axis, and the rays in this regime are called *paraxial rays*. In *paraxial optics*, or *first-order optics*, approximations are acceptably accurate for calculations in imaging. The first approximation made is for the rays' angle. The sine function can be given by the Taylor expansion, as seen in Eq. (2.11). In the paraxial regime, the angles are relatively small. Therefore, the Taylor series for the sine can be truncated after the first element. Therefore, the sine can be approximated as $\sin(u) = u$. Figure 2.7 shows the discrepancy between the sine of an angle and the Taylor expansion using one or two terms [54, 56, 61].

$$\sin(u) = \sum_{i=0}^{\infty} \frac{(-1)^i}{(2i+1)!} x^{2i+1} = u - \frac{u^3}{3!} + \frac{u^5}{5!} - \frac{u^7}{7!} + O(u^9) \qquad (2.11)$$

As a rule of thumb, the discrepancy should not exceed 3%. Thus, the approximated maximum angle for the approximation using the Taylor expansion with one term is 30°. Two other trigonometric first-order approximations are $\tan(u) = u$ and $\cos(u) = 1$ [54].
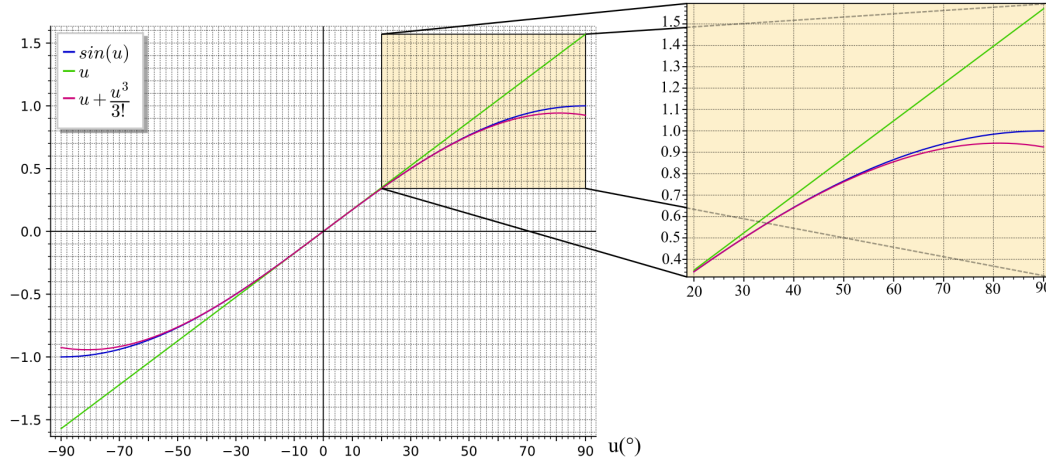
FIGURE 2.7: Representation of the comparison between the sine and the Taylor series truncated with one or two terms.

The sagitta of a surface, represented as z in Fig. 2.8, is the distance from the edge of the lens to its vertex. It is given by a Taylor series as seen in Eq. (2.12). When using the paraxial region, this series can also be reduced to the first term as $z(r) = (c\,r^2)/2$. Another assumption in paraxial optics is the surface being rotationally symmetric about the optical axis [6, 56, 60].

$$z(r) = \frac{1}{2}c\,r^2 + \frac{1}{2^3}c^3\,r^4 + \frac{1}{2^4}c^5\,r^6 + O(r^8) \qquad (2.12)$$

where $r = \sqrt{x^2 + y^2}$, and c is the curvature of the lens given by $1/R$.

The *Aperture Stop* (AS) is an opening that limits the diameter of the beam of axial rays entering an optical system. The ray at the edge of this aperture is called *marginal ray* (MR). The ray from the object edge that crosses the optical axis in the AS position is called the *chief ray* (CR). Those two rays are the most important ones for *Paraxial Ray-tracing*. The *Field Stop* (FS) is an aperture that limits the maximum angle of the incoming rays. Thus, this stop limits the *Field of View* (FoV). The angular FoV is the angle for the maximum object diameter imaged by the system. The linear FoV is the transverse distance to the optical axis that allows the rays to be imaged by the system. For convenience, the *Half Field of View* (HFoV) is frequently used.

The AS and FS do not necessarily have to be physical diaphragm in the system. It can be simply an optical element with a size limiting the height or angle of the incoming rays [7, 56, 60].

The *entrance pupil* (EnP) is the image of the AS from the object space. Its position is found by the intersection of the CR with the optical axis in object space, as represented in yellow in Fig. 2.8, and the MR's height at this position defines the EnP radius. The *exit pupil* (ExP) has the same construction as the EnP, but the CR intersection position, represented in pink, and the MR height at this position are given from the image space. Similarly, the image of the FS is called *Entrance Window* in object space, and *Exit Window* in image space. The *back focal distance* (BFD) is the physical distance between the vertex of the back of the lens and the image space focal point

F, while the *front focal distance* (FFD) is the distance between the vertex of the front of the lens and the object space focal point F' [6, 7, 60].

The angles in object space for the MR and CR are u and $\bar{u}$, while the angles in image space for the MR and CR are u' and $\bar{u}'$, as seen in Fig. 2.8. These notations shall be used in the following chapters.
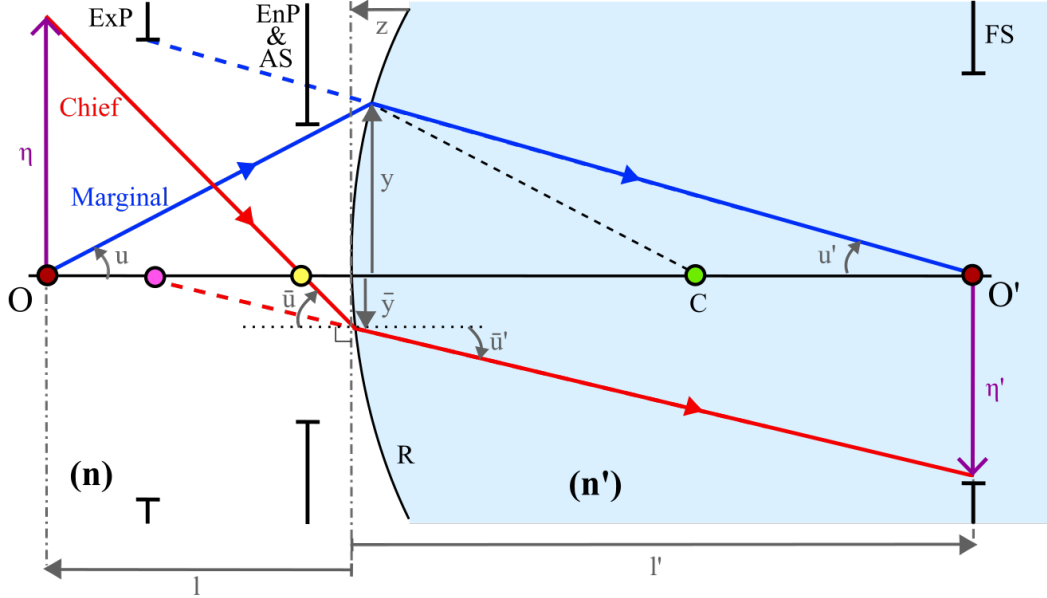
FIGURE 2.8: Ray-tracing of the paraxial marginal and chief rays between two mediums. C is the center of curvature of the surface with radius R.

An object at a distance l from the vertex of a spherical surface produces an image at a distance l' from the same. Thus, one can use the paraxial properties of a single surface to find their relationship with the refractive indices of the mediums encompassing them, as seen in Eq. (2.13).

$$\frac{n'}{l'} - \frac{n}{l} = (n' - n)\,c \tag{2.13}$$

In paraxial optics, a ray is refracted or reflected at the interface between two different mediums. The height at which the CR intersects the surface is $\bar{y}$ and for the MR is y. The angles before and after the interface are $\bar{u}$ and $\bar{u}'$ for the CR, and u and u' for the MR. By knowing that the power of a surface is given by Eq. (2.14), and using Eq. (2.13), one can easily obtain Eq. (2.15). This is known as the *refraction equation* [7, 54–56].

$$\phi = (n' - n)\,c \tag{2.14}$$

$$n'u' = n\,u - y\,c(n' - n) = n\,u - y\,\phi \tag{2.15}$$

Using geometry, one can also obtain the relationship between the height of the ray intersecting different surfaces, as seen in Fig. 2.9. This relationship is demonstrated in Eq. (2.16), this is called the *transfer equation*.

$$y_{i+1} = y_i + u'_i\,d_i \tag{2.16}$$

Equation (2.15) and Eq. (2.16) are used for *paraxial raytracing*. Paraxial ray-tracing is a convenient and straightforward method for calculating the image or object position and height and the angular FoV of an optical system. This approach calculates the ray's height, angle with the optical axis, refractive index, and curvature for each interface in an optical system unto the final image. This type of ray-tracing, in particular, is called the *ynu method*, as it is implied in the name, an approach using the refractive indices, heights, and angles of the rays. Paraxial ray-tracing allows for a ray to be traced in a system with several surfaces [7, 54–56].
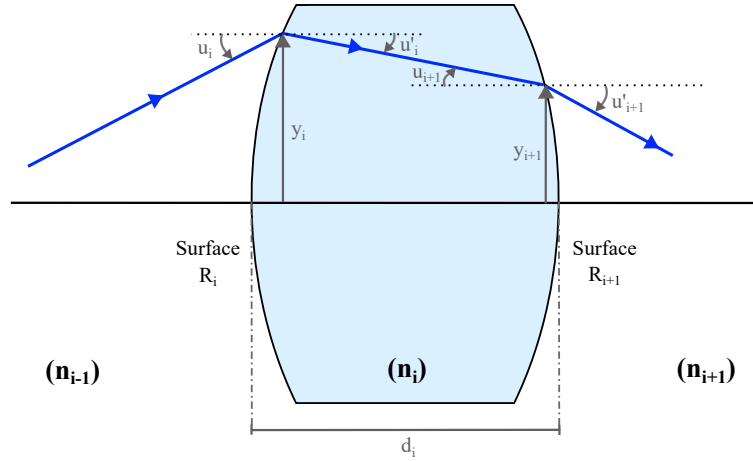
FIGURE 2.9: Ray-tracing through two surfaces.

The *numerical aperture* (NA) of an optical system defines the light cone accepted by the optical system and is given by the RI and angle of the MR in object or image space. The larger the NA, the larger the ray angle. Considering a lens that contains the AS at its edge, for an object at infinity, the distance l' obviously becomes the focal length f'. Therefore, the NA in image space is directly related to the lens's focal length and diameter. Furthermore, this relationship shows a direct relationship between the NA and the *f-number* ($F_{/\#}$). The $F_{/\#}$ defines how fast an optical system is, i.e., how much time is necessary for gathering the same amount of light. A low $F_{/\#}$ presents a larger entrance pupil or shorter focal length, gathering more light in less time than the same lens with a higher $F_{/\#}$. These relationships can be seen in Eq. (2.17) [62].

$$NA' = n' \sin(u') = \frac{n' D}{2 f'} = \frac{n'}{2 F_{/\#}} \tag{2.17}$$

where NA' is the numerical aperture in image space, and $D = 2R$.

The *lateral magnification* of an optical system, m, is given by the ratio between the image and object sizes. The geometry of the triangles for object and image space for the MR can be used to obtain a relationship between the lateral magnification and the NA, as seen in Eq. (2.18). For an afocal system, the lateral magnification is simply the ratio between the height of the collimated bundle in object and image space [54, 55].

$$m = \frac{\eta'}{\eta} = \frac{n \sin(u)}{n' \sin(u')} = \frac{n u}{n' u'} \tag{2.18}$$

Rearranging Eq. (2.18), one can obtain a relationship between the object and image heights and the paraxial numerical aperture in object and image space. This relation is called the *Lagrange invariant*, and it can be seen in Eq. (2.19). The Lagrange invariant shows the relationship between the system's numerical aperture with ray height at each surface, and its value is constant, independent of the ray choice and the number of surfaces. The energy of an optical system is preserved upon both transfer and refraction between surfaces. This invariant is important for calculating aberrations, as will be seen in the following sections [5, 54–56].

$$\eta n u = \eta' n' u' \tag{2.19}$$

In paraxial ray-tracing, both MR and CR are usually the choice of rays traced through the surfaces. As the power of a surface is the same for both rays, it is possible to deduce the relationship between their angles and heights by applying Eq. (2.15) to each one. [7, 54–56].

$$\Lambda = n(\overline{u}\,y - u\,\overline{y}) = n'(\overline{u'}\,y - u'\,\overline{y}) \tag{2.20}$$

In first-order optics, an optical system is assumed to focus a single object point into a single, or *stigmatic*, image point. However, in reality, an optical system suffers from *optical aberrations*. That means that the rays focus on a small area instead of a point, even in a well-corrected system. Optical aberrations are imperfections in an optical system's image. They are classified into two different types, *monochromatic aberrations* and *chromatic aberrations*, as will be seen in Sections 2.2 and 2.1. In the case of well-corrected systems for aberrations, the system still presents a limitation in resolution due to the wave nature of the light, the diffraction of the system's aperture. The diameter of the maximum brightness on the diffraction pattern is called the *Airy disk*. The diffraction happens in an optical element due to the wavelets interfering with each other, so a circular aperture will present an energy distribution around the focal region with a Bessel function shape, i.e., a maximum brightness surrounded by rings with different intensities, as seen in Fig. 2.10a. All the points falling inside of the Airy disk distribution cannot be resolved; for that, they have to satisfy the *Rayleigh Criterion*. The Rayleigh Criterion states that the separation of two point sources, p_1 and p_2, must be not less than the radius of the Airy disk for them to be resolvable, as seen in Fig. 2.10b. In other words, the peak of the central maxima of one Airy disk must coincide with the first minima of the other one. The Rayleigh Criterion can also be given in an angular form, $sin(\alpha)$. The relationships of the Airy disk and Rayleigh Criterion with the $F_{/\#}$ and wavelength is given by Eq. (2.21). A system is said to be diffraction-limited if the optical aberrations are smaller than the Airy disk [54].

$$D_{Airy} = 2.43952\,\lambda\,F_{/\#} = 2\,d_{Rayleigh} = 2\,f\,\sin(\alpha) \tag{2.21}$$

where D_{Airy} is the Airy disk diameter, $d_{Rayleigh}$ is the distance between the two Airy disk's peaks, and $sin(\alpha)$ is the angular resolution.

(a)   (b)
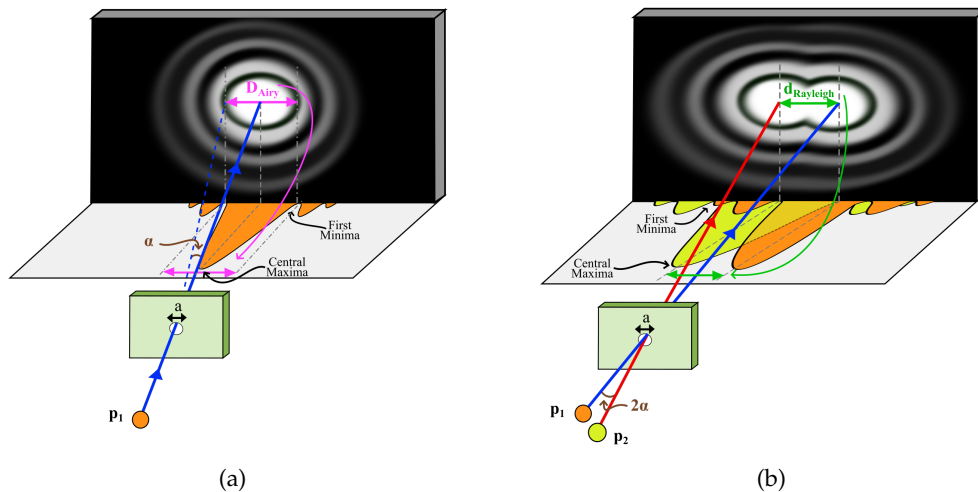
FIGURE 2.10: (*a*) Diffraction pattern for a small aperture demonstrating the Airy disk, and (*b*) two point sources, p_1 and p_2, being resolved by satisfying the Rayleigh Criterion. *a* is the aperture size, and α is the angular resolution.

For a finer detailed image, the optical resolution limit has to be minimal. For that, the $F_{/\#}$ shall be decreased, or the aperture size increased. The *resolving power* is the ability of the optical system to resolve two points in object space. It is given by the inverse of the optical resolution. Thus, the larger the value, the finer the image [5].

The following sections will define each subgroup of the optical aberrations.

2.1 Chromatic Aberrations

Chromatic aberrations are the aberrations in which the image suffers from different wavelengths not focusing at the point. This happens because of the relationship between the wavelength and the refractive index, as previously seen in Eq. (2.4) and Eq. (2.5). For instance, taking the most straightforward refractive index equation presented here, Cauchy's equation seen in Eq. (2.4), truncated after the second term.

This relationship between wavelength and refractive index means that a refractive medium presents a different optical power for each wavelength. As expected, a mirror will not present chromatic aberration.

One can notice that the refractive index is proportional to the inverse of the square of the wavelength. Thus, two equally spaced wavelengths in the spectrum will not be equally spaced in the image plane.

As previously mentioned, different materials present different dispersions, i.e., different rates in which the power of the medium changes with the wavelength.

There are two different chromatic aberrations, *Longitudinal Chromatic Aberration* (LCA) and *Transverse Chromatic Aberration* (TCA) [54].

2.1.1 Longitudinal Chromatic Aberration

LCA occurs with on-axis rays. The rays from different wavelengths focus at different positions in the optical axis as they present different focal lengths due to the different optical powers through the spectrum. Thus, as the name implies, this is a purely longitudinal aberration. Therefore, if the image plane is placed at the position

of one wavelength, the others will be out of focus, either diverging or converging. Consequently, each wavelength presents a different BFL.

Figure 2.11 illustrates the effect of LCA. In this example, using the visible spectrum, the blue wavelength is closer to the lens, while the red wavelength is farther away, with the green in between. Remembering Cauchy's Eq. (2.5), it is trivial to deduce that shorter wavelengths present a high refractive index, and longer wavelengths a low refractive index [5]
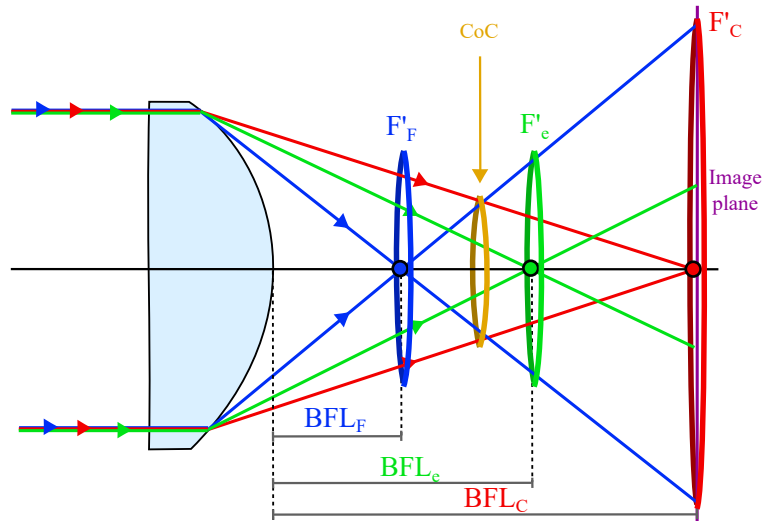
FIGURE 2.11: LCA in an optical system. F_F', F_e', and F_C' are the focal point of the blue, green and red, respectively. CoC is the circle of least confusion. As can be seen, the image plane placed in the CoC position presents the smallest spot size.

If the image plane, for example, is placed at the position of the green focal point, then the blue rays have already focused and started diverging while the red ones are still converging when it intersects the image plane. Therefore, the image formed is a combination of adequately focused wavelengths with others out of focus. The final result of the image plane placed at each of the focal points can be seen in Fig. 2.12. Notice that the system's image is similar to defocus but for different wavelengths. As we place the image plane in one of the wavelength's focal points, we can see that this wavelength focuses in the center of the image plane while the other ones are defocused. The image plane can also be placed in the CoC position so that the spot size due to wavelength defocus is minimized.

The lower the Abbe Number, the higher the dispersion. Furthermore, the higher the refractive index, the lower the Abbe Number. As an example, Fig. 2.13 illustrates the relationship between RI and Abbe Number for different glasses from the Schott catalog for the visible light, with a wavelength classified as the *primary wavelength*, i.e., the wavelength considered as the reference one. The spectral lines considered here are F, d, and C from the Fraunhofer lines. They are associated with the elements Hydrogen blue, Mercury green, and Hydrogen red, respectively. And their wavelengths are $\lambda_F = 486\ nm$, $\lambda_d = 546\ nm$, $\lambda_C = 656.27\ nm$. For simplicity, they shall be simply called blue, yellow, and red from now on. By convention, the spectral line d is frequently considered as the primary wavelength. Equation Eq. (2.22) gives the Abbe Number for the visible spectrum [56].

$$V_e = \frac{(n_d - 1)}{(n_F - n_C)} \tag{2.22}$$
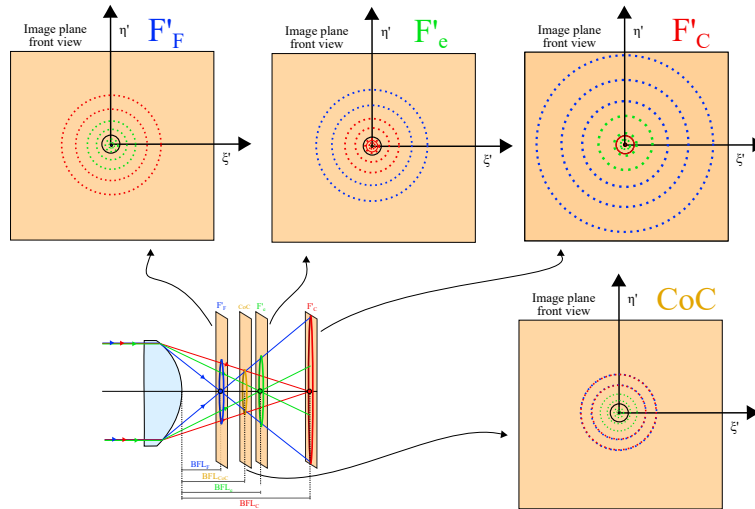
FIGURE 2.12: Zoom of the front view of the image plane for different positions in an optical system with LCA.
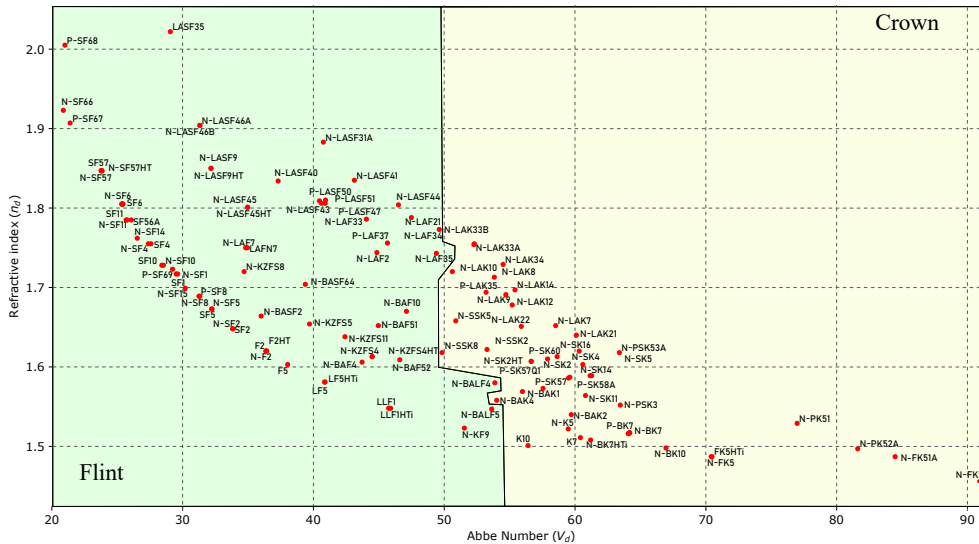
FIGURE 2.13: Relationship between RI and Abbe Number for different glasses from Schott catalog. Best seen with zoom.

where n_e is the green, n_C is the blue, and n_F is the red refractive indices for the same medium, respectively.

Considering the simplified thin lens in air, Eq. (2.23), one can derive the chromatic variation of a lens with the dispersion, δn, of the medium [56].

$$\phi = (n-1)(c_1 - c_2) \tag{2.23}$$

Equation Eq. (2.24) demonstrates not only the relationship mentioned above but also the fact that the radius of curvature is not needed to calculate the variation in optical power as long as the optical power is given.

$$\delta\phi = \delta n(c_1 - c_2) = \phi\frac{\delta n}{(n-1)} \tag{2.24}$$

This aberration is also known as *first-order chromatic aberration* [56].

Due to the difference in refractive indices and Abbe number in different materials, it is possible to combine them in order to balance the dispersion, thus correcting the LCA, especially when combining crown and flint glasses. For this purpose, a converging crown lens is combined with a diverging flint lens. This combination is called a *doublet*. This method only corrects LCA for a pair of wavelengths on opposite positions in the spectrum. Thus, if one wants to correct more wavelengths, adding more lenses to the system is necessary. The residual chromatic aberration in the system is called *Secondary Spectrum* [56]. The doublet can be cemented or spaced. The spaced doublet adds more degrees of freedom for aberration correction than the cemented one. Figure 2.14 illustrates a doublet focusing rays with different wavelengths. The secondary spectrum, $\delta BFL_{(F-d)}$, is the distance between the BFL of the F and d wavelengths. This results in the yellow wavelength suffering from defocus if the image plane is located at the focal point of the blue and the red wavelengths.
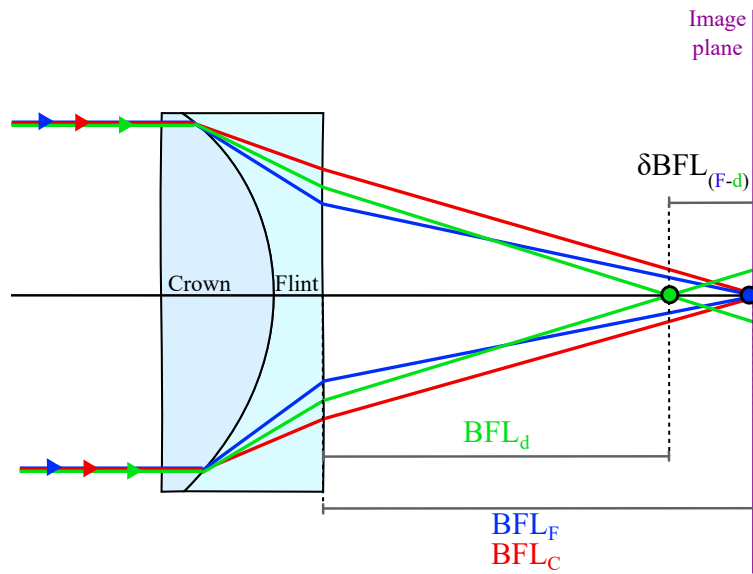
FIGURE 2.14: Secondary spectrum in a doublet corrected for two wavelengths, in this case, red and blue. The central wavelength, yellow, is seen at a distance $\delta BDL_{(F-d)}$ from the other two. Notice that the yellow wavelength is illustrated in green for image clarity purposes.

Figure 2.15 illustrates the characteristic BFD curve of a thin lens for different wavelengths in a system with secondary spectrum. As can be noticed, as aforementioned, there are several pairs of wavelengths with the same BFD. In this example, in which the spectral bands F and C are the same, the BFL difference between them and the spectral band d can be seen [56].

The condition for a system to have the primary spectrum corrected is that the difference in the power variation between two wavelengths in a spectrum to be equal to zero, as seen in Eq. (2.25).

$$\delta\Phi_{(C-F)} = 0 \tag{2.25}$$

Therefore, combining Eq. (2.22) and Eq. (2.25) gives the relationship between the optical power and Abbe number for each element of the doublet to correct LCA in Eq. (2.26) [56].

$$\frac{\phi_1}{V_1} + \frac{\phi_2}{V_2} = 0 \tag{2.26}$$
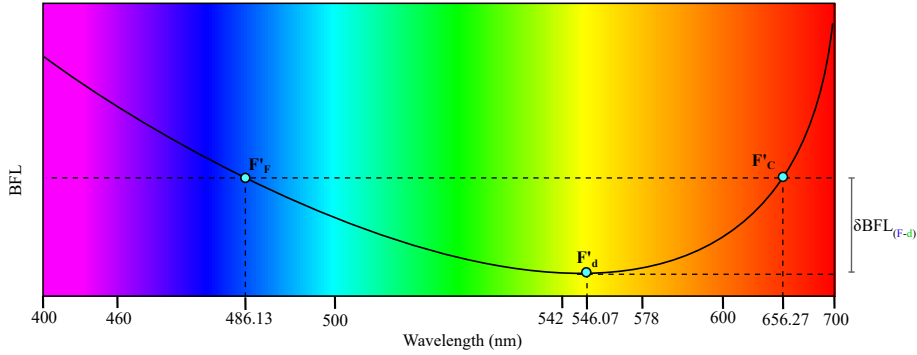
FIGURE 2.15: Secondary spectrum in an achromat for the spectral bands F, C, and d.

Remembering that the optical power of an optical system in a thin lens approximation is the sum of the individual optical powers, as seen in Eq. (2.9), one can deduce the optical power necessary for each individual element as seen in Eqs. (2.27) and (2.28). Thus, each optical element shall have the same optical power but with opposite signs to cancel out and correct LCA [56].

$$\phi_1 = \frac{\phi \, V_1}{V_1 - V_2} \tag{2.27}$$

and

$$\phi_2 = \frac{-\phi \, V_2}{V_1 - V_2} \tag{2.28}$$

One can also use the space between the lenses to their advantage to correct LCA. For instance, it is even possible to correct LCA using two lenses with the same material if the distance between them is properly chosen. In this case, one can calculate what is the optimal distance by using the thick lens equation. For instance, the distance in the equation shall be taken as the distance between the thin lenses. Using Eq. (2.23), one can obtain the overall optical system of the thin lens using the same material combined, as in Eq. (2.29) [63].

$$\Phi = \phi_1 + \phi_2 - \phi_1 \, \phi_2 \, d \tag{2.29}$$

For convenience, the terms $(c_1 - c_2)$ for the curvature of a lens shall be denoted as C_i. Thus, this term for the first lens shall be denoted as C_1 and the second lens C_2. Using Eqs. (2.23) and (2.29) leads to Eq. (2.30).

$$\Phi = (n - 1) \, C_1 + (n - 1) \, C_2 - (n - 1)^2 \, C_1 \, C_2 \, d \tag{2.30}$$

In order to make the system achromatic, the derivative of Eq. (2.30) as a function of the refractive index should be zero, as seen in Eq. (2.25). This gives Eq. (2.31).

$$\frac{\delta \Phi}{\delta n} = C_1 + C_2 - 2 \, (n - 1) \, C_1 \, C_2 \, d = 0 \tag{2.31}$$

For practical purposes, multiplying Eq. (2.31) by $(n - 1)$ transforms the equation in terms of optical power instead of C_1. Moreover, with this, it is possible to obtain the relationship between the lenses' distance and the optical power of each one, as seen in Eq. (2.32).

$$d = \frac{\phi_1 + \phi_2}{2 \, \phi_1 \, \phi_2} \tag{2.32}$$

As this derivation takes the thin lenses approach into consideration, one can also use the approximation $\phi = \frac{1}{f}$ to obtain what is the distance between the lenses in function of their focal lengths, as in Eq. (2.33).

$$d = \frac{f_1 + f_2}{2} \tag{2.33}$$

When the power of the individual elements is not exactly the same, the residual LCA can be calculated, for example, by the difference in optical power of the doublet using the helium yellow (d) and hydrogen red (F) spectrum range [56]. This relation can be seen in Eq. (2.34) for a doublet.

$$\delta\Phi_{(d-F)} = \left(\frac{\phi_1}{V_{1\,(d-F)}} + \frac{\phi_2}{V_{2\,(d-F)}} \right) = 0 \tag{2.34}$$

where $V_{1\,(d-F)}$ and $V_{2\,(d-F)}$ are the specific Abbe numbers for the spectrum ranging from the spectral line d to F for each lens of the doublet.

The Abbe number for this range is given by Eq. (2.35).

$$V_{(d-F)} = \frac{(n_d - 1)}{(n_F - n_d)} \tag{2.35}$$

The relative partial dispersion is given by their relationship with the refractive indices or the Abbe number for the C to F lines range, and for the d to F lines range, as seen in Eq. (2.36).

$$p = \frac{(n_F - n_d)}{(n_F - n_d)} = \frac{V_{(C-F)}}{V_{(d-F)}} \tag{2.36}$$

Thus, it is possible to express Eq. (2.34) in terms of partial dispersion, Abbe number, and overall optical power of a system. This relation can be seen in Eq. (2.37).

$$\delta\phi_{(d-F)} = \Phi \frac{(p_1 - p_2)}{(V_1 - V_2)} = 0 \tag{2.37}$$

From Eq. (2.37), one can notice that, for a system to be free from secondary spectrum, there are two conditions to be fulfilled. The first one is that the Abbe number of the glasses should be different, but the relative partial dispersion should be equal [56].

2.1.2 Transverse Chromatic Aberration

The magnification of an optical system is wavelength-dependent. The chief ray of off-axis rays sits at different positions along the image plane for each wavelength, presenting a transversal displacement. That means the image size changes for different wavelengths. This displacement is called *Transverse Chromatic Aberration* (TCA) or *lateral color*. As seen in Fig. 2.16, they are caused by the angular offset, $\theta_{(F-C)}$, of the outgoing chief rays [64]. This effect is commonly seen in prisms separating white light into several colors. In addition, the magnitude of TCA is affected by the position of the AS. This occurs because the AS positioning alters the system's chief rays.

As seen in Eq. (2.38), the TCA can be quantified as the difference $\delta\eta_{(F-C)}$ in the height of the focal point of two extreme rays, in this case, blue and red.

$$\delta\eta_{(F-C)} = \eta_C - \eta_F \tag{2.38}$$
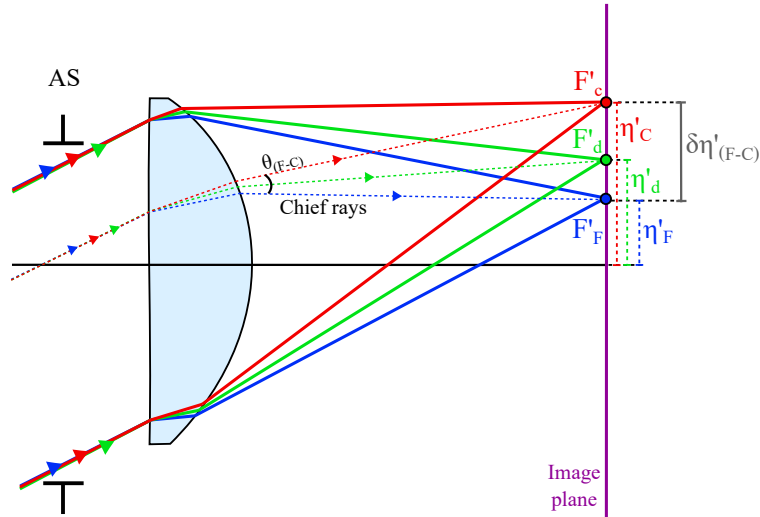
FIGURE 2.16: Transverse chromatic aberration in an optical system. Again, the yellow wavelength is being represented by the green color.

In reality, the PP of different wavelengths do not coincide in a system with TCA, as seen in Fig. 2.17 [64]. However, as the system's distance to the image plane is usually significantly larger than the distance between the PPs, this first approximation is often used [55].
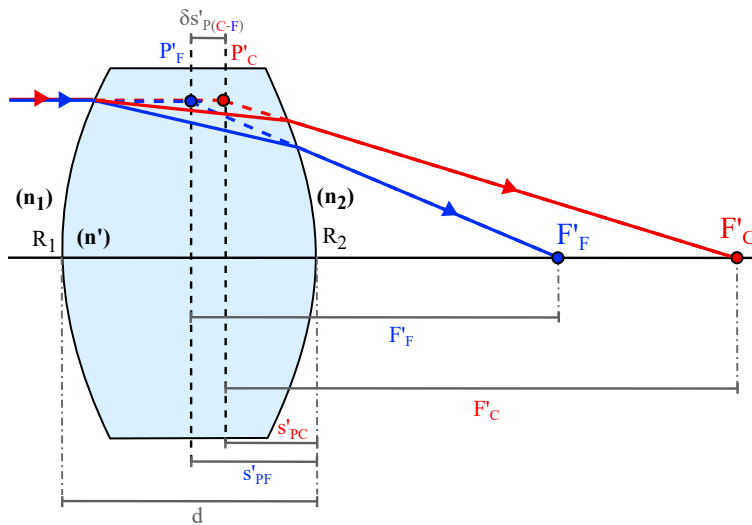
FIGURE 2.17: Principal planes for different wavelengths not coinciding.

Equation (2.39) demonstrates the relationship between the principal plane and the back surface of a lens.

$$s'_P = \frac{-F'(n(\lambda) - 1)d}{R_1 n(\lambda)} \tag{2.39}$$

It is clear that the distance from the principal plane to the lens's back surface depends on the refractive index, and therefore depends on the wavelength.

The distance between the principal planes can be quantified by using Eq. (2.39) for each wavelength, resulting in Eq. (2.40).

$$\delta s'_{P(C-F)} = \frac{-d}{R_1}\left[(F_F - F_C) - \frac{(F_F n_c - F_C - F_C n_F)}{n_C n_F}\right] \tag{2.40}$$

In this case, in which the distance between the principal planes is not neglected, the primary lateral color can be calculated in function of the distance between the principal planes and the angle formed by one of the principal rays with the optical axis, as seen in Fig. 2.18. Equation (2.41) shows this relationship [64].
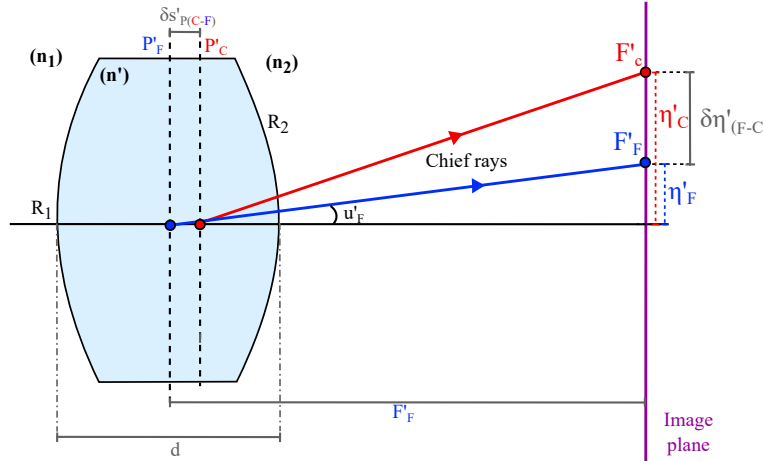
FIGURE 2.18: TCA in a lens considering the distinct PP of different wavelengths.

$$TCA = \delta s'_{P(C-F)} tan(u'F) = \delta s'_{P(C-F)} \frac{\eta'_F}{F'_F} \tag{2.41}$$

2.2 Monochromatic Aberrations

Monochromatic aberrations are imperfections in the image that do not depend on the wavelength of the light. They are directly related to the aperture and field of an optical system. The larger the aperture or field, the larger the optical aberrations. The rays, in this case, deviate from the paraxial region. Two approaches can be used to quantify the monochromatic aberrations by using a ray or a wave perspective. A reference sphere (RS) is used as the ideal wavefront with radius R_{rs}, and an aberrated with radius R_{ab} does not coincide with the RS, neither does their rays. The rays from the RS do not have the same OPL as the rays from an aberrated wavefront. Commonly, the intersection of the CR with the image plane can also be used as the reference point of an ideal system in imaging. Other rays are then traced to quantify the deviation of their focal point from the reference one. In the ray perspective, the aberrations can be divided into longitudinal and transverse. The transverse aberrations, $\delta\xi'$ in the x-axis and $\delta\eta'$ in the y-axis, can be quantified by the axial distance from the position in which a ray intersects the image plane of the reference point. The longitudinal aberrations, δz, can be quantified as the distance of a ray intersecting the optical axis and the reference point. In addition, for particular cases, in which the image is at infinity, i.e., a collimated beam, the aberrations can also be quantified as a function of the angle between a ray and the CR, $\delta u'$. This is called angular aberration. In the wave perspective, the wavefront aberration, δW, is quantified as the displacement of the aberrated wavefront from the RS where all

rays focus at a single point [54]. Figure 2.19 illustrates the wave and ray aberrations in an optical system.
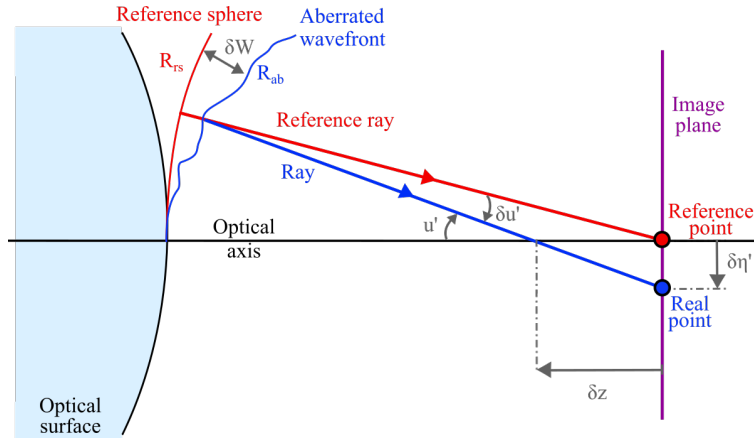
FIGURE 2.19: Wave and ray aberrations.

The transverse aberrations in terms of angular displacement is given by $\delta\xi' = R_{rs}\delta u'$ in the x-axis, and $\delta\eta' = R_{rs}\delta u'_y$ in the y-axis. The angle $\delta u'_{x,y}$ can be defined in terms of the wavefront as Eqs. (2.42) and (2.43) [56].

$$\delta u'_x = \frac{-1}{n'}\frac{\delta W}{\delta x} \tag{2.42}$$

$$\delta u'_y = \frac{-1}{n'}\frac{\delta W}{\delta y} \tag{2.43}$$

The RS's location is commonly not known so that one can define relative pupil coordinates x_{rel} and y_{rel} as the ratio between the RS and the marginal ray coordinate, as seen in Eqs. (2.44) and (2.45). As these coordinates are relative, their values vary between -1 and 1 [56].

$$x_{rel} = \frac{x_{rs}}{x_{marg}} \tag{2.44}$$

$$y_{rel} = \frac{y_{rs}}{y_{marg}} \tag{2.45}$$

The transversal displacements can be then given as Eqs. (2.46) and (2.47).

$$\delta\xi' = \frac{-1}{n'\sin(u')}\frac{\delta W}{\delta x_{rel}} \tag{2.46}$$

$$\delta\eta' = \frac{-1}{n'\sin(u')}\frac{\delta W}{\delta y_{rel}} \tag{2.47}$$

Considering that Eqs. (2.46) and (2.47) have a differential relationship, the wavefront can be given in an integral form by Eq. (2.48) and Eq. (2.49) [56].

$$W_x = n'\sin(u')\,R_{rs}\int \delta\xi'\,dx \tag{2.48}$$

$$W_y = n'\sin(u')\,R_{rs}\int \delta\eta'\,dy \tag{2.49}$$

The wavefront aberration can be described by $W(x, y, \xi', \eta')$, and due to the symmetry of the system, it can be defined using the polar coordinates of the pupil. Figure 2.20 shows the diagram of the coordinate axis for the meridional (y-axis) and sagittal (x-axis) planes. The axes x and y in the pupil are parallel to the ξ' and η' in the image plane, respective. The polar coordinates are given by $r^2 = x^2 + y^2$, $x = r \sin(\phi)$, and $y = r \cos(\phi)$. Considering an optically centered lens that is rotationally symmetric in the optical axis, one can simplify the wavefront in terms of r, η, and ϕ. The triangle ABC gives the dependence of the wavefront aberration on the terms of the sides of the triangle, given by η^2, r^2, and $r^2 + \eta^2 - 2\eta r \cos(\phi)$, with the latter simplified as $\eta r \cos(\phi)$ as the other terms are already previously included [54, 56].
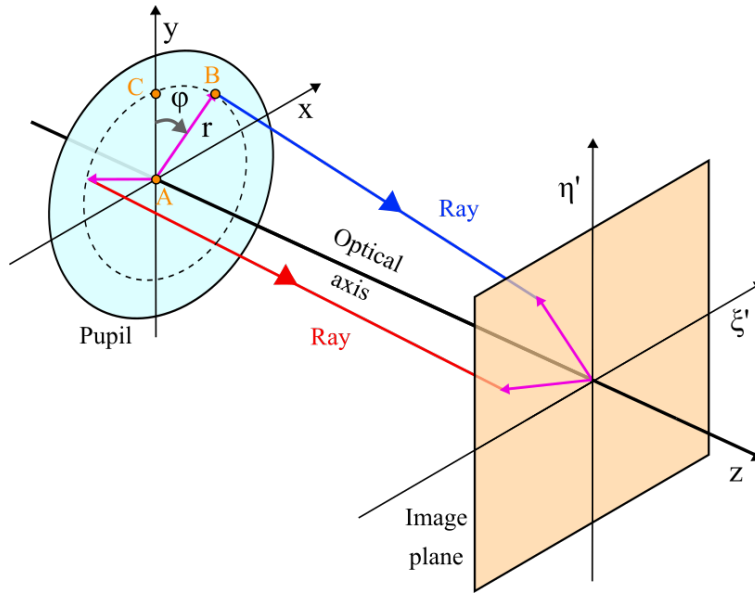
FIGURE 2.20: Optical aberrations in polar coordinates.

The wavefront aberrations can be expanded into a power series with a Taylor expansion using the three variables aforementioned. Each term is correlated with different types of aberration, and the most relevant terms are the third-order aberrations, demonstrated in Eq. (2.50) [54, 56].

$$W(\eta, r, \phi) = \underbrace{\overbrace{w_{020}\, r^2}^{\text{Not real aberration}}}_{\text{Defocus}} + \underbrace{w_{111}\, \eta\, r \cos(\phi)}_{\text{Tilt}} + \underbrace{w_{040}\, r^4}_{\text{Spherical}} + \underbrace{w_{131}\, \eta\, r^3 \cos(\phi)}_{\text{Coma}} + \underbrace{w_{222}\, \eta^2\, r^2 \cos^2(\phi)}_{\text{Astigmatism}} +$$

$$\underbrace{w_{220}\, \eta^2\, r^2}_{\text{Field Curvature}} + \underbrace{w_{311}\, \eta^3\, r \cos(\phi)}_{\text{Distortion}}$$

(2.50)

The notation W_{ijk} for power series expansion of the wavefront gives a direct relation between the suffixes i, j, and k and the power of the terms r, η, and ϕ, as seen in Eq. (2.51). The usefulness of these relations is the straightforward identification of the aberrations' nature by knowing the suffixes [56].

$$W_{ijk}(\eta, r, \phi) = \sum_{i,j,k} w_{ijk}\, \eta^i\, r^j\, \cos^k(\phi)$$

(2.51)

The only on-axis monochromatic aberration is SA. And the off-axis monochromatic aberrations are *coma*, *astigmatism*, *field curvature*, and *distortion*.

2.2.1 Defocus and Tilt

The first two terms of Eq. (2.50) are *Defocus* and *Tilt* are the *First-order aberrations*. This name is given by the sum of the exponents of their variables η and r in ray aberrations being equal to 1. In terms of wavefront aberration, this sum is equal to 2. The first-order aberrations are not considered real aberrations as they do not compromise the image quality as they still produce a stigmatic focal point. They are simply a mismatch between the formed image's position or angle and the image plane of the RS [54, 56].

Defocus is simply the image plane being closer or farther than the image formation of an optical system. This can be fixed by moving the image plane or the optical system to match them. As demonstrated in Fig. 2.21, the RS wavefront focuses in the image plane, with the aberrated wavefront focusing on the optical axis with a shift from the reference point by a distance δz. The wavefront aberration of defocus is given by $w_{020} r^2$, or $w_{020} y^2$ considering the rotational symmetry of the system around the optical axis. The transverse ray aberration of defocus can be quantified using Eq. (2.47) and the defocus term $w_{020} r^2$, obtaining Eq. (2.52) [56].
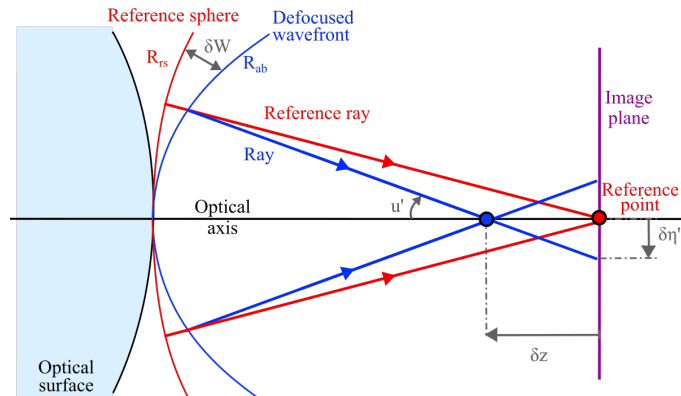
FIGURE 2.21: Defocus on an optical system.

$$\delta\eta' = \frac{-2\,y}{n'\,\sin(u')} w_{020} \tag{2.52}$$

The defocus ray aberration can also be quantified in terms of δz, as seen in Eq. (2.53) [54].

$$W_{def} = \frac{-n'}{2}\delta z\,\sin^2(u') \tag{2.53}$$

An image plane positioned at the focal point of the RS results in the real rays reaching the image plane creating equally spaced rings. Figure 2.22 illustrates the rays intersecting the image plane in a system with defocus. The front view of the image plane being intersected by the rays is called a *Spot Diagram*. This is a valuable tool to quickly identify the possible aberrations present in an optical system. It is not as accurate as other methods, but as different aberrations present different shapes of the spot diagram, it can work as a starting point for identifying the aberrations [56].
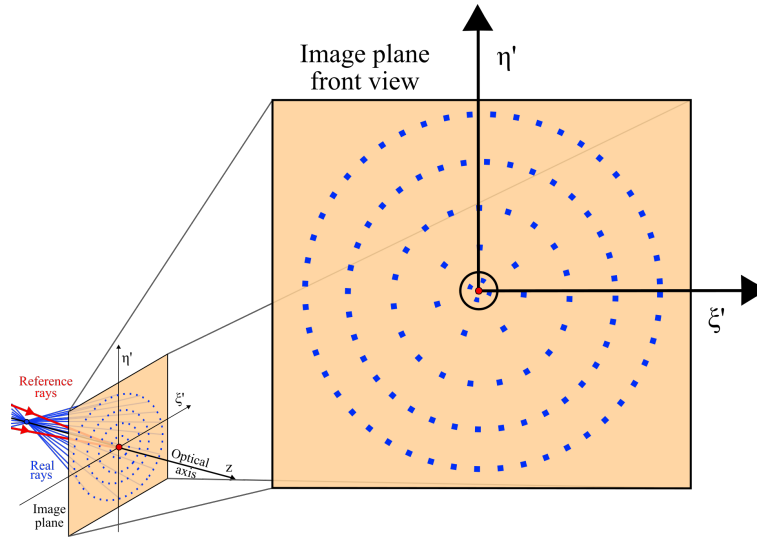
FIGURE 2.22: Zoom of the front view of the image plane in an optical system with defocus.

Tilt occurs when the wavefront is at an angle with the RS, presenting an angle mismatch, θ, between the aberrated and the RS rays. This results in a lateral displacement between the image point of the wavefront and the RS image, as seen in Fig. 2.23. The transverse aberration can be quantified by Eq. (2.54). The wavefront aberration of tilt is given by $w_{111}\,\eta\,r\cos(\phi)$ or $w_{111}\,\eta\,y$ [56].
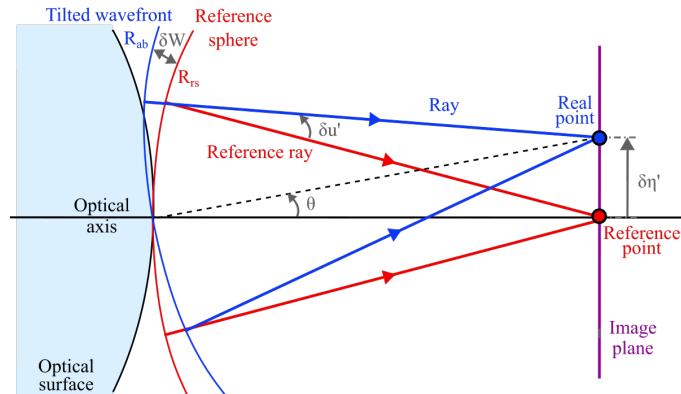
FIGURE 2.23: Tilt in an optical system.

$$\delta\eta' = \frac{-\eta'}{n'\sin(u')}w_{111} \tag{2.54}$$

The tilt ray aberration can also be quantified in terms of the angle between the rays θ, as seen in Eq. (2.55) [54].

$$W_{tilt} = -n\,r\,\theta\,\cos(\phi) = -\frac{n\,y\,\delta\eta'}{R_{rs}} \tag{2.55}$$

Equation (2.54) shows that the transverse aberration of a system with tilt is constant once the image size η' is defined. It is trivial to notice that the tilt will still produce a stigmatic focal point. However, this point is laterally displaced. Thus, the object size is proportional to the displacement of the image. Figure 2.24 shows the difference in magnification of the optical system, with the point in blue being the

location of the focal point of the aberrated wavefront, while the red point shows the reference point [56].
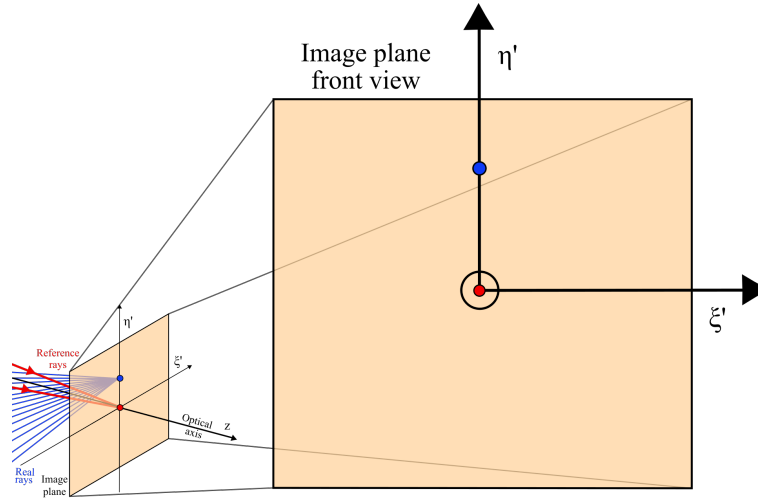
FIGURE 2.24: Zoom of the front view of the image plane in an optical system with tilt.

2.2.2 Spherical Aberration

SA depends only on the pupil radius, and this is the only on-axis monochromatic aberration. This occurs because of the difference in optical power of a spherical surface depending on the angle of the incoming collimated ray and the normal to the surface at different heights. Thus, rays from different pupil radii focus at different positions along the optical axis [59]. As seen in Fig. 2.25, the angle of a collimated bundle with a spherical surface varies depending on the ray height when the surface is intersected. The central region presents a slight variation between these angles, so the paraxial approximation is valid. Therefore, the rays from the aperture zones in the central region focus the rays relatively close to each other in the optical axis. As the height of the rays moves towards the edge of a surface, the increase in the angle between the rays and the normal to the surface evidently increases, so the paraxial approximation ceases to be sufficiently accurate in those zones. Using Snell's law, it is trivial to notice that the paraxial zone is less refracted than the rays farther from the optical axis. Thus, the paraxial rays focus on the optical axis farther away from the surface than the marginal rays. The spherical ray aberration is proportional to r^3, while the wavefront aberration is proportional to r^4. This aberration does not depend on the field η' or the azimuth ϕ [56].

The faster the system, i.e., the smaller the $F_{/\#}$, the more SA it will present. On the other hand, the smaller the radius of curvature, the higher the curvature; therefore, the system also presents more SA due to the more significant variance in the angles between the rays from different aperture zones and the normal to the surface.

The longitudinal aberration, δz is simply given by the distance between the closest focal point to the surface, and the farthest focal point, as seen in Fig. 2.25 as the focal points F_1' and F_5', this relation can be seen in Eq. (2.56) [7].

$$\delta z = F_5' - F_1' \tag{2.56}$$

The transverse aberration is given by the distance between the reference point in the image plane and the height of the farthest ray intersecting the image plane. The
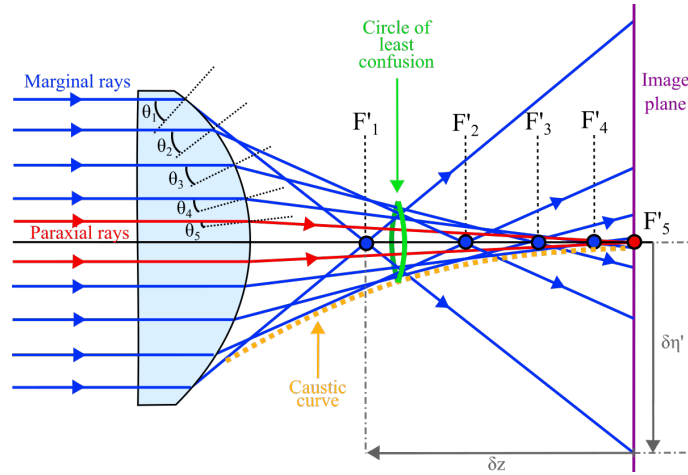
FIGURE 2.25: SA in an optical system.

transverse aberration is given by Eq. (2.57) for the x-z axis, and by Eq. (2.58) for the y-z axis. One can easily notice that both axes have a similar solution, and that is due to the rotational symmetry of the system around the optical axis [59].

$$\delta \xi' = \frac{-4\,x^3}{n'\,\sin(u')}w_{040} \tag{2.57}$$

$$\delta \eta' = \frac{-4\,y^3}{n'\,\sin(u')}w_{040} \tag{2.58}$$

The SA wavefront is given by Eq. (2.59).

$$W_{SA} = w_{040}\,r^4 = w_{040}\,(x^2 + y^2)^2 \tag{2.59}$$

Due to the nature of the focal points being at different positions in the optical axis for different aperture zones, the image plane has to be chosen properly to minimize the spot size. The optimal position is a compromise between the paraxial and marginal rays. That is, the position in which the waist of the beam is the smallest. This position is known as the *Circle of Least Confusion* (CoC). Figure 2.26 illustrates the image plane in three different positions. The orange plane is the position of the marginal rays' focal point, the green plane is the position of the CoC, and the pink plane is the position of the paraxial rays' focal point. As can be seen, the smallest spot can be achieved by the position of the CoC. The spot size is still suffering from SA, but the majority of the energy in the system is in the central region [56].

The curve formed by the outgoing beam's height concerning different focal lengths in the optical axis is called the *Caustic Curve*; it is illustrated in orange in Fig. 2.25 [65].

Both defocus and SA present a spot diagram with rings surrounding the reference point. However, while defocus presents a constant energy distribution through the equally spaced rings, as in Fig. 2.22, SA presents an energy distribution in which the rings are not equally spaced, as seen in Fig. 2.27 [56]. Therefore, they can be combined in order to decrease the spot size. Thus, the CoC is the optimal position in which the defocus balances SA in an optical system.
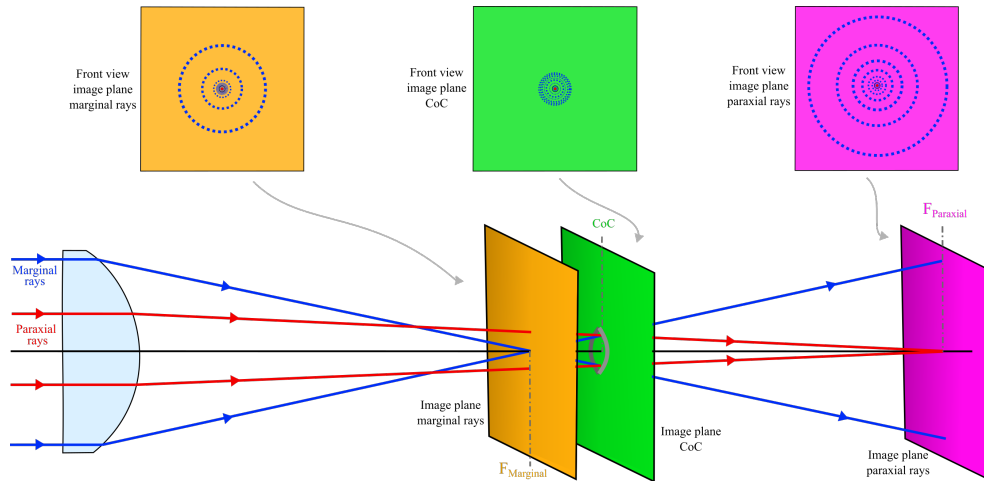
FIGURE 2.26: CoC in an optical system with SA.
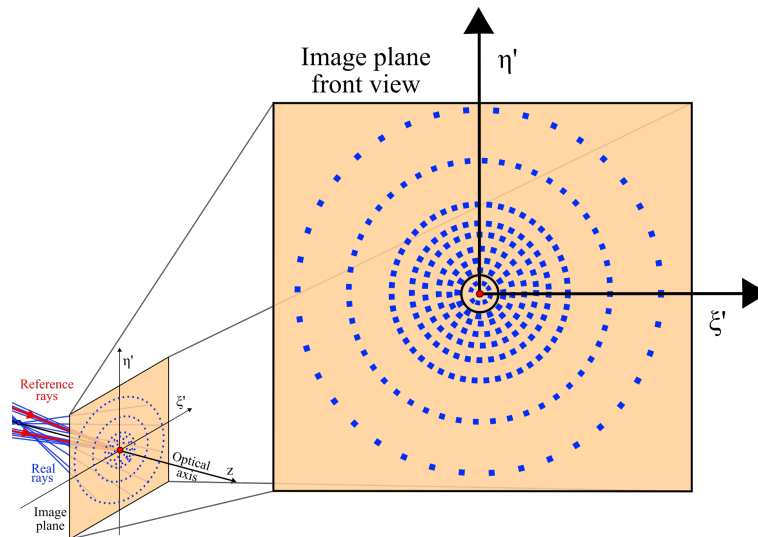
FIGURE 2.27: Zoom of the front view of the image plane in an optical system with SA.

2.2.3 Coma

The symmetry of the surfaces of an optical element is not maintained for an off-axis incident beam. Therefore, the angle at which the bundle meets the surface is different depending on the annular zone of the surface. As a result, different aperture zones of an optical element focus the rays into different transversal positions, presenting a comet-like image shape aberration known as coma. Similar to SA, the marginal rays focus in a different position from the chief ray. Unlike SA, the aperture size is not the only term influencing how much aberration is present in the system, but also the angle of the oblique rays. Thus, the larger the aperture size or field angle, the larger the coma present in the system. This is given by the fact that the focal point position of the aperture zones becomes more evident and farther away from each other as the field angle increases [5]. Figure 2.28 shows the geometry of coma. Different annular zones present different magnifications. Thus, each zone images at different heights; not only that, the shape of the image formed for different aperture zones is circular.

In the case of off-axis aberrations, the reference point does not necessarily lie in
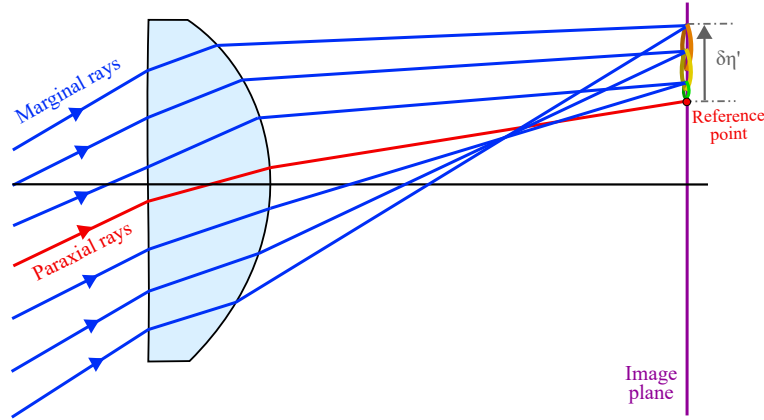
FIGURE 2.28: Coma in an optical system.

the optical axis, and the centroid of the spot diagram can be used as the reference. The coordinates of the centroid can be given by Eqs. (2.60) and (2.61).

$$\Delta x_c = \frac{1}{N} \sum_j \Delta x_j \tag{2.60}$$

$$\Delta y_c = \frac{1}{N} \sum_j \Delta y_j \tag{2.61}$$

where N is the total number of rays being traced and j is the index for each ray.

The *Root-Mean-Square* (RMS), or *Gaussian Moment*, uses the centroid as reference to calculate the deviation of the rays in the image plane, the RMS radius is given by Eq. (2.62) [66].

$$\Delta r_{RMS} = \sqrt{\frac{1}{N} \sum_j [(\Delta x_j - \Delta x_c)^2 + (\Delta y_j - \Delta y_c)^2]} \tag{2.62}$$

Sagittal coma is the difference between the reference point and the closest point of the circle formed by the largest annular zone of the pupil. Tangential coma is the difference between the reference point and the farthest point of the circle formed by the same aperture zone [66]. The area of the sagittal coma concentrates a significant proportion of the energy in the system [7]. Figure 2.29 illustrates the sagittal and tangential coma.

Coma is one of the aberrations considered as the most compromising to the image quality because the asymmetry makes it challenging to find the image position and the optimal CoC [5]. The wavefront aberration for coma s given by Eq. (2.63). One can quickly notice that the wavefront in the y-z plane is proportional to y^3, while it is 0 in the x-z axis [56].

$$W = w_{131}\, \eta\, r^3 \cos\phi = w_{131}\, \eta\, (x^2 + y^2)\, y = w_{131}\, \eta\, r^2\, y \tag{2.63}$$

Coma can also be quantified in terms of transverse aberrations as shown in Eqs. (2.64) and (2.65).

$$\delta\eta' = \frac{-3}{n' \sin u'} w_{131}\, \eta'\, y^2 \tag{2.64}$$

$$\delta\xi = 0 \tag{2.65}$$

As seen in Eq. (2.64), coma is proportional to the field angle η'. Thus, this is one of the off-axis aberrations that affect an optical system quality the most, even for small angles [56].
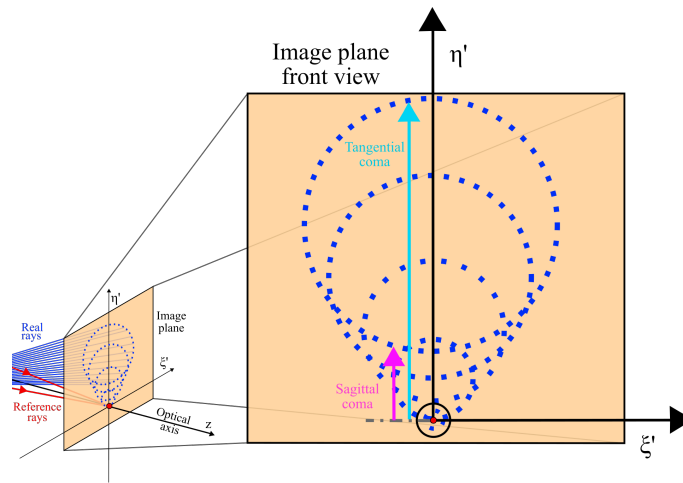
FIGURE 2.29: Zoom of the front view of the image plane in an optical system with coma.

2.2.4 Astigmatism

Off-axis rays depend not only on the aperture zone of the pupil but also on the plane it lies on. For a ray bundle in the tangential plane, the rays meet the lens surface with a tilt in the sagittal plane. Due to the different paths of the sagittal and tangential rays, they present different focal lengths. That means that the lens presents different optical power depending on the plane that the rays lie on. This aberration is known as astigmatism. Figure 2.30 illustrates a bundle of rays in the sagittal and tangential orientations focusing on their respective focal points [5].
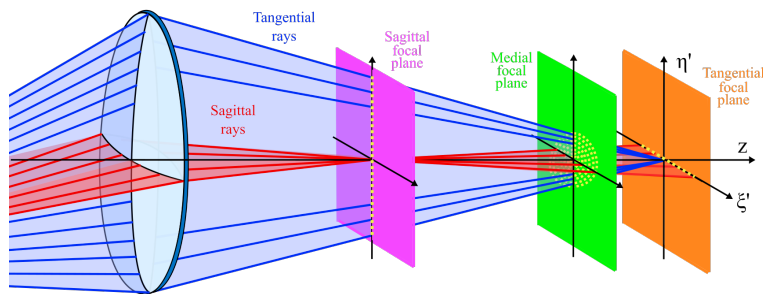
FIGURE 2.30: Astigmatism in an optical system.

The rays being refracted in the sagittal plane end up having a longer OPL inside of the lens than the rays in the tangential plane, as if the lens was thicker for the sagittal plane [5]. Figure 2.31 illustrates the OPL of the rays in the sagittal and tangential orientations inside of a lens. As can be seen, the distance t_2 is greater than t_1 for different off-axis angles in the vertical orientation.

When the image plane is placed at the sagittal rays' focus, the image formed is a vertical line. This means that while the sagittal rays produce a focal point in this position, the tangential rays have either not focused and therefore are converging, or have previously focused and are diverging when intersecting the image plane. Meanwhile, the same logic applies if the image plane is placed at the tangential
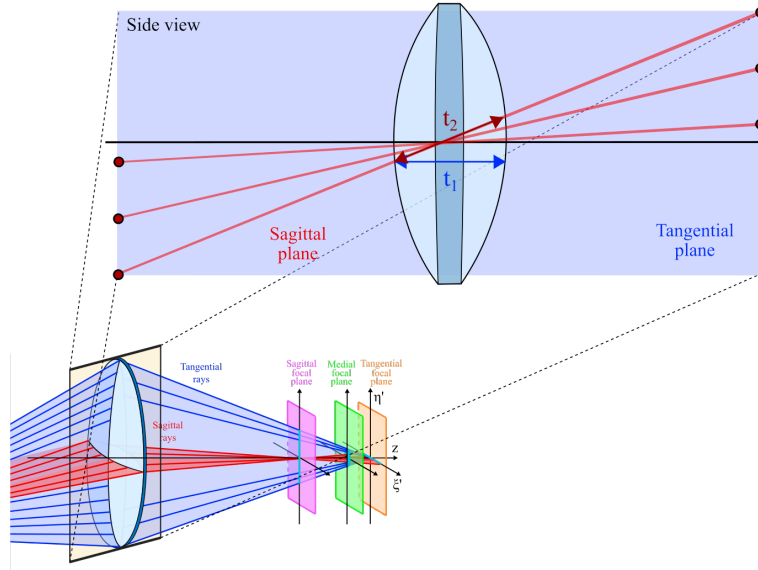
FIGURE 2.31: Side view of astigmatism.

rays' focus, creating a horizontal line as the sagittal rays are diverging or converging when they intersect the image plane. The best approach to minimize the spot size is to place the image plane in between the sagittal and tangential focal points, known as the *Medial Focal Plane*. This will form a more symmetric image with a circular shape. This relation can be seen in Fig. 2.30 with the whole schematic of astigmatism, while the front view of the focal planes can be seen in Fig. 2.32 [56].
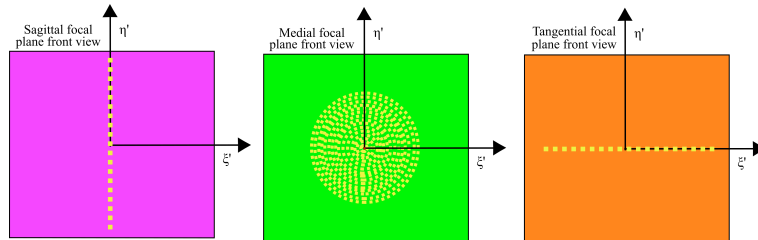
FIGURE 2.32: Front view of astigmatism in an optical system.

The transverse ray aberrations for astigmatism can be quantified as Eqs. (2.66) and (2.67).

$$\delta \eta' = \frac{-2}{n' \sin(u')} w_{222} \, \eta'^2 \, y \tag{2.66}$$

$$\delta \xi = 0 \tag{2.67}$$

The wavefront aberration of astigmatism can be quantified with Eq. (2.68).

$$W = w_{222} \, \eta'^2 \, r^2 \cos^2(\phi) = w_{222} \, \eta'^2 \, y^2 \tag{2.68}$$

Astigmatism has a particular ellipsoidal shape when it is not in either of the planes aforementioned. Indeed, most optical systems that suffer from astigmatism demonstrate this shape, either on the horizontal or vertical orientations. Figure 2.33 illustrates an example in which the image formed is closer to the sagittal focus than to the tangential focus [56].
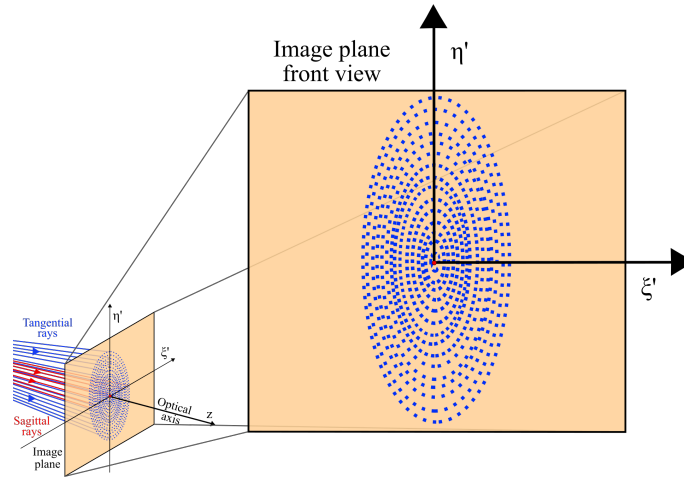
FIGURE 2.33: Zoom of the front view of the image plane in an optical system with astigmatism.

2.2.5 Field Curvature

The image formed by different field angles does not focus on a plane. The larger the field angle, the larger the displacement of the focal point from the image plane, as seen in Fig. 2.34. Thus, the image is formed into a curved surface. It is known as Field Curvature. This aberration is similar to astigmatism. However, it does not depend on the azimuth angle [56].
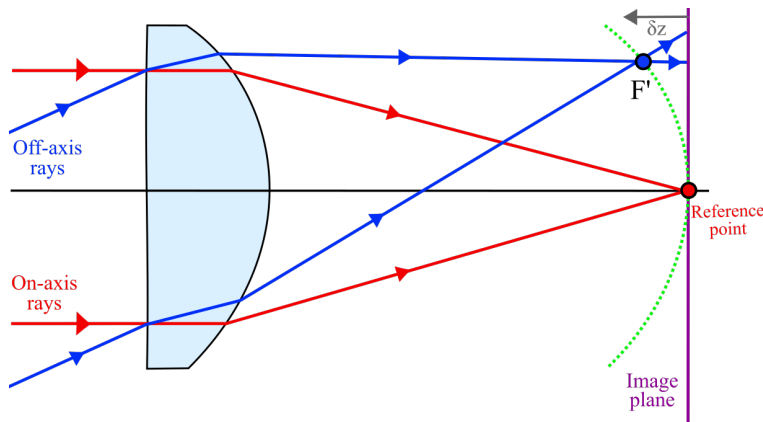
FIGURE 2.34: Field curvature in an optical system.

The transverse ray aberrations are given by Eqs. (2.69) and (2.70).

$$\delta\eta' = \frac{-2}{n'\sin(u')} w_{220}\, \eta'^2\, y \tag{2.69}$$

$$\delta\xi' = \frac{-2}{n'\sin(u')} w_{220}\, \eta'^2\, x \tag{2.70}$$

The wavefront aberration is given by Eq. (2.71).

$$W = w_{220}\, \eta'^2\, r^2 = w_{220}\, \eta'^2\, (x^2 + y^2) \tag{2.71}$$

From Eqs. (2.69) to (2.71) it is noticeably that this aberration is basically a defocus proportional to the square of the field angle η'.

Figure 2.35 shows the image formed by a system with field curvature. Notice that the image plane front view looks similar to defocus. However, this aberration happens with off-axis rays only [54].
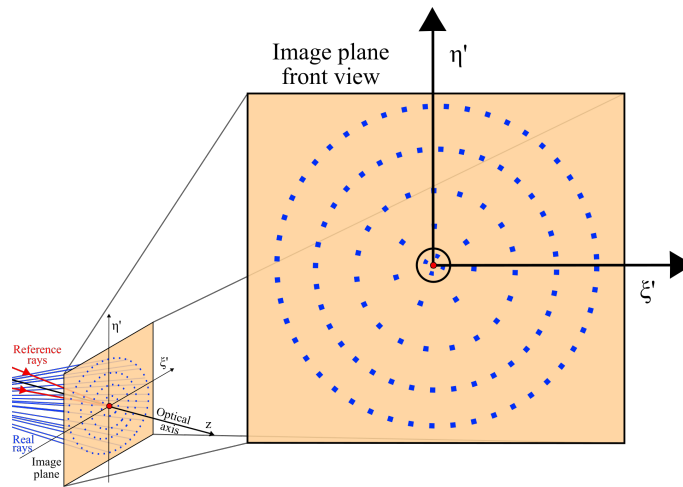
FIGURE 2.35: Zoom of the front view of the image plane in an optical system with field curvature.

The coefficient w_{220} of the field curvature can be split into two; the coefficient equivalent to astigmatism w_{222}^* and the coefficient w_{220p}, with the latter being the *Petzval Curvature*. Petzval curvature is the curvature in which the image formed by an object is sharp. This is not held if the system presents astigmatism, and the Petzval curvature is three times farther away from the tangential surface than the sagittal one, as in Eq. (2.72) and illustrated in Fig. 2.36. On the other hand, if the system does not present astigmatism, the field curvature has the same radius as Petzval [67].

$$\delta s_p = \frac{3\,\delta s_{sag} - \delta s_{tan}}{2} \tag{2.72}$$
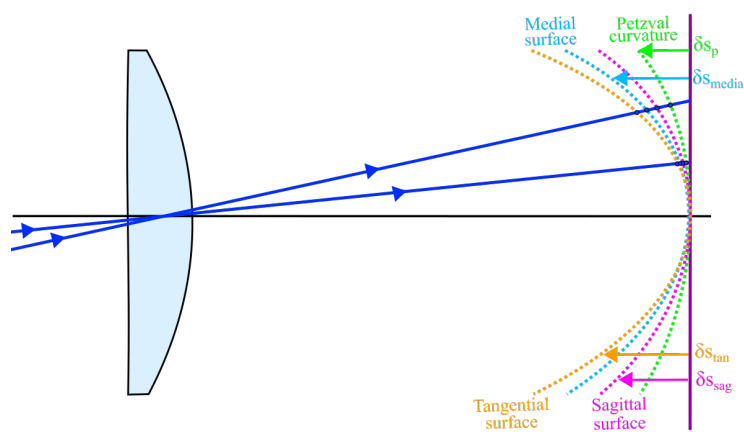
FIGURE 2.36: Petzval curvature in an optical system.

The Petzval radius is given by the optical element surface radius and its respective refractive indices before and after the surface, as seen in Eq. (2.73).

$$R_p = \frac{-n\,R}{n' - n} \tag{2.73}$$

The Petzval radius can be calculated not only for a single surface but also for an optical system with several surfaces. One can easily extend Eq. (2.73) into a complete mathematical formulation for that purpose, using each surface's radius of curvature and their respective refractive indices, as seen in Eq. (2.74). Indeed, Eq. (2.73) is a simplified version of Eq. (2.74).

$$\frac{1}{R_p} = -n_i' \sum_i \frac{n_i' - n_i}{n_i \, n_i' \, R_i} \tag{2.74}$$

Petzval curvature does not depend on the rays' height or angle, unlike the aberrations aforementioned. Thus, as seen in Eq. (2.74), only the lens parameters influence this quantity [54].

2.2.6 Distortion

The object points with different distances to the optical axis present different transverse magnifications. As a result, the image shape is geometrically altered while the image is sharp. The points farther away from the paraxial region still maintain the image quality, i.e., it still presents a sharp image. However, the points fall at a distance from the ideal image point. This creates an effect in which the image seems distorted, and that is the reason why this aberration is called *distortion* [5].

The shape of the image depends on the orientation of the change in magnification. There are two types of distortion. If the magnification increases farther away from the optical axis, the image formed presents a shape in which the lines appear to be curved outwards with the borders farther away from the reference points than the central region. Thus, due to the pincushion appearance of the shape formed, this is known as *pincushion distortion* or positive distortion. While if it decreases, the lines appear to be curved inwards, creating a barrel shape; thus, this is known as *barrel distortion*, or negative distortion [5].

The transverse ray aberration is given by Eq. (2.69).

$$\delta\eta' = \frac{-1}{n' \sin(u')} w_{311} \, \eta'^3 \tag{2.75}$$

The wavefront aberration is given by Eq. (2.71).

$$W = w_{311} \, \eta'^3 \, r \cos\phi = w_{311} \, \eta'^3 \, y \tag{2.76}$$

Distortion is typically quantified as a fraction between the transversal distance from the paraxial and real points and the transversal distance of the paraxial point to the optical axis, as seen in Eq. (2.77) [56].

$$Dist. = \frac{\delta\eta'}{\eta'} = \frac{\eta'_{real} - \eta'_{parax.}}{\eta'_{parax.}} \tag{2.77}$$

Figure 2.37 illustrates an optical system with pincushion and barrel distortion, respectively. Notice that the AS position influences the type of distortion present. In the case of a positive lens, a barrel distortion will be present if the AS is positioned before the lens, whereas a pincushion distortion will be present if the AS is placed after the lens. The location of the AS in the case of a negative lens will cause the opposite distortion to that of the positive lens [66].

Practically, this aberration is not as critical as the other ones for the image quality, up to a certain degree, as it can be corrected using image processing. In fact, barrel distortion can be seen as a feature in some optical systems for specific applications.

(a) Pincushion (positive) distortion.

(b) Barrel (negative) distortion.
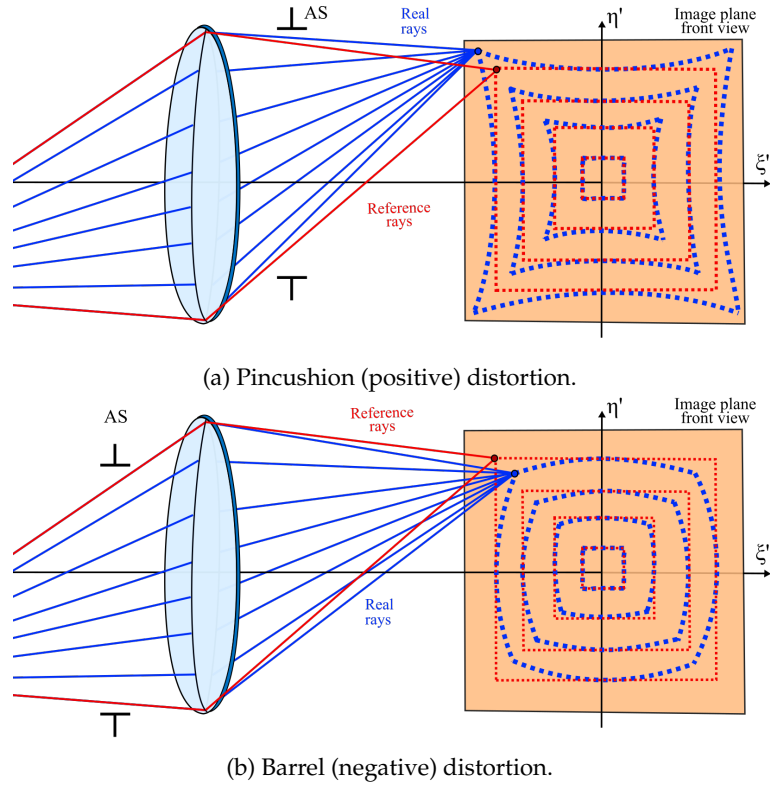
FIGURE 2.37: Distortion in an optical system.

For example, fish-eye lenses present significant distortion through which a larger FoV is achieved [68].

2.3 Seidel Coefficients

The *Seidel coefficients* are composed of the third-order aberrations. As seen in the previous sections, the wavefront aberrations can be converted into transverse ray aberrations by differentiating them. The name of the third-order aberrations comes from the fact that the sum of the exponents of the aperture r and the field η' in terms of ray aberrations is 3, while for the wavefront aberration, it is 4. For the Seidel analysis, paraxial ray-tracing is used once it provides a good approximation for the calculations; there is little difference for the real ray-tracing. Furthermore, the rays being traced to quantify the wavefront aberrations are the paraxial marginal, and chief rays [56].

In order to facilitate calculating the Seidel coefficients, we shall define two quantities, A and $\bar{A}$, using the paraxial approximation. These quantities are merely the Eq. (2.7) simplified combined with the paraxial incidence angle for a spherical surface Eq. (2.78), resulting in Eqs. (2.79) and (2.80). These quantities are known as *Refraction Invariant*, and they are useful for calculating the Seidel sums for calculating the quantity of primary aberration in an optical system by summing the contribution of primary aberration from each surface [56, 66].

$$i = h\,c + u \tag{2.78}$$

$$A = n\,i = n'\,i' = n(h\,c + u) = n'(h\,c + u') \tag{2.79}$$

and

$$\bar{A} = n\,\bar{i} = n'\,\bar{i'} = n(\bar{h}\,c + \bar{u}) = n'\,\bar{i'} = n'(\bar{h}\,c + \bar{u'}) \tag{2.80}$$

in which A is the refraction invariant for the marginal ray, and $\bar{A}$ for the chief ray in each surface.

Here, the angle between the normal to the surface and the ray is defined as i, as seen in Fig. 2.38.
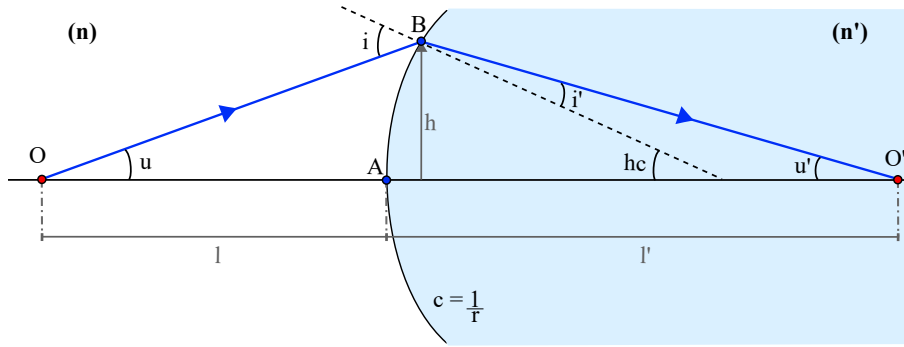
FIGURE 2.38: Schematic of the refraction invariant.

The wavefront aberration for a single surface can be calculated using the difference in paths between the marginal ray and the optical axis from the object O to the image O':

$$W = [OAO'] - [OBO'] = n(OA - OB) + n'(AO' - BO') \tag{2.81}$$

The distance OA and AO' is straightforward as it is simply the distance between the object O to the surface vertex A, l, and the surface vertex A to the image O', l' [56].

The distances OB and BO' can be obtained using the Pythagorean theorem, the sagitta of the surface in Eq. (2.12) truncated after the second term, and the paraxial approximation when h is significantly smaller than l, that leads to the difference in paths being:

$$OA - OB = -\frac{1}{2}\left(c - \frac{1}{l}\right)\left[h^2 + \frac{c^2\,h^4}{4} + \frac{h^4}{4\,l}\left(c - \frac{1}{l}\right)\right] \tag{2.82}$$

and

$$AO' - BO' = -\frac{1}{2}\left(c - \frac{1}{l'}\right)\left[h^2 + \frac{c^2\,h^4}{4} + \frac{h^4}{4\,l'}\left(c - \frac{1}{l'}\right)\right] \tag{2.83}$$

Thus, substituting Eq. (2.81) by Eqs. (2.82) and (2.83) and simplifying it by using Eq. (2.13) leads to:

$$W = \frac{h^4}{8}\left[\frac{n'}{l'}\left(c - \frac{1}{l'}\right)^2 - \frac{n}{l}\left(c - \frac{1}{l}\right)^2\right] \tag{2.84}$$

The solution in Eq. (2.84) can be further simplified by using the refractive invariant Eqs. (2.79) and (2.80):

$$W = \frac{h^4}{8}\left[\frac{n'}{l'}\left(\frac{A}{n'h}\right)^2 - \frac{n}{l}\left(\frac{A}{nh}\right)^2\right] = \frac{A^2 h}{8}\left(\frac{u}{n} - \frac{u'}{n'}\right) \tag{2.85}$$

If we define $\delta\frac{u}{n} = \frac{u'}{n'} - \frac{u}{n}$, the final wavefront aberration for a system with SA is:

$$W = -\frac{A^2 h}{8}\delta\left(\frac{u}{n}\right) \tag{2.86}$$

This solution assumes paraxial approximations. In reality, there will be a discrepancy between the height for the paraxial and the real rays when the ray angle increases and the assumption of $\sin(i) = i$ does no longer hold. As we are considering SA, the field does not influence the aberration, so all the proportionality of wavefront aberrations is related to the aperture size. For the Seidel SA coefficient, the term $\frac{1}{8}$ is removed. This leads to:

$$S_1 = -A^2 h \delta\left(\frac{u}{n}\right) \tag{2.87}$$

The off-axis Seidel coefficients can be defined using the same terms, but in this case, also including the chief ray refraction invariant $\bar{A}$, and the Lagrange invariant Λ previously defined in Eq. (2.20). The Seidel coefficient defined in Eq. (2.87) is related to each surface. To consider the overall Seidel sum in the system, one needs to use the sum of the coefficients for each surface. This sum is demonstrated in Table 2.1 for each aberration. This table also describes the relationship between the wavefront aberration and the Seidel coefficients. [56, 66].

TABLE 2.1: Seidel coefficients and sum.

Aberration	Seidel terms	Seidel sum	Wavefront coefficient
SA	S_I	$-\sum A^2 h \delta\left(\frac{u}{n}\right)$	$w_{040} = \frac{1}{8}S_I$
Coma	S_{II}	$-\sum \bar{A} A h \delta\left(\frac{u}{n}\right)$	$w_{131} = \frac{1}{2}S_{II}$
Astigmatism	S_{III}	$-\sum \bar{A}^2 h \delta\left(\frac{u}{n}\right)$	$w_{222} = \frac{1}{2}S_{III}$
Petzval field	S_{IV}	$-\sum \Lambda^2 c \delta\left(\frac{1}{n}\right)$	$w_{220} = \frac{1}{4}(S_{III} + S_{IV})$
Distortion	S_V	$-\sum\left\{\frac{\bar{A}^3}{A} h \delta\left(\frac{u}{n}\right) + \frac{\bar{A}}{A}\Lambda^2 c \delta\left(\frac{1}{n}\right)\right\}$	$W_{311} = \frac{1}{2}S_V$
Axial color	C_I	$\sum A h \delta\left(\frac{\delta n}{n}\right)$	$w_{020} = \frac{1}{2}C_I$
Lateral color	C_{II}	$\sum \bar{A} h \delta\left(\frac{\delta n}{n}\right)$	$w_{111} = C_{II}$

The sagittal and tangential fields can be calculated by the sum of astigmatism and Petzval field coefficients S_{III} and D_{IV}, with the sagittal field being the sum $S_{III} + S_{IV}$, and the tangential field being the sum $3 S_{III} + S_{IV}$.

The Seidel coefficients are limited to the third-order aberrations, which means that they do not ultimately hold all the aberrations affecting the image quality in an optical system. However, their correction significantly increases image quality.

Chapter 3

Aplanatic correction

A good approach to creating an aplanatic optical system is to start by correcting SA. There are many methods that can be used. However, many of them greatly minimize the SA but do not correct it completely. Those methods are still important as they give a good starting point in an optical design. Other methods go beyond and provide complete SA correction. It is also worth noting that when elements free from SA are combined, they do not necessarily result in aplanatic correction.

This chapter deals with SA and aplanatic correction using refractive and reflective systems. It is also possible to correct SA using diffractive systems or metasurfaces, however, they have not been used in the research presented here.

3.1 Methods for SA correction

3.1.1 Lens bending

As previously seen in Chapter 2, the more curved a surface is, the more it suffers from SA. In fact, as seen in Fig. 2.25, the more curved the surface is, the greater the difference between the angles between the rays and the normal to the surface in different aperture zones. Thus, from Eq. (2.7), it is trivial to notice that this results in a larger discrepancy in the focal length for different aperture zones due to the rays being refracted in different angles. Therefore, designing a lens with a surface that is less curved is ideal for SA reduction as it reduces this difference in the angles for different aperture zones.

Figure 3.1 illustrates the difference in the angles aforementioned. As can be seen, the lens with a smaller RoC presents a large SA, i.e., it presents a large difference between the incoming rays and the surface. In this case, $\theta_{ML1} > \theta_{ML2}$. And the lens with a larger RoC produces an image with less SA as the deviation of the angles is not as critical as the previous case. However, when using the method of increasing the RoC of a single surface of the lens will also result in a change in its focal length. Thus, the correction of SA by changing only one surface of the lens comes with a compromise of increasing its focal length [66].

As an example, two lenses have been designed. The first one with half the RoC of the second one, while maintaining the same diameter. As seen in Fig. 3.2, the first one presents an evident SA, while the second one, while it also presents SA, it is significantly reduced by a factor of $1/r^3$. However, the effective focal length (EFFL) doubles, which means that the system becomes less compact.

For that reason, when applying the lens bending method, both surfaces of the lens are normally used to maintain the optical power of the lens while decreasing the SA. One can optimize the shape of both surfaces of a lens to balance the SA using a good balance of the RoC of both surfaces and the object position. This can be done using the Coddington factors [54].

(a)

(b)
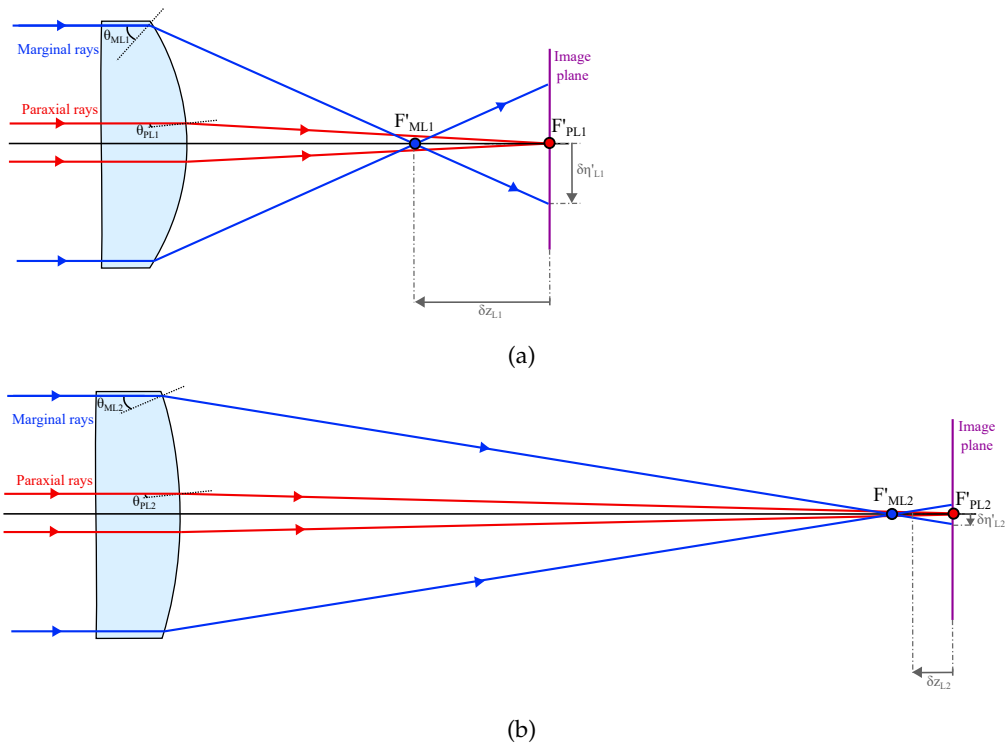
FIGURE 3.1: Layout for (*a*) a lens with a small RoC, L1, and (*b*) a lens with a larger RoC, L2. The angle between an incoming ray and the curved surface of the plano-convex lenses, L1 and L2, is larger for the L1 lens considering that it is more curved, i.e., presents a smaller RoC. Thus, the marginal ray bends more for this lens, focusing farther away than the paraxial rays focus, which increases the SA.
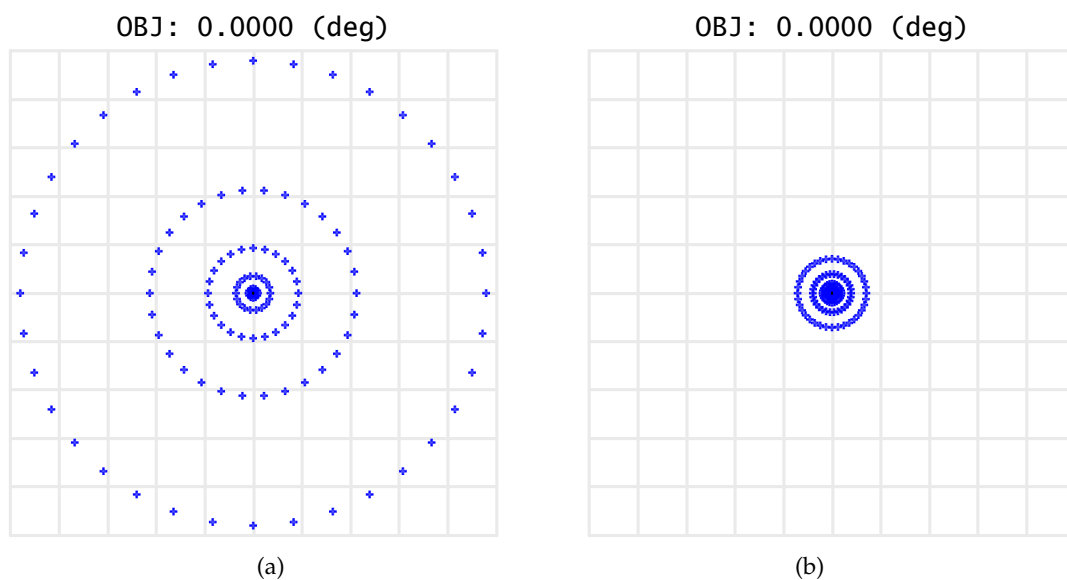
FIGURE 3.2: Spot diagrams for (*a*) a lens with a low RoC, and (*b*) a lens with a larger RoC. It shows on-axis image spots for both lenses. It is noticeable that a lens with a larger RoC presents less SA. Both grids represent the same scale.

3.1.2 Coddington factors

In order to balance the SA in a lens by optimizing both of its surfaces, one needs to find the relation between the RoC of the surfaces, and the optimal object position [54].

As previously seen, the shape of the surfaces of the lens influences the SA correction. Section 3.1.1 considered the case in which only one of the surfaces of the lens changes its shape in order to minimize SA. However, adding an extra degree of freedom, of changing both of the surfaces of a lens, one can achieve a better SA correction by balancing the SA introduced by each surface. This method uses the thin lens approximation.
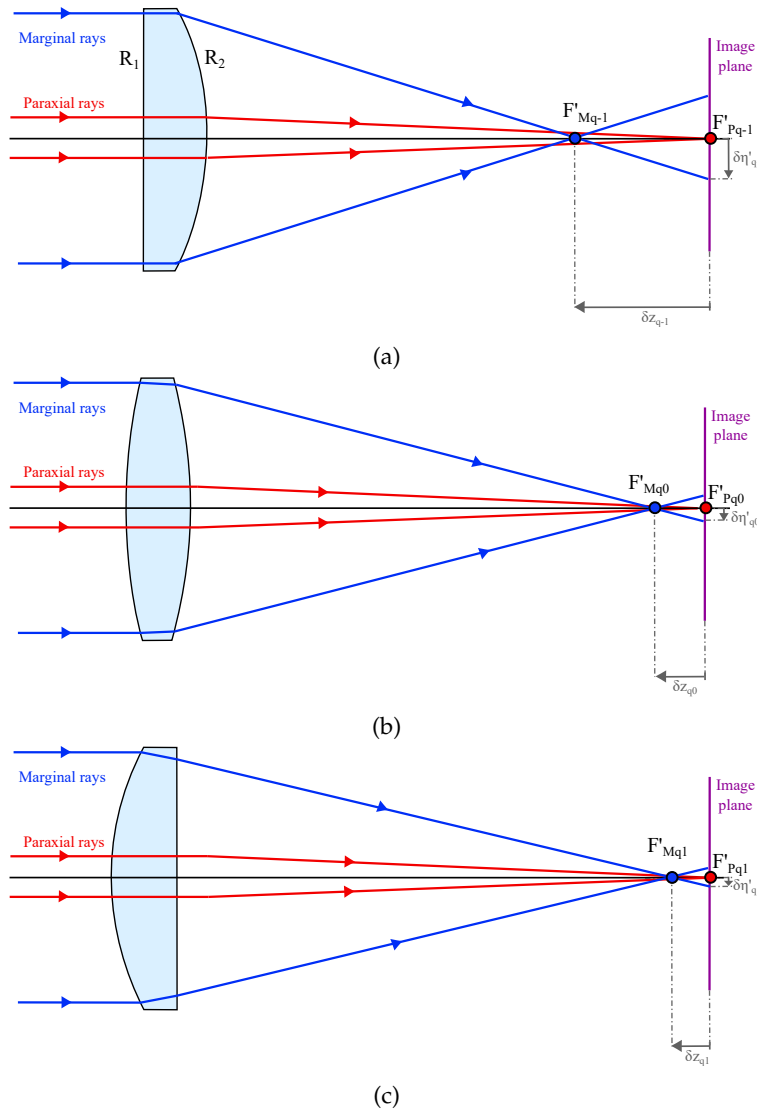
FIGURE 3.3: Layout for a single lens with a Coddington shape factor of (*a*) $q = -1$ (*b*) $q = 0$, and (*c*) $q = 1$.

The symmetry of the surfaces of the lens can be calculated using a parameter, known as the Coddington shape factor q [56, 69]:

$$q = \frac{R_1 + R_2}{R_2 - R_1} = \frac{c_1 + c_2}{c_2 - c_1} \tag{3.1}$$

Different Coddington shape factors define what type of the lens is designed. Plano-convex lenses present a $q = \mp 1$, plano-convex lenses a $|q| < 1$, and meniscus a $|q| > 1$. They result in different amounts of SA in an optical system [66].

Figure 3.4 illustrates the results for the optical systems presented in Fig. 3.3 using a BK7 glass with a refractive index of $n = 1.5168000345$. It is evident that, in this case, the plano-convex lens, with $q = -1$, presents the worst result. And the best result is achieved with the plano-concave lens, with $q = 1$. The former does not have SA balancing as the first surface is normal to the incoming rays, so all the focusing happens on the second surface. The latter presents a better SA correction as the SA introduced by the second lens presents a better opposite SA sign from the first surface compared to the other optical designs in Fig. 3.3.

(a)

(b)

(c)
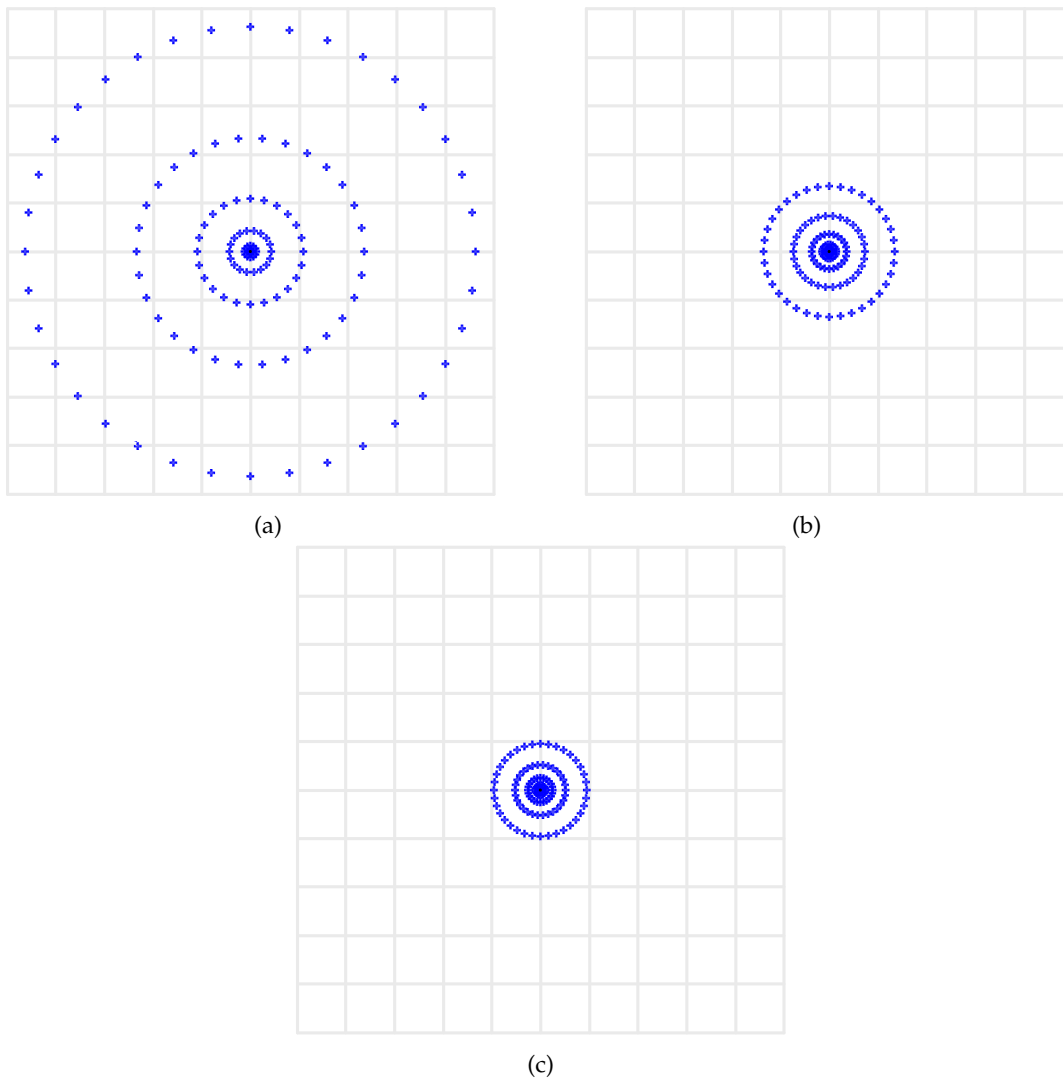
FIGURE 3.4: Spot diagrams for a singlet with a Coddington shape factor of (a) $q = -1$, (b) $q = 0$, and (c) $q = 1$. All grids represent the same scale.

Another factor that influences the SA in a lens is the object and image positions. The configuration of the object and image location can be described using the Coddington position factor p:

$$p = \frac{s' - s}{s' + s} = 1 - \frac{2f}{s'} \tag{3.2}$$

This factor can also be described by the magnification of the lens using the lateral magnification seen in Eq. (2.19) [56]:

$$p = \frac{m+1}{m-1} \qquad (3.3)$$

The position factor, however, is not a parameter as free as the shape factor considering that, in many cases, the object distance from the lens is predefined in an optical system [56].

Different Coddington position factors define the position at which the object and image are located. For a collimated incoming beam with the outgoing beam focusing at a finite position the factor is $p = -1$, for a finite object and image focal points with magnification 1 the factor is $p = 0$, and for a finite object position with collimated outgoing beam the factor is $p = 1$. They result in different amount of SA in an optical system [66].
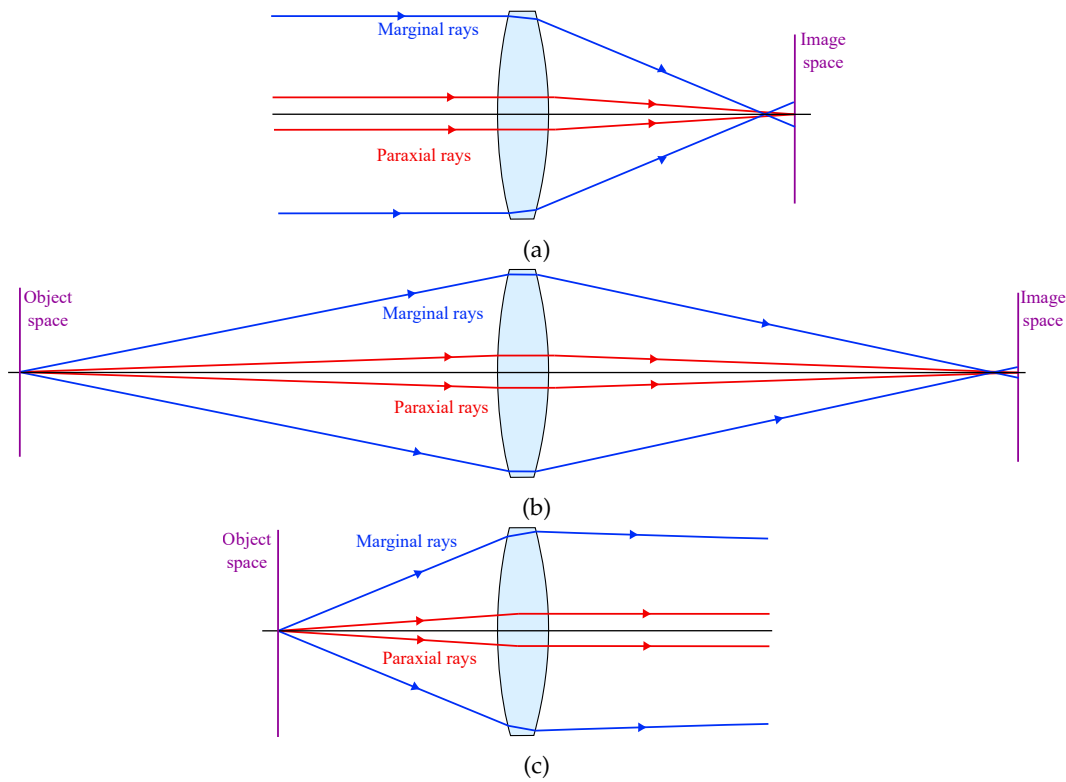
FIGURE 3.5: Layout for a single with a Codding position factor of (a) $p = -1$ (b) $p = 0$, and (c) $p = 1$, in this case, SA can be quantified by using a paraxial lens to focus the light as it does not affect image quality.

Figure 3.6 illustrates the results of the optical systems presented in Fig. 3.5 using the same lens with a BK7 glass with a refractive index of $n = 1.5168$ while changing the object position.

For a thin lens, the SA coefficient in terms of proportionality with the Coddington's factors is given by [70]:

$$k_{SA}(n,p,q) \propto \frac{n^3 + (n+2)\,q^2 + (3\,n+2)\,(n-1)^2\,p^2 + 4\,(n^2-1)\,p\,q}{32\,n\,(n-1)^2} \qquad (3.4)$$

(a)

(b)

(c)
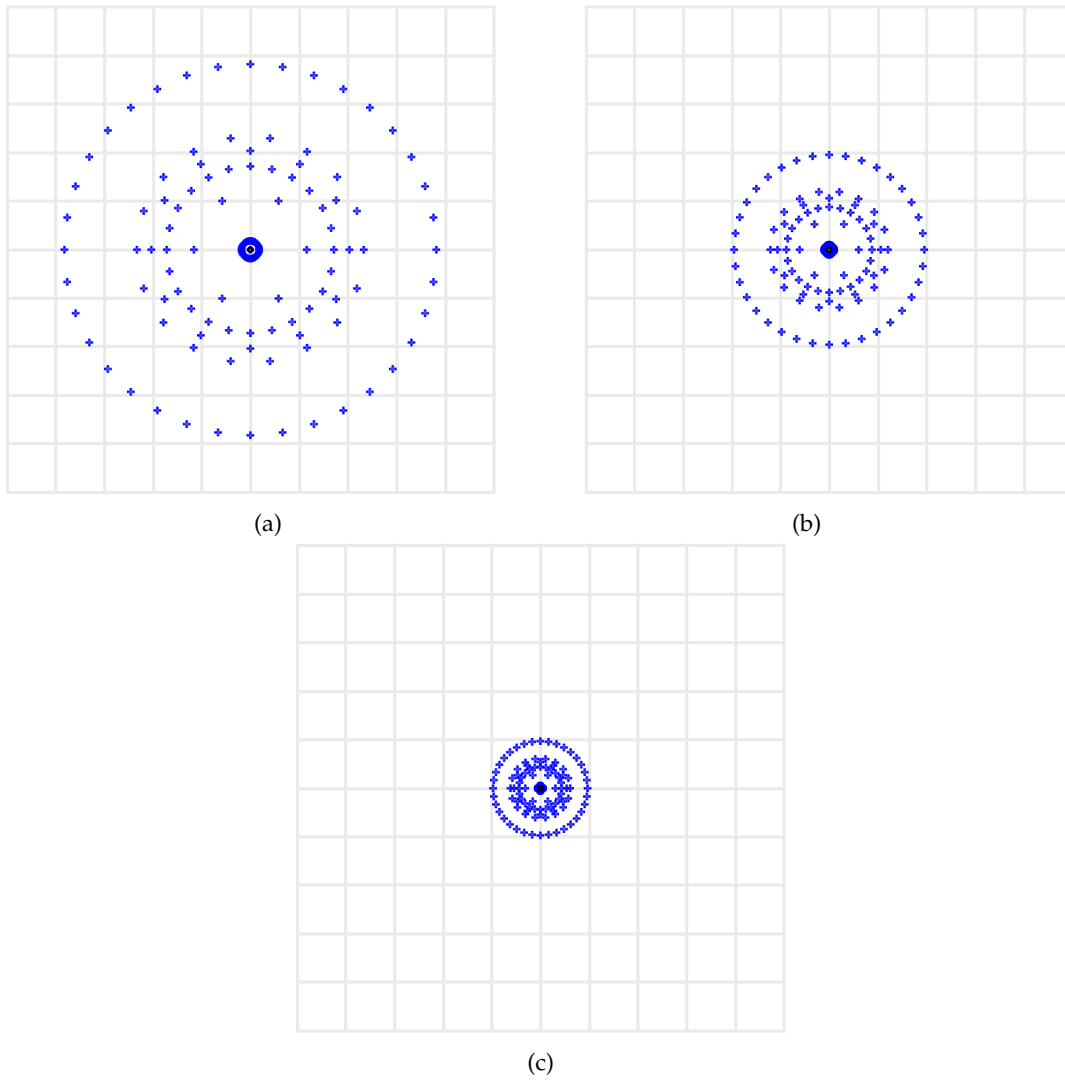
FIGURE 3.6: Spot diagrams for a singlet with a Coddington position factor of (a) $p = -1$, (b) $p = 0$, and (c) $p = 1$. All grids represent the same scale.

One can obtain the optimal Coddington shape factor in which the SA is minimized in terms of the Coddington position factor and refractive index of the lens:

$$q = -\frac{2\left(n^2 - 1\right)p}{n + 2} \tag{3.5}$$

When the Coddington position factor p is defined for an optical system, the optimal Coddington shape factor q changes with the RI of the lens, as seen in Figs. 3.7 to 3.9. When the position factor $p = 0$, it is clear that the optimal shape factor p is constant, also being zero. This relationship can be seen in Fig. 3.8, in accordance with Eq. (3.5) [66].

The examples given in Fig. 3.3 demonstrate this relationship between the shape factor q and the position factor p, with the best results being the one closest to the $q = 1$ in the case of a collimated incoming beam (p = -1). The RI in those examples are approximately $n = 1.5$ as the blue line in Fig. 3.7, showing that this is in accordance with Eq. (3.5).
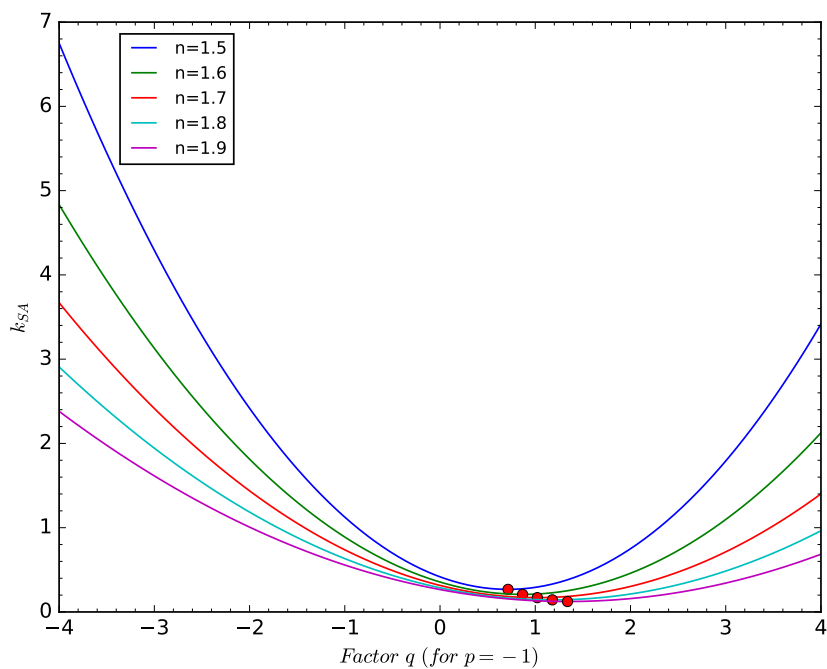
FIGURE 3.7: SA k_{SA} depending on the Coddington factor q for a position factor of $p = -1$ for different RI. The points in red represent the optimal shape factor to minimize SA depending on the RI.
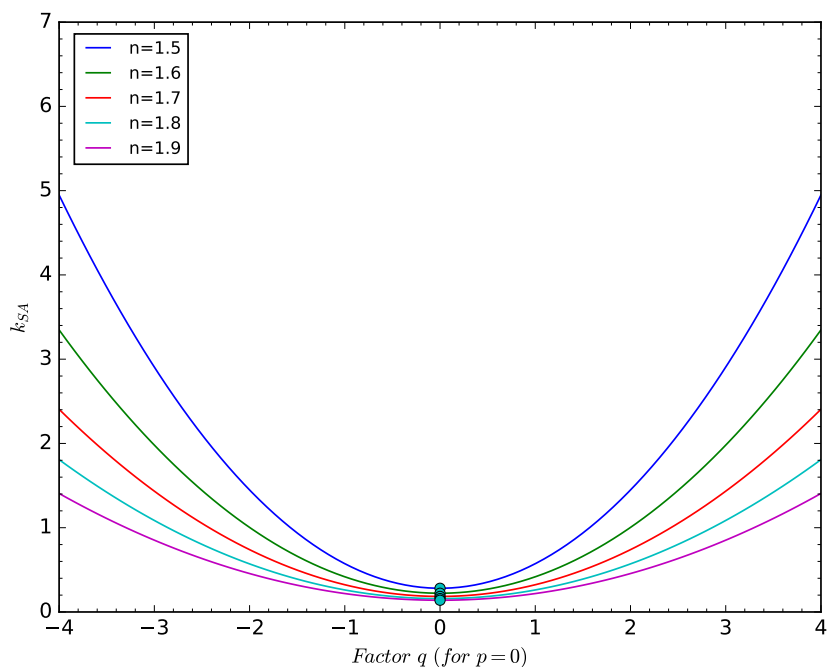
FIGURE 3.8: SA k_{SA} depending on the Coddington factor q for a position factor of $p = 0$ for different RI. The points in cyan represent the optimal shape factor to minimize SA depending on the RI.
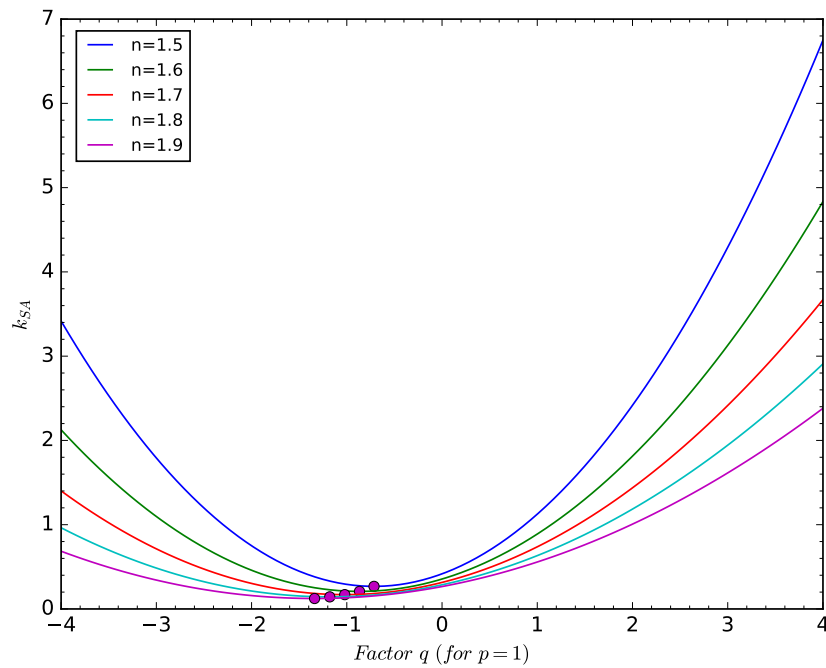
FIGURE 3.9: SA k_{SA} depending on the Coddington factor q for a position factor of $p = 1$ for different RI. The points in magenta represent the optimal shape factor to minimize SA depending on the RI.
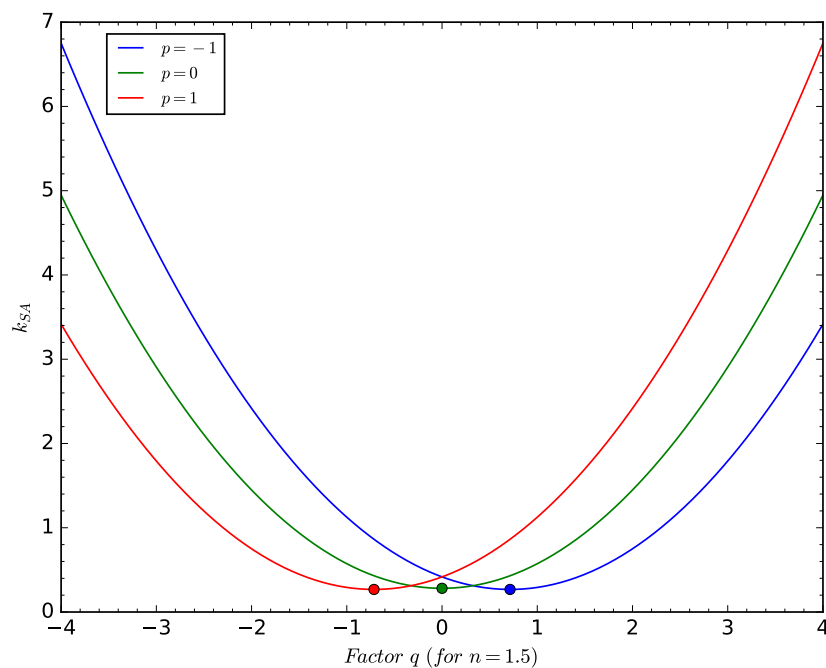
FIGURE 3.10: SA k_{SA} depending on the Coddington factor q for different position factors p for the same RI. The points represent the optimal shape factor to minimize SA for each position factor.

The point with the minimal SA in a lens shows a linear relationship between the

shape and position factors. Figure 3.10 illustrates the change in the optimal shape factor q for different position factors p while maintaining the same refractive index for the lens. As p decreases, the optimal q increases.

3.1.3 Power splitting and combination

(a)

(b)
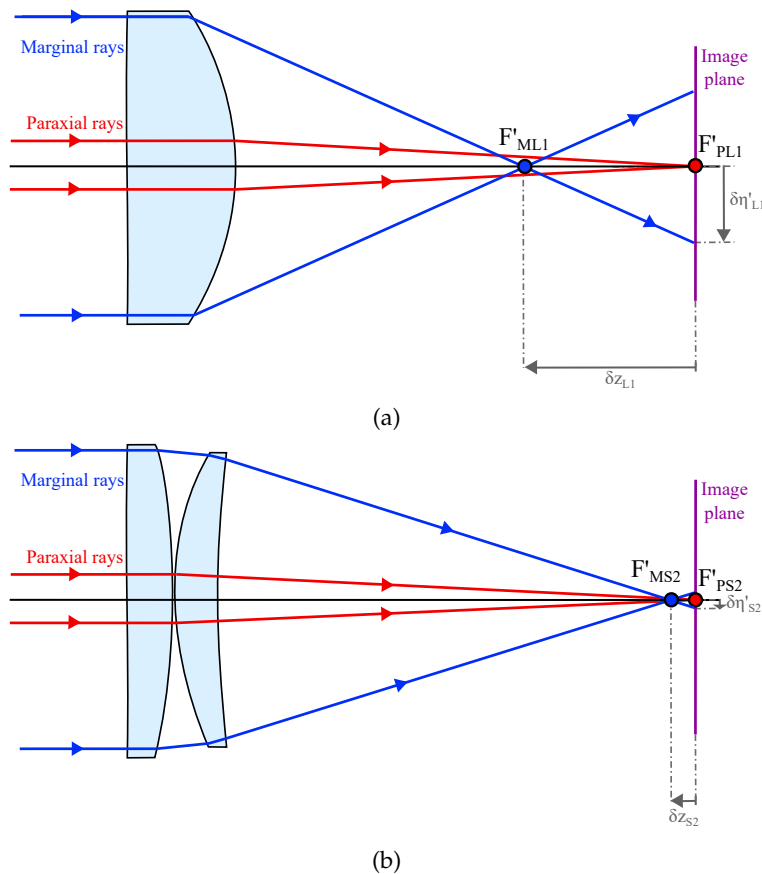
FIGURE 3.11: Layout for (a) a single lens, L1, and (b) a system composed of two lenses with the same combined optical power as the single lens, S2.

The power of a lens depends on the RI of the material and the RoC. As previously seen in Section 3.1.4, the lower the RI, or the more curved the RoC, the more the lens introduces SA. Considering that the power of an optical system is the sum of each individual lens, as seen in Eq. (2.29), one can split a single lens into several lenses so that the RoC of each lens is increased, making them less curved than the original lens. This, decreasing SA while keeping the same optical power and focal length.

This is a method commonly used in an optical system, as it can help decrease not only SA but also other aberrations. In fact, splitting a single element into several elements increases the degrees of freedom in an optical system allowing not only changing the RoC to correct aberrations, but also to use different materials so that the refractive index can also help in the aberration correction process, as will be seen in Sections 3.1.4 and 3.1.5 [66].

Fig. 3.11 illustrates the idea. As an example, two optical systems have been designed, both using the same material for all the lenses, with the same diameter and $F/\#$. The first system, Fig. 3.11a, is composed of a singlet, and the second, Fig. 3.11b,

is composed of two lenses. It is important to notice that the optical power of both systems is the same, otherwise it would not be a fair comparison.

The results can be seen in Fig. 3.12. The spot diagram demonstrates a significant decrease in SA even when the materials used are the same in both cases, i. e., the same RI, so that only the power splitting is used to achieve those results.
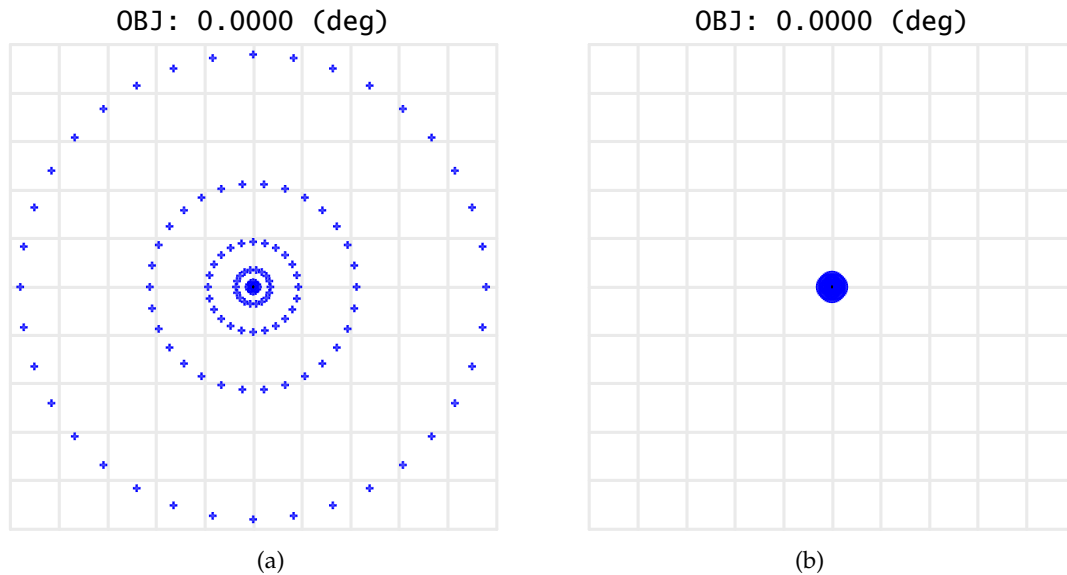
FIGURE 3.12: Spot diagrams for (*a*) a single lens, and (*b*) a system with two lenses with a combined optical power similar to the single lens. It shows on-axis image spots for both lenses. It is noticeable that a lens split into two presents less SA. Both grids represent the same scale.

3.1.4 Refractive index

The RI of a lens also influences the SA introduced into an optical system. If the RI of a single is increased, in order to keep the same optical power, its RoC increases, resulting in a less curved lens. As seen in the previous sections, increasing the RoC helps SA correction.

Flint glasses normally present higher RI than crown glasses. Thus, they can be a good choice for SA correction. However, they present a low Abbe Number, making them present a high dispersion. Therefore, this solution is more suitable for monochromatic systems [66].

The best choice of material for SA correction is Germanium. It presents one of the highest RI with a low dispersion. That means it can correct SA without a huge increase in LCA. However, the wavelength range of this glass is between $\lambda = 2000.0$ *nm* to $\lambda = 14000.0$ *nm* [71].

To illustrate the idea, two singlets have been designed with the same $F/\#$ and diameter as seen in Fig. 3.13. The RI depends on the wavelength, so both systems were tested for the same wavelengths ranging from $\lambda = 486.1$ *nm* to $\lambda = 656.3$ *nm*. The first lens is composed of BK7, a crown lens with a RI of $n_d = 1.5168$ and Abbe number $V_d = 64.17$. The second lens is composed of SF66, a flint lens with a RI of $n_d = 1.9229$ and Abbe number $V_d = 20.88$.
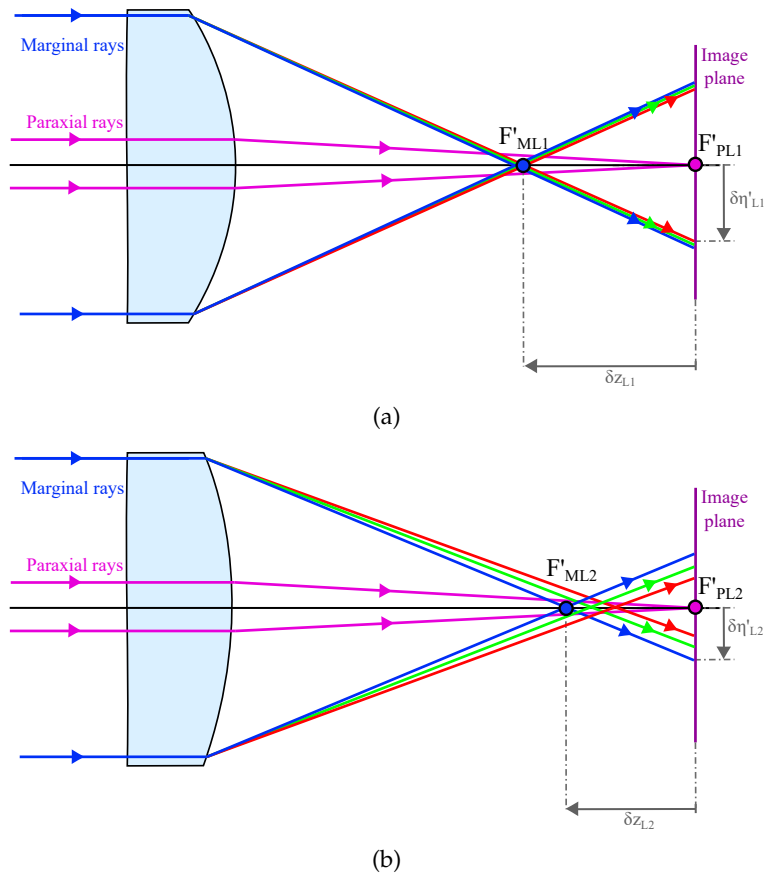
FIGURE 3.13: Layout for a single lens composed of (*a*) a BK7 glass, L1, and (*b*) a SF66, L2
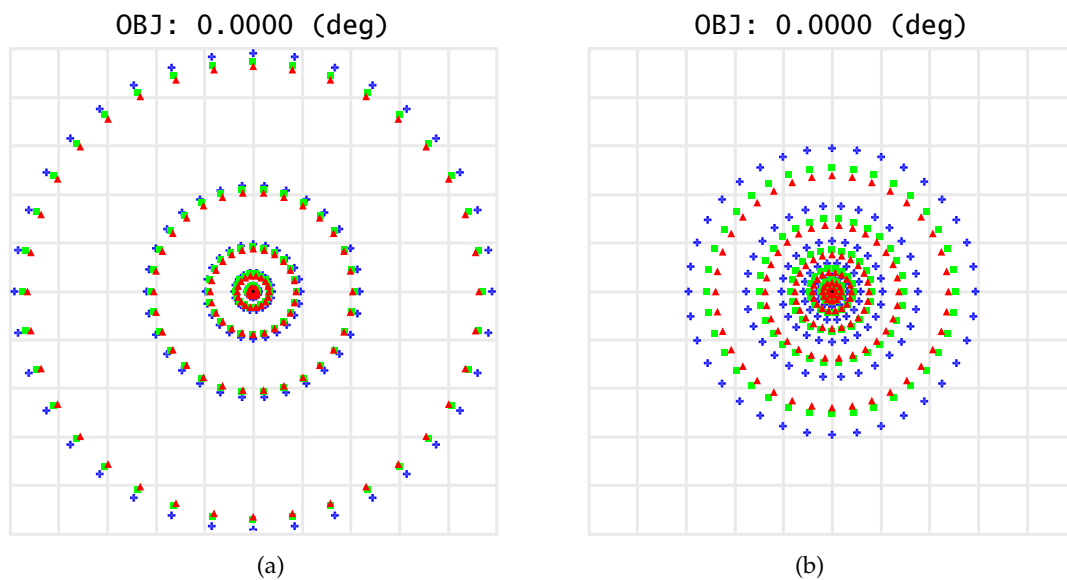
FIGURE 3.14: Spot diagrams for a lens with (*a*) a high RI, and (*b*) a low RI. It shows on-axis image spots for both lenses. It is noticeable that a lens with higher RI presents less SA. Both grids represent the same scale.

Fig. 3.14 demonstrates the results of the simulations. As expected, the SF66 lens provides better results in terms of SA correction than the BK7. However, it is clearly seen how the SF66 presents more LCA as the material has a low Abbe Number.

3.1.5 Doublets

(a)

(b)

(c)

(d)
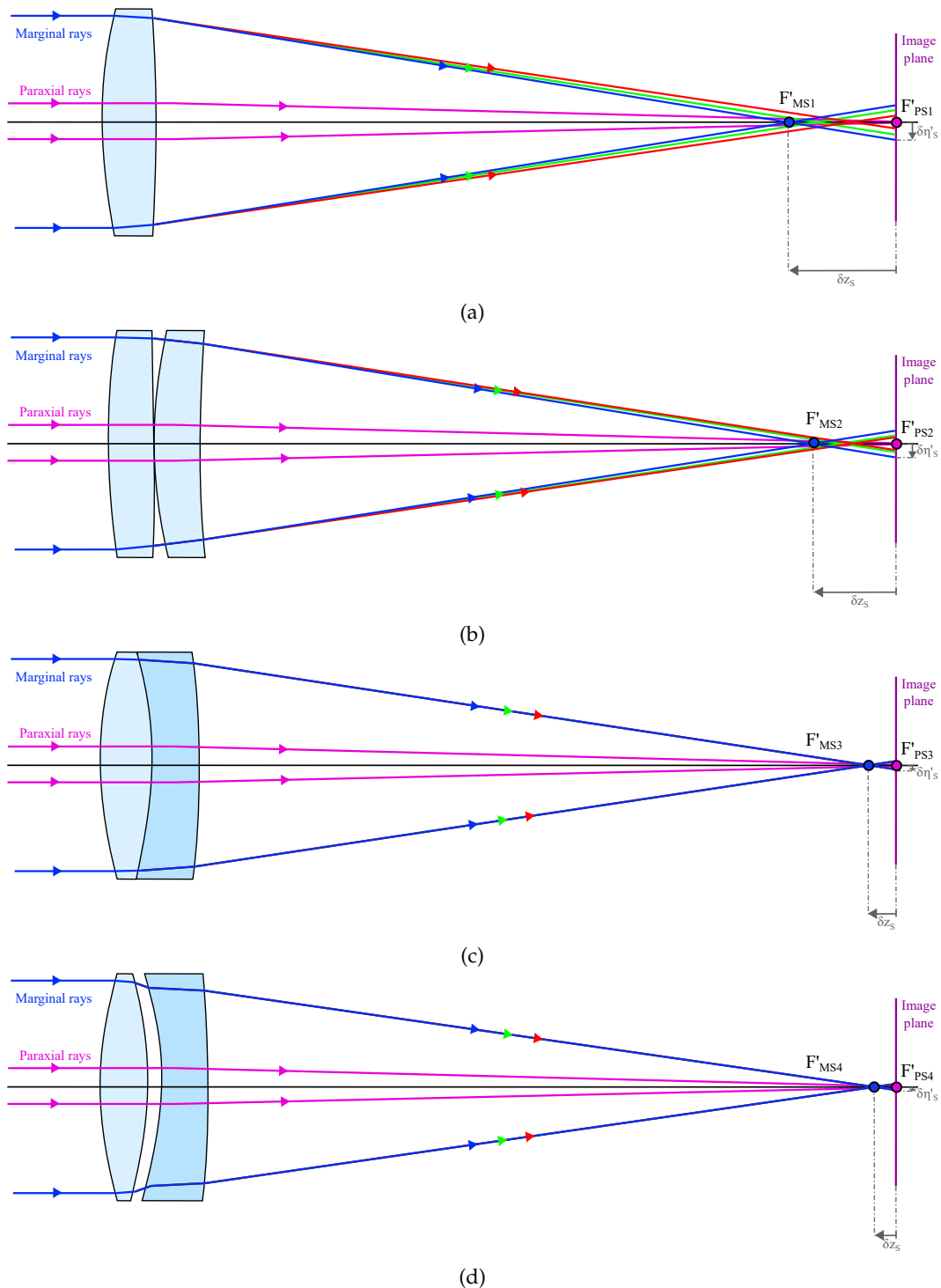
FIGURE 3.15: Layout for (*a*) a singlet, S1, (*b*) two lenses with the same material, S2, (*c*) a cemented doublet, S3, and (*d*) an air-spaced doublet, S4.

As previously seen in Section 3.1.3, splitting a lens into more lenses decreases the SA. If one splits a singlet into two lenses to minimize SA, but instead of using the same material, using two different materials with one generally being a positive crown and one being generally a negative flint, it is possible to obtain even greater image correction. This happens because one extra degree of freedom is added into

the system, which is the RI of the second material to be used in one of the lenses. This combination of two lenses with two different materials is called a doublet. They can be composed of two lenses in contact with the same central RoC, known as cemented doublets, or two lenses spaced between themselves, known as air-spaced doublets.

The cemented doublets are commonly used because they provide a good aberration correction while being compact. They are usually preferred over a singlet in many applications. A proper choice of the materials and the lenses' RoC results in a significant SA and LCA reduction [66].
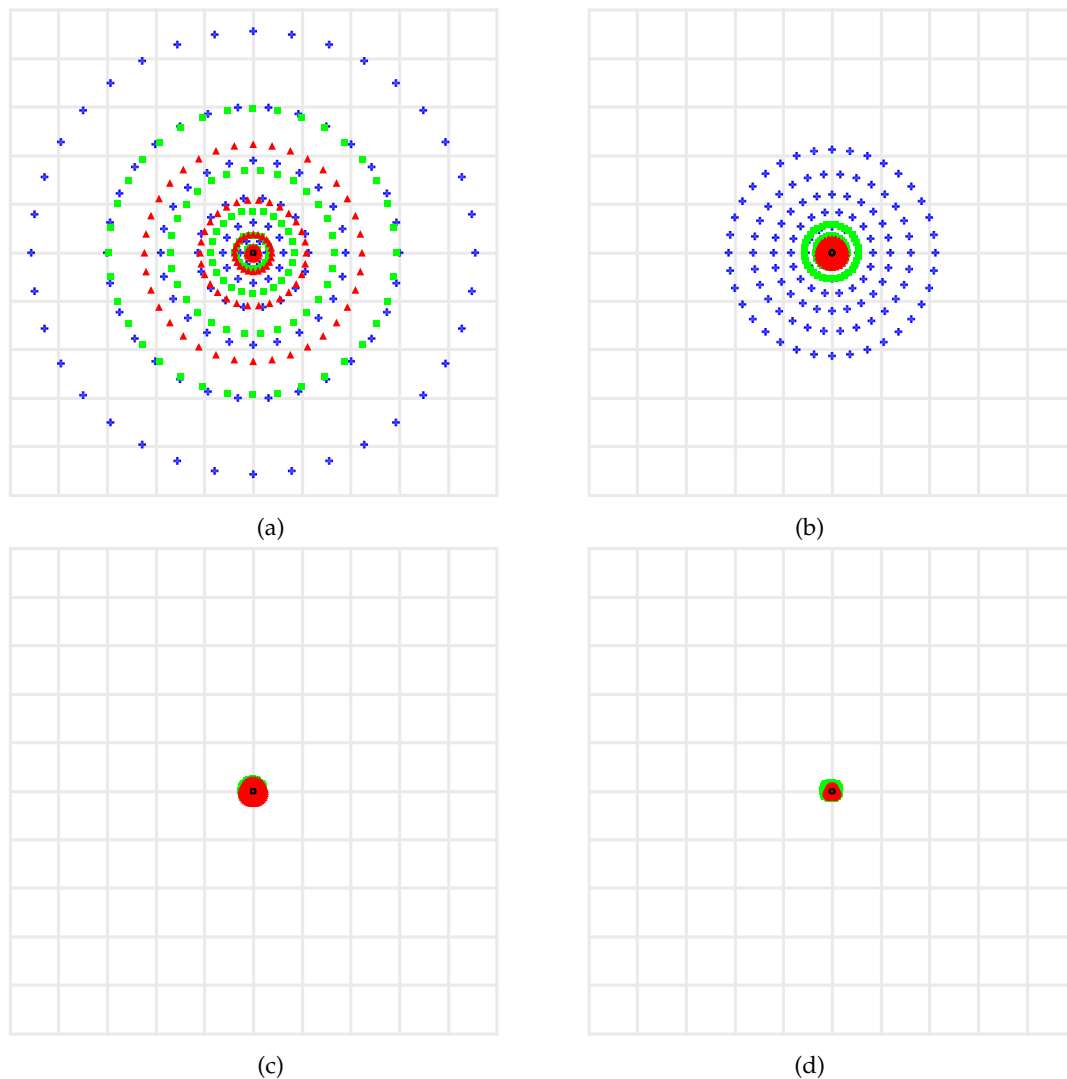
FIGURE 3.16: Spot diagrams for (*a*) a singlet, (*b*) a system with two lenses with the same material, (*c*) a cemented doublet, and (*d*) an air-spaced doublet. It shows on-axis image spots for both lenses. All grids represent the same scale.

The air-spaced doublet presents the same benefits as the cemented doublet. However, considering that they have two extra degrees of freedom, the distance between the lenses and the RoC of the internal surfaces, the aberrations correction could possibly be improved even further.

The doublets do not only correct for SA but also for LCA, so that it also tackles the problem presented with the power splitting technique using the same material for the lenses. This results in a smaller image spot size on-axis when using a wide

wavelength band. This method is a combination of the methods presented in Sections 3.1.3 and 3.1.4 [66].

Four different optical systems were designed with the same focal length and $F/\#$ for a fair comparison, as illustrated in Fig. 3.15. The first one is composed of a singlet, Fig. 3.15a, the second one of two lenses with the same material (BK7), Fig. 3.15b, the third one of a cemented doublet with two different materials (BK7 and SF5), Fig. 3.15c, and the forth one of an air-spaced doublet (also composed of BK7 and SF5), Fig. 3.15c.

Figure 3.16 demonstrates the image spot size for all four systems. It is noticeable how the worst performance is presented by the singlet, as in Fig. 3.16a, it presents a significant SA and LCA. Splitting the singlet into two lenses of the same material, as in Fig. 3.16b, reduces the spot size, as was also previously seen in Fig. 3.12, but it still demonstrates a significant SA and LCA. Using a cemented doublet, as seen in Fig. 3.16c, significantly tackled the SA and LCA issue presented in the previous two examples. However, the air-spaced doublet, as seen in Fig. 3.16d, exceeded the image quality of all the other systems presented.

3.1.6 Aspherical surfaces

In 984, the mathematician Ibn Sahl first discovered the stigmatic refractive surface. However, Sahl was not able to formulate a general equation [72]. In 1637, René Descartes described how a refractive lens can be free from spherical aberration if conics of revolution are used. These surfaces of revolution received the name of Cartesian Ovals [64], also known as Descartes' Ovoids [55]. In 1944, Luneburg used Fermat's principle of stationary optical paths to show that the Cartesian Ovals can be represented by a fourth-order curve in the meridional section. If one of the conjugate points (object or image) is located at infinity, the Cartesian Oval reduces to a second-order curve of a conicoid of revolution [73]. Figure 3.17 illustrates the different conic sections.
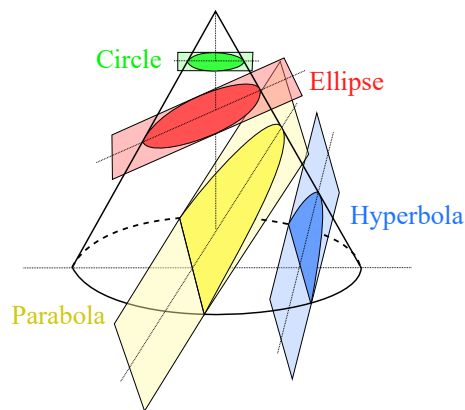
FIGURE 3.17: Conic sections demonstrating the shape of hyperbola, parabola, ellipse, and circle.

Conic surfaces are often used in optical systems due to their properties to correct SA. They can be used for refractive and reflective elements. The lenses or mirrors designed with conic surfaces are known as aspheric elements [74].

Using Fermat's Principle and the properties of the ellipse, one can easily deduce that if the eccentricity of the ellipse is properly chosen, the ovoid is free from SA [55].
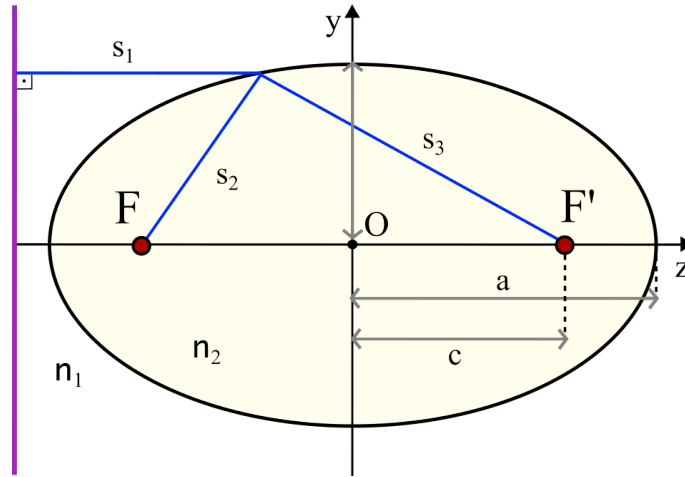
FIGURE 3.18: Cartesian Ovals. s_1 is the incident ray, s_2 and s_3 are the paths to both optical focii of an ellipsoid.

As illustrated in Fig. 3.18, a line s_1 parallel to the directrix of an oblate ellipsoidal surface (or ellipsoid of revolution), represented in purple, is located at a distance $\pm\frac{a}{\varepsilon}$ from the center of the ellipse O, where a is the semi-major axis and ϵ the eccentricity of the surface. The eccentricity of an ellipse is given by the semi-focal separation c divided by the semi-major axis, as seen in Eq. 3.6, and the equation of the ellipse seen in Fig. 3.7, where b is the semi-minor axis [75]. The vector sum law states that the sum of two vectors from the focal points of an ellipse is constant, as shown in Eq. 3.8 [76].

$$\varepsilon = \frac{c}{a} \tag{3.6}$$

$$\frac{z^2}{a^2} + \frac{y^2}{b^2} = 1 \tag{3.7}$$

$$(s_2 + s_3) = cte \tag{3.8}$$

where s_2 and s_3 are two segments from the ellipse's focal points to the ellipse points. They can be expressed as Eqs. 3.9 and 3.10.

$$s_2 = \sqrt{(z - c)^2 + y^2} \tag{3.9}$$

$$s_3 = \frac{a}{\varepsilon} - z = (a - \varepsilon z) \tag{3.10}$$

Algebraically manipulating the Eqs. 3.7 and 3.9 gives Eq. 3.11. Thus, Eqs. 3.10 and 3.11 can be combined into Eq. 3.12 that shows the eccentricity of the ellipse in terms of lines s_2 and s_3.

$$s_2 = \frac{(a - \varepsilon z)}{\varepsilon} \tag{3.11}$$

$$s_2 = \varepsilon s_3 \tag{3.12}$$

Now, considering that s_1, s_2, and $s3$ are light rays, one can use Fermat's principle to derive the OPL of the system, as shown in Eq. 3.13 [56].

$$(n_1 s_1 + n_2 s_3) = cte \tag{3.13}$$

Finally, manipulating the Eqs. 3.12 and 3.13 demonstrates that the only solution possible is the concave or convex surface of a lens being a conicoid of revolution with the eccentricity ε equal to the ratio of the refractive indices at the chosen wavelength [77–80]. Therefore, for a lens to be free from spherical aberration and guarantee its stigmatic property, the Eq. 3.14 must be satisfied.

$$\varepsilon = \frac{n_1}{n_2} \tag{3.14}$$

where n_1 and n_2 are the refractive indices before and after the aspherical surface, respectively.
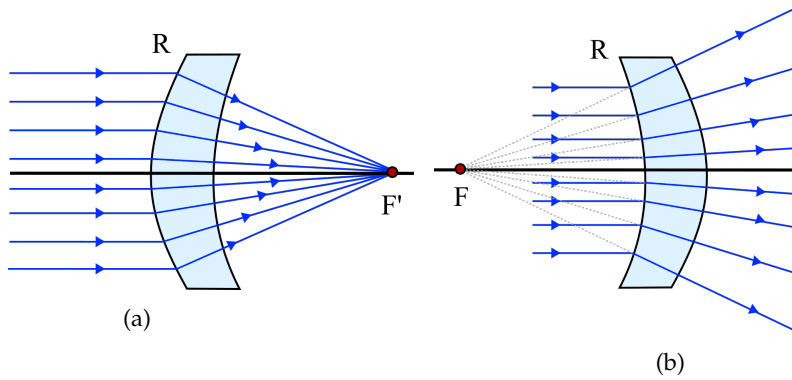
FIGURE 3.19: Ray-tracing through a lens free from spherical aberration using ellipsoidal surfaces for a (a) converging lens, and for (b) a diverging lens.

The surface's Schwarzschild constant, or conic constant k, is related to the eccentricity ε as $k = -\varepsilon^2$ [54, 81]. From that, one can obtain the relation between the refractive index, at the chosen wavelength, and the conic constant as in Eq. 3.15.

$$k = -\left(\frac{n_1}{n_2}\right)^2 \tag{3.15}$$

For an ellipsoid of revolution surface, the rays are refracted at the first surface of the lens, so in this case, n_1 is the refractive index of the air, and n_2 is the refractive index of the lens, as seen in Eq. 3.16.

$$k_e = -\frac{1}{n^2} \tag{3.16}$$

One can extend this solution for a collimated beam into a plano-convex or plano-concave lens, as shown in Fig. 3.20. In this case, n_1 and n_2 is the refractive index of glass and air, respectively. Considering that $n_1 > n_2$, the eccentricity is greater than one, therefore this surface represents a hyperboloid of revolution. [82].

$$k_h = -n^2 \tag{3.17}$$

where k_h is the conic constant, and n is the refractive index of a lens at a given wavelength. The surface height, y, as a function of sag z, is given by $y^2 = 2Rz - (1 - n^2)z^2$, where R is the radius of curvature of the surface at its vertex. This equation

represents a conicoid of revolution and does not require any higher-order aspheric coefficients.
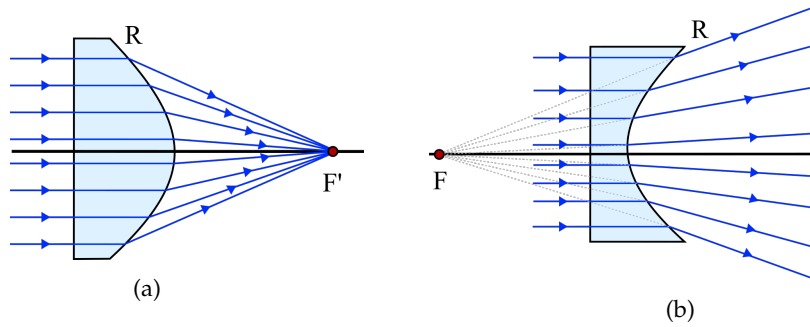
FIGURE 3.20: Ray-tracing through a lens free from spherical aberration using hyperboloidal surfaces for a converging lens (a), and for a diverging lens (b).

For reflective systems, the ellipsoidal and hyperboloidal surfaces are free from SA when the object is located at one focal point, and consequently the image is located at the second focal point [55]. When considering an object at infinity, one can identify the optimal shape of a concave mirror to be free from SA [55].

Figure 3.21 illustrates this solution, which is a parabola.
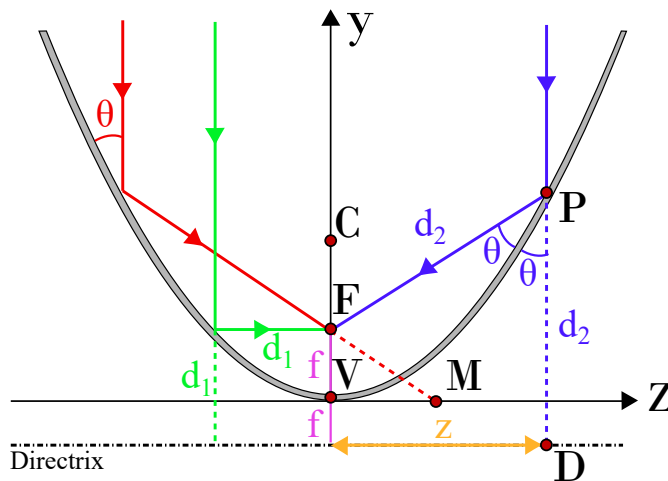
FIGURE 3.21: A parabolic mirror stigmatically focusing at the focal point F.

Considering that the distance between the focal point and the vertex of a mirror is given by f, and that the distance between the vertex of the directrix of the parabola is of the same absolute value but opposite sign $-f$, one can obtain what is the distance $\overline{PD}$:

$$\overline{PD} = d_2 = y + f \tag{3.18}$$

Using the properties of the parabola, the distance between a point in the parabola and the focal point is the same as between this point and the directrix .Thus, the distances $\overline{PD}$ and $\overline{FP}$ are the same. Therefore, the distance d_2 can be calculated in terms of y, z, and f:

$$d_2 = \sqrt{(y - f)^2 + z^2} \tag{3.19}$$

Combining Eqs. (3.18) and (3.19) and rearranging it gives:

$$y = \frac{z^2}{4f} \tag{3.20}$$

The conic section equation is given by [54]:

$$y = \frac{c\,z^2}{1 + \sqrt{1 - (1+k)\,z^2\,c^2}} \tag{3.21}$$

where c is the curvature of the mirror, defined as $c = \dfrac{1}{R}$, with the R being the RoC.

Combining Eqs. (3.20) and (3.21) gives the relationship:

$$\frac{(1+k)\,z^2}{R^2} = 0 \tag{3.22}$$

Therefore, for a mirror to be free from SA with the object at infinity, the conic constant should be $k = -1$, equivalent to an eccentricity of $\varepsilon = 1$.

3.1.7 GRIN media

Gradient index (GRIN) lenses are inhomogeneous isotropic media in which the RI gradually changes through the lens. Those gradual changes can present different structures. Thus, they can manipulate the light rays in different manners. In fact, the use of a GRIN media increases the degrees of freedom in an optical system [66].
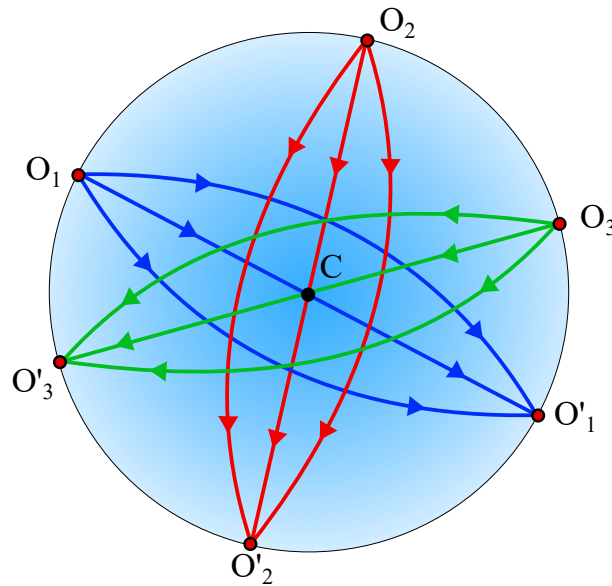
FIGURE 3.22: Representation of the Maxwell's fisheye lens. C is the center of the sphere.

J. C. Maxwell stablished in 1854 that a medium with a spherically symmetric RI distribution around a point can give a solution in which each point in a sphere produces a sharp image. This was later referred to as *Maxwell's fisheye lens*. However, initially, this was a theoretical solution with only the points around or inside of the lens being able to image sharply. Figure 3.22 illustrates the lens, with O being the object and O' being the image, both at the surface of the sphere. If one uses half of

the Maxwell's fisheye lens, it is also possible to collimate light [83]. The RI is given by:

$$n(r) = \frac{n_0}{1 + \left(\dfrac{r}{R}\right)} \tag{3.23}$$

with n_0 being the initial RI at the center of the lens, R the radius of the lens, and r the radial distance from the center C.
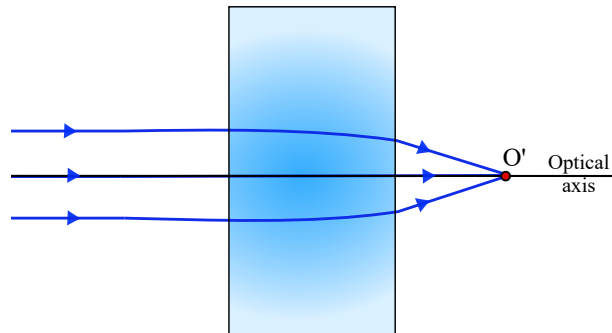
FIGURE 3.23: Representation of the Wood lens.

Unlike mirrors and homogeneous lenses, it is possible to focus a collimated incoming beam while using flat surfaces in a lens with an appropriate GRIN structure. This is the case of the solution described by R. W. Wood. He developed a gelatin cylinder in 1905 that allowed him to make a lens with flat surfaces and a GRIN structure that changed with radial symmetry along the optical axis. The RI of the lens was highest in the center and gradually fell as it approached the cylinder's edge. His lens would concentrate a collimated beam at a certain distance from the cylinder's second surface outside of the lens [84]. Figure 3.23 illustrates this lens.
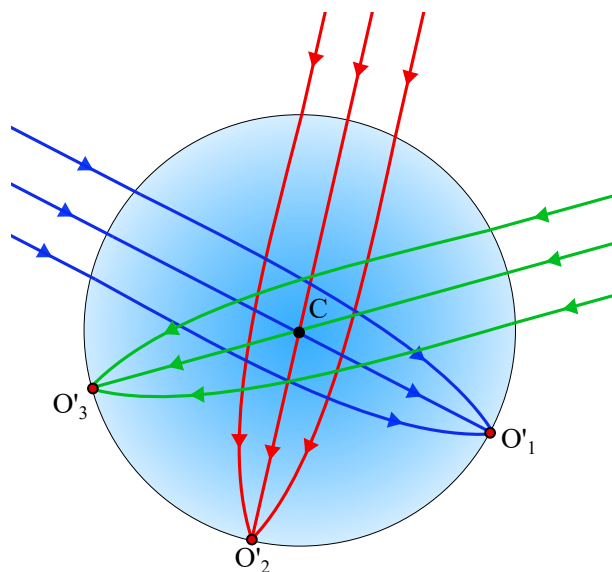
FIGURE 3.24: Representation of the Luneburg lens. C is the center of the sphere.

It was in 1964 that the Maxwell's fisheye lens was revisited by R. Luneburg. He proposed a spherical lens with a spherical concentric GRIN media for focusing light from a collimated beam on the opposed side of the sphere [85]. Figure 3.24 illustrates collimated beams being focused at the points O' at the surface of the sphere. The RI is given by:

$$n(r) = \sqrt{2 - \left(\frac{r}{R}\right)^2} \tag{3.24}$$

This type of media has been explored following the previous work of the researchers mentioned above [86].

It is possible to determine the trajectory of light rays in the GRIN media using Fermat's principle.

$$\delta \int_A^B n(\mathbf{x}, \mathbf{y}, \mathbf{z}) \, ds = 0 \tag{3.25}$$

where ds is the differential length of the path between A and B [86].

Considering that the length ds can be a path in three dimensions, the length can be described in terms of $x(s)$, $y(s)$, and $z(s)$. Considering the gradient, all three functions have a partial differential equation given by [87]:

$$\frac{d}{ds}\left(n\frac{dx}{ds}\right) = \frac{\partial n}{\partial x} \tag{3.26}$$

$$\frac{d}{ds}\left(n\frac{dy}{ds}\right) = \frac{\partial n}{\partial y} \tag{3.27}$$

$$\frac{d}{ds}\left(n\frac{dz}{ds}\right) = \frac{\partial n}{\partial z} \tag{3.28}$$

If one defines a vector denominated as $r(s)$ and the gradient of n being Δn, Eqs. (3.26) to (3.28) takes the form:

$$\frac{d}{ds}\left(n\frac{d\mathbf{r}}{ds}\right) = \nabla n \tag{3.29}$$

which is known as the *ray equation* [87].

If one considers the wavefront instead of the rays, the relationship is given by the *Eikonal equation*:

$$\nabla S^2 = \left(\frac{\partial S}{\partial x}\right)^2 + \left(\frac{\partial S}{\partial y}\right)^2 + \left(\frac{\partial S}{\partial z}\right)^2 = n^2 \tag{3.30}$$

with ∇S being the gradient of the optical path.

A slab with a radial GRIN structure can present different optical properties along its length. Its GRIN structure is given by [88]:

$$n(r) = n_0\left[1 - \left(\frac{g}{2}\right)r^2\right] \tag{3.31}$$

where g the gradient constant. This is a approximated form of the generic radial GRIN media described as [66]:

$$n^2(r) = n_0^2\left[1 - (gr)^2 + N_4\,(gr)^4 + N_6\,(gr)^6 + ...\right] \tag{3.32}$$

where N_4 and N_6 are the gradient coefficients of the RI.

The light ray's profile inside the lens takes a parabolic form.
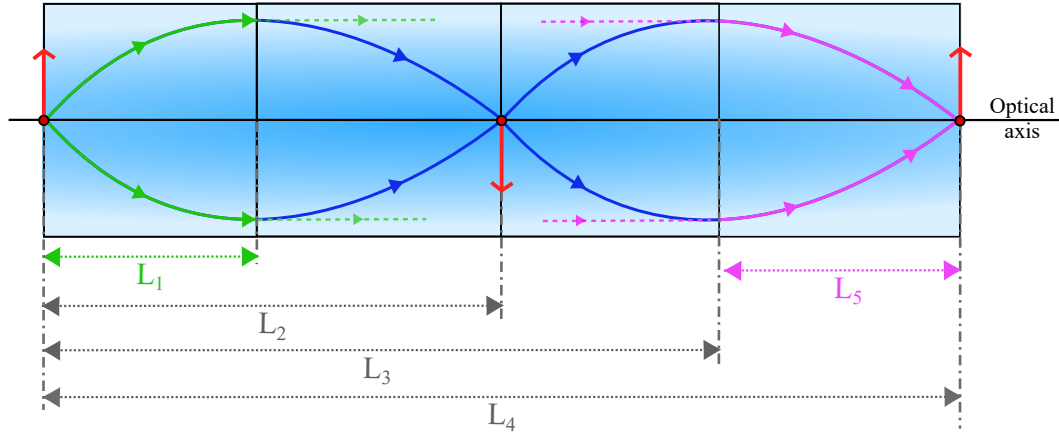
FIGURE 3.25: Representation of a slab with a radial GRIN structure.

Figure 3.25 illustrates the slab, it is known as SELFOC due to the self-focusing properties of the cylinder. The ray oscilating inside of the lens presents a period p of $\dfrac{2\pi}{\sqrt{g}}$. A pitch is given by the complete sinusoidal path [88].

A lens with the lengths $L_1 = \dfrac{p}{4}$ and $L_3 = \dfrac{3p}{4}$ collimates light from an object from the first surface of the slab. A length of $L_2 = \dfrac{p}{2}$ generates an inverted image while $L_4 = p$ generates an upright image.

A narrow slice of the cylindrical slab, specifically a slice of length L_5, is used to make a Wood lens [67]. Furthermore, the last section L_5 is actually an element called *Mikaelian lens* [83]. It can focus collimated light into the opposed surface of the lens. The GRIN structure of the Mikaelian lens is given by [66]:

$$n(r) = \frac{n_0}{\cosh\left(\dfrac{\pi}{2\,L_5}\,r\right)} \tag{3.33}$$

The GRIN lenses can also take an axial structure. They are given by:

$$n(z) = n_0 + n_z\,z \tag{3.34}$$

where n_z is the gradient coefficient of the RI in the z-axis [66].

This type of structure does not influence the trajectory of a collimated beam, as seen in Fig. 3.26a, unless a spherical (or aspherical) surface is used, as seen in Fig. 3.26b [66].

In lenses with spherical or aspherical surfaces, the preceding GRIN structures, spherical and radial, can also be employed. This is a typical combination since it aids in the correction of aberrations.

When considering the degree of freedom contributed to the system, the GRIN media can not only correct aberrations, but also have the ability to reduce the number of components or their sizes in an optical system. There are several benefits of utilizing GRIN lenses. As previously seen, GRIN lenses can be used to converge light rays, resulting in a less curved surface or thinner or lighter lenses with the same optical power as a conventional curved lens [89].
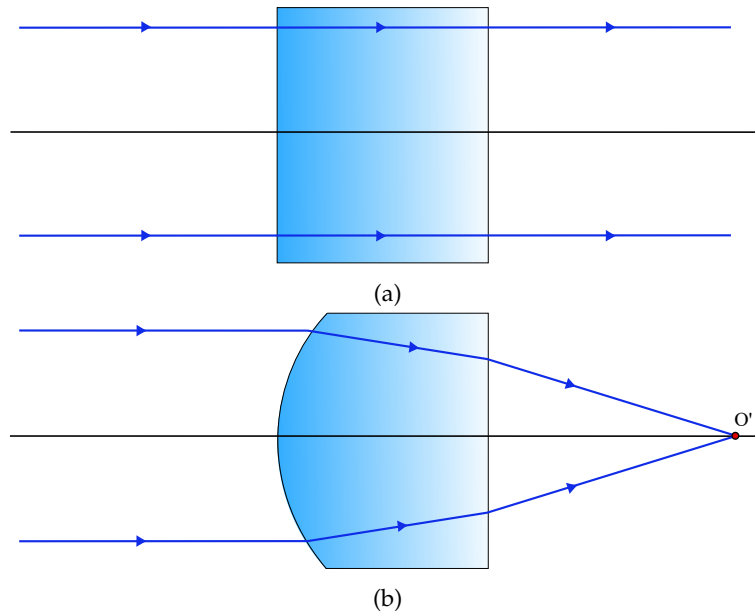
FIGURE 3.26: Layout for a GRIN lens with an axial structure and (*a*) flat surfaces, and (*b*) a curved surface followed by a flat one.

The manufacturing of GRIN lenses can involve different techniques. Some of them involve the use of stacked nanolayers of polymers compressed using high pressure and heat, or the use of ink-jet printing. The former involves the surfaces of the lens being compressed and then being molded by either bending the entire block with a GRIN structure or bending it such that the GRIN structure takes on a certain form [90, 91]. The latter involves the use of droplets with various RI being deposited into a surface/mold [92]. Even though the manufacturing techniques for GRIN media keep advancing, there are a few limitations. Until now, the cost of manufacturing GRIN lenses is high. Not only that, the materials available for printing a high-quality GRIN lens are restricted. Also, the RI variation required to achieve the light manipulation required for the lens could also be larger than the materials available can possibly cover [93].

As will be seen in Chapter 4, GRIN media can be used to create a lens free from SA, such as the *Ilinsky GRIN lens* [94]. In some configurations, their use can replace aspherical surfaces. In fact, it is possible to obtain a lens free from SA with spherical surfaces.

The usage of lenses with a freeform GRIN structure has sparked a lot of attention in recent years. This provides an additional degree of freedom, allowing for more flexibility in the design of optical systems for several applications [95–103]. However, this adds to the manufacturing process's complexity.

3.2 Methods for aplanatic correction

3.2.1 Abbe Sine Condition

The Sine Condition was initially proposed by Ernst Abbe, and for this reason, later known as the Abbe Sine Condition (ASC). He realized that the objective of microscopes free from SA could also be free from coma if the magnification of all annular zones of a lens was the same. That means that Eq. (2.18) must hold for all annular zones [66].

A lens or other optical system must satisfy the sine Abbe condition in order to create sharp images of both off-axis and on-axis objects. Figure 3.27 illustrates two rays, one paraxial and one marginal. In a lens free from SA, for it to also be free from coma,the magnification over the aperture to be the same, the magnification of the marginal and paraxial rays must be the same [66]. That means:

$$m = \frac{n\,u}{n'\,u'} = M = \frac{n\,\sin U}{n'\,\sin U'} \tag{3.35}$$

So this yields to the relationship between the angles of both rays:

$$\frac{\sin U}{u} = \frac{\sin U'}{u'} \tag{3.36}$$

remembering that the paraxial approximation $\sin u = u$ has been used for the paraxial ray but not for the marginal ray.
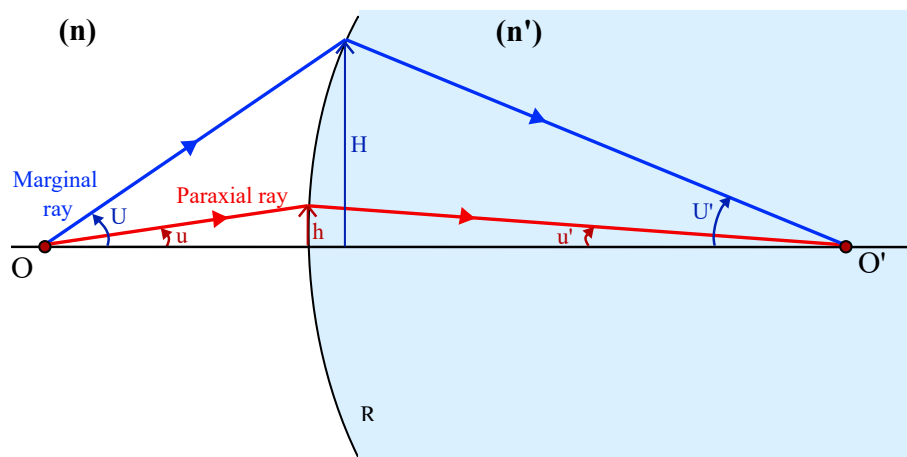
FIGURE 3.27: Abbe sine condition for finite object and image.

This relationship holds when the object and image are at a finite distance. If the object is at infinity and the image finite, as illustrated in Fig. 3.28, the relationship is given by:

$$\frac{H}{h} = \frac{\sin U'}{u'} \tag{3.37}$$
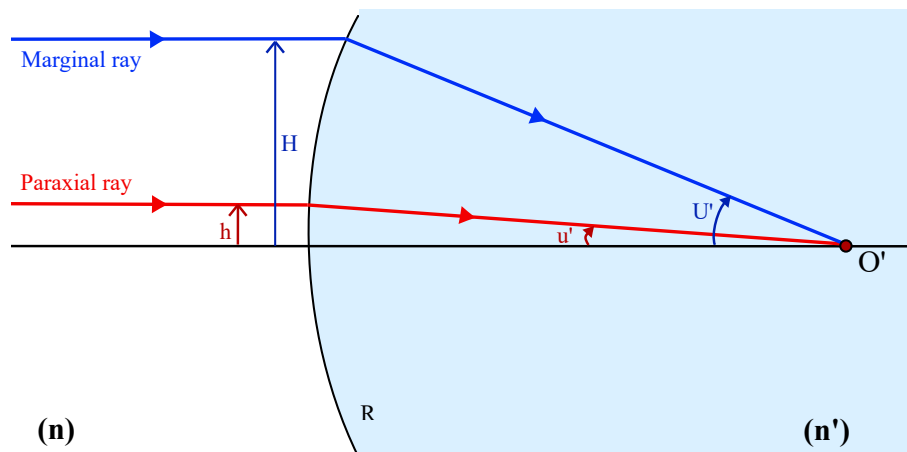
FIGURE 3.28: Abbe sine condition for an object at infinity and a finite image.

If both the object and image are at infinity, as illustrated in Fig. 3.29, the relationship is given by:

$$\frac{H_1}{h_1} = \frac{H_2}{h_2} \tag{3.38}$$
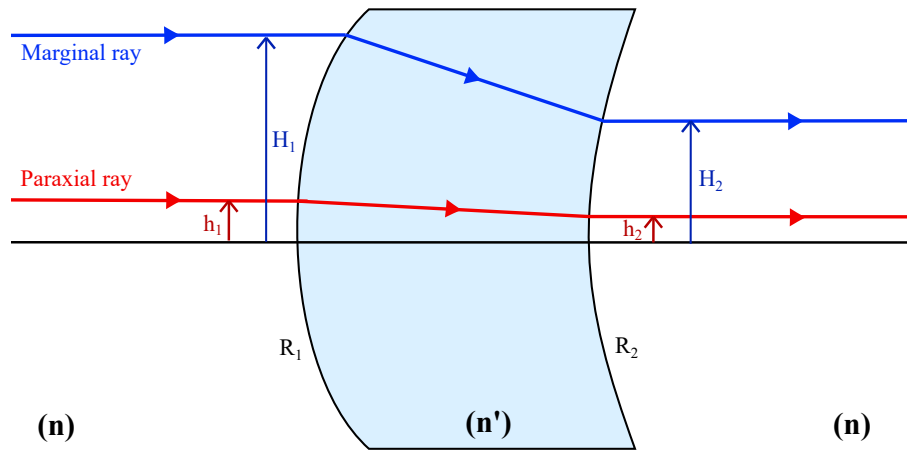
FIGURE 3.29: Abbe sine condition for an object and image both at infinity, i.e, afocal.

It is important to notice that these relationships must hold for all the rays in the pencil for satisfying the ASC, thus, being aplanatic.

Also, not all systems free from SA satisfy the ASC condition. As an example, a Cassegrain telescope is free from SA, but not coma. Both mirrors of the Cassegrain are correct for SA individually, but when combined do not satisfy the ASC, so the telescope is not aplanatic. The RC, as previously mentioned, is a variant of the Cassegrain, in this case, each mirror presents SA that cancel out when combined. They are arranged in a manner that they satisfy the ASC, being aplanatic [56].

3.2.2 Aplanatic surfaces
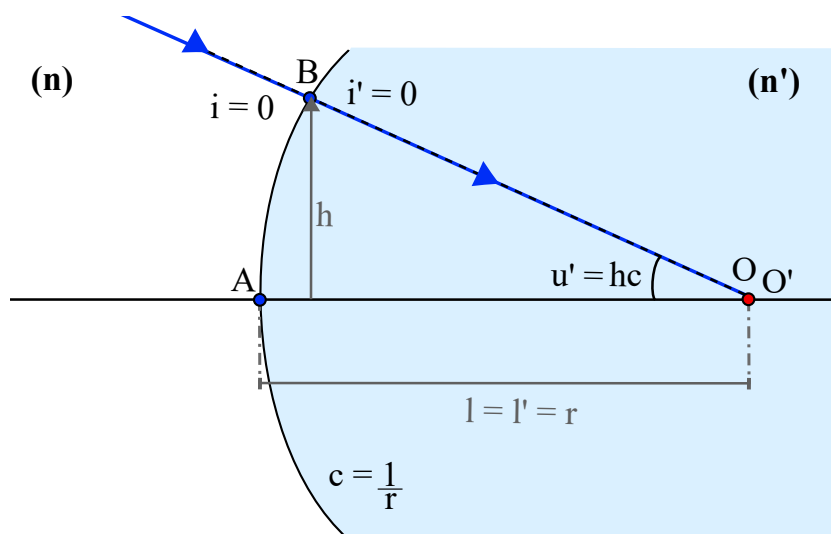
FIGURE 3.30: Aplanatic surface when $i = 0$, i.e., concentric surface.

Spherical surfaces can also be free from SA under certain conditions. Considering Eq. (2.86), a system can be free from SA if W from Eq. (2.86) is equal to zero. For that, there are different possibilities: $A = 0$, $h = 0$, or $\delta\left(\frac{u}{n}\right) = 0$. Figure 2.38 illustrates a spherical surface with its corresponding angles and distances [66].

The first possibility, when $A = 0$, and consequently $n\,i = n\,i' = 0$, gives two possibilities, $n = 0$ or $i = 0$. It is obvious that n cannot be zero, so that leaves the only alternative being $i = 0$. That means that the incoming angle is not refracted by the surface. Thus, $i' = 0$ and $u' = hc = l' = r$. So the marginal ray meets the surface with an angle which is concentric to the image point. Moreover, the object and image, O and O', can be located at the same position in the optical axis, with their distances l and l' being the same. Figure 3.30 illustrates this case. This surface is free from SA and coma, but suffers from other aberrations [66]. Remembering that the magnification of the system is given by $m = \dfrac{n\,l'}{n'\,l}$. For a concentric surface this magnification takes the form of:

$$m_c = \frac{n}{n'} \tag{3.39}$$
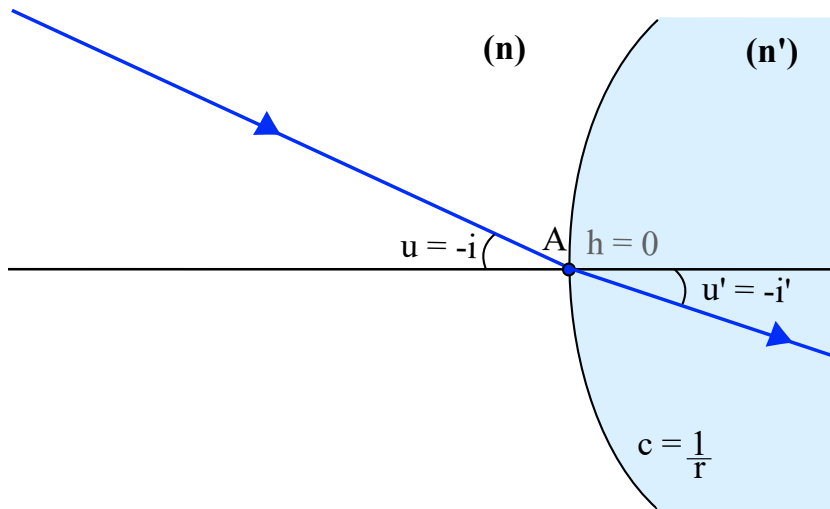
FIGURE 3.31: Aplanatic surface when $h = 0$, i.e., the ray intersects the vertex. In this case, $n' > n$.

In the second possibility, where $h = 0$, the ray intersects the surface at the vertex. This surface is free from SA, coma, and astigmatism but suffers from other aberrations. That means that it is not only aplanatic, but also anastigmatic. This type of surface is suitable for field lenses. The distances for the object and image are then $l = l' = 0$, and the angles are $u = -i$ and $u' = -i'$ [66]. Figure 3.31 illustrates this case. This surface is not only free from SA and coma but also from astigmatism, i.e., anastigmatic.

In the third possibility, with $\delta\left(\frac{u}{n}\right) = 0$, guarantees that the SA, coma, and astigmatism of the surface is corrected. This is evident when considering the Seidel coefficients of those three aberrations in Table 2.1. Remembering that $\delta\left(\frac{u}{n}\right) =$

$\left(\frac{u'}{n'}\right) - \left(\frac{u}{n}\right)$, this means that $\left(\frac{u'}{n'}\right) = \left(\frac{u}{n}\right)$. This solution is many times referred to as the aplanatic surface [7, 56]. Combining $\delta\left(\frac{u}{n}\right) = 0$ and Eq. (2.15) gives:

$$-\frac{h\,n}{r} = u\,(n'+n) \tag{3.40}$$

Replacing the angles u and u' in Eq. (3.40) by the distance between the object and image yields:

$$l = r\frac{n+n'}{n} \tag{3.41}$$

and

$$l' = r\frac{n+n'}{n'} = \frac{n}{n'}\,l \tag{3.42}$$

Considering that both l and l' are of the same sign, it means that an image cannot be real if the object is real. Thus, at least one, image or object, must virtual when the other one is real.

For convergent lenses, the object is virtual and located at the intersection of the optical axis with the projection of the incoming ray. The image is real located at the intersection of the optical axis with the refracted ray. If $n > n'$, the convergence decreases, with the object farther away from the aplanatic surface. Therefore, $l' > l$. If $n < n'$, the convergence increases, with the object closer to the aplanatic surface. Therefore, $l' < l$. This relationship can be seen in Fig. 3.32.
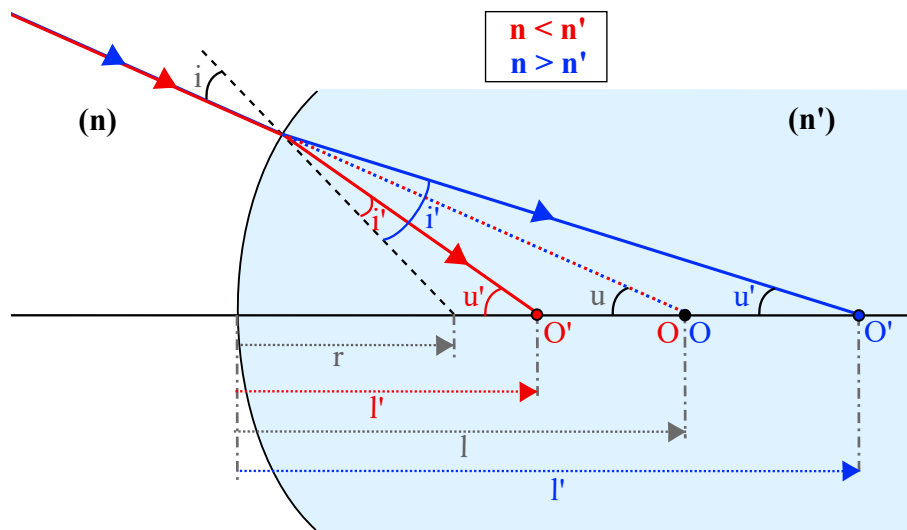
FIGURE 3.32: Convergent aplanatic surfaces.

For divergent lenses, the object is real and located at the intersection of the optical axis with the refracted ray. The image is virtual and located at the intersection of the optical axis with the projection of the incoming ray. If $n > n'$, the divergence decreases, with the object closer to the aplanatic surface. Therefore, $l' > l$. If $n < n'$, the convergence increases, with the object farther away from the aplanatic surface. Therefore, $l' < l$. This relationship can be seen in Fig. 3.33.

In summary, for both convergent and divergent lenses, when $n > n'$, have their object closer to the aplanatic surface and the ray's convergence/divergence decreases.

When $n < n'$, have their object farther away from the aplanatic surface and the ray's convergence/divergence increases.
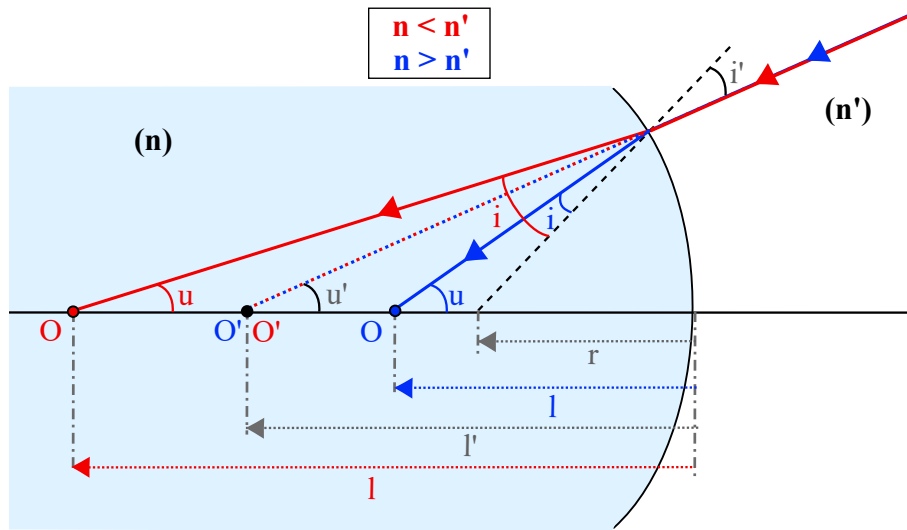
FIGURE 3.33: Divergent aplanatic surfaces.

The combination of aplanatic and concentric surfaces results in an aplanatic lens. There are four different combinations possible for an aplanatic lens, all using concentric and aplanatic surfaces.

	S1	S2	Effect on the ray
■	Ap.	Ap.	Parallel offset
■	Ap.	Conc.	Convergence ↑
■	Conc.	Conc.	Nothing
■	Conc.	Ap.	Convergence ↓
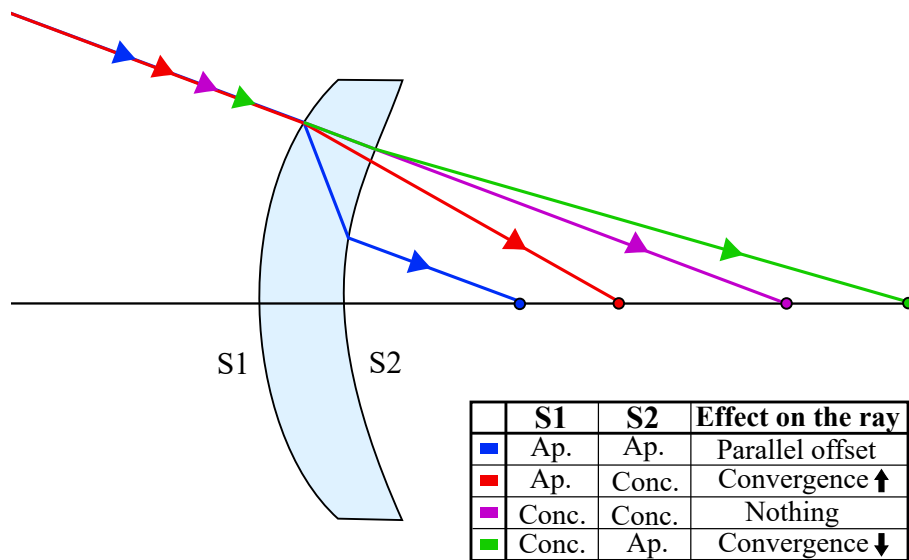
FIGURE 3.34: Combination of surfaces for aplanatic lenses.

Figure 3.34 illustrates the effects of these combinations on a ray for a convergent lens. The first and second surfaces of the lens were denominated *S*1 and *S*2. First case is if *S*1 and *S*2 are both aplanatic, the ray is refracted at both surfaces, resulting in a ray parallel to the incoming ray but with an offset, represented in blue. Second case is if *S*1 is aplanatic but *S*2 is concentric, the ray refracts in the first surface but not in the second surface and the convergence increases, respresented in red. Third

case is if *S*1 and *S*2 are both concentric, nothing happens to the ray, so it passes through both surfaces unaltered, represented in magenta. Fourth and last case is if *S*1 is concentric and *S*2 aplanatic, the ray is unaffected by the first surface and refracts in the second one and the convergence decreases, represented in green [66].

3.2.3 Symmetry principle

The *symmetry principle* uses the symmetry of the elements in an optical system around the AS. If a lens is free of SA but still has coma, an aplanatic system can be designed by combining it with a symmetrical one with respect to the aperture stop, allowing all off-axis aberrations that are odd functions of field angle, such as lateral color, coma, and distortion, to be eliminated. However, this cannot be done at the same time, because while the correct stop position can give zero coma, it may require a slightly distinct stop position when the lenses [66]. Figure 3.35 illustrates an aplanatic system using this method. It is comprised of two aspherical lenses that are each free of SA in this example. Because of this symmetry, coma can be eliminated.

The lenses are similar for finite-to-finite imaging, as in the case of Fig. 3.35, so all three aberrations can be corrected at once. Nevertheless, for typical objectives, imaging is from infinity to finite distance, and lenses cannot be identical, so a compromise with the stop position is needed to minimize coma and lateral color together, with coma usually taking priority.
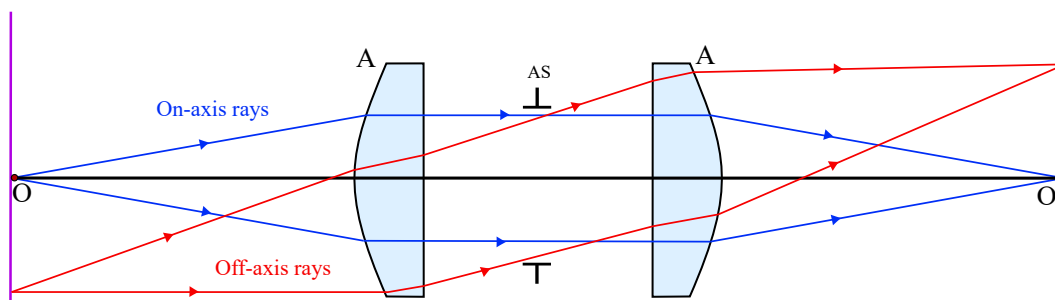
FIGURE 3.35: Symmetry principle using two lenses with a flat and an aspheric surface each.

The system's magnification, which is always 1, limits this method [66]. Even with only two aspherical lenses, it is a useful approach since it may be used for afocal and relay systems, as well as field correctors. When it comes to systems with several lenses, the possibilities are significantly expanded.

3.3 Conclusion

Various techniques for aplanatic corrections were presented. Systems free from SA are a good starting point when developing aplanatic systems. Thus, solutions for SA correction based on lens features like as RoC, dividing a single lens into multiple, and the use of aspherical surfaces and GRIN media are advantageous. The ASC must be satisfied in order to guarantee the aplanatic correction. The symmetry of the elements in an optical axis around the AS or aplanatic surfaces can also be used for aplanatic correction.

Chapter 4

Aplanatic GRIN lenses corrector with spherical surfaces

As seen in previous chapters, aplanats are regularly made of aspheres [104–106], freeform surfaces [107, 108], diffractive optics [109], or even metasurfaces [110]. However, only a few of them are made with a spherical surface [111], especially when considering all of the surfaces being spherical, such as the two systems presented in this Section using gradient-index lenses. Both of the systems have spherical surfaces and a spherical GRIN structure.

In this Section 4.1, the system presented is an $f/2.5$ afocal aplanatic system using two GRIN lenses, with the first positive and the second negative. In Section 4.2, the system presented is an $f/2.2$ aplanatic field curvature corrector using two GRIN lenses, with the first negative and the second positive.

4.1 An aplanatic afocal GRIN system

For a converging lens with spherical surfaces to be free from SA for a collimated beam, one approach is to use a GRIN structure. For that, an appropriate GRIN structure is needed. This is achievable if the GRIN structure and the second surface of the lens do not change the trajectory of the rays, i.e., the GRIN structure is iso-indicial, and the second surface is concentric to the first surface focus. To start, a necessary condition is for the second surface to be concentric to the focal point. Figure 4.1 illustrates the geometry of the lens. The RI on the vertex of the first surface at the point A is the initial RI, n_0. The RI at the point C is given by n.

Using Snell's law for the ray at the point C yields:

$$n = \frac{\sin \gamma_1}{\sin \beta_1} \tag{4.1}$$

Using the law of sines for the triangle $C\,O_1\,F'$ yields to:

$$\frac{(f - R_0)}{\sin \beta_1} = \frac{l_1}{\sin \gamma_1} \tag{4.2}$$

Thus, using Eqs. (4.1) and (4.2) gives:

$$n = \frac{l_1}{(f - R_0)} \tag{4.3}$$

The relationship between the refractive indices n and n_0 is given by:

$$n = \frac{n_0\, l_1}{f} \tag{4.4}$$

Combining Eqs. (4.2) and (4.4) and rearranging gives the focal length related to the RI n_0 and RoC:

$$f = \frac{R_0 \, n_0}{(n_0 - 1)} \tag{4.5}$$

The distance l_1 is given by:

$$l_1 = \sqrt{x^2 + y^2 + (z - f)^2} \tag{4.6}$$

So, combining Eqs. (4.4) to (4.6) and rearranging yields the GRIN RI structure for a positive lens with spherical surfaces to be free from spherical aberration as in Eq. (4.7). This is known as the Ilinsky lens [94].

$$n = \frac{(n_0 - 1)}{R_0} \sqrt{x^2 + y^2 + \left(z - \frac{R_0 \, n_0}{(n_0 - 1)}\right)^2} \tag{4.7}$$
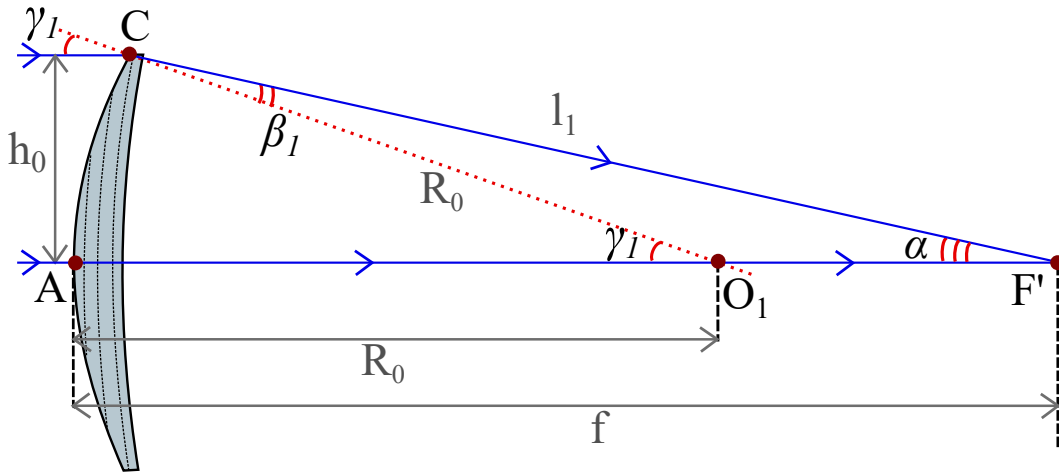
FIGURE 4.1: Ray-tracing in the convergent lens using a GRIN structure. O_1 represents the center of curvature of the positive lens, l_1 is the distance between the vertex of its first surface to the focal point, R_0 is the RoC of the first surface, and f is the focal length of the first surface.

Using the same idea, a negative lens can also be free from spherical aberration with a similar GRIN structure. If the negative GRIN lens is placed in the converging beam of the positive one and the GRIN structure is carefully chosen, an aplanatic afocal system is formed. In this case, the first surface of the second lens is concentric to the focus while the second surface collimates the stigmatic beam. The refractive indices at the point A must be the same as the point B, and point C the same as point E, for the system to be also corrected for coma.

Both lenses have to share a common focal point F', so the focal length, thickness, and RoC of the second lens has to be taken into consideration. Figure 4.2 illustrates the schematic of the negative lens.

Considering that the first surface of the lens is concentric to the focus, the thickness d of the lens has to be considered in order to obtain the RI at the points G and H. The relationship between the RI at the point A and H is given by:

$$n_0^* = n_0 \frac{(d + S_F)}{S_F} \tag{4.8}$$

Similarly to Eq. (4.4), the relationship between the RI at the points G and H are given by:

$$n^* = \frac{n_0^* \, l_2}{(S_F + d)} \tag{4.9}$$

The distance l_2 is given by:

$$l_2 = \sqrt{x^2 + y^2 + (z - S_F - d)^2} \tag{4.10}$$

Combining Eqs. (4.8) to (4.10) gives the structure of the second lens as seen in Eq. (4.11).

$$n^* = \frac{n_0^*}{(S_F + d)} \cdot \sqrt{x^2 + y^2 + (z - S_F - d)^2} = \frac{n_0}{S_F} \cdot \sqrt{x^2 + y^2 + (z - S_F - d)^2} \tag{4.11}$$

and

$$S_F = \frac{r \cdot f}{R_0} \tag{4.12}$$

where n_0^* is the refractive index at the vertex of the first surface of the negative lens, d is the thickness, r is the radius of curvature, and S_F is the focal length of the negative meniscus.

Figure 4.3 illustrates the ray-tracing through this system.
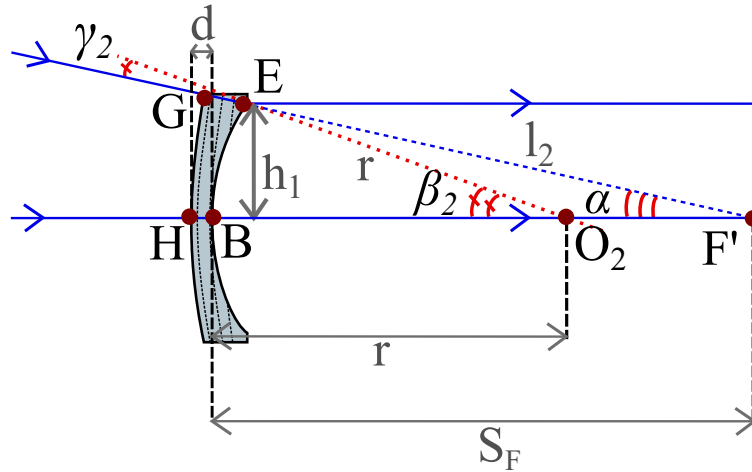
FIGURE 4.2: Ray-tracing in the divergent lens using a GRIN structure. O_2 represents the center of curvature of the negative lens, l_2 is the distance between the vertex of its second surface to the focal point, r is the RoC of the second surface, and S_F is the focal length of the second surface.

As previously seen in Chapter 3, a system free from spherical aberration is guaranteed to also be free from all orders of linear coma if the ASC is satisfied. In order for this to be the case, the angular magnification for all the aperture zones in the system must be constant. In an afocal system, the magnification is given by the ratio between the marginal rays object and image heights, as in Eq. (3.38) [56, 66, 112, 113].
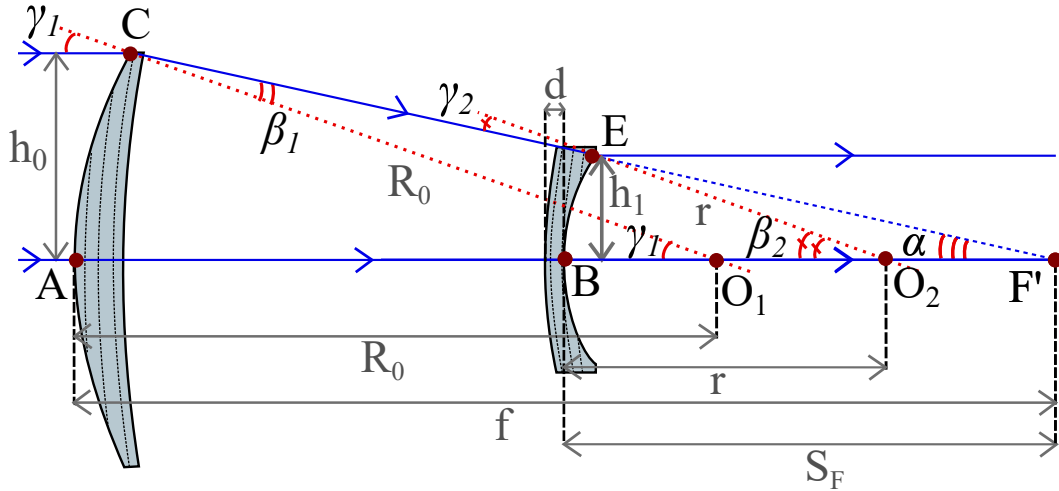
FIGURE 4.3: Ray-tracing in the afocal aplanatic system using two GRIN lenses.

To verify that the solution satisfies the ASC, the geometry of the system has to guarantee that all the rays of the system have the same magnification. The magnification of the system is given by:

$$\frac{h_1}{h_0} = \frac{\overline{EF'}}{\overline{CF'}} = M \tag{4.13}$$

where h_0 and h_1 are the heights of the images for the first and second lenses, respectively.

The height of the rays at the point C and G are given by:

$$h_0 = R_0 \sin \gamma_1 \tag{4.14}$$

and

$$h_1 = r \sin \beta_2 \tag{4.15}$$

Using the law of sines in Fig. 4.3 gives:

$$\frac{R_0}{sin\alpha} = \frac{\overline{CF'}}{sin\gamma_1} \tag{4.16}$$

for the first lens, and

$$\frac{r}{sin\alpha} = \frac{\overline{EF'}}{sin\beta_2} \tag{4.17}$$

for the second lens.

For a concentric spherical surface, O_1 is equal to O_2, so the α angle is the same for both of the lenses. Therefore:

$$\sin \alpha = \frac{R_0 \sin \gamma_1}{\overline{CF'}} = \frac{r \sin \beta_2}{\overline{EF'}} \tag{4.18}$$

Rearranging Eq. (4.18) leads to

$$\frac{\overline{EF'}}{\overline{CF'}} = \frac{r \sin \beta_2}{R_0 \sin \gamma_1} = \frac{h_1}{h_0} \tag{4.19}$$

which is precisely Eq. (4.13), proving that the Abbe Sine Condition is satisfied. Thus, the system is guaranteed to be free from all orders of spherical aberration and coma.

4.2 An aplanatic GRIN field corrector

The afocal system from Section 4.1 can also be transformed into an aplanatic field corrector if the lenses are swapped so that the negative lens is the first one in the system, and the positive lens is the second one. This field corrector can be introduced in the converging beam of an optical system, illustrated as *a* in Fig. 4.4. The condition for this system to have the field corrected is that its astigmatism be opposed to that of the GRIN corrector. A good example of field correction is for telescopes, as will be seen in Section 4.3.2 [114]. Changing the distance *D* between the lenses, considering that the ray coming out of the first lens is collimated, leads to a decrease or increase of the lenses' field curvature without deviating from the aplanatic conditions.

Again, Eq. (4.12) has to be satisfied in order to guarantee the aplanaticity of the system, and the changes in the distance D do not affect it.
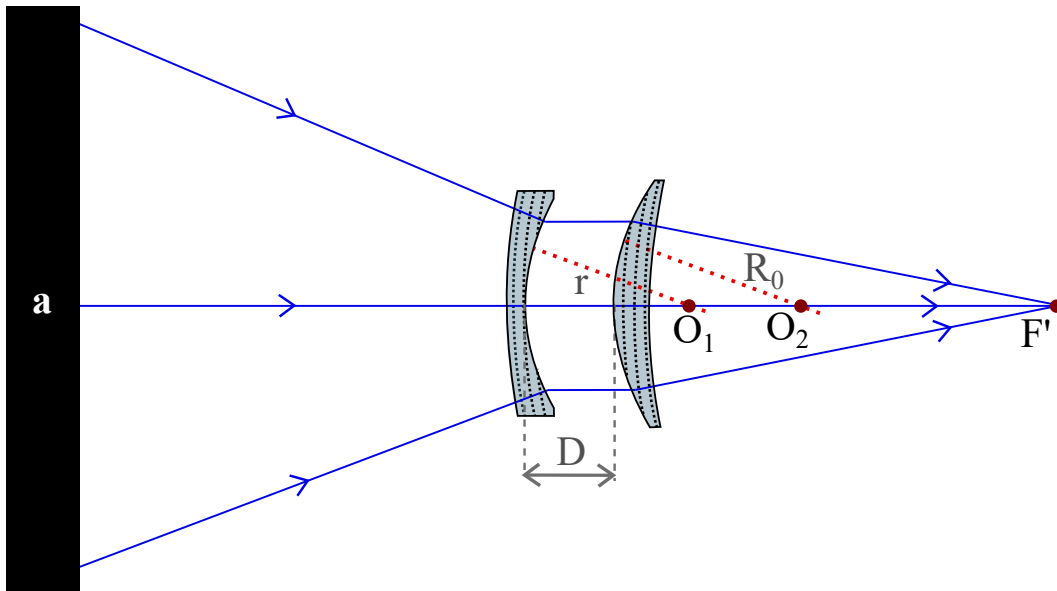
FIGURE 4.4: Ray-tracing in the aplanatic field corrector using two GRIN lenses (negative and positive, respectively). *a* is the converging system to be corrected, D is the distance between the second and third surfaces, which can be changed to introduce the system's correct overall field curvature.

4.3 Numerical examples of GRIN aplanatic systems

4.3.1 Afocal optical system

To illustrate this idea, an $F/7.4$ afocal GRIN system has been designed to demonstrate the aplanatic solution in the ray-tracing software OpticStudio (The C code for the DLLs of the GRIN structures can be seen in Appendix A). The entrance pupil diameter is 10 *mm*. The wavelength used for this example is $\lambda = 0.55\ \mu m$. The monochromatic light is considered because the chromatic dispersion depends on the materials used to create the GRIN structure. The layout of this system can be

seen in Fig. 4.3. Table 4.1 shows the parameters that have been used for the afocal GRIN system in this numerical example.

TABLE 4.1: Optical and design parameters of the aplanatic afocal GRIN system. R1 and R1′ are the first and second surfaces of the positive lens. R2 and R2′ are the first and second surfaces of the negative lens. IMA is the image space.

	Radius (mm)	Thickness (mm)	Semi-diameter (mm)	Material
R1	7.500	1.500	5.100	Positive GRIN
R1′	18.500	13.25	4.937	
R2	5.250	0.25	1.438	Negative GRIN
R2′	1.875	2.00	1.284	
IMA	Infinity		1.305	

The positive GRIN lens RI starts at 1.60 at the first surface, and ends at 1.48 at the second surface, as seen in Fig. 4.5. The negative GRIN lens RI starts at 1.68 at the first surface, and ends at 1.60 at the second surface, as seen in Fig. 4.6.
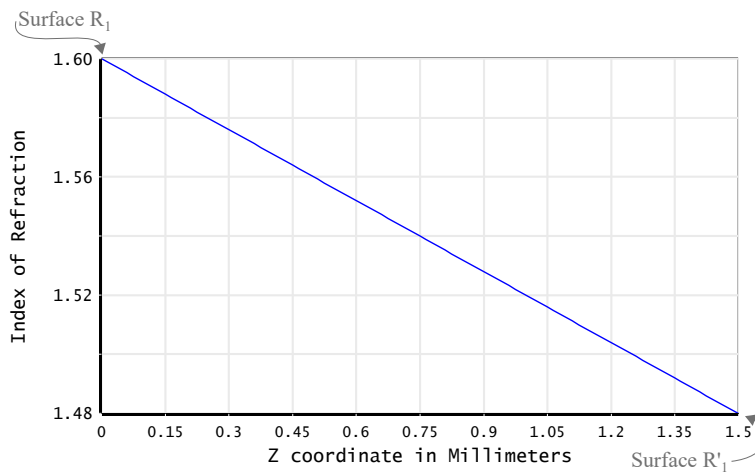
FIGURE 4.5: RI variation between the first and second surface of the positive lens.
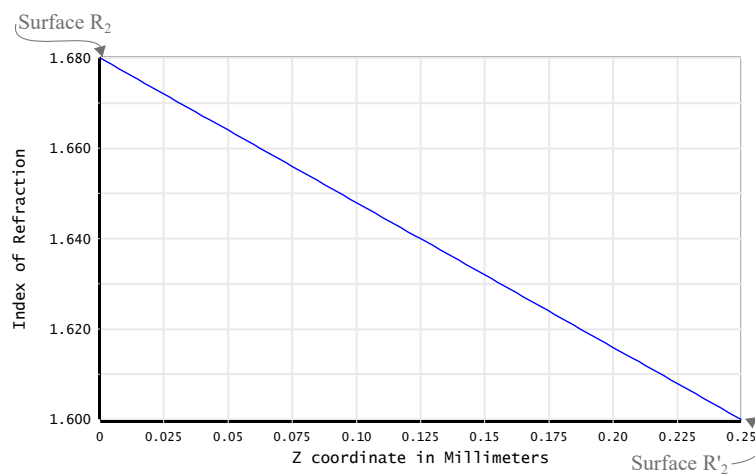
FIGURE 4.6: RI variation between the first and second surface of the negative lens.
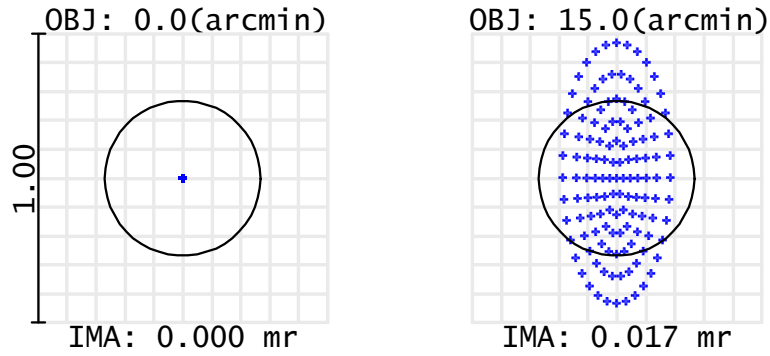
FIGURE 4.7: Spot diagram for the aplanatic afocal GRIN system. It shows the on-axis rays, as well as the off-axis rays. The Airy disk radius is 0.2684 *mr* (equivalent to 55.36 arcsec), and it is shown as a black circle.

Fig. 4.7 shows the spot diagram of the afocal system. As can be noticed, the system is free from spherical aberration and coma, but it presents an evident astigmatism.
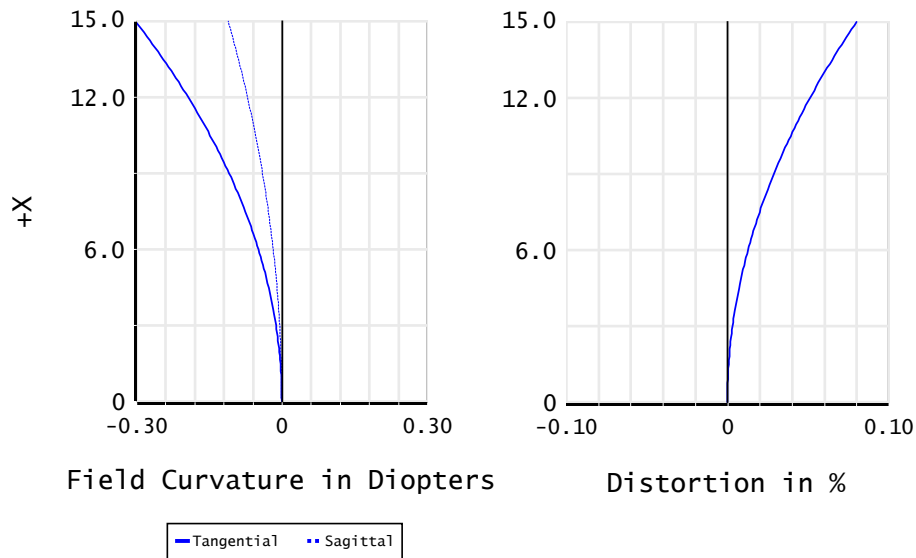
FIGURE 4.8: Field curvature and distortion in the aplanatic afocal GRIN system.

Figure 4.8 shows the astigmatism and field curvature in the afocal system. The system also presents distortion, but, it is not a limiting factor.
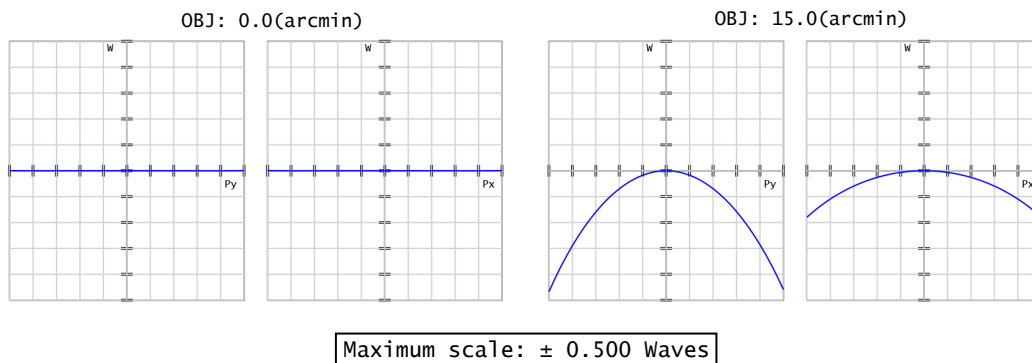
FIGURE 4.9: Optical path difference fan in the aplanatic afocal GRIN system.

Figure 4.9 shows the optical path difference (OPD) in the afocal GRIN system also validating the aplanatic solution with the presence of astigmatism.

4.3.2 Field corrector

A good example of an application of field correction using the GRIN system is Gregorian telescopes. Introducing the GRIN lenses into the telescope flattens the medial surface, i.e., the surface between the tangential and sagittal field curvature, creating a catadioptric telescope [66]. To illustrate the idea, a Gregorian telescope has been analyzed with and without the GRIN field corrector. The Gregorian telescope with the GRIN field corrector is seen in Fig. 4.10.Table 4.1 gives the parameters that have been used for the afocal GRIN system in this numerical example.

TABLE 4.2: Optical and design parameters of the aplanatic GRIN corrector system.

	Radius (mm)	Thickness (mm)	Semi-diameter (mm)	Conic k	Material
M1	-1800.000	-1275.355	310.000	-0.963	MIRROR
M2	600.352	781.212	66.950	-0.405	MIRROR
R2	780.510	15.000	36.240		Negative GRIN
R2'	281.010	239.400	35.642		
R1	281.010	20.000	39.604		Positive GRIN
R1'	745.510	745.510	38.851		
IMA	Infinity		12.547		
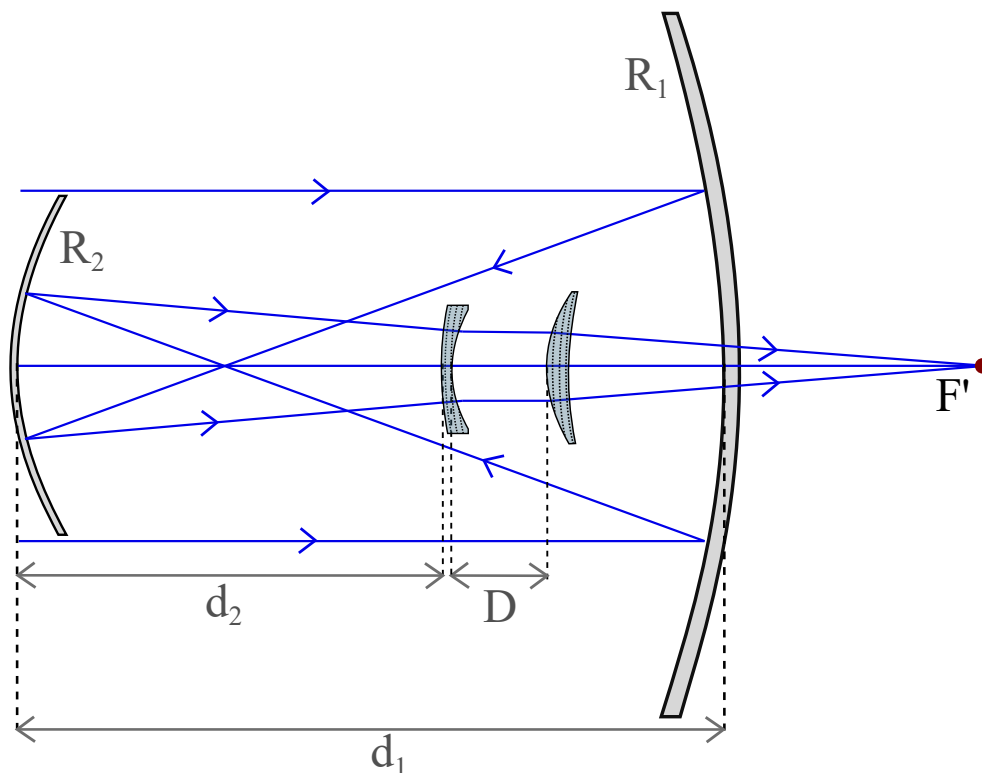
FIGURE 4.10: Ray-tracing of the Gregorian telescope combined with the field corrector using two GRIN lenses. The distance D can be optimized to obtain a field curvature of the same magnitude with the opposite to the telescope so that the system's overall field curvature is corrected.

The negative GRIN lens RI starts at 1.611 at the first surface, and ends at 1.58 at the second surface, as seen in Fig. 4.11. The positive GRIN lens RI starts at 1.58 at the first surface, and ends at 1.539 at the second surface, as seen in Fig. 4.12.
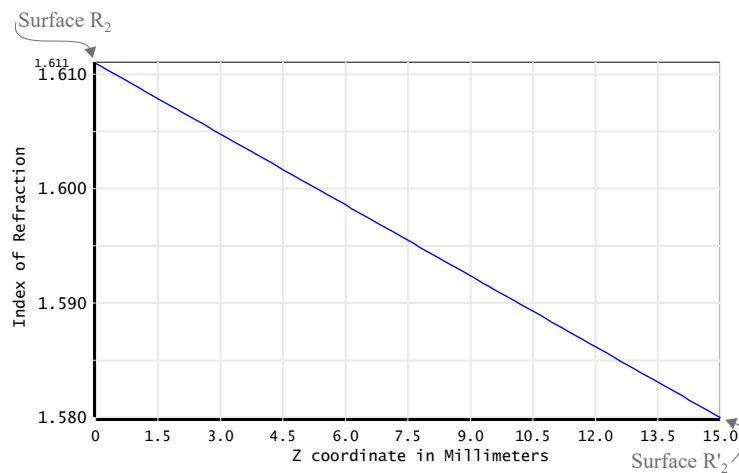
FIGURE 4.11: RI variation between the first and second surface of the negative lens.
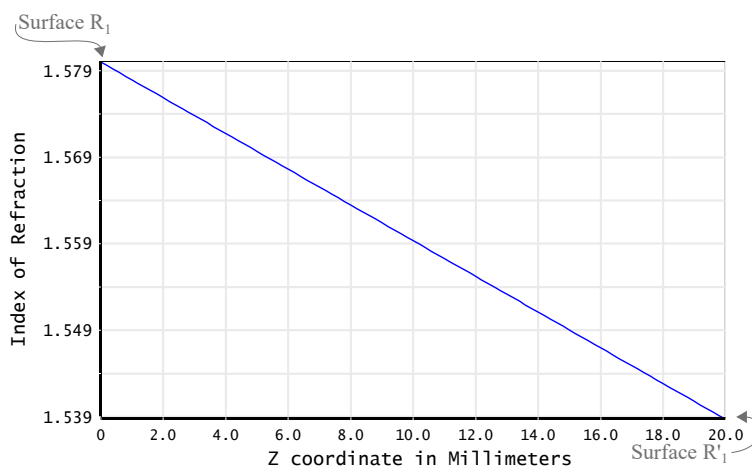
FIGURE 4.12: RI variation between the first and second surface of the positive lens.

Fig. 4.13 shows the spot diagram of the Gregorian telescope without and with the GRIN corrector. As can be noticed, both of them are free from spherical aberration and coma. The spot diagram of the original Gregorian, Fig. 4.13a, demonstrates the presence of astigmatism and field curvature. As can be seen in Fig. 4.13b, the GRIN corrector flattened the field as expected.

Figure 4.14 shows the astigmatism and field curvature in the Gregorian telescope with and without the GRIN corrector. It is evident how the field has been flattened by balancing the sagittal and tangential fields. The system presents an increase in distortion, but, it is not a limiting factor for image quality. The sagittal field curvature of the original Gregorian telescope changed from 0.2878 *mm* to 0.1765 *mm*, and the tangential one from 0.1641 *mm* to 0.1764 *mm* compared to the telescope with the GRIN corrector.
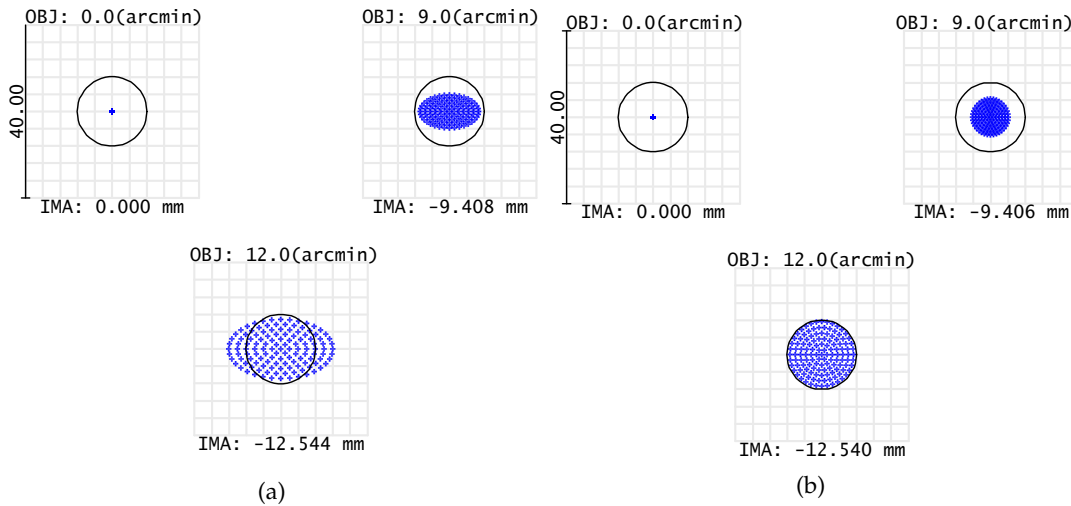
FIGURE 4.13: Spot diagrams for the Gregorian telescope (*a*) original design, (*b*) and with the GRIN corrector. It shows the on-axis rays, as well as the off-axis rays. The Airy disk radius is 8.038 μm, and it is shown as a black circle.
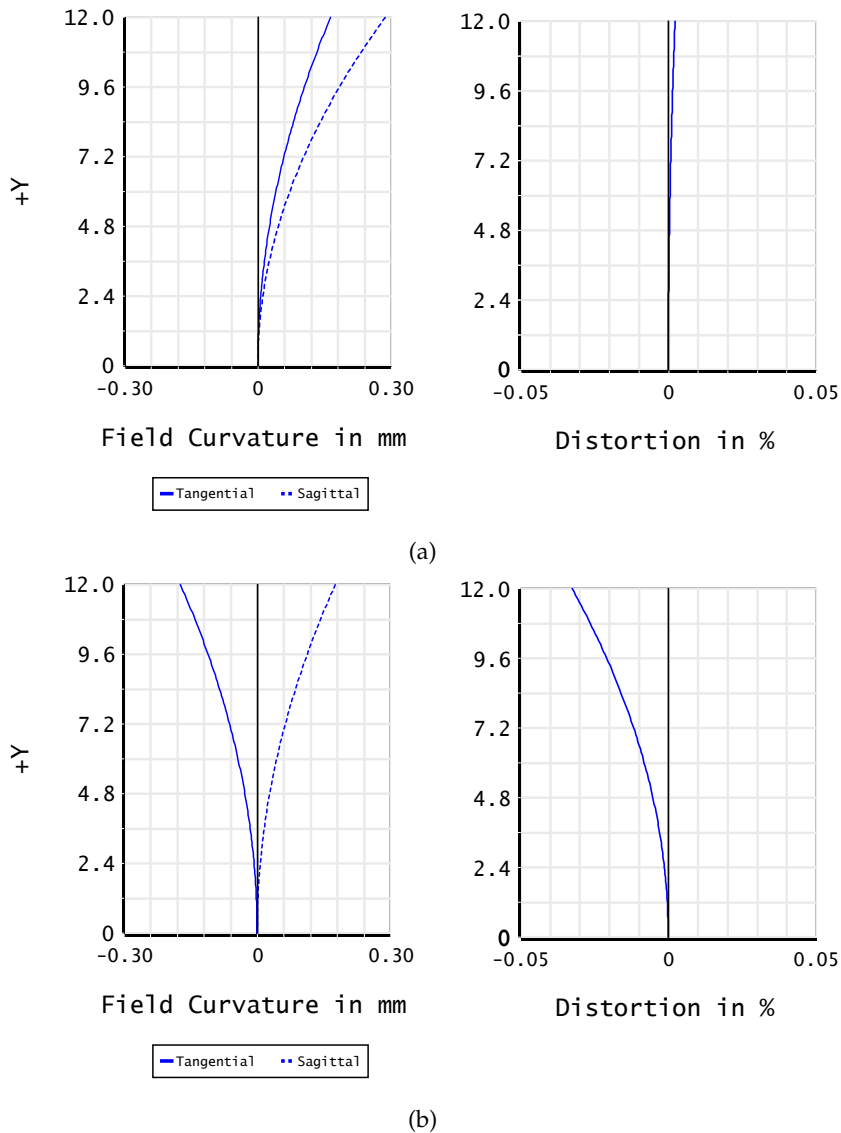
FIGURE 4.14: Field curvature and distortion in the Gregorian telescope (*a*) original design, (*b*) and with the GRIN corrector.
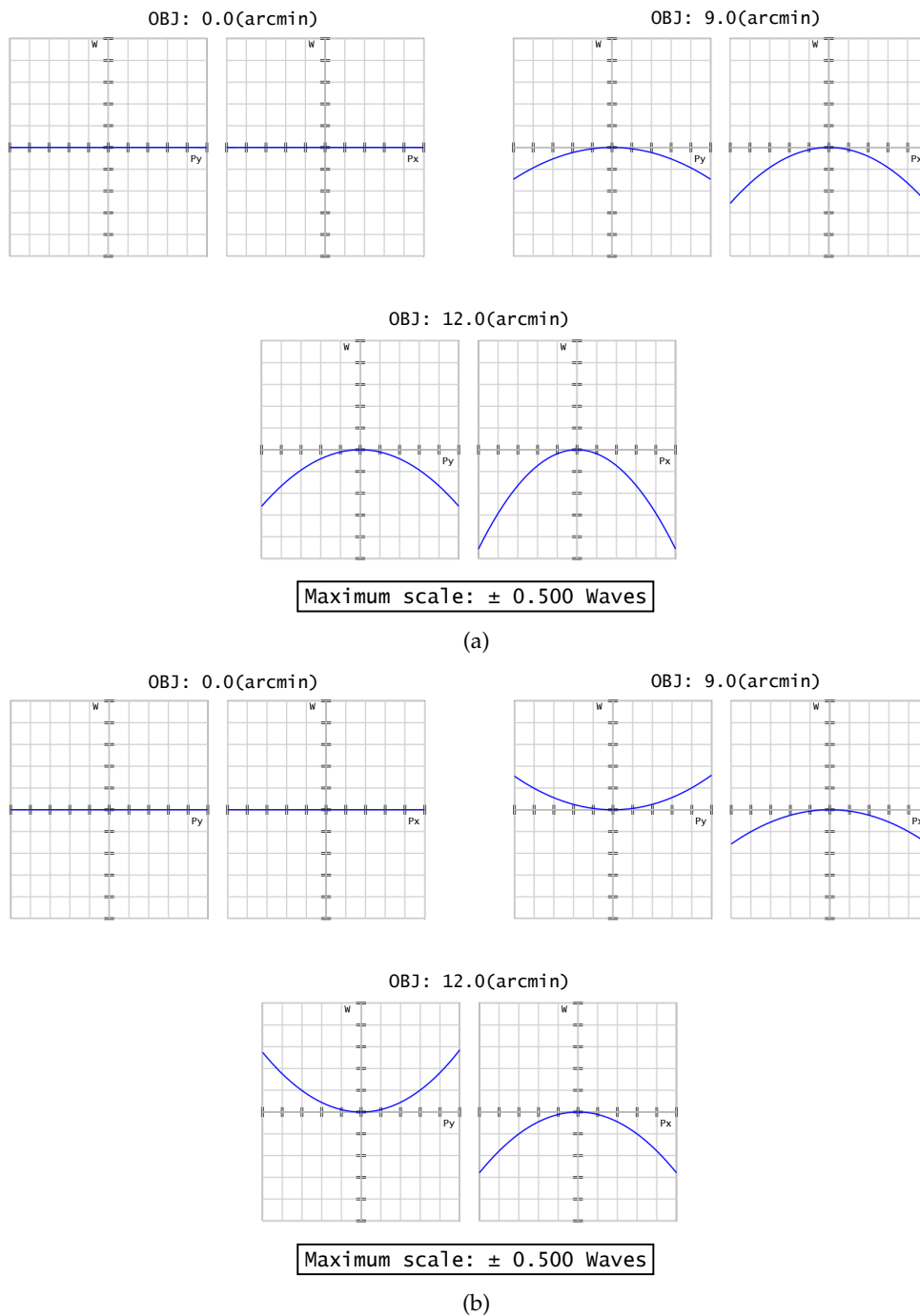
FIGURE 4.15: Optical path difference fan in the Gregorian telescope (*a*) original design, (*b*) and with the GRIN corrector. It can be seen that the medial surface has been flattened.

Figure 4.15 shows the optical path difference (OPD) in the Gregorian telescope without and with the GRIN system, also validating the aplanatic solution with the presence of astigmatism. The field has been evidently flattened in the system with the GRIN corrector.

It is important to notice that the use of the GRIN field corrector can be applied to systems other than Gregorian telescopes. The order of the astigmatism in the GRIN corrector has to be opposed to that of the optical system for it to be corrected. The distance between the GRIN pair influences the amount of astigmatism introduced

into the system, so this can be used as a degree of freedom to adapt this solution to other optical systems.

4.4 Conclusion

An aplanatic field corrector using GRIN lenses, individually free from SA, has been analytically designed to flatten the medial surface of aplanatic Gregorian telescopes for a symmetric image.

Chapter 5

Aplanatic meniscus lens corrector for Ritchey-Chrétien telescopes

As seen in Chapter 1, the Ritchey-Chrétien (RC) is an aplanatic telescope widely used in astronomy. The field curvature and astigmatism restrict the FoV of these aplanatic telescopes.

There are several ways to improve the RC, such as using correctors or curved image planes. The aplanatic meniscus lens proposed in this paper does not introduce spherical aberration or coma into the RC telescope for a given wavelength. This ensures that the meniscus can be inserted or removed from the system without any need to alter the telescope's original design while preserving its aplanatic correction [3]. Furthermore, the FoV of the RC system can be significantly increased by introducing this aplanatic meniscus due to the fact that the meniscus has intrinsic astigmatism comparable to that of the telescope but of the opposite sign. As a result, the total astigmatism in the RC can be reduced if the meniscus has an appropriate axial thickness and is placed in the telescope's converging beam such that it operates in an afocal mode.

The closest solution to the aplanatic meniscus is Rosin's two-lens corrector [25]. His solution has been tested by the author of the thesis in the optical design software OpticStudio, and the conclusions are: the field curvature introduced by the concentric and aplanatic surfaces of the corrector is not enough to correct that of the RC. In addition, the aplanatic surfaces introduce a significant axial chromatic aberration into the system when the pair is placed close to the primary mirror as suggested in [25]. This results in a significant degradation in image quality. The chromatic aberration for larger systems, such as the $f/10$ $4m$ RC used here, already affects the system in such a way that the system is not diffraction limited even for on-axis rays. It is possible to optimize the position in which the pair is implemented in the RC, while maintaining the concentric and aplanatic surfaces, and also the thickness of the lenses. However, even with this optimization, with the pair being placed closer to the focal point, the FoV is reduced compared to the RCm due to a strong lateral color in the Rosin corrector.

In Section 5.1, a method to estimate the FoV in RC telescopes is presented, and an analytical solution for the meniscus shape is given in Section 5.2. Numerical examples are given in Section 5.2.1. As shown in Section 5.2.2, the proposed meniscus can be used to extend the FoV in RC systems of various sizes, including extremely large telescopes (ELTs).

5.1   Astigmatism in the RC telescope

FIGURE 5.1: Optical layout of the RC telescope. The primary and secondary mirrors diameters are D_1 and D_2, respectively. The primary and secondary mirrors are M_1 and M_2. The distance between the primary and the secondary mirror is d_1. The focal length of the primary mirror and the overall system is given by f_1 and f, respectively. F' is the focal point of the system. θ_{RC} is the maximum half-FoV of the RC telescope. Figure not to scale.

Given the radius of curvature of the primary mirror r_1 and the secondary magnification m_2, one can design an RC telescope using Eqs. (5.1) to (5.3) to obtain the radius of curvature r_2 of the secondary mirror, and the conic constants k_1 for the primary mirror and k_2 for the secondary mirror [115].

$$r_2 = \frac{2m_2}{(m_2 + 1)}(f_1 - d_1), \tag{5.1}$$

$$k_1 = -1 + \frac{2(f_1 - d_1)}{d_1 m_2^2}, \tag{5.2}$$

$$k_2 = -\left[\left(\frac{m_2 - 1}{m_2 + 1} \right)^2 + \frac{2f}{d_1(m_2 + 1)^3} \right]. \tag{5.3}$$

where d_1 is the axial distance between the mirrors, f_1 and f_2 are the focal lengths of the primary and secondary mirrors, respectively, and f is the focal length of the telescope. The magnification of the secondary mirror, m_2, is given by f/f_1. Figure 5.1 illustrates the parameters used above to design an RC telescope.

Assuming that the RoC of the two mirrors of the RC are r_1 and r_2, and that the distance between the mirrors is d_1, we have the sag of the image surface for tangential astigmatism, z_t, as a function of the field angle θ_{RC}:

$$z_t = \frac{A}{B} tan^2(\theta_{RC}), \tag{5.4}$$

with

$$
\begin{aligned}
A = {} & 12\, d_1^4(k_2 + 1) - 12\,(k_2 r_1 + r_1 - 2\, r_2)d_1^3 + 6\, d_1(r_1 - 2\, r_2)r_1 r_2 \\
& + 2\,(r_1 - r_2)r_1 r_2{}^2 + 3\left[(k_2 + 1)r_1{}^2 - 8\, r_1 r_2 + 4\, r_2{}^2\right]d_1^2,
\end{aligned}
\tag{5.5}
$$

and

$$
B = 4\,(2\, d_1 - r_1 + r_2)^2 r_2,
\tag{5.6}
$$

The Petzval surface sag is given by:

$$
z_p = \frac{f^2 \tan^2 \theta_{RC}}{R_p}
\tag{5.7}
$$

where f is the effective focal length of the RC and R_p is the Petzval radius of curvature, which is defined as:

$$
R_p = \frac{r_1 r_2}{2(r_1 - r_2)}
\tag{5.8}
$$

Using the fact that the Petzval surface is three times closer to the sagittal image surface than to the tangential surface:

$$
(z_t - z_p) = 3(z_s - z_p)
\tag{5.9}
$$

One can estimate the sagittal surface sag z_s:

$$
z_s = \frac{1}{3}\left\{ z_t + \frac{f^2 \tan^2(\theta_{RC})}{R_p} \right\}
\tag{5.10}
$$

The optimal image surface with a nearly round image spot occurs approximately midway between the tangential and sagittal surfaces, and the sag of this surface is given by:

$$
z_m = \frac{z_t + z_s}{2}
\tag{5.11}
$$

If residual astigmatism in the RC is comparable to the system's depth of focus, then astigmatism will have little impact on image quality [116]. The depth of focus is defined as:

$$
\Delta z = \pm 2\lambda_0 (F/\#)^2.
\tag{5.12}
$$

where λ_0 is the primary wavelength, and $F/\#$ is the system's f-number.

In other words, equating the sag of the optimal image surface, Eq. (5.11), to the depth of focus, Eq. (5.12) and solving for $\tan(\theta_{RC})$, one can obtain a good approximation for the maximum half-FoV of the RC operating with a flat detector as given by:

$$
\tan(\theta_{RC}) = (F/\#)\sqrt{\frac{12 B R_p \lambda}{B f^2 + 4\, A R_p}}.
\tag{5.13}
$$

The comprehensive derivation of Eq. (5.13) is given in Appendix B.

The plots showing this dependence of the maximum field angle θ_{RC} on the entrance pupil diameter D and the telescope f-number F/# will be given in Section 5.2.1.
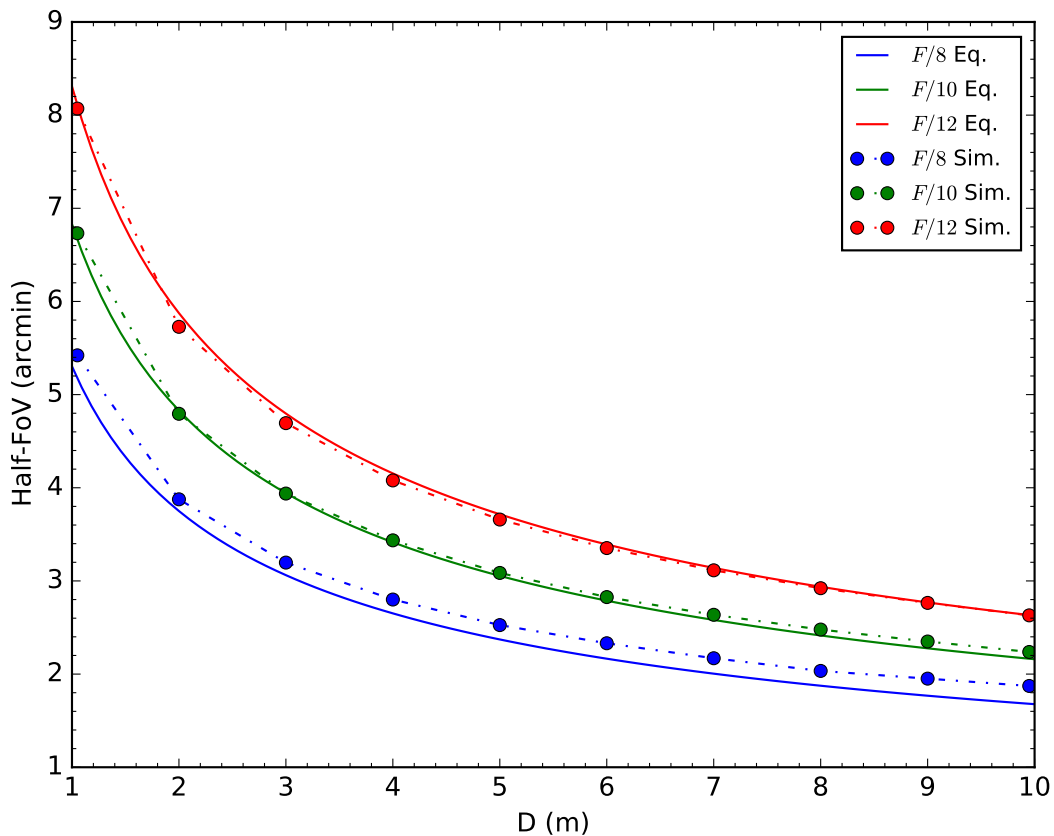
FIGURE 5.2: Maximum diffraction-limited half-FoV obtained on a flat detector using the Eq. (5.13) compared to the predicted field using simulations in OpticStudio. The entrance pupil diameter D in the range of 1 - 10 m and the focal ratio $F/\#$ in the range of 8 - 12.

Figure 5.2 shows the relation between the estimated maximum half-FoV from Eq. (5.13), and the simulation results as function of the entrance pupil diameter for the RC. Three different $F/\#$ have been considered assuming a flat image surface for all systems. The optical designs for different $F/\#$ of the RC telescopes presented here were carried out by keeping the first mirror's parameters constant while changing the secondary mirror.

5.2 An afocal aplanatic meniscus lens

Using Fermat's principle, one can show that a plano-convex lens can be made free from spherical aberration for a collimated beam if the lens' convex surface is a conicoid of revolution with the eccentricity equal to the refractive index of the lens material at a given wavelength [77–80].

Figure 3.20 illustrates the case in which a hyperboloid of revolution lens is used. A plano-convex lens focuses a collimated beam while a concave-plano surface converges a collimated beam. Thus, similarly, to collimate a converging stigmatic beam, one can use a concave-plano lens with a hyperboloidal surface, while the plano-convex lens featuring the same hyperboloidal surface will restore the original stigmatic converging beam, as seen in Fig. 5.3.
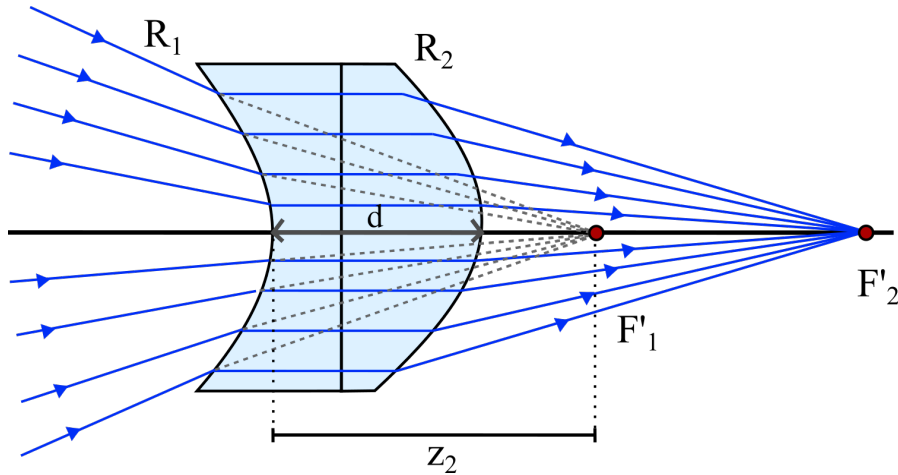
FIGURE 5.3: Ray-tracing in the aplanatic meniscus. F'_1 is the focal point of the RC, and F'_2 is the focal point of the RCm. Figure not to scale.

Furthermore, due to the internal surfaces of the pair being flat, both lenses can be combined in a single meniscus lens, shown in Fig. 5.4, which works as an afocal lens in a converging beam. The direct relation between the conic constant of the hyperboloidal surfaces and refractive index of the lens is given by Eq. (3.17).

where k_h is the conic constant, and n is the refractive index at a given wavelength.
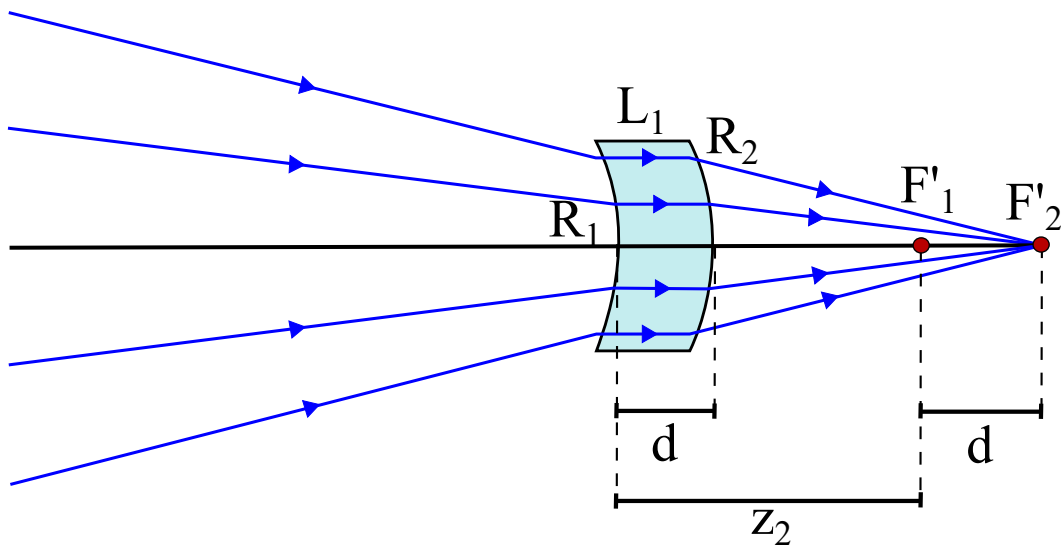
FIGURE 5.4: Ray-tracing in the aplanatic meniscus. F'_1 is the focal point of the RC, and F'_2 is the focal point of the RCm. Figure not to scale.

We shall note that such a meniscus lens is free from spherical aberration at a given wavelength, and due to its convex-concave symmetry (the sag equation for the front and back surfaces is identical), the angular magnification is preserved for all rays in the beam before and after the lens. As a result, the lens satisfies the Abbe Sine Condition [117]. Therefore, it is also free from coma[64].

For a given distance z_2 from the telescope focus F'_1 to the meniscus's anterior surface, its radius of curvature R_1 should be chosen so that the refracted rays form a collimated beam inside the lens as shown in Fig. 5.4. This condition is met if the optical power of the anterior lens surface is equal to the inverse of the distance z_2,

and from this relation, we find:

$$R_1 = -(n-1)z_2. \tag{5.14}$$

The central thickness d of the meniscus and its axial position from the telescope focus determine the amount of astigmatism introduced into the RC. We shall denote an RC system combined with the aplanatic meniscus as RCm. The new focal point position F_2' for the RCm system is at a distance d from the initial RC focal point F_1', since the radius of curvature of the posterior meniscus surface $R_2 = R_1$, where R_1 is given by Eq. (5.14).

The meniscus working as an aplanatic afocal lens preserves the RC system's aplanatic correction for a given wavelength and does not introduce any field curvature. However, astigmatism introduced by the meniscus lens's anterior and posterior surfaces with a finite thickness does not strictly cancel, and the residual astigmatism of the meniscus, as we shall see later, can be used to balance intrinsic astigmatism in the original RC system. The closer the meniscus lens is to the telescope's focus, the more curved its surfaces become, see Eq. (5.14), and as a result, the less central thickness is required to produce the same amount of residual astigmatism. Given the complexity of calculating total astigmatism in the RCm system analytically, including third- and fifth-orders, it is easier to find the meniscus's optimal central thickness that maximizes the FoV of the RCm by numerical optimization with exact ray-tracing. The meniscus corrector was designed and analyzed using the ray-tracing software OpticStudio [118].

5.2.1 Numerical Example of astigmatism correction

TABLE 5.1: Optical and design parameters of the RCm system. The primary and secondary mirrors are M1 and M2. The anterior and posterior surfaces of the meniscus lens are R1 and R2, respectively. The image space is IMA. CO is a surface that has been used to create a central obscuration for the incoming rays in the area of the secondary mirror, its value is from 0 to 624.0 mm. The primary mirror has been set to have a circular aperture radius between 280 to 2010 mm. The entrance pupil is 4 m.

	Radius(mm)	Thickness(mm)	Semi-Diameter(mm)	Conic k	Material
CO	Infinity	8600.0	624.00		
M1	-24400.0000	-8540.0	2010.00	-1.0797357	Mirror
M2	-10532.3741	11250.0	624.00	-4.3174794	Mirror
R1	-343.5283	13.8	136.00	-2.1258739	Silica
R2	-343.5283	750.00	136.00	-2.1258739	
IMA	-8521.8305		101.367		

To demonstrate the correction with an aplanatic meniscus lens, we start with an $F/10$ RC telescope with an entrance pupil diameter of 4 m. The optical layout of the RCm can be seen in Fig. 5.5. The aplanatic meniscus corrector is introduced behind the primary mirror M1 at a distance of 2.71 m. The meniscus is located at a distance $z_1 = 11.25$ m from the vertex of the secondary mirror M2. Table 5.1 describes the main optical parameters of the RCm system.
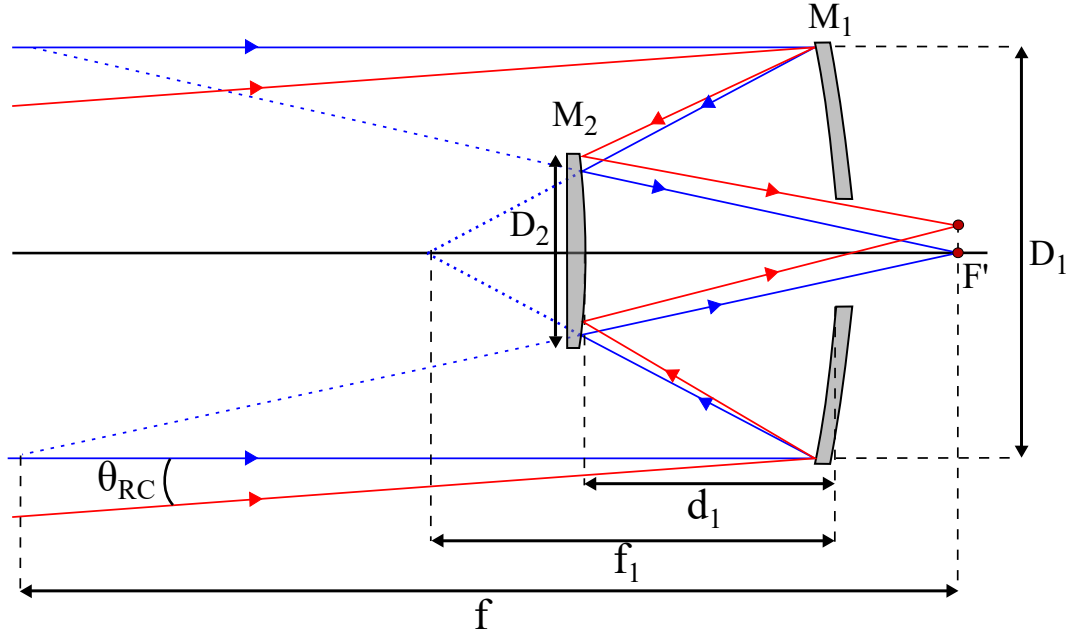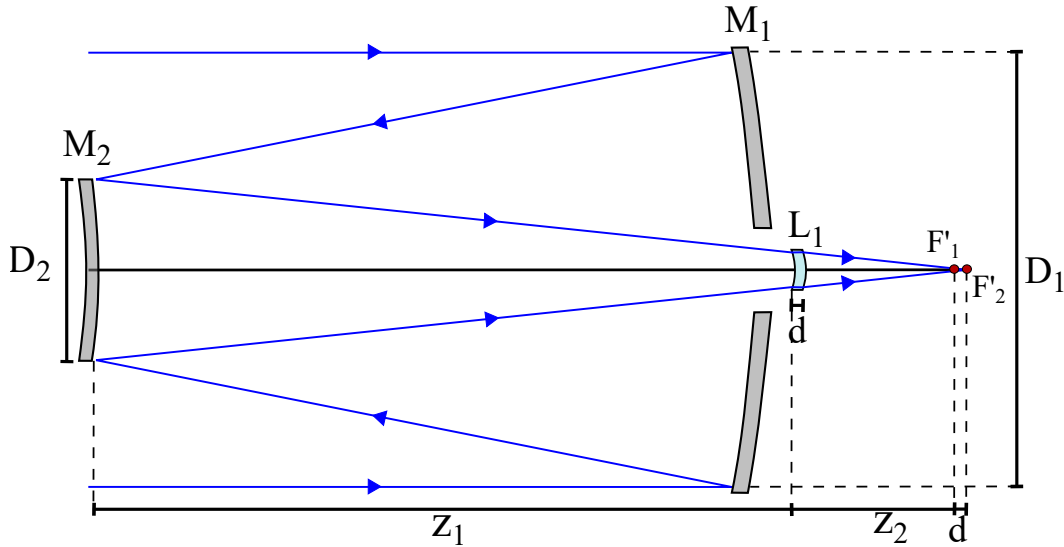
FIGURE 5.5: Optical layout of the RCm system. The primary and secondary mirrors diameters are D_1 and D_2, respectively. The distance between the secondary mirror and the meniscus is z_1. The distance between the meniscus first surface and the RC focal point F'_1 is z_2. The axial thickness of the meniscus is d. Figure not to scale.

The axial thickness of the meniscus is $d = 13.8\ mm$, while its optical semi-diameter is 136.0 mm. The material chosen for the meniscus is fused silica since it is a high-purity glass that covers a wide spectral range of transparency between 0.2 μm and 3.7 μm [119]. Besides, the fused silica also exhibits high-temperature stability and low thermal shock properties, making it an optimal choice for telescopic optics [120].

For the visible light using a wavelength range from $\lambda = 0.4\ \mu m$ to $\lambda = 0.7\ \mu m$, the refractive index of silica at the primary wavelength $\lambda = 0.6\ \mu m$ is $n =1.458$ and from Eq. (3.17) this corresponds to the conic constant $k = -2.126$ for both surfaces of the meniscus.

The RoC of the meniscus lens is defined by the distance from the posterior surface of the meniscus to the telescope focus z_2 and refractive index of the lens, according to Eq. (5.14). Therefore, the initial position of the lens can be tested for an arbitrary distance such that say $z_1/z_2 > 10$. The thickness of the lens is used as a free parameter to correct astigmatism. However, there is a mechanical constraint on the central thickness d of the lens. Here we used the manufacturing limit with $d = D/20$, where D is the lens's optical diameter. If the lens's optimal thickness to correct astigmatism falls below this limit and becomes too thin, the lens should be placed farther away from the telescope focal point. Since increasing z_2 makes the lens less curved, this, in turn, also increases the thickness of the lens required to correct astigmatism. To illustrate this, as seen in Fig. 5.6, the RoC for different z_2 related to the thickness demonstrates the trend of the thickness decreasing as the RoC increases. The larger systems requires a thicker meniscus, considering that the lens is also larger in diameter.

If the telescope operates over a broad wavelength range, the FoV might be limited by the lateral color; see discussion in 5.2.2. Thus, the distance z_2 has to be optimized by balancing astigmatism correction and controlling the lateral color. For our example $z_2 = 750\ mm$ and $z_1/z_2 = 15.0$. The diameter of the meniscus is comparable to the linear size of the full field, and for large telescopes, it can exceed 200 mm.

The maximum full-FoV increases from 12.84 to 17.40 arcmins, which is 1.36 times the FoV of the original RC system. This is equivalent to increasing the sky area by
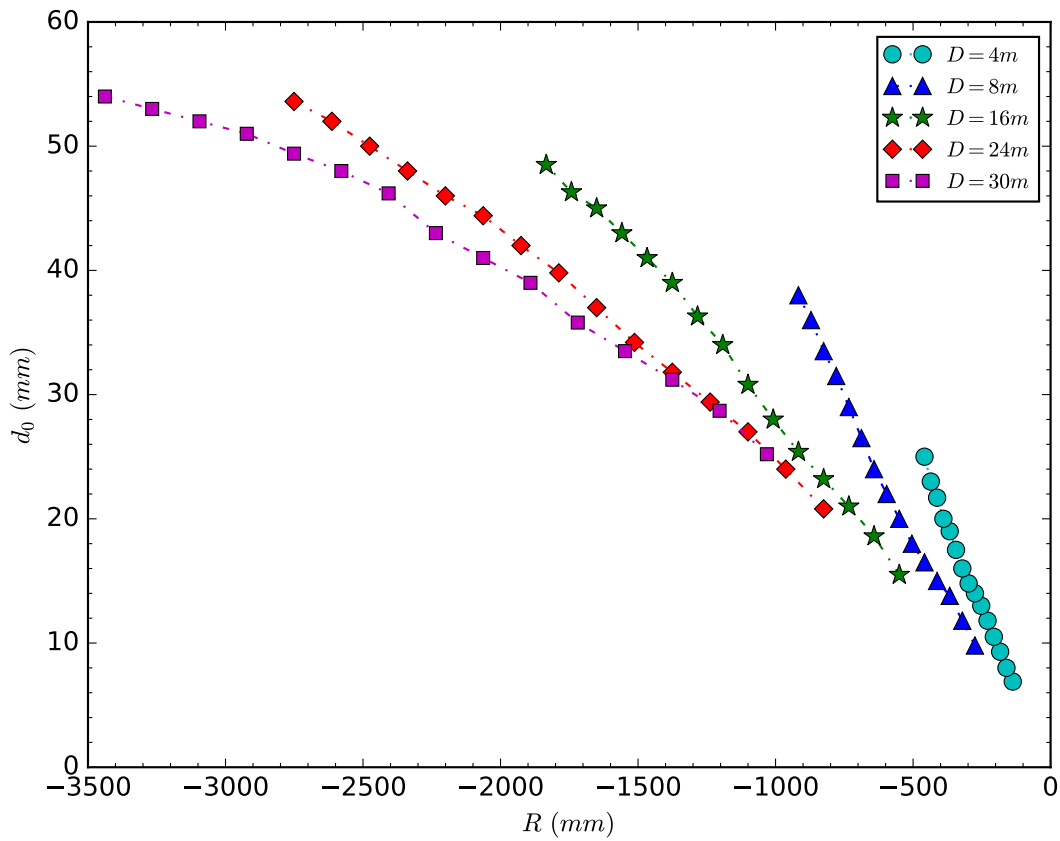
FIGURE 5.6: Thickness of the meniscus related to its RoC.

almost 1.84 times.
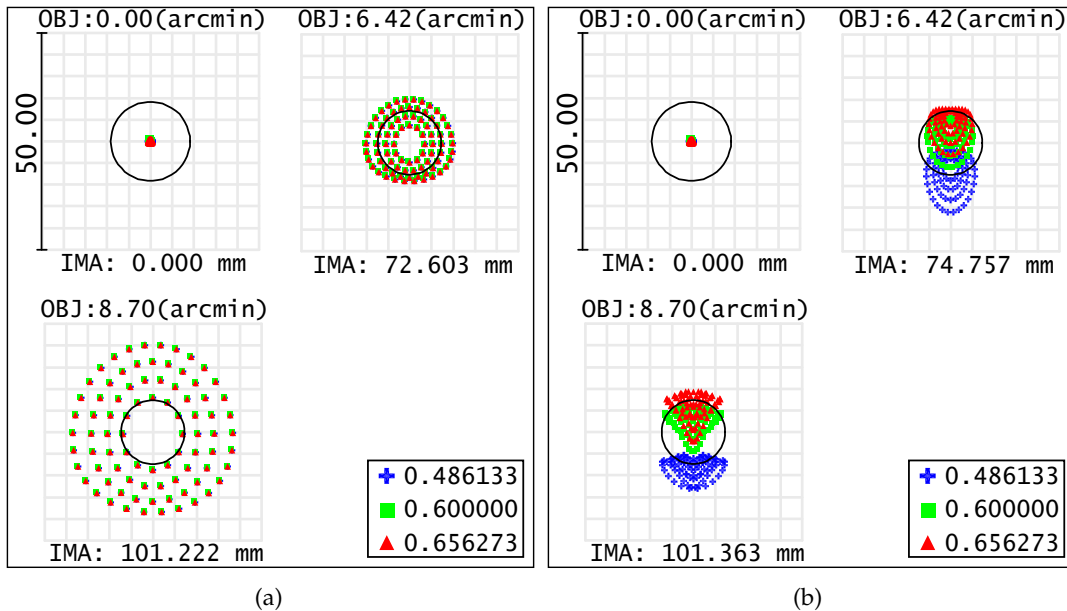
FIGURE 5.7: Spot diagrams for (*a*) the classical RC telescope, and (*b*) the RCm system. It shows on-axis and off-axis image spots at the maximum half FoV for the RC and RCm. The Airy disk radius is 7.32 μm, and it is shown as a black circle.
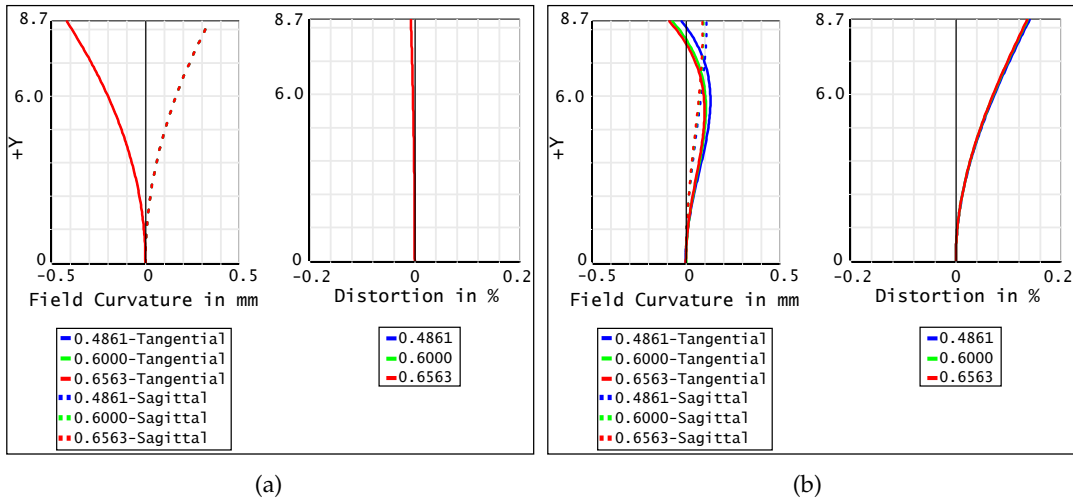
FIGURE 5.8: Field curvature and distortion for (*a*) the classical RC telescope, and (*b*) the RCm system. The *Y*-axis unit is arcmin.
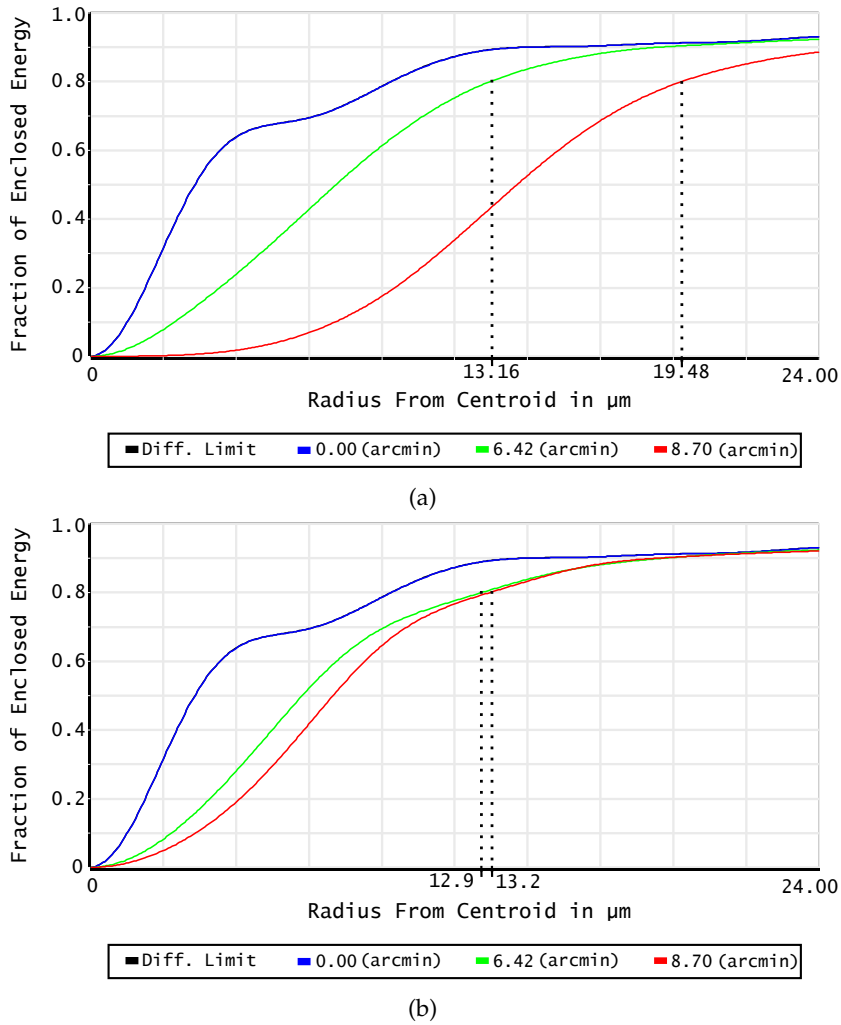
FIGURE 5.9: Encircled energy at 80 % for (*a*) the classical RC telescope, and (*b*) the RCm system.

The curved image surface used for the RCm is flatter than the one used for the RC system. The radius of curvature of the image surface for the RC is -4012.6017 *mm*, which is 2.1 times more curved than that in the RCm system, so the lens not only corrects astigmatism but also flattens the image surface. If one uses only third-order aberrations, then Petzval curvature is not changed by the meniscus lens since $R_1 = R_2$. However, when the best image surface is considered, the field curvature is more balanced by astigmatism, and as a result, the best image surface becomes less curved.

For the numerical example, using visible light, the optical performance for the two systems is presented in Figs. 5.7 to 5.9. At the edge of 8.70 arcmins half FoV, which is the maximum half FoV for a diffraction-limited RC, the RCm forms a smaller image spot. This is because the third- and fifth-order astigmatism present in the RCm are better balanced in comparison to the RC system, as shown in Fig. 5.8. The meniscus introduces a small positive distortion (less than 0.2 percent). We can also see in Fig. 5.7 (b) that lateral color is present. However, it is not critical, and by narrowing the spectral band, one can reduce the image spot size even further.

Comprehensive numerical results for this example, represented by Configuration 2 in Section 5.2.2, and two other optical designs are presented in Tables 5.2 and 5.3.

5.2.2 Numerical Results

As mentioned above, the meniscus lens suffers from lateral color, limiting the useful FoV of the RCm, but as we show later in this section, this problem can be reduced by careful consideration of the system's meniscus position. To keep the lateral color to a minimum, the meniscus should be placed as close as possible to the telescope focus F_1'. Since $R_2 = R_1$ in the meniscus design, the transverse lateral color in the system can be estimated using paraxial ray-tracing Eq. (5.15) [82]:

$$LC = (n(\lambda_2) - n(\lambda_1))\left(\frac{\bar{u}_1 d}{R_1}\right) z_2 = -(n(\lambda_2) - n(\lambda_1))\left(\frac{\bar{u}_1 d}{n(\lambda_p) - 1}\right), \qquad (5.15)$$

where $n(\lambda_1)$ and $n(\lambda_2)$ are the meniscus' refractive index for any two wavelengths, (λ_p) being the primary wavelength, and $\bar{u}_1$ is the chief ray angle after the first surface for the primary wavelength. Notice that the lateral color depends on the chief ray angle $\bar{u}_1$ and the thickness of the lens d.

The chief ray angle $\bar{u}_1$ increases linearly as the lens approaches the telescope focus and becomes more curved, whereas the optimal lens thickness d decreases more rapidly. Therefore, the product term $\bar{u}_1 d$ decreases. Thus, lateral color also decreases.

As the meniscus approaches the telescope focus, z_2 is reduced. Considering Eq. (5.14), for the lens to remain working in an afocal mode, the meniscus surfaces must become more curved. As a consequence, the optimal central thickness required for astigmatism correction decreases. The practical limit of how small the central thickness can be depends on the manufacturing process and structural stability of a thin glass shell. Therefore, as mentioned earlier, one has to consider a maximum permissible diameter-to-thickness ratio, which in our analysis we previously set to $D_{lens}/d = 20$.

A number of the RC telescope designs have been considered here to verify the gain in aberration-free FoV after inserting the aplanatic meniscus near the telescope
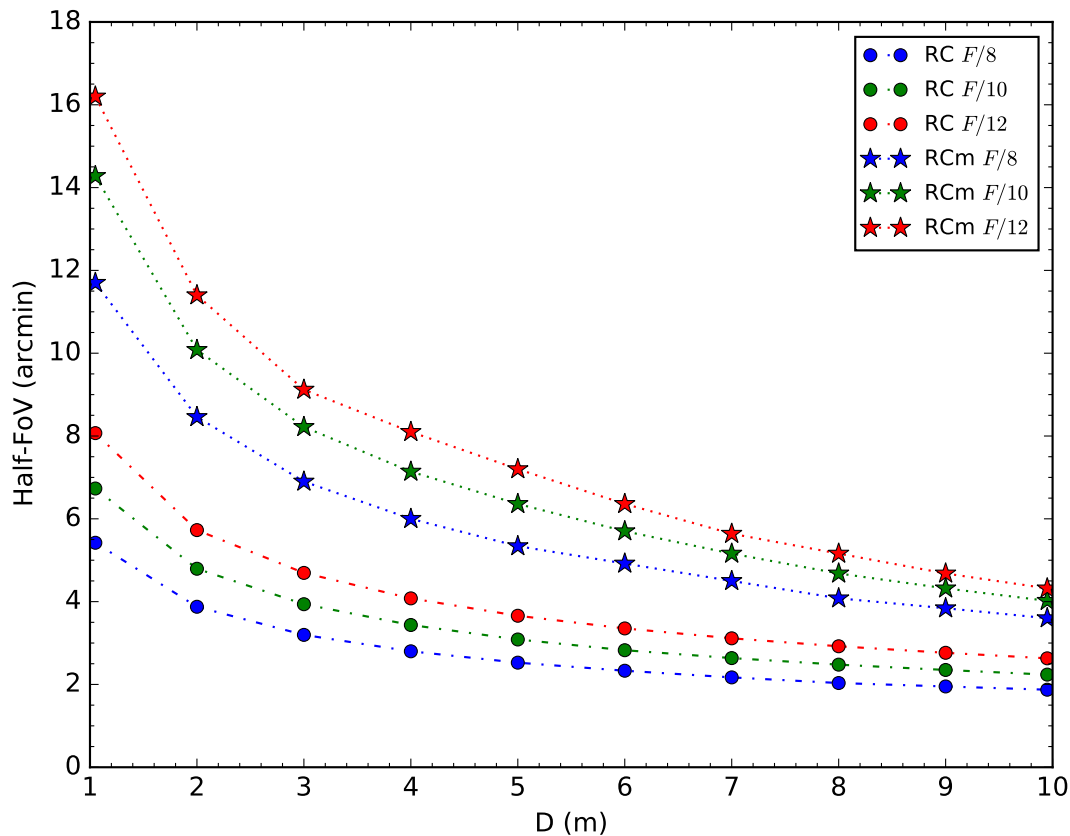
FIGURE 5.10: The maximum diffraction-limited half-FoV attainable on a flat detector in RC and RCm systems with the entrance pupil diameter D in the range of 2 - 10 m and the focal ratio $F/\#$ in the range of 8 - 12.

focus. Figure 5.10 shows the relation between the maximum half-FoV obtained through ray-tracing simulations for the RC and the corrected RCm telescopes as a function of the entrance pupil diameter. Three different $F/\#$ have been considered assuming a flat image surface for all systems.

Scaling up the RC system will increase ray aberrations relative to the Airy disk size, which is inversely proportional to the entrance pupil diameter. As a result, the maximum FoV for a diffraction-limited system is reduced in a non-linear manner, see Eq. (5.13). The most prevalent aberration in an RC system is astigmatism, and after being corrected with the help of an aplanatic meniscus, the remaining field curvature limits the field. Another limiting factor is the lateral color introduced by the meniscus. The image spot size in an RCm system is affected by lateral color, but it can be kept smaller than the original image spot size imposed by intrinsic astigmatism in the RC system.

We should note that the FoV gain is somewhat reduced with the increase of the entrance pupil diameter. This happens because as the system's size increases, the diameter of the meniscus increases, and due to the diameter-to-thickness ratio limitations, the meniscus has to be placed farther away from the focal point of the RC so that the astigmatism is not over-corrected. Therefore, the lateral color increases, becoming the main limiting factor of the system. Also, it is important to mention that the increase in FoV is still significant with the use of the aplanatic meniscus in those cases.

A trend can be noticed in Fig. 5.10. Faster systems produce higher FoV gains

when the meniscus is used. This occurs because the ratio of the diameter of the meniscus to its thickness, $D_{lens}/d = 20$, is limited to 20. When comparing telescopes with the same diameter D but differing $F/\#$, the RC astigmatism increases noticeably. As a result, a thicker meniscus is required, which allows the lens to be positioned closer to the focal point while keeping the $D_{lens}/d = 20$ ratio, decreasing lateral color.

To find the optimal minimum thickness of the meniscus, d_0, depending on the position of the meniscus, a range of entrance pupil diameters for an $F/10$ telescope have been simulated using a flat image plane for different values of Z, which is the ratio between the distance of the meniscus to the secondary mirror and to the focal point F_1', as defined in Eq. (5.16). Our findings can be seen in Fig. 5.11. Thus, the closer the meniscus approaches the focal point F_1', the thinner the meniscus must be to balance astigmatism in the RCm system.
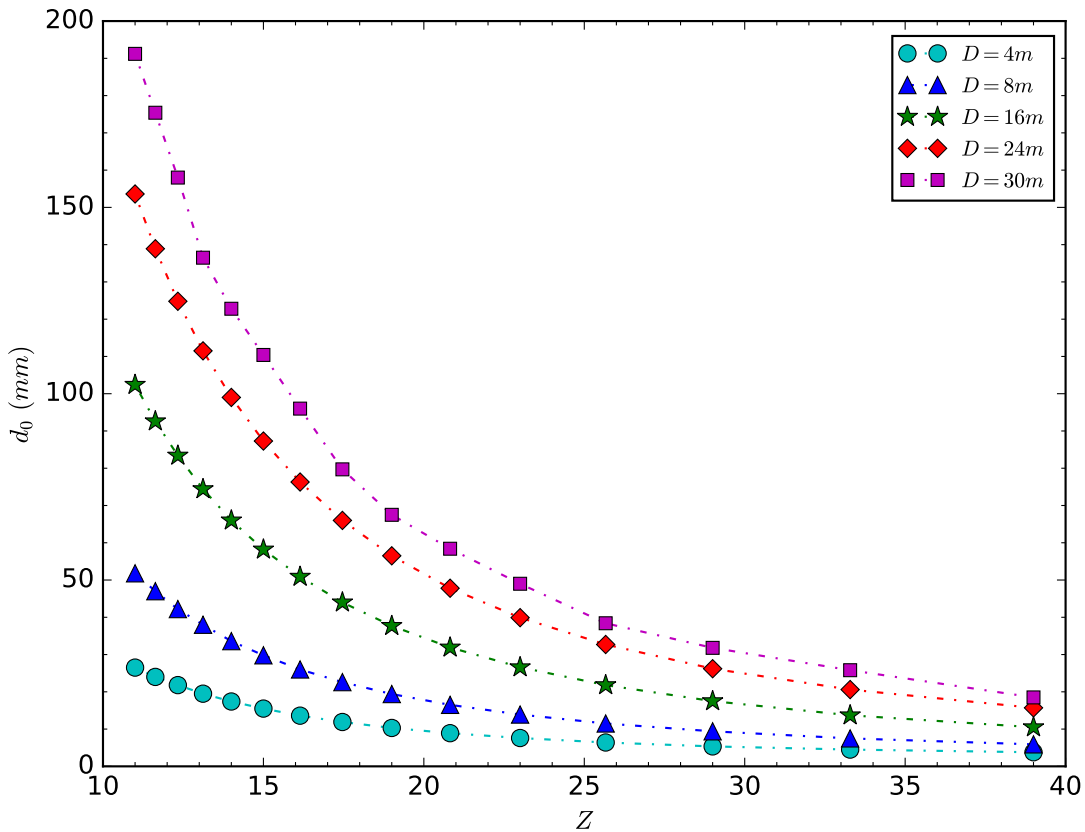
FIGURE 5.11: The minimum thickness for the meniscus to correct astigmatism for different $F/10$ telescope entrance pupil diameters using a flat image surface as a function of the ratio $Z = z_1/z_2$, see Fig. 5.5. The diameter-to-thickness ratio is kept at 20.

It is important to note that these results take into account the constraint of diameter-to-thickness ratio, which is kept smaller than 20 for the lens manufacturability.

$$Z = \frac{z_1}{z_2} \tag{5.16}$$

When diameter-to-thickness criteria are not used, the FoV starts to decline for higher Z values. As mentioned before, the thickness of the meniscus needed to correct astigmatism diminishes due to the lens surfaces being more curved. Otherwise, the overall astigmatism is over-corrected. Astigmatism compensation requires two

optimal factors, the radius of curvature of the surfaces of the meniscus and their axial separation d.

The closer the meniscus moves towards the primary mirror, i.e., farther away from the focal point, the less curved the surfaces will be. Consequently, its central thickness must be increased to correct the RC's astigmatism, thus increasing the lateral color accordingly. For greater Z values, the meniscus is closer to the focal point. Hence, the surfaces are more curved, requiring less central thickness to balance astigmatism, and increasing the diameter-thickness ratio. If the diameter-to-thickness ratio complies with the manufacturing limits, then at some point, the meniscus thickness might become greater than the optimal thickness d_0, and astigmatism will be over-corrected.

Figure 5.12 illustrates the maximum HFoV in an $F/10$ RCm with an entrance pupil of 4 m for monochromatic and polychromatic light. It is clear to see that the maximum FoV achieved in an RCm with monochromatic light is significantly larger for lower values of Z. As aforementioned, this occurs because the main factor limiting the FoV becomes the TCA as the meniscus is placed farther away from the focal point. It is also evident that the FoV starts decreasing for Z values that are too low even for the monochromatic light. That happens because as we are dealing with high-order astigmatism, the meniscus ceases to correct it as the lens becomes significantly less curved and thicker, so the astigmatism is under-corrected.
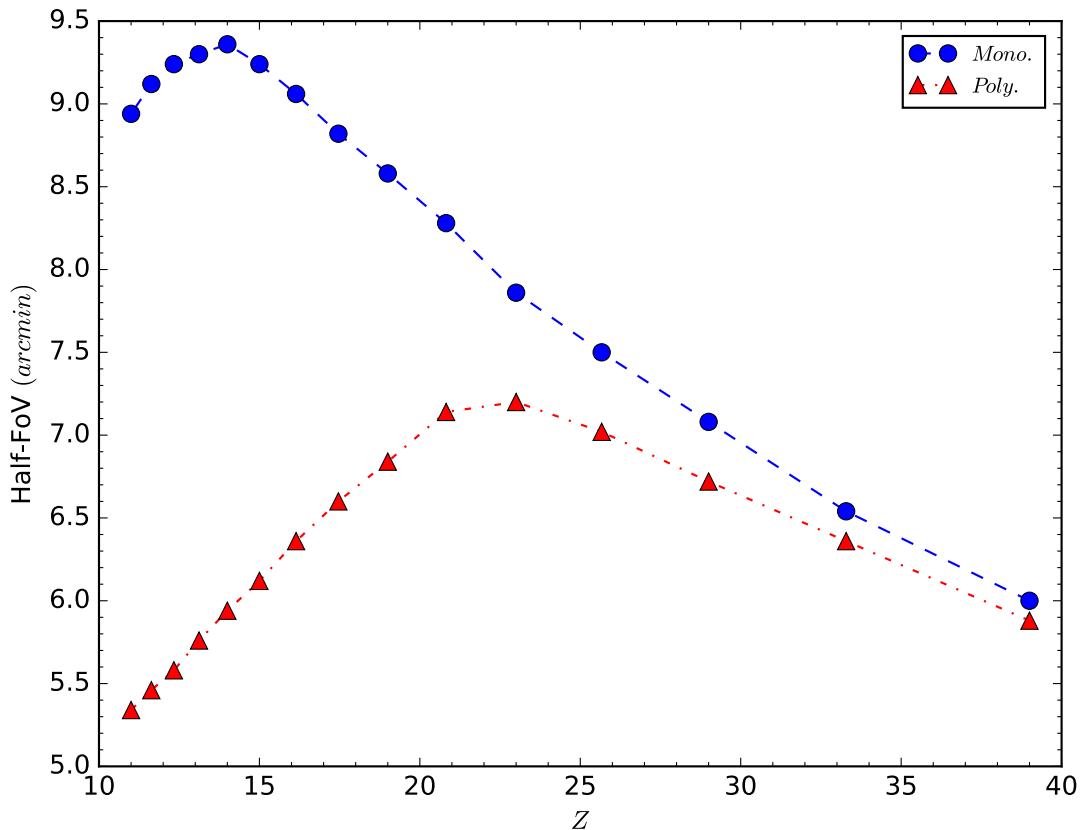
FIGURE 5.12: Maximum diffraction-limited HFoV in a 4 m $F/10$ RCm system using monochromatic and polychromatic light. With the first using the $\lambda = 0.600 \ \mu m$ wavelength, and the latter considering a wavelength range between $\lambda_F = 0.4861 \ \mu m$ and $\lambda_C = 0.6563 \ \mu m$.

The overall astigmatism in the system, up to the seventh-order, has been calculated using the Zernike coefficients as in Eq. (5.17). The Noll notation was chosen for the Zernike polynomials, where the first index is 1, and the cosine and sine terms are even and odd, respectively [121].

$$Astig. = 2\left(\sqrt{6}Z_6 - 3\sqrt{10}Z_{12} + 6\sqrt{14}Z_{24} \right). \tag{5.17}$$

Configurations 1 to 3 correspond to the telescopes with an $F/\# = 10$ and the system entrance pupil diameter equal to 2, 6, and 8 m, respectively. The results from Tables 5.2 and 5.3 demonstrate a significant improvement in FoV size of the original RC designs, showing an increase of up to 1.79 times in the object area from an RC telescope and a major reduction in total astigmatism. Furthermore, in every optical design reviewed, meniscus distortion is below 0.3%. Thus, image scale is not compromised.

TABLE 5.2: Different configurations simulated for the RC and RCm telescopes. The entrance pupil diameter is D_1. FoV is the full FoV of the telescopes, and $EE80$ is the encircled energy at 80%. The values of the EE80 for the RC are given for the encircled energy at the maximum half-FoV of the RCm.

Config.	D_1 (m)	EE80 RC (μm)	EE80 RCm (μm)	FoV RC (arcmin)	FoV RCm (arcmin)	FoV increase	Object Area increase	IMA Plane
1	2	38.65	13.88	9.828	19.44	1.98x	3.91x	Flat
2	4	19.48	13.20	12.84	17.40	1.36x	1.84x	Curved
3	8	18.64	12.97	9.240	11.52	1.25x	1.55x	Curved

TABLE 5.3: Supplementary ray-tracing simulation results for the various RC and RCm optical designs. Lat. Col. is lateral color, Astig. is astigmatism, and Dist. is distortion in the system.

Config.	Max. FoV (arcmin)	RMS Diam. RC (μm)	RMS Diam. RCm (μm)	Lat. Col. RCm (μm)	Astig. RC (waves)	Astig. RCm (waves)	Dist. RCm (%)
1	19.44	56.608	14.522	18.714	-0.9918	0.2440	0.2465
2	17.40	30.406	14.632	18.854	-1.5891	-0.3401	0.1373
3	11.52	24.124	14.622	18.633	-1.5117	-0.2136	0.0504

As can be seen in Tables 5.2 and 5.3, the maximum FoV demonstrates a larger FoV gain for a flat image surface. We should note that the most effective configuration for FoV gain is the first one, in a system with a 2*m* entrance pupil diameter and a flat image plane. This happens because the curved image surface can correct the field curvature in both systems. However, as the final image in the RCm is already flatter than the one in the RC, the curved image surface has less impact on the RCm. Consequently, the FoV increase from the RC, and the RCm is smaller. Nevertheless, a less curved sensor can be desirable for manufacturing purposes.

5.2.3   Numerical optimization alternative

TABLE 5.4: Parameters used for the modified RCm. The parameters numerically optimized are marked in **bold**.

	Radius(mm)	Thickness(mm)	Semi-Diameter(mm)	Conic k	Material
M1	-24400.0000	-8540.0	2000.0	-1.0797357	Mirror
M2	-10532.3741	**10252.9**	600.0	-4.3174794	Mirror
R1	**-820.0013**	**22.0**	220.0	**-4.2029961**	Silica
R2	-820.0013	**1747.1**	220.0	**-4.2029961**	
IMA	**-9325.7034**		146.77		
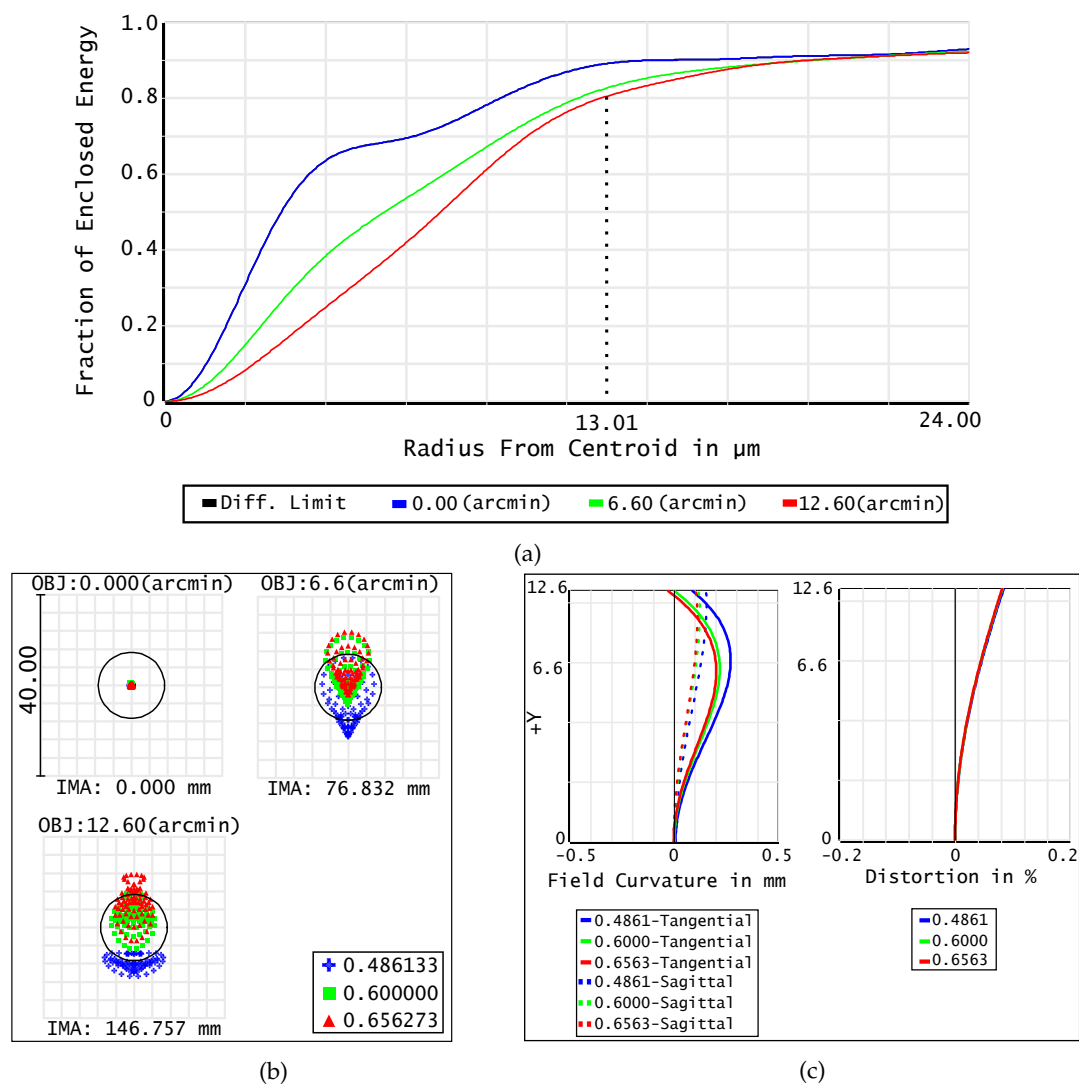
FIGURE 5.13: Simulation results for the modified RCm, showing (*a*) the encircled energy at 80 %, (*b*) the spot diagram, and (*c*) the field curvature.

It is desired to optimize the meniscus parameters (central thickness and the radius of curvature of the surface) with exact ray-tracing to further increase the FoV of the RCm. This allows us to obtain additional gain in the FoV, which can be doubled. However, this approach will lead to a deviation of the aplanatic properties of the

system. Figure 5.13 shows the results of the numerical example from Section 4, the entrance pupil diameter is 4 m, the meniscus is re-optimized for d and R_1.

The optimized parameters obtained for the RCm are shown in Table 5.4. It is worth noticing that the radius of curvature and the conic constant of both surfaces were kept equal for optimisation stability. In this example, the maximum full-FoV increases from 13.2 arcmins of the original RC to 25.2 arcmins in the RCm optimized, representing a 1.91 times increase in FoV and 3.64 times in object area. A noticeable coma can be seen in the spot diagram Fig. 5.13b for the intermediate field point. Thus, as expected, the system is no longer aplanatic. However, the FoV with diffraction-limited image quality is significantly increased.

5.3 Conclusion

An aplanatic meniscus has been analytically described to increase the FoV of RC telescopes by correcting astigmatism and flattening the image. This solution requires no modifications to the original design of the telescope.

Chapter 6

Quasi-aplanatic pair for increasing the FoV in Ritchey-Chrétien telescopes

The quasi-aplanatic pair presented in this chapter to increase the FoV slightly introduces coma into the RC telescope. The spherical aberration is corrected for a given wavelength, but the pair presents spherochromatism. Similarly to the meniscus presented in Chapter 5, this pair does not require any modification to the RC's parameters. Therefore, it can be easily introduced into an existing RC. The intrinsic astigmatism of the pair is comparable to, but of opposite sign to that of the RC. As a result, the overall astigmatism in the system can be decreased when the pair is placed in the RC's converging beam operating in an afocal mode. In addition to the astigmatism correction, the image is flattened. Hence, the FoV of the RC is significantly increased [3]. The difference between this solution and the meniscus solution previously presented in Chapter 5 is that one can easily adjust the distance between the pair to correct astigmatism for each spectral band due to the collimated beam between the lenses [4]. Moreover, the diameter-to-thickness limitation does not affect the pair as much as the meniscus considering that due to the reduction of the TCA at the cost of introducing LCA, and knowing that LCA is not affected by the thickness of the lens, the thickness of each lens of the pair can be increased for manufacturing purposes. However, this solution requires a proper material selection for each lens so that the lateral color is reduced. This leads to a significant reduced material selection to satisfy this condition. In addition, the material's maximum diameter for manufacturing can also limit the size of the RC in which this solution can be used.

In Section 6.1, an analytical solution for the pair shape is presented. A numerical example of astigmatism correction is given in Section 6.2. And numerical results for different spectral bands using a flat image plane for small telescopes and a curved image plane for larger telescopes are demonstrated in Section 6.3.

6.1   A quasi-aplanatic pair of lenses

A plano-convex and concave-plano lens can present an aplanatic solution if their surfaces are a conicoid of revolution with eccentricity equal to the lens material's refractive index at a given wavelength, in this case, a hyperboloidal of revolution surface, as seen in Section 3.1.6.

As seen in Section 5.2, an afocal pair can be created, demonstrated in Fig. 5.3.

Equation (5.14) gives the relation necessary between the hyperboloidal surfaces' conic constant and the refractive index at a given wavelength.

The lenses are individually free from spherical aberration for a given wavelength if their material is the same, and when combined, due to the convex-concave symmetry of the pair, all rays' angular magnification in the beam before and after the lens is preserved, satisfying the Abbe Sine Condition, which means that the system

is also free from coma[64, 117]. In the case of both materials being the same, the solution can be reduced to a single meniscus that is aplanatic as was introduced in Chapter 5. However, the meniscus introduces lateral color, which becomes the new limiting factor of the system. To keep the lateral color to a minimum, the meniscus can be introduced as close to the focal point as possible, which results in a thinner lens. Moreover, due to the lens's thickness decreasing, the diameter-to-thickness ratio quickly reaches the manufacturing limits for a meniscus. Besides, as only one material is used in this case, even though the lateral color is minimal when using a single meniscus if this meniscus is split into two lenses to ease the manufacturing process or the alignment of the surfaces, the overall thickness of the two lenses combined introduces too much lateral color. For that reason, a quasi-aplanatic pair using two different materials is presented in this chapter.

It is easier to align two hyperbolic surfaces if they are a pair of the concave-plano and plano-convex lens. Therefore, the two lenses can be used separated by a variable distance d. However, unlike the aplanatic meniscus, this pair cannot correct astigmatism while keeping the lateral color to a minimum as each lens's thickness has to consider the diameter-to-thickness ratio individually, making the pair have a larger overall thickness combined.

To decrease the lateral color while maintaining the system free from spherical aberration, one can deviate slightly from the lens's aplanatic condition by keeping both lenses free from spherical aberration individually while using different materials for each lens with a similar refractive index while the Abbe number is different. By doing so, the pair becomes quasi-aplanatic, with some residual coma and spherochromatism. In order to achieve this, the curved surface of the lenses RoC, R_1 and R_2, and their conic constants, k_1 and k_2, are no longer the same, but they are very similar.

For a distance z_2 from the anterior surface of the first lens to the focal point F_1' of the telescope, the radii of curvature R_1 and R_2 have to be properly chosen so that the rays are collimated in between the outer surfaces of the pair and refocused at a point F_2' as shown in Fig. 6.1. This relation can be seen in Eq. (6.1).
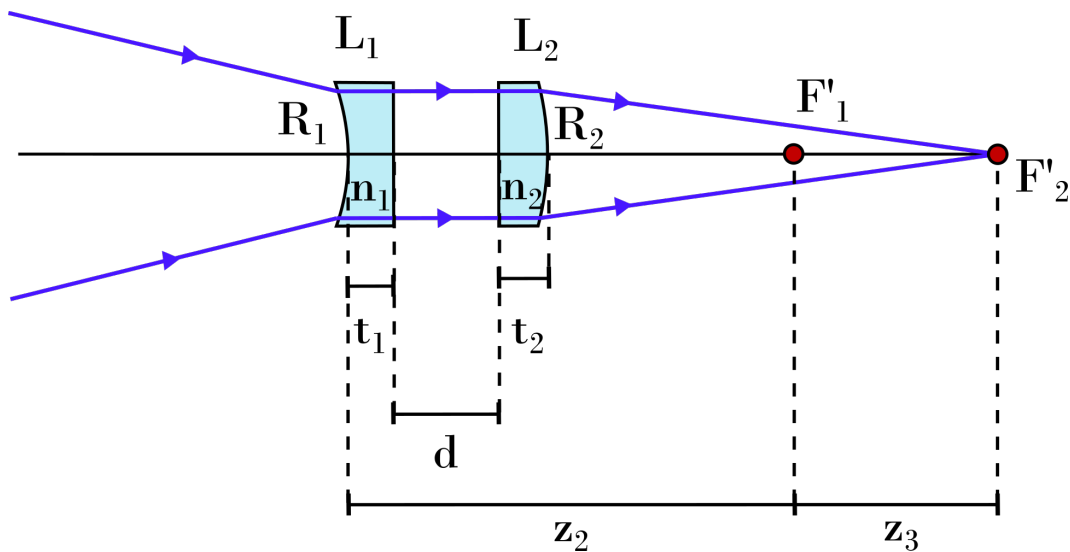
FIGURE 6.1: Ray-tracing in the quasi-aplanatic pair. F_1' and F_2' are the focal points of the RC and RC with the pair, respectively.

$$R_i = -\tau_{i0} z_2 \tag{6.1}$$

with

$$\tau_{ij} = n_i(\lambda_j) - 1 \tag{6.2}$$

where $i = 1, 2$ is the first and second lenses, respectively. $n_i(\lambda_j)$ is the refractive index of the surface at a given wavelength j, with $j = 0$ a given wavelength in the lenses chosen appropriately to minimize the spherochromatism in the system. Furthermore, $j = 1, 3$ refers to any two extreme wavelengths used in the spectral bands.

The distance between the RC and the RCp focal point is z_3, which is the sum of the thickness of the lenses and the distance between them, as in Eq. (6.3).

$$z_3 = t_1 + d + t_2 \tag{6.3}$$

where d is the distance between the lenses, and t_1 and t_2 are the thickness of the first and second lens, respectively.

The distance between the outer surfaces of the pair determines astigmatism in the system. The RC telescope combined with the quasi-aplanatic pair is denoted as RCp.

An estimate of the transverse lateral color and the axial chromatic focal shift in the system is given by Eqs. (6.4) and (6.5)), respectively [82].

$$LC = \left[(\tau_{11} - \tau_{13}) \left(\frac{\bar{y}_1}{R_1} \right) - (\tau_{21} - \tau_{23}) \left(\frac{\bar{y}_2}{R_2} \right) \right] z_2 \tag{6.4}$$

where τ_{11} and τ_{13} are related to the refractive index for any two extreme wavelengths for the first lens, τ_{21} and τ_{23} related to the second lens, and $\bar{y}_1$ and $\bar{y}_2$ are the chief ray heights at the external surfaces of the pair for the primary wavelength.

$$\Delta f_{12} = -R_1 R_2 \left(\frac{1}{\tau_{11} \tau_{21} \xi_1 + R_2 \tau_{11} - R_1 \tau_{21}} - \frac{1}{\tau_{13} \tau_{23} \xi_3 + R_2 \tau_{13} - R_1 \tau_{23}} \right) \tag{6.5}$$

with

$$\xi_k = d + \frac{t_1}{n_1(\lambda_k)} + \frac{t_2}{n_2(\lambda_k)} \tag{6.6}$$

Overall astigmatism, up to the tertiary, can be calculated using the Zernike coefficients as demonstrated in Eq. (5.17) using the Noll notation.

6.2 Numerical example of astigmatism correction

To illustrate this idea, an $F/10$ RC telescope has been designed with and without the aplanatic pair in the system to demonstrate the FoV gain in the RCp telescope. The entrance pupil diameter is 4 m. The layout of the RCp can be seen in Fig. 6.2. The first lens is placed at a distance z_1 from the secondary mirror, while the second lens is separated from the first one by a variable distance d. The distance between the focal points of the RC and the RCp is z_3. Table 6.1 demonstrates the parameters that have been used for the RCp in this numerical example.
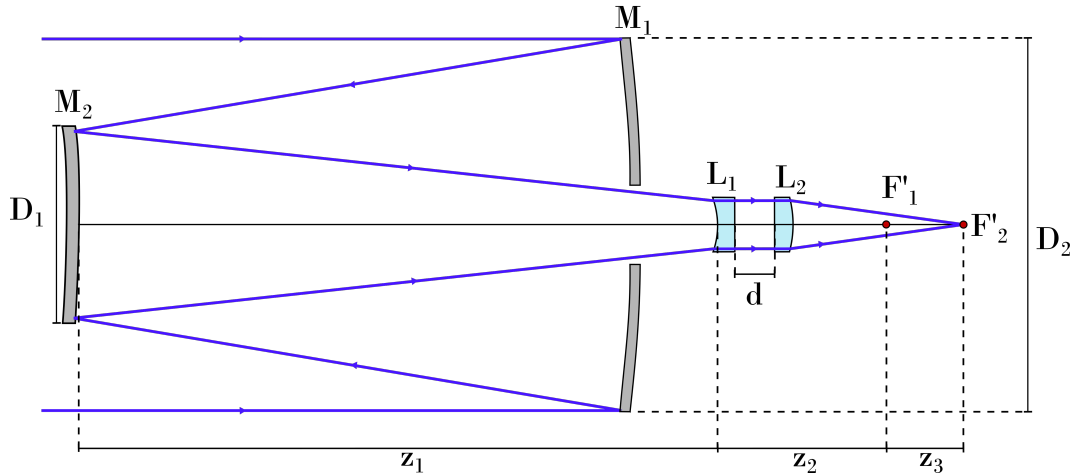
FIGURE 6.2: Optical layout of the RCp. The diameter of the primary and secondary mirrors are D_1 and D_2, respectively. The distance between the secondary mirror and the aplanatic pair is z_1. The distance between the first surface of the first lens and the RC focal point F'_1 is z_2. The axial distance between the two lenses is d.

The glasses chosen for the example were $P-SK57$ and $N-SK5$ due to their similar refractive index and different Abbe number. The refractive indices for the wavelength $\lambda_0 = 0.550 \ \mu m$ are $n_{L1} = 1.5891$ and $n_{L2} = 1.5912$ while their Abbe numbers are $V_{L1d} = 59.60$ and $V_{L2d} = 61.27$, respectively. Notice that the materials chosen are just an example to illustrate this correction. Other factors such as thermal expansion, manufacturing limitation on the diameter of the lens, purity of the glass, and other properties have to be considered for the material's optimal choice.

TABLE 6.1: Optical and design parameters of the RCp system. M1 and M2 are the primary and secondary mirrors. The external surfaces of the pair are R1 and R2, while the internal ones are defined as R1' and R2'. IMA is the image space and it varies with the spectral bands. The distance d between the lenses is also variable.

	Radius (mm)	Thickness (mm)	Semi-diameter (mm)	Conic k	Material
M1	-24400.00	-8540.00	2000.00	-1.07973571	MIRROR
M2	-10532.37	10500.00	600.00	-4.31747940	MIRROR
R1	-889.05	30.00	234.00	-2.53669329	P-SK57
R1'	Infinity	d	234.00	0.00000000	
R2'	Infinity	30.00	234.00	0.00000000	N-SK5
R2	-892.05	1499.76	234.00	-2.54306809	
IMA	Curved		111.79		

The image plane is curved for both the RC and the RCp, with the RCp presenting a flatter image than the RC, almost three times less curved. For this numerical example, using different spectral bands, the optical performance of the two systems are presented in the Figs. 6.3 to 6.6. For the maximum Half-FoV for a diffraction-limited RCp, the RC presents a significantly larger spot size, which is evidently larger than the Airy disk. This happens because all astigmatism orders summed in the RCp flattens the image.

(a)
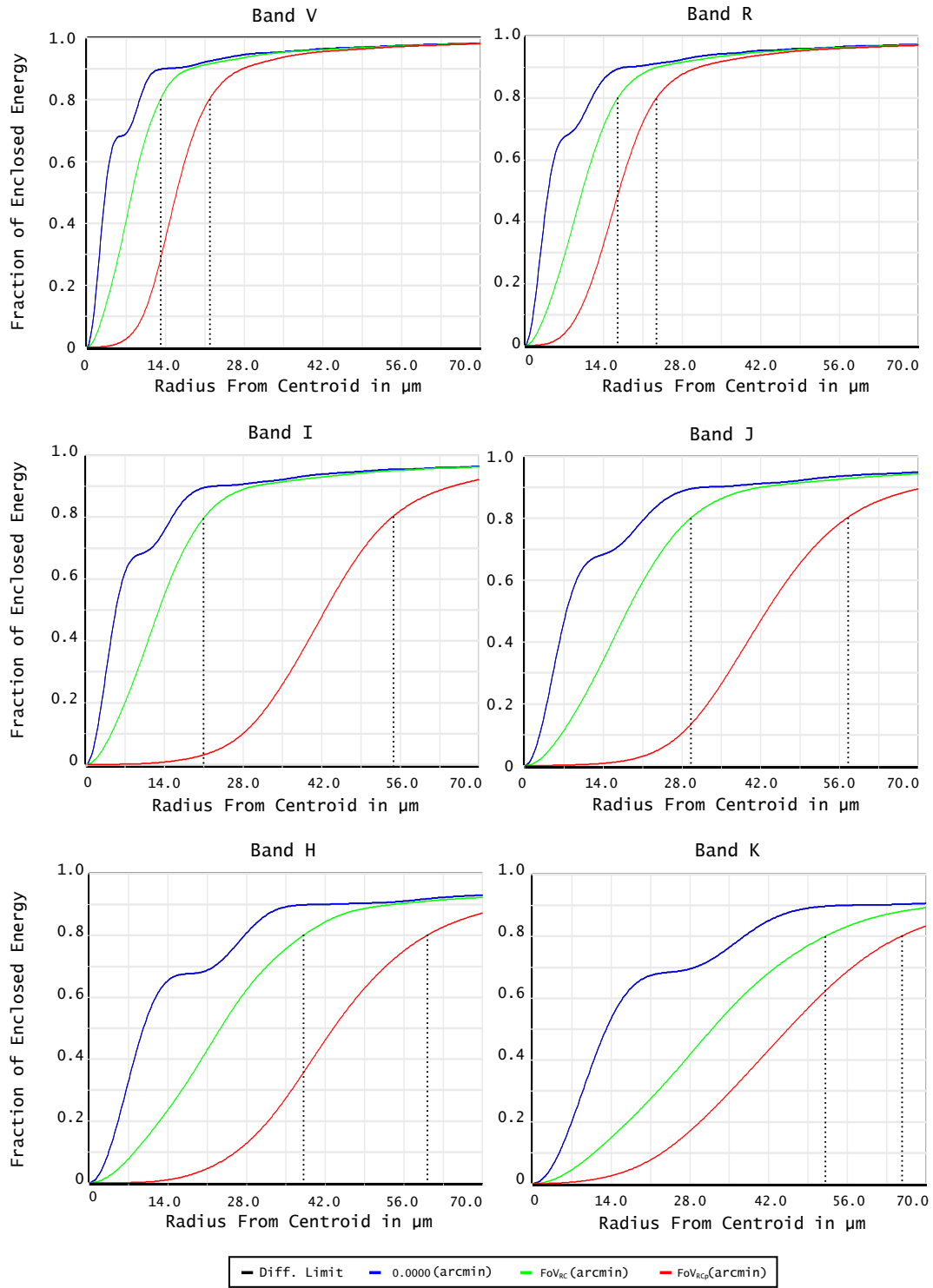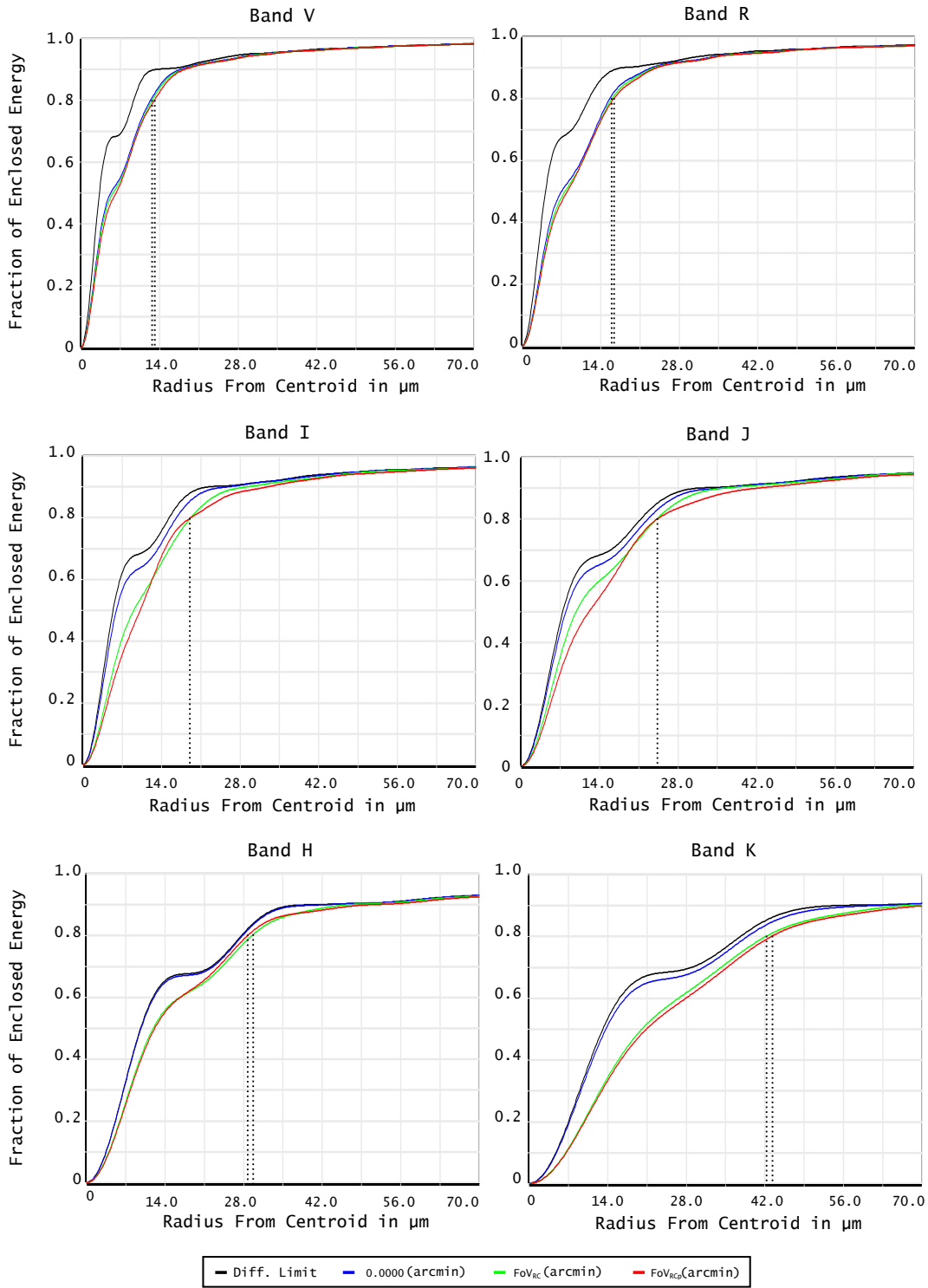
FIGURE 6.3: Encircled energy at 80 % for (*a*) the classical RC telescope, (*b*) and for the RCp.
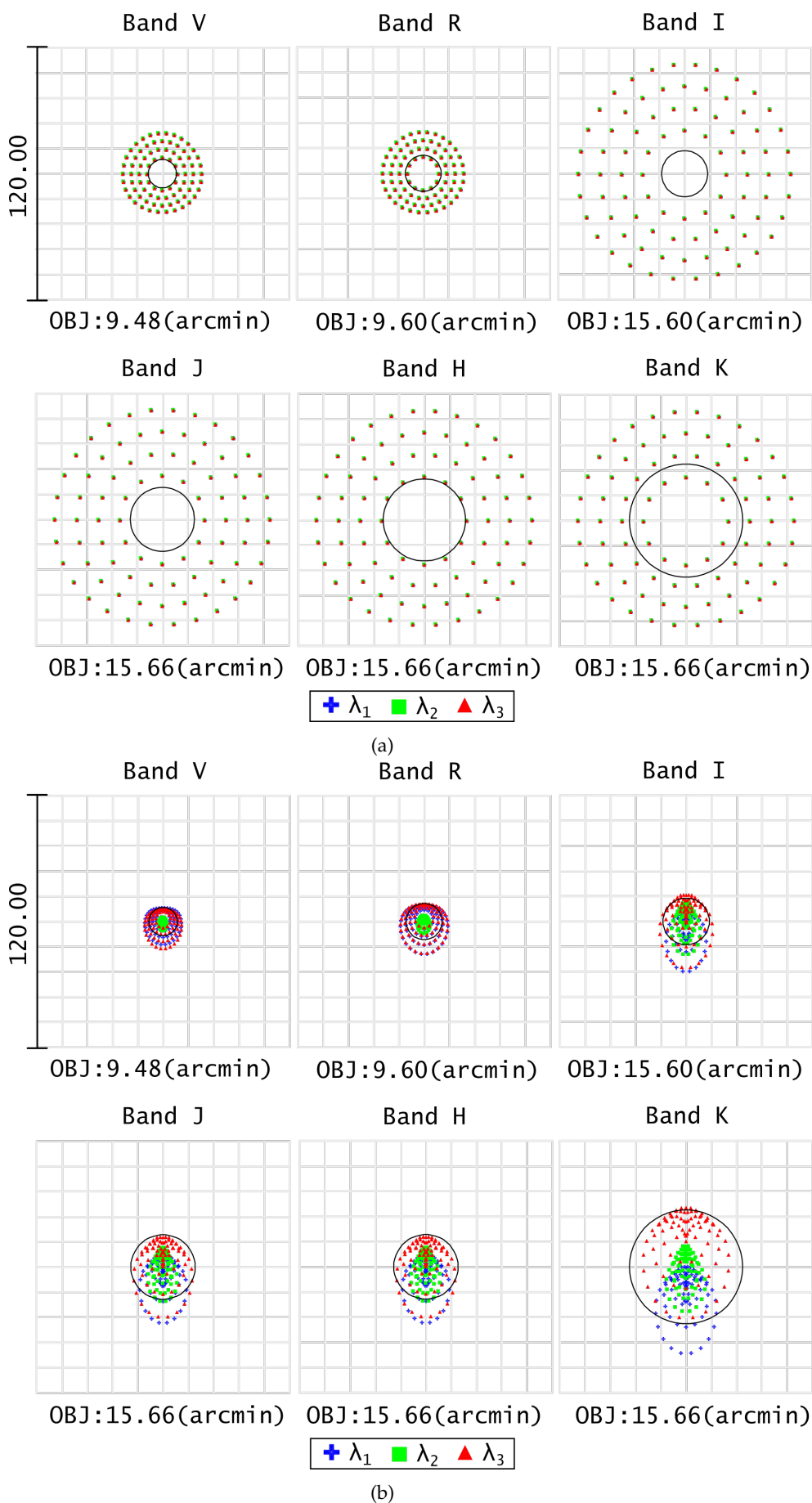
FIGURE 6.4: Spot diagram for (*a*) the classical RC telescope, (*b*) and for the RCp. It shows the rays for the maximum half FoV for a diffraction limited image for the RCp. The Airy disk radius for each band in Table 6.5, and it is represented as the black circle.
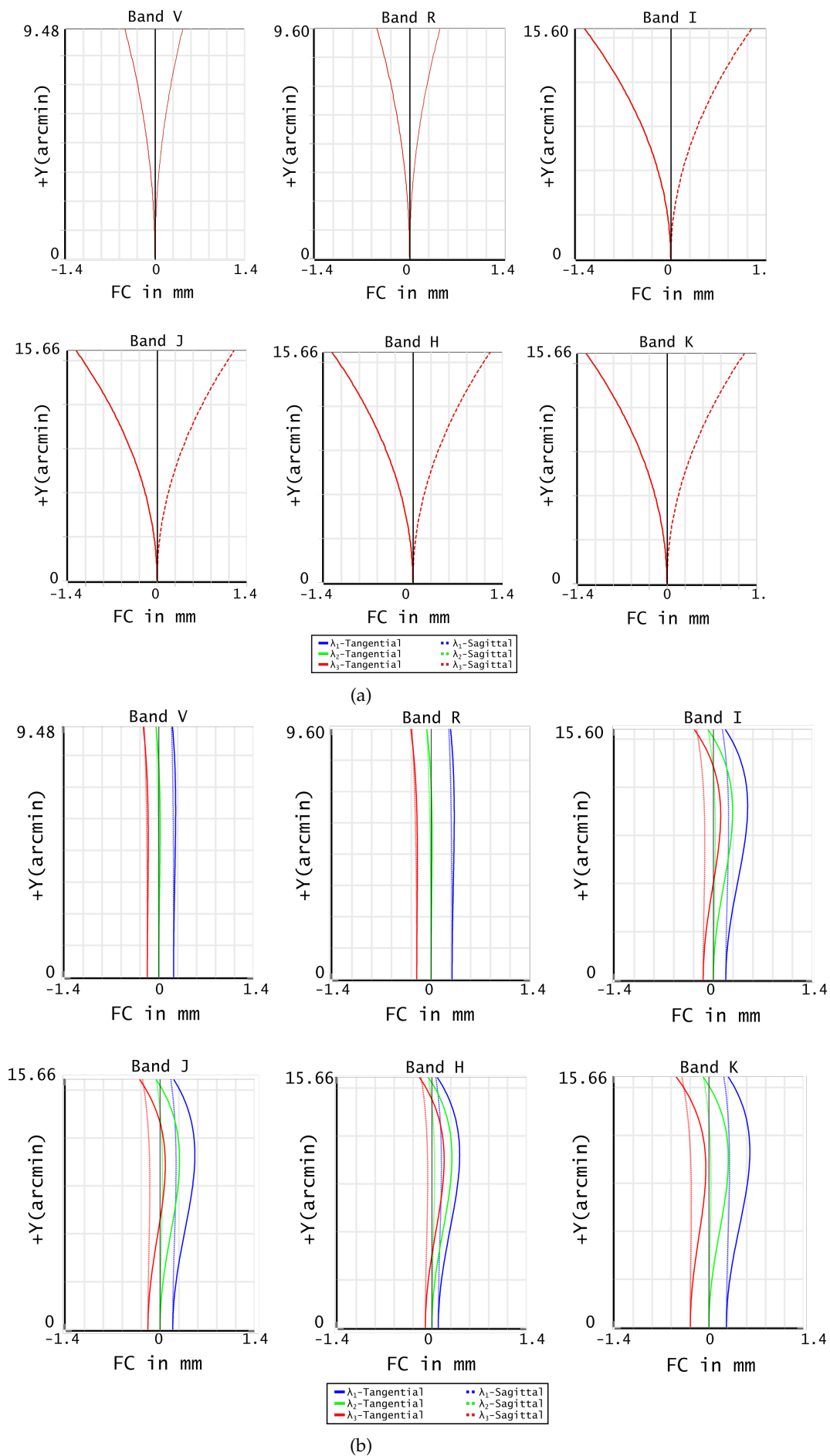
FIGURE 6.5: Field curvature and distortion for (*a*) the classical RC telescope, (*b*) and for the RCp.
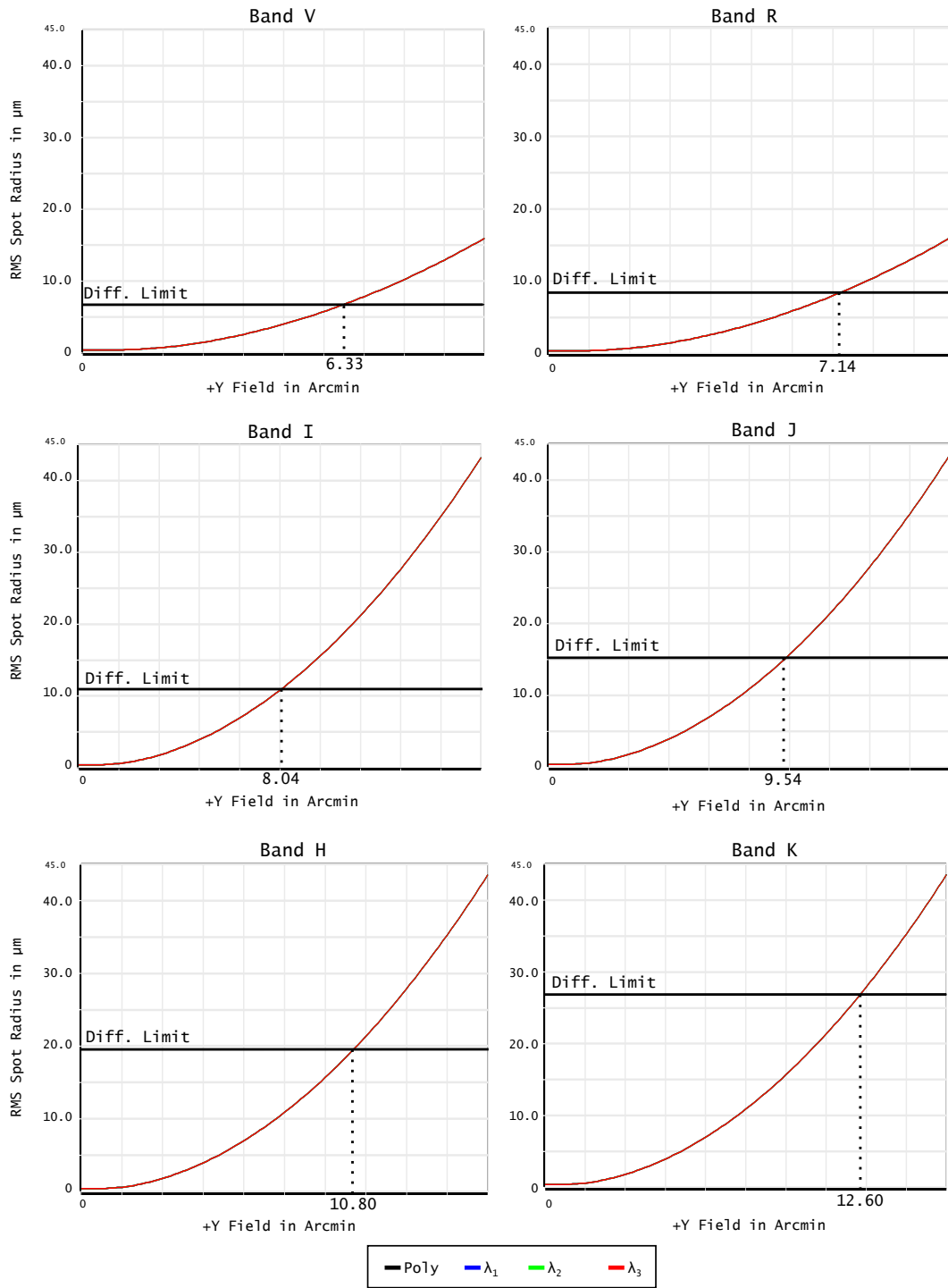
(a)
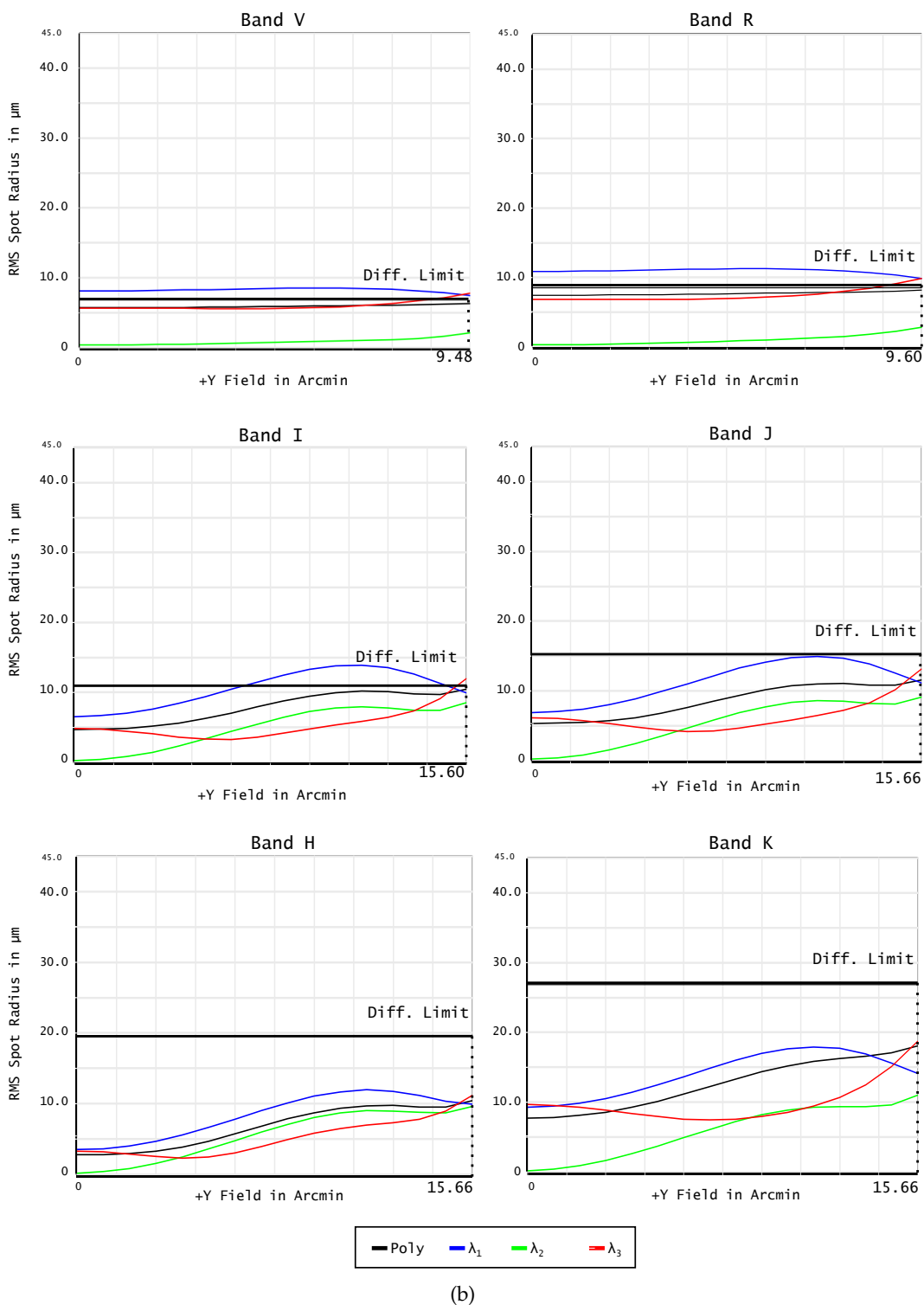
FIGURE 6.6: RMS vs Field for (*a*) the classical RC telescope, (*b*) and for the RCp.

Tables 6.4 and 6.5 in Section 6.3 show the comprehensive numerical results for this system.

6.3 Numerical results

Different spectral bands for RC telescopes have been tested for a $f/10$ 2 m with a flat image plane and a $f/10$ 4 m with a curved image plane. The combined spectral bands analyzed range from 0.505 μm to 2.440 μm. However, the blue band has not been considered as it is the least relevant of all bands since the atmospheric turbulence in this band is the strongest of all for terrestrial telescopes, particularly for the larger telescopes because their Airy disk is smaller [122]. Section 6.3.1 and Section 6.3.2 demonstrate two numerical examples. The first one using a flat detector and the second a curved one, respectively.

When analyzing Fig. 6.7, one can see that the FoV increase is significant for different spectral bands in a flat image plane, with the spectral K presenting a decline considering that this spectral band covers a large wavelength range. Thus, the chromatic aberration becomes more evident, especially as the lenses aspherical surfaces were optimized for the primary wavelength $\lambda_0 = 0.550$ μm. Figure 6.7 shows the exhaustive numerical results for this example.
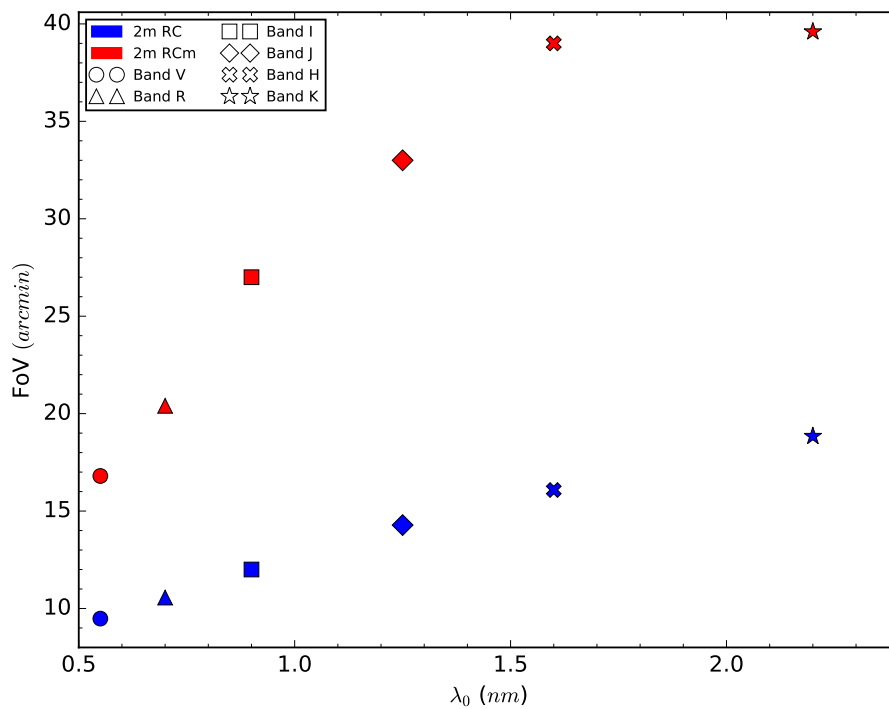
FIGURE 6.7

When analyzing Fig. 6.8, one can see that the FoV is also significant for different spectral bands in a curved detector. The band R covers a relatively large wavelength range, and considering that the FoV of the RC has been increased by using a curved detector, the FoV increase is significantly decreased. In fact, this spectral band presents the smallest FoV increase compared to the bands in which the diameter-to-thickness ratio is not a limiting factor. The last four bands can be seen to have a similar FoV, which means that the FoV increase is decreased as the wavelength increases, while the RC continues having its FoV increased. This decrease in

FoV for the last bands are due to the diameter-to-thickness ratio limiting the system. Figure 6.8 shows the exhaustive numerical results for this example.
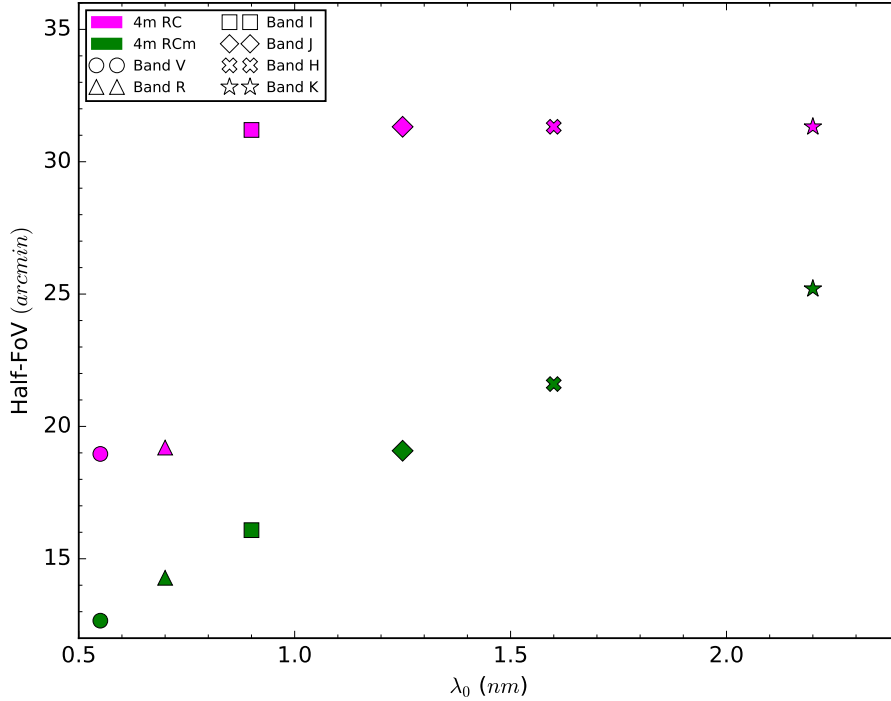
FIGURE 6.8

6.3.1   Flat image plane

For smaller telescopes, a flat image plane was chosen because the surface becomes too curved, and the manufacturing of steeply curved sensors might be challenging. Thus, a flat image plane was used in this example.

TABLE 6.2: Simulation results for the RC and RCp telescopes. The entrance pupil diameter is 2 m. The full-FoV is represented by FoV, d is the distance between the lenses, FoV incr. is the FoV increase, Obj. area incr. is the object area increase, and the encircled energy at 80% is *EE*80.

Band	λ range (μm)	EE80 RC (μm)	EE80 RCp (μm)	FoV RC (*arcmin*)	FoV RCp (*arcmin*)	FoV incr.	Obj. area inc.	d (*mm*)
V	0.505-0.595	29.51	13.33	9.48	16.80	1.77	3.14	2.0
R	0.590-0.810	42.19	17.12	10.56	20.40	1.93	3.73	7.0
I	0.780-1.020	73.55	21.53	12.00	27.00	2.25	5.06	13.0
J	1.060-1.440	108.90	30.24	14.28	33.00	2.31	5.34	18.0
H	1.500-1.700	151.00	39.46	16.08	39.00	2.43	5.88	22.0
K	1.960-2.440	157.80	52.84	18.84	39.60	2.10	4.42	26.0

TABLE 6.3: Supplementary results for the ray-tracing simulations for the RC and RCp telescopes. The transverse lateral color is Lat. Col., the astigmatism is Astig., the axial color is Ax. Col., and the distortion is Dist.

Band	Astig. RC (wave)	Astig. RCp (wave)	Airy Disk (μm)	RMS RC (μm)	RMS RCp (μm)	Ax. Col. RCp (μm)	Lat. Col. RCp (μm)	Dist. RCp (%)
V	-0.8080	0.2173	6.710	21.110	6.107	221.344	4.479	0.0596
R	-0.9361	0.3609	8.542	31.179	8.220	289.400	11.505	0.1000
I	-1.2754	0.5777	10.990	54.702	10.572	186.601	13.214	0.1979
J	-1.3718	0.5817	15.260	81.772	15.162	217.640	21.595	0.3174
H	-1.4968	0.4783	19.520	114.258	19.314	115.581	15.645	0.4588
K	-1.1223	0.3500	26.890	117.805	26.552	334.495	58.673	0.4931

The FoV can increase up to almost 2.5 times, equivalent to an increase in the object area size almost six times, showing worse gains for the bands with a smaller wavelength. That happens because the Airy disk radius is smaller in those bands. Thus the spherochromatism and chromatic aberration demonstrate a high significance in the RCp FoV.

6.3.2 Curved image plane

Larger telescopes, considered here as telescopes with an entrance pupil larger than 2 m, were analyzed using a curved image plane as the image size is larger than 100 mm and the curvature is not steep, such as in this example.

TABLE 6.4: Numerical results for the RC and RCp telescopes using a curved image plane for an entrance pupil diameter of 4 m. IMA is the radius of curvature of the image.

Band	EE80 RC (μm)	EE80 RCp (μm)	FoV RC (arcmin)	FoV RCp (arcmin)	FoV incr.	Obj. area incr.	IMA RC (mm)	IMA RCp (mm)
V	21.74	13.05	12.66	18.96	1.50	2.24	-3939.4347	-10464.5951
R	23.40	16.50	14.28	19.20	1.35	1.81	-3932.6399	-10846.7392
I	54.53	19.24	16.08	31.20	1.94	3.77	-3931.3610	-11654.1530
J	57.33	24.64	19.08	31.32	1.64	2.70	-3924.3100	-11530.8538
H	60.10	29.47	21.60	31.32	1.45	2.10	-3921.3111	-11514.7464
K	65.55	43.17	25.20	31.32	1.24	1.55	-3918.9489	-11790.0771

The FoV in the last three spectral bands (J, H, and K) is kept constant due to the limitations in the size of the lens. As can be seen in Fig. 6.3, the FoV could be increased regarding image quality. However, that results in vignetting so the FoV has to be kept constant for those three bands [5]. The systems with a curved image plane presents a smaller FoV increase than for flat image planes. This is the result of the RCm flattening the image, so the curved image plane does not affect much the image quality in this case, thus, does not affect much the maximum FoV. Considering that the RC presents a significant field curvature, a curved image plane highly affects its maximum FoV. Therefore, the curved sensor provides a great benefit for the RC

while not for the RCm. Moreover, the image plane for the RCm is less curved than for the RC. This eases the mechanical manufacturing limits of the detector [123].

TABLE 6.5: Supplementary results for the ray-tracing simulations of the telescopes with an entrance pupil diameters of 4 m and a curved image.

Band	Astig. RC (*wave*)	Astig. RCp (*wave*)	Airy disk (*µm*)	RMS RC (*µm*)	RMS RCp (*µm*)	Ax. Col. RCp (*µm*)	Lat col. RCp (*µm*)	d (mm)
V	-2.0584	0.0003	6.71	15.043	5.935	389.081	0.828	1.4
R	-1.6585	-0.0003	8.54	15.425	7.696	501.926	3.258	3.0
I	-3.4063	0.0018	10.98	40.719	9.134	321.486	12.670	14.2
J	-2.4714	-0.0013	15.25	41.030	10.106	368.340	14.835	16.1
H	-1.9308	0.0001	19.53	41.029	8.741	191.841	8.953	17.8
K	-1.4042	-0.0025	26.84	41.029	16.657	534.325	39.489	21.3

6.4 Conclusion

A quasi-aplanatic pair has been analytically described to increase the FoV of RC telescopes by correcting astigmatism and flattening the image. Different spectral bands can be individually corrected by changing the separation between the pair.

Chapter 7

Conclusion and Future Work

An analytical solution for aplanatic optical systems using GRIN lenses with curved surfaces has been presented. The first solution is an afocal system in which the inner surfaces are concentric to the focus, and so is the GRIN structure. This results in a system free from spherical aberration and coma, but presenting astigmatism and field curvature. The second solution uses the astigmatism seen in this first solution to correct field curvature in optical systems. For that, the lenses have to be swapped and placed in the converging beam of an optical system in which the astigmatism is of the oppose astigmatism. As an example, a Gregorian telescope has been designed and tested with and without the GRIN corrector. The results demonstrated a good field curvature correction. The distance between the lenses influences on the amount of astigmatism introduced into the system. Thus, this can be applied to other optical systems.

A meniscus has been analytically designed to increase the FoV of RC telescopes. This approach does not deflect them from their aplanatic solution. By increasing the FoV, the object area size can be significantly increased by a factor of 1.5 to 4 times, depending on the entrance pupil size and its image plane shape. The advantage of the aplanatic meniscus solution over other approaches is its incorporation and removal of existing RC telescopes without remodeling their optical design. Given manufacturing limits, the meniscus' optimal position to minimize lateral color and achieve a larger FoV has also been demonstrated. Besides, an equation estimating the approximated maximum FoV of an RC telescope has also been presented.

The RCm can be designed in different entrance pupil sizes and $F/\#$, showing promising results for telescopes with an entrance pupil up to $8m$. However, because of the smaller FoV of larger systems and the lateral color added with the thicker meniscus, the telescopes with a larger entrance pupil display a lower gain in FoV compared to the smaller ones.

A quasi-aplanatic pair has been analytically described to increase the FoV of RC telescopes by correcting astigmatism and flattening the image. The pair present a collimated beam between them. Therefore, the distance between the lenses can be optimized to correct astigmatism for different spectral bands. The pair must be composed of two lenses with materials in which the refractive indices are similar, but the Abbe numbers are distinct. By doing so, one can decrease the lateral color in the system at the cost of adding axial chromatic aberration. With a proper choice of the materials used, this axial chromatic aberration, though, is not enough to compromise the system ultimately, still showing an FoV gain using the pair in the RC. The spectral bands from V to K have been tested and demonstrated promising results as theoretically expected. The band B was not considered as this band can be challenging for terrestrial observations due to strong turbulence in this wavelength range. Depending on the entrance pupil's size, the FoV of the RCp can be almost 2.5 times larger than the RC.

Future study will entail investigating the polymers available for ink-jet printing in such a way that the aplanatic optical system employing GRIN lenses may also be made achromatic. As a result, this method has a major advantage over strict aplanatic aspherical lenses in general.

The prospect of combining the meniscus or refractive pair with additional lenses to go beyond the aberration correction in RC telescopes while maintaining the aplanatic properties and astigmatism correction, in order to increase the FoV even further, is also to be investigated.

As is typical in science, future work will not be restricted to the research outlined above, but additional solutions may emerge during the investigation process.

Appendix A

DLL code for SA free GRIN lenses in OpticStudio

LISTING A.1: OpticStudio C code for ray-tracing the positive GRIN lens

```c
#include <windows.h>
#include <math.h>
#include <string.h>
#include "usersurf.h"

/* Adapted from Zemax sample grin.c */

int
__declspec(dllexport) APIENTRY UserDefinedSurface(USER_DATA* UD,
    FIXED_DATA* FD);

/* a generic Snells law refraction routine */
int
Refract(double thisn, double nextn, double* l, double* m, double* n,
    double ln, double mn, double nn);

BOOL
WINAPI DllMain(HANDLE hInst, ULONG ul_reason_for_call, LPVOID lpReserved)
{
    return TRUE;
}

/* this DLL models a GRIN surface similar to the GRIN 1 surface type. */

int
__declspec(dllexport) APIENTRY UserDefinedSurface(USER_DATA* UD,
    FIXED_DATA* FD)
{
    int i;
    double p2, r2, alpha, index, N, A, x, y, z, f;
    double power, a, b, c, rad, t, zc, casp;
    switch (FD->type)
    {
    case 0:
        /* ZEMAX is requesting general information about the surface */
        switch (FD->numb)
        {
        case 0:
            /* ZEMAX wants to know the name of the surface */
             /* do not exceed 12 characters */
            strcpy(UD->string, "GRIN positive");
            break;
        case 1:
```

```c
41              /* ZEMAX wants to know if this surface is rotationally
    symmetric */
42              /* it is, so return any character in the string; otherwise,
    return a null string */
43              strcpy(UD->string, "1");
44              break;
45          case 2:
46              /* ZEMAX wants to know if this surface is a gradient index
    media (it is) */
47              strcpy(UD->string, "1");
48              break;
49          }
50          break;
51      case 1:
52          /* ZEMAX is requesting the names of the parameter columns */
53          /* the value FD->numb will indicate which value ZEMAX wants. */
54          /* returning a null string indicates that the parameter is unused.
    */
55          switch (FD->numb)
56          {
57          case 1:
58              /* All GRINs must use paramter 1 as Delta T !!!!!!!!!!!!!! */
59              strcpy(UD->string, "Delta T");
60              break;
61          case 2:
62              strcpy(UD->string, "N0");
63              break;
64          case 3:
65              strcpy(UD->string, "A");
66              break;
67          default:
68              UD->string[0] = '\0';
69              break;
70          }
71          break;
72      case 2:
73          /* ZEMAX is requesting the names of the extra data columns */
74          /* the value FD->numb will indicate which value ZEMAX wants. */
75          /* they are all "Unused" for this surface type */
76          /* returning a null string indicates that the extradata value is
    unused. */
77          switch (FD->numb)
78          {
79          default:
80              UD->string[0] = '\0';
81              break;
82          }
83          break;
84      case 3:
85          /* ZEMAX wants to know the sag of the surface */
86          /* if there is an alternate sag, return it as well */
87          /* otherwise, set the alternate sag identical to the sag */
88          /* The sag is sag1, alternate is sag2. */
89
90          UD->sag1 = 0.0;
91          UD->sag2 = 0.0;
92
93          /* if a plane, just return */
94          if (FD->cv == 0) return(0);
95          p2 = UD->x * UD->x + UD->y * UD->y;
96          alpha = 1 - (1 + FD->k) * FD->cv * FD->cv * p2;
97          if (alpha < 0) return(-1);
98          UD->sag1 = (FD->cv * p2) / (1 + sqrt(alpha));
```

```
99          if (alpha != 1.0) UD->sag2 = (FD->cv * p2) / (1 - sqrt(alpha));
100         break;
101    case 4:
102         /* ZEMAX wants a paraxial ray trace to this surface */
103         /* x, y, z, and the optical path are unaffected, at least for this
     surface type */
104         /* for paraxial ray tracing, the return z coordinate should always
     be zero. */
105         /* paraxial surfaces are always planes with the following normals
     */
106
107         UD->ln = 0.0;
108         UD->mn = 0.0;
109         UD->nn = -1.0;
110         power = (FD->n2 - FD->n1) * FD->cv;
111         if ((UD->n) != 0.0)
112         {
113             (UD->l) = (UD->l) / (UD->n);
114             (UD->m) = (UD->m) / (UD->n);
115
116             (UD->l) = (FD->n1 * (UD->l) - (UD->x) * power) / (FD->n2);
117             (UD->m) = (FD->n1 * (UD->m) - (UD->y) * power) / (FD->n2);
118
119             /* normalize */
120             (UD->n) = sqrt(1 / (1 + (UD->l) * (UD->l) + (UD->m) * (UD->m))
     );
121             /* de-paraxialize */
122             (UD->l) = (UD->l) * (UD->n);
123             (UD->m) = (UD->m) * (UD->n);
124         }
125         break;
126    case 5:
127         /* ZEMAX wants a real ray trace to this surface */
128         if (FD->cv == 0.0)
129         {
130             UD->ln = 0.0;
131             UD->mn = 0.0;
132             UD->nn = -1.0;
133             if (Refract(FD->n1, FD->n2, &UD->l, &UD->m, &UD->n, UD->ln, UD
     ->mn, UD->nn)) return(-FD->surf);
134             return(0);
135         }
136         /* okay, not a plane. */
137         a = (UD->n) * (UD->n) * FD->k + 1;
138         b = ((UD->n) / FD->cv) - (UD->x) * (UD->l) - (UD->y) * (UD->m);
139         c = (UD->x) * (UD->x) + (UD->y) * (UD->y);
140         rad = b * b - a * c;
141         if (rad < 0) return(FD->surf);  /* ray missed this surface */
142         if (FD->cv > 0) t = c / (b + sqrt(rad));
143         else            t = c / (b - sqrt(rad));
144         (UD->x) = (UD->l) * t + (UD->x);
145         (UD->y) = (UD->m) * t + (UD->y);
146         (UD->z) = (UD->n) * t + (UD->z);
147         UD->path = t;
148         zc = (UD->z) * FD->cv;
149         rad = zc * FD->k * (zc * (FD->k + 1) - 2) + 1;
150         casp = FD->cv / sqrt(rad);
151         UD->ln = (UD->x) * casp;
152         UD->mn = (UD->y) * casp;
153         UD->nn = ((UD->z) - ((1 / FD->cv) - (UD->z) * FD->k)) * casp;
154         if (Refract(FD->n1, FD->n2, &UD->l, &UD->m, &UD->n, UD->ln, UD->mn
     , UD->nn)) return(-FD->surf);
155         break;
```

```c
156      case 6:
157          /* ZEMAX wants the index, dn/dx, dn/dy, and dn/dz at the given x,
         y, z. */
158          N = FD->param[2];
159          A = FD->param[3];
160          x = UD->x;
161          y = UD->y;
162          z = UD->z;
163
164          f = N / ((N - 1) * (FD->cv));
165
166          r2 = x * x + y * y + (z - f) * (z - f);
167
168          index = N * sqrt(r2) / f;
169
170          /* do not return stupid data */
171          if (index < 1.0) index = 1.0;
172          UD->index = index;
173
174          /* now the derivatives */
175          UD->dndx = N * x / (f * sqrt(r2));
176          UD->dndy = N * y / (f * sqrt(r2));
177          UD->dndz = N * (z - f) / (f * sqrt(r2));
178
179          break;
180      case 7:
181          /* ZEMAX wants the "safe" data. */
182          /* this is used by ZEMAX to set the initial values for all
         parameters and extra data */
183          /* when the user first changes to this surface type. */
184          /* this is the only time the DLL should modify the data in the
         FIXED_DATA FD structure */
185          FD->param[1] = 1.0; /* Delta T */
186          FD->param[2] = 1.6; /* N0 */
187          FD->param[3] = 0.0; /* A */
188          for (i = 4; i <= 8; i++) FD->param[i] = 0.0;
189          for (i = 1; i <= 200; i++) FD->xdata[i] = 0.0;
190          break;
191      }
192      return 0;
193 }
194
195 int
196 Refract(double thisn, double nextn, double* l, double* m, double* n,
         double ln, double mn, double nn)
197 {
198      double nr, cosi, cosi2, rad, cosr, gamma;
199      if (thisn != nextn)
200      {
201          nr = thisn / nextn;
202          cosi = fabs((*l) * ln + (*m) * mn + (*n) * nn);
203          cosi2 = cosi * cosi;
204          if (cosi2 > 1) cosi2 = 1;
205          rad = 1 - ((1 - cosi2) * (nr * nr));
206          if (rad < 0) return(-1);
207          cosr = sqrt(rad);
208          gamma = nr * cosi - cosr;
209          (*l) = (nr * (*l)) + (gamma * ln);
210          (*m) = (nr * (*m)) + (gamma * mn);
211          (*n) = (nr * (*n)) + (gamma * nn);
212      }
213      return 0;
214 }
```

LISTING A.2: OpticStudio C code for ray-tracing the negative GRIN lens

```c
#include <windows.h>
#include <math.h>
#include <string.h>
#include "usersurf.h"

/* Adapted from Zemax sample grin.c */

int
__declspec(dllexport) APIENTRY UserDefinedSurface(USER_DATA* UD,
    FIXED_DATA* FD);

/* a generic Snells law refraction routine */
int
Refract(double thisn, double nextn, double* l, double* m, double* n,
    double ln, double mn, double nn);

BOOL
WINAPI DllMain(HANDLE hInst, ULONG ul_reason_for_call, LPVOID lpReserved)
{
    return TRUE;
}

/* this DLL models a GRIN surface similar to the GRIN 1 surface type. */

int
__declspec(dllexport) APIENTRY UserDefinedSurface(USER_DATA* UD,
    FIXED_DATA* FD)
{
    int i;
    double p2, r2, alpha, index, N, A, x, y, z, f;
    double power, a, b, c, rad, t, zc, casp;
    switch (FD->type)
    {
    case 0:
        /* ZEMAX is requesting general information about the surface */
        switch (FD->numb)
        {
        case 0:
            /* ZEMAX wants to know the name of the surface */
            /* do not exceed 12 characters */
            strcpy(UD->string, "GRIN negative");
            break;
        case 1:
            /* ZEMAX wants to know if this surface is rotationally
    symmetric */
            /* it is, so return any character in the string; otherwise,
    return a null string */
            strcpy(UD->string, "1");
            break;
        case 2:
            /* ZEMAX wants to know if this surface is a gradient index
    media (it is) */
            strcpy(UD->string, "1");
            break;
        }
        break;
    case 1:
        /* ZEMAX is requesting the names of the parameter columns */
        /* the value FD->numb will indicate which value ZEMAX wants. */
```

```
54          /* returning a null string indicates that the parameter is unused
       . */
55          switch (FD->numb)
56          {
57          case 1:
58              /* All GRINs must use paramter 1 as Delta T !!!!!!!!!!!!!!! */
59              strcpy(UD->string , "Delta T");
60              break;
61          case 2:
62              strcpy(UD->string , "N0");
63              break;
64          case 3:
65              strcpy(UD->string , "A");
66              break;
67          default:
68              UD->string [0] = '\0';
69              break;
70          }
71          break;
72      case 2:
73          /* ZEMAX is requesting the names of the extra data columns */
74          /* the value FD->numb will indicate which value ZEMAX wants. */
75          /* they are all "Unused" for this surface type */
76          /* returning a null string indicates that the extradata value is
       unused. */
77          switch (FD->numb)
78          {
79          default:
80              UD->string [0] = '\0';
81              break;
82          }
83          break;
84      case 3:
85          /* ZEMAX wants to know the sag of the surface */
86          /* if there is an alternate sag, return it as well */
87          /* otherwise , set the alternate sag identical to the sag */
88          /* The sag is sag1, alternate is sag2. */
89
90          UD->sag1 = 0.0;
91          UD->sag2 = 0.0;
92
93          /* if a plane, just return */
94          if (FD->cv == 0) return(0);
95          p2 = UD->x * UD->x + UD->y * UD->y;
96          alpha = 1 - (1 + FD->k) * FD->cv * FD->cv * p2;
97          if (alpha < 0) return(-1);
98          UD->sag1 = (FD->cv * p2) / (1 + sqrt(alpha));
99          if (alpha != 1.0) UD->sag2 = (FD->cv * p2) / (1 - sqrt(alpha));
100         break;
101     case 4:
102         /* ZEMAX wants a paraxial ray trace to this surface */
103         /* x, y, z, and the optical path are unaffected , at least for
       this surface type */
104         /* for paraxial ray tracing , the return z coordinate should
       always be zero. */
105         /* paraxial surfaces are always planes with the following normals
        */
106
107         UD->ln = 0.0;
108         UD->mn = 0.0;
109         UD->nn = -1.0;
110         power = (FD->n2 - FD->n1) * FD->cv;
111         if ((UD->n) != 0.0)
```

```c
112        {
113            (UD->l) = (UD->l) / (UD->n);
114            (UD->m) = (UD->m) / (UD->n);
115
116            (UD->l) = (FD->n1 * (UD->l) - (UD->x) * power) / (FD->n2);
117            (UD->m) = (FD->n1 * (UD->m) - (UD->y) * power) / (FD->n2);
118
119            /* normalize */
120            (UD->n) = sqrt(1 / (1 + (UD->l) * (UD->l) + (UD->m) * (UD->m))
    );
121            /* de-paraxialize */
122            (UD->l) = (UD->l) * (UD->n);
123            (UD->m) = (UD->m) * (UD->n);
124        }
125        break;
126    case 5:
127        /* ZEMAX wants a real ray trace to this surface */
128        if (FD->cv == 0.0)
129        {
130            UD->ln = 0.0;
131            UD->mn = 0.0;
132            UD->nn = -1.0;
133            if (Refract(FD->n1, FD->n2, &UD->l, &UD->m, &UD->n, UD->ln, UD
    ->mn, UD->nn)) return(-FD->surf);
134            return(0);
135        }
136        /* okay, not a plane. */
137        a = (UD->n) * (UD->n) * FD->k + 1;
138        b = ((UD->n) / FD->cv) - (UD->x) * (UD->l) - (UD->y) * (UD->m);
139        c = (UD->x) * (UD->x) + (UD->y) * (UD->y);
140        rad = b * b - a * c;
141        if (rad < 0) return(FD->surf);  /* ray missed this surface */
142        if (FD->cv > 0) t = c / (b + sqrt(rad));
143        else            t = c / (b - sqrt(rad));
144        (UD->x) = (UD->l) * t + (UD->x);
145        (UD->y) = (UD->m) * t + (UD->y);
146        (UD->z) = (UD->n) * t + (UD->z);
147        UD->path = t;
148        zc = (UD->z) * FD->cv;
149        rad = zc * FD->k * (zc * (FD->k + 1) - 2) + 1;
150        casp = FD->cv / sqrt(rad);
151        UD->ln = (UD->x) * casp;
152        UD->mn = (UD->y) * casp;
153        UD->nn = ((UD->z) - ((1 / FD->cv) - (UD->z) * FD->k)) * casp;
154        if (Refract(FD->n1, FD->n2, &UD->l, &UD->m, &UD->n, UD->ln, UD->mn
    , UD->nn)) return(-FD->surf);
155        break;
156    case 6:
157        /* ZEMAX wants the index, dn/dx, dn/dy, and dn/dz at the given x,
    y, z. */
158        N = FD->param[2];
159        A = FD->param[3];
160        x = UD->x;
161        y = UD->y;
162        z = UD->z;
163
164        r2 = x*x + y*y + (z-1/FD->cv)*(z-1/FD->cv);
165
166        index = N*sqrt(r2)/(1/FD->cv-FD->thic);
167
168        /* do not return stupid data */
169        if (index < 1.0) index = 1.0;
170        UD->index = index;
```

```
171
172            /* now the derivatives */
173            UD->dndx = N*x/((1/FD->cv-FD->thic)*sqrt(r2));
174            UD->dndy = N*y/ ((1 / FD->cv - FD->thic)*sqrt(r2));
175            UD->dndz = N*(z-1/FD->cv)/((1 / FD->cv - FD->thic)*sqrt(r2));
176
177            break;
178        case 7:
179            /* ZEMAX wants the "safe" data. */
180             /* this is used by ZEMAX to set the initial values for all
       parameters and extra data */
181             /* when the user first changes to this surface type. */
182             /* this is the only time the DLL should modify the data in the
       FIXED_DATA FD structure */
183            FD->param[1] = 1.0; /* Delta T */
184            FD->param[2] = 1.6; /* N0 */
185            FD->param[3] = 0.0; /* A */
186            for (i = 4; i <= 8; i++) FD->param[i] = 0.0;
187            for (i = 1; i <= 200; i++) FD->xdata[i] = 0.0;
188            break;
189        }
190        return 0;
191 }
192
193 int
194 Refract(double thisn, double nextn, double* l, double* m, double* n,
       double ln, double mn, double nn)
195 {
196        double nr, cosi, cosi2, rad, cosr, gamma;
197        if (thisn != nextn)
198        {
199            nr = thisn / nextn;
200            cosi = fabs((*l) * ln + (*m) * mn + (*n) * nn);
201            cosi2 = cosi * cosi;
202            if (cosi2 > 1) cosi2 = 1;
203            rad = 1 - ((1 - cosi2) * (nr * nr));
204            if (rad < 0) return(-1);
205            cosr = sqrt(rad);
206            gamma = nr * cosi - cosr;
207            (*l) = (nr * (*l)) + (gamma * ln);
208            (*m) = (nr * (*m)) + (gamma * mn);
209            (*n) = (nr * (*n)) + (gamma * nn);
210        }
211        return 0;
212 }
```

Appendix B

Derivation of the equation for the maximum FoV in an RC
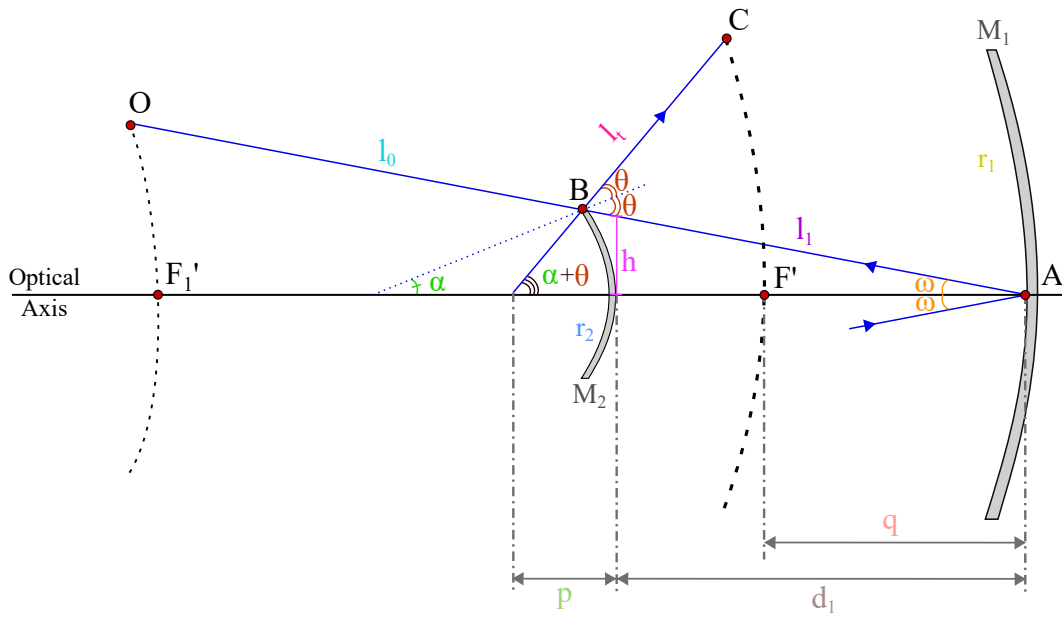
FIGURE B.1: Layout of a RC with its respective angles, distances, and RoC.

For facilitating the clarity of the derivation, a few abbreviations have been used:

$$t = \tan\omega, \tag{B.1}$$

$$y' = \frac{dy}{dz}, \tag{B.2}$$

$$y'' = \frac{d^2y}{dz^2}, \tag{B.3}$$

$B(y, z)$ is the point on the second mirror M_2. $C(y_3, z_3)$ is the point of the tangential focal surface. Considering the geometry of the triangle around the angle ω and the distance d_1, y is given by:

$$y = (d_1 + z)\,t \tag{B.4}$$

Thus, the sag of the surface is given by:

$$z = \frac{d_1{}^2\,t^2}{2\,r} + \frac{d_1{}^4\,t^4\,[(1+k)\,d_1 - 4\,r]}{8\,r^3} + \dots \tag{B.5}$$

where k is the conic constant.

The tangent of $\alpha + \theta$ is given by:

$$\tan(\alpha + \theta) = \frac{y}{p - z} \tag{B.6}$$

Thus, the distance p is given by:

$$p = z + \frac{y \cos \alpha \, \theta}{\sqrt{1 - \cos^2 \alpha \, \theta}} \tag{B.7}$$

The distance q is given by:

$$q = \frac{(-2 d_1 + r_1)}{2} \frac{r_2}{(2 d_1 - r_1 + r_2)} - d_1 \tag{B.8}$$

The height h by:

$$h = d_1 t \tag{B.9}$$

Then z by:

$$z = \frac{h^4 \left(\frac{4 r_2}{d_1} + k + 1\right)}{8 \, r_2{}^3} + \frac{h^2}{2 \, r_2} \tag{B.10}$$

The RoC of the primary or secondary mirror, M_1 and M_2, respectively, assuming local sphere with radius rs is given by:

$$R_s = r_s = \frac{(1 + (y')^2)^{3/2}}{y''} \tag{B.11}$$

Both mirrors are conicoids of revolution with conic constant k, so the radius r_s for M_2 is given by:

$$r_s = \frac{(r_2{}^2 - k y^2)^{3/2}}{r_2{}^2} \tag{B.12}$$

For M_2, y is given by:

$$y^2 = 2 r_2 z - (k + 1) z^2 \tag{B.13}$$

Thus, the first and second derivatives of y with respect to z are given by:

$$y' = \frac{r_2 - (k + 1) z}{y} \tag{B.14}$$

and

$$y'' = -\frac{1}{y^3} (r_2 - (k + 1) z)^2 - \frac{(k + 1)}{y} \tag{B.15}$$

The tangent of α is given by the derivative of z with respect to y. Using , the tangent is given by:

$$\tan \alpha = \frac{dz}{dy} = z' = \frac{y}{r_2 - (k + 1) z} \tag{B.16}$$

The cosine of θ is the same as the cosine of $\alpha + \omega$. Thus:

$$
\begin{aligned}
\cos \theta &= \cos \alpha + \omega = \cos \alpha \cos \omega - \sin \alpha \sin \omega \\
&= \frac{1}{\sqrt{1 + \tan^2 \alpha}} \frac{1}{1 + t^2} - (\tan \alpha \, \cos \alpha)\,(t \, \cos \omega) \\
&= \frac{1 - \tan \alpha \, t}{\sqrt{1 + \tan^2 \alpha} \, \sqrt{1 + t^2}}
\end{aligned}
\tag{B.17}
$$

The cosine of $\alpha + \theta$ is given by:

$$
\begin{aligned}
\cos (\alpha + \theta) &= \cos \alpha \cos \theta - \sin \alpha \sin \theta \\
&= \cos \theta (\cos \alpha - \sin \alpha \tan \theta) = \cos \theta \cos \alpha \, (1 - \tan \alpha \tan \theta) \\
&= \cos \theta \frac{1}{\sqrt{\tan^2 \alpha + 1}} (1 - \tan \alpha \frac{\sqrt{1 - \cos^2 \theta}}{\cos \theta})
\end{aligned}
\tag{B.18}
$$

The distance between the vertex of M_1 and the edge of M_2, AB, is given by:

$$
AB = l_1 = \frac{(d_1 + z)}{\cos \omega} = (d_1 + z) \sqrt{1 + t}
\tag{B.19}
$$

The Coddington equation for the tangential cross-section is given by [124]:

$$
\frac{n_1 \cos^2 \theta_1}{l_t} - \frac{n_0 \cos^2 \theta_0}{l_0} = \frac{n_1 \cos \theta_1 - n_0 \cos \theta_0}{r_s}
\tag{B.20}
$$

Considering that $\theta_1 = \theta_0 = \theta$, $n_0 = 1$ and $n_1 = -1$, Eq. (B.20) can be simplified to:

$$
\frac{\cos^2 \theta}{l_t} - \frac{\cos^2 \theta}{l_0} = -\frac{2 \cos \theta}{r_s}
\tag{B.21}
$$

so,

$$
\frac{1}{l_t} = \frac{1}{l_0} - \frac{2}{r_s \cos \theta}
\tag{B.22}
$$

where, for M_1, $l_0 = -\dfrac{r_1 \cos \omega}{2} - l_1$, since at ∞:

$$
\frac{\cos \omega}{l_t} - \frac{\cos \omega}{\infty} = -\frac{2}{r_1},
\tag{B.23}
$$

$$
l_t - l_1 = l_0,
\tag{B.24}
$$

and

$$
\frac{\cos \omega}{l_t} = -\frac{2}{r_1}
\tag{B.25}
$$

Therefore, Eq. (B.22) becomes:

$$
\frac{1}{l_t} = \frac{1}{-\dfrac{r_1}{2} \cos \omega - l_1} - \frac{2}{r_s \cos \theta}
\tag{B.26}
$$

Then l_t becomes:

$$l_t = -\frac{r_s \cos\theta \left(2\,l_1\sqrt{t^2+1} - r_1\right)}{2\left(\sqrt{t^2+1}\,(r_s\,\cos\theta + 2\,l_1) - r_1\right)} \tag{B.27}$$

The height of the point C is given by:

$$y_3 = y + l_t\,\sin\alpha + \theta \tag{B.28}$$

And the sagitta of the tangential focal surface is given by:

$$z_3 = -(z + d_1 + q) + l_t\,\cos(\alpha + \theta) \tag{B.29}$$

in this case, $q < 0$.

Combining Eqs. (B.8), (B.10), (B.16) to (B.18) and (B.27) with Eq. (B.29) and simplifying it for t yields to Eq. (5.13).

Bibliography

[1] M. C. Rocha and A. V. Goncharov, "Aplanatic meniscus lens corrector for ritchey-chrétien telescopes", Opt. Express **30**, 6076–6089 (2022).

[2] M. C. Rocha, A. V. Goncharov, and C. Dainty, "Aplanatic afocal system using two grin lenses with spherical surfaces", in Novel optical systems, methods, and applications xxii, Vol. 11105 (International Society for Optics and Photonics, 2019), p. 111050C.

[3] M. C. Rocha and A. V. Goncharov, "An aplanatic meniscus lens for correcting astigmatism in ritchey-chrétien telescopes", in Advances in optical and mechanical technologies for telescopes and instrumentation iv, Vol. 11451 (International Society for Optics and Photonics, 2020), 114514E.

[4] M. C. Rocha and A. V. Goncharov, "A quasi-aplanatic refractive pair for correcting astigmatism in ritchey-chrétien telescopes", in Optical design and engineering viii, Vol. 11871 (SPIE, 2021), p. 1187108.

[5] G. Asimellis, *Geometrical optics*, Lectures in optics (SPIE Press, 2020).

[6] V. N. Mahajan, *Aberration theory made simple*, Vol. 6 (SPIE Press, 1991).

[7] W. J. Smith, *Modern optical engineering: the design of optical systems* (McGraw-Hill Education, 2008).

[8] W. Wall, *A history of optical telescopes in astronomy* (Springer, 2018).

[9] Y. B. Pierre, *The design and construction of large optical telescopes*, 2003.

[10] T. Andersen, A. L. Ardeberg, J. Beckers, A. Goncharov, M. Owner-Petersen, et al., "The euro50 extremely large telescope", in Future giant telescopes, Vol. 4840 (International Society for Optics and Photonics, 2003), pp. 214–225.

[11] V. Y. Terebizh, *Survey telescope optics* (2019).

[12] W. Wetherell and M. Rimmer, "General analysis of aplanatic cassegrain, gregorian, and schwarzschild telescopes", Applied Optics **11**, 2817–2832 (1972).

[13] R. A. Sampson, "Ii. on a cassegrain reflector with corrected field", Philosophical Transactions of the Royal Society of London. Series A, Containing Papers of a Mathematical or Physical Character **213**, 27–66 (1913).

[14] F. E. Ross, "Lens systems for correcting coma of mirrors", The Astrophysical Journal **81**, 156 (1935).

[15] V. Y. Churilosvkii, "Concerning a new type of astrophotographic objective with apochromatic, aplanatic, anastigmatic, and orthoscopic correction", Trudy LITMO **1**.

[16] A. V. M. O. A. Mel'nikov G. G. Slyusarev and N. F. Kuprevich, "Sovremeniy teleskop", The Modern Telescope.

[17] A. Meinel, "Aspheric field correctors for large telescopes.", The Astrophysical Journal **118**, 335 (1953).

[18] S. Rosin, "Corrected cassegrain system", Applied Optics **3**, 151–152 (1964).

[19]I. S. Bowen, "5. the 200-inch hale telescope", Transactions of the International Astronomical Union **8**, 750–754 (1954).

[20]C. Wynne, "Field correctors for large telescopes", Applied Optics **4**, 1185–1192 (1965).

[21]D. Schulte, "Prime focus correctors involving aspherics", Applied Optics **5**, 313–317 (1966).

[22]S. Gascoigne, "On ritchey-chrétien systems", The Observatory **85**, 79–81 (1965).

[23]P. P. Argunov, "Catadioptric telescope", New Technology in Astronomy.

[24]D. Schulte, "Anastigmatic cassegrain type telescope", Applied optics **5**, 309–311 (1966).

[25]S. Rosin, "Ritchey chrétien corrector system", Applied Optics **5**, 675–676 (1966).

[26]P. Argunov, "Isochromatic mirror-lens telescope systems with spherical optics.", Astronomicheskii Vestnik **6**, 52–61 (1972).

[27]G. M. Popov, "Mirror-lens isochromatic systems of catadioptric type", Izv. Krym. Astrofiz. **36**.

[28]C. Wynne, "Afocal correctors for paraboloidal mirrors", Applied Optics **6**, 1227–1231 (1967).

[29]C. Wynne, "Ritchey-chrétien telescopes and extended field systems", The Astrophysical Journal **152**, 675 (1968).

[30]H Köhler, "The optical system for the 3.5-m eso telescope", Applied Optics **7**, 241–247 (1968).

[31]R. Wilson, "Corrector systems for cassegrain telescopes", Applied optics **7**, 253–263 (1968).

[32]I. N. Refsdal, "Flat-field cassegrain-type telescope", Applied Optics **7**, 1645–1647 (1968).

[33]S. Rosin and M. Amon, "Extending the stellar field of view of ritchey-chrétien telescopes", Applied optics **11**, 1623–1629 (1972).

[34]C. Wynne, "Wide field cassegrain telescopes", Monthly Notices of the Royal Astronomical Society **163**, 357–367 (1973).

[35]C. Wynne, "A new wide-field triple lens paraboloid field corrector", Monthly Notices of the Royal Astronomical Society **167**, 189–198 (1974).

[36]C. Harmer and C. Wynne, "A simple wide-field cassegrain telescope", Monthly Notices of the Royal Astronomical Society **177**, 25P–30P (1976).

[37]S. Ding-Qiang and W. Lan-Juan, "A flat-field reflecting focal reducer", Optica Acta: International Journal of Optics **29**, 391–394 (1982).

[38]C Cao and R. Wilson, "An improved prime focus corrector for f/3 true or quasi ritchey-chrétien primaries", Astronomy and Astrophysics **133**, 37–48 (1984).

[39]H. W. Epps and D. Fabricant, "Field correctors for wide-field ccd imaging with ritchey-chrétien telescopes", The Astronomical Journal **113**, 439 (1997).

[114]D. T. Puryayev and A. V. Goncharov, "Aplanatic four-mirror system for optical telescopes with a spherical primary mirror", Optical Engineering **37**, 2334–2342 (1998).

[0]V. Y. Terebizh, "New designs of survey telescopes", Astronomische Nachrichten **332**, 714–742 (2011).

[40]S. Chuprakov, "Mirror-lens system with a meniscus corrector containing a chromatic surface", Journal of optical technology **71**, 791–794 (2004).

[41]Y. A. Klevtsov, "Isoplanatic focal-length converter for a catadioptric telescope with a meniscus corrector", Journal of Optical Technology **73**, 535–538 (2006).

[42]V. Y. Terebizh, "Wide-field corrector for a gregory telescope", arXiv preprint astro-ph/0605361 (2006).

[43]A. Rakich and N. J. Rumsey, "A new prime-focus corrector for paraboloid mirrors", Advanced Optical Technologies **2**, 111–116 (2013).

[44]P. Corke, *Robotics, vision and control: fundamental algorithms in matlab® second, completely revised*, Vol. 118 (Springer, 2017).

[45]H. Gernsheim and A. Gernsheim, "The history of photography: from the camera obscura to the beginning of the modern era", (1969).

[46]D. Raynaud, *Critical edition of ibn al-haytham's on the shape of the eclipse* (Springer, 2016).

[47]G. Asimellis, *Introduction to optics*, Lectures in optics (SPIE Press, 2020).

[48]L. Rayleigh, "X. on pin-hole photography", The London, Edinburgh, and Dublin Philosophical Magazine and Journal of Science **31**, 87–99 (1891).

[49]M Young, "Pinhole optics", Applied Optics **10**, 2763–2767 (1971).

[50]P. Petzval, "I. on the camera obscura", The London, Edinburgh, and Dublin Philosophical Magazine and Journal of Science **17**, 1–15 (1859).

[51]B. E. Saleh and M. C. Teich, *Fundamentals of photonics* (john Wiley & sons, 2019).

[52]R. A. Shelby, D. R. Smith, and S. Schultz, "Experimental verification of a negative index of refraction", science **292**, 77–79 (2001).

[53]F. A. Jenkins, H. E. White, and D. G. Brukhard, "Fundamentals of optics", American Journal of Physics **26**, 272–272 (1958).

[54]H. Gross, *Handbook of optical systems, volume 1, fundamentals of technical optics*, Vol. 1 (2005).

[55]D. Malacara-Hernández and Z. Malacara-Hernández, *Handbook of optical design* (CRC Press, 2017).

[56]M. J. Kidger, "Fundamental optical lens design", in (SPIE Bellingham, 2001).

[57]A. Romano and R. Cavaliere, "Geometric optics: theory and design of astronomical optical systems using mathematica (r)(modeling and simulation in science, engineering and technolo)", (2018).

[58]M. Schaub, J. Schwiegerling, E. Fest, R. H. Shepard, and A. Symmons, *Molded optics: design and manufacture* (CRC press, 2016).

[59]K. J. Kasunic, *Optomechanical systems engineering* (John Wiley & Sons, 2015).

[60]A. Ahmad, *Handbook of optomechanical engineering* (CRC Press, 2017).

[61]M. Bass, *Handbook of optics: volume i-geometrical and physical optics, polarized light, components and instruments* (McGraw-Hill Education, 2010).

[62]A. Rowlands, *Physics of digital photography* (IOP Publishing, 2017).

[63]J. R. Meyer-Arendt, "Introduction to classical and modern optics", Englewood Cliffs: Prentice-Hall (1989).

[64]R. Kingslake and R. B. Johnson, *Lens design fundamentals* (Academic Press, 2009).

[65] A Cornejo and D Malacara, "Caustic coordinates in platzeck-gaviola test of conic mirrors", Applied optics **17**, 18–19 (1978).

[66] H. Gross, H. Zügge, M. Peschka, and F. Blechinger, *Handbook of optical systems, aberration theory and correction of optical systems*, Handbook of Optical Systems (Wiley, 2007).

[67] J. Bentley and C. Olson, "Field guide to lens design", in (Society of Photo-Optical Instrumentation Engineers (SPIE), 2012).

[68] N. Bellas, S. M. Chai, M. Dwyer, and D. Linzmeier, "Real-time fisheye lens distortion correction using automatically generated streaming accelerators", in 2009 17th ieee symposium on field programmable custom computing machines (IEEE, 2009), pp. 149–156.

[69] T. T. Smith, "Spherical aberration in thin lenses", Physical Review **19**, 276 (1922).

[70] H. Coddington, *A treatise on the reflection and refraction of light: being part i. of a system of optics* (1829).

[71] J. H. Burnett, S. G. Kaplan, E. Stover, and A. Phenis, "Refractive index measurements of ge", in Infrared sensors, devices, and applications vi, Vol. 9974 (International Society for Optics and Photonics, 2016), p. 99740X.

[72] R. G. González-Acuña and H. A. Chaparro-Romo, "Stigmatic optics", (2020).

[73] R. K. Luneburg, *Mathematical theory of optics* (Univ of California Press, 1966).

[74] R. G. González-Acuña, H. A. Chaparro-Romo, and J. C. Gutiérrez-Vega, "Analytical lens design", (2020).

[75] R. A. Adams and C. Essex, *Calculus: a complete course*, Vol. 4 (Addison-Wesley Boston, 1999).

[76] V. Gutenmacher and N. B. Vasilyev, *Lines and curves: a practical geometry handbook* (Springer Science & Business Media, 2004).

[77] G. Kweon and C. Kim, "Aspherical lens design by using a numerical analysis", Korean Physical Society **51**, 93 (2007).

[78] R. G. González-Acuña and H. A. Chaparro-Romo, "General formula for bi-aspheric singlet lens design free of spherical aberration", Applied optics **57**, 9341–9345 (2018).

[79] R. G. González-Acuña, H. A. Chaparro-Romo, and J. C. Gutiérrez-Vega, "Exact equations for stigmatic singlet design meeting the abbe sine condition", Optics Communications, 126415 (2020).

[80] A. Silva-Lora and R. Torres, "Superconical aplanatic ovoid singlet lenses", JOSA A **37**, 1155–1165 (2020).

[81] H. G. Rutten and M. A. Van Venrooij, *Telescope optics: a comprehensive manual for amateur astronomers* (Willmann-Bell, 2002).

[82] V. N. Mahajan, *Optical imaging and aberrations: ray geometrical optics*, Vol. 45 (SPIE press, 1998).

[83] A. Mikaelian and A. Prokhorov, "V self-focusing media with variable index of refraction", in *Progress in optics*, Vol. 17 (Elsevier, 1980), pp. 279–345.

[84] R. W. Wood, *Physical optics* (Macmillan, 1905).

[85] R. K. Luneburg, *Mathematical theory of optics* (University of California Press, 2021).

[86] E. Merchand, *Gradient index optics* (Elsevier, 2012).

[87]B. E. Saleh, M. C. Teich, and B. E. Saleh, *Fundamentals of photonics*, Vol. 22 (Wiley New York, 1991).

[88]M. J. Riedl, *Optical design fundamentals for infrared systems*, Vol. 48 (SPIE press, 2001).

[89]M. Ponting and H. Fein, "Reduced swap polymeric, nanolayered, spherical, gradient refractive index (grin) lenses in imaging systems", in Optical fabrication and testing (Optical Society of America, 2017), OW1B–2.

[90]M. Ponting, A. Hiltner, and E. Baer, "Polymer nanostructures by forced assembly: process, structure, and properties", in Macromolecular symposia, Vol. 294, 1 (Wiley Online Library, 2010), pp. 19–32.

[91]X. Xu and M. E. Savard, *Method of manufacturing a grin lens*, US Patent 5,917,105, 1999.

[92]B. McMorrow, R. Chartoff, P. Lucas, and W. Richardson, "Polymer matrix nanocomposites by inkjet printing", in 2005 international solid freeform fabrication symposium (2005).

[93]R. Magazine, B. van Bochove, S. Borandeh, and J. Seppälä, "3d inkjet-printing of photo-crosslinkable resins for microlens fabrication", Additive Manufacturing **50**, 102534 (2022).

[94]R. Ilinsky, "Gradient-index meniscus lens free of spherical aberration", Journal of Optics A: Pure and Applied Optics **2**, 449 (2000).

[95]D. H. Lippman, N. S. Kochan, T. Yang, G. R. Schmidt, J. L. Bentley, et al., "Freeform gradient-index media: a new frontier in freeform optics", Optics Express **29**, 36997–37012 (2021).

[96]A. J. Yee, W. Song, N. Takaki, T. Yang, Y. Zhao, et al., "Design of a freeform gradient-index prism for mixed reality head mounted display", in Digital optics for immersive displays, Vol. 10676 (International Society for Optics and Photonics, 2018), 106760S.

[97]T. Yang, N. Takaki, J. Bentley, G. Schmidt, and D. T. Moore, "Efficient representation of freeform gradient-index profiles for non-rotationally symmetric optical design", Optics Express **28**, 14788–14806 (2020).

[98]D. H. Lippman, R. Chou, A. X. Desai, N. S. Kochan, T. Yang, et al., "Polychromatic annular folded lenses using freeform gradient-index optics", Applied Optics **61**, A1–A9 (2022).

[99]D. H. Lippman and G. R. Schmidt, "Prescribed irradiance distributions with freeform gradient-index optics", Optics Express **28**, 29132–29147 (2020).

[100]N. S. Kochan, G. R. Schmidt, and D. T. Moore, "Freeform gradient index generalized coddingtons equations", JOSA A **39**, 509–516 (2022).

[101]D. H. Lippman, R. Chou, A. X. Desai, N. S. Kochan, T. Yang, et al., "Design of annular folded lenses using freeform gradient-index optics", in International optical design conference (Optical Society of America, 2021), 120781S.

[102]L. Yang, R. Wu, J. Zhang, and Y. Dai, "Optical design of freeform lenses for illuminating hard-to-reach areas", in Optical design and testing xi, Vol. 11895 (SPIE, 2021), pp. 24–31.

[103]A. M. Boyd, "Optical design of multi-material, general rotationally symmetric grin lenses", in Advanced optics for imaging applications: uv through lwir iv, Vol. 10998 (International Society for Optics and Photonics, 2019), 109980J.

[104] J. Braat and P. F. Greve, "Aplanatic optical system containing two aspheric surfaces", Applied optics **18**, 2187–2191 (1979).

[105] K. Varughese, K. Banerjee, and R Hradaynath, "Design of fast aplanatic ir objectives using high refractive-index materials", Applied optics **22**, 347–353 (1983).

[106] A. Head, "The two-mirror aplanat", Proceedings of the Physical Society. Section B **70**, 945 (1957).

[107] B. Narasimhan, P. Benitez, J. C. Miñano, M. Nikolic, and D. Grabovickic, "Three surface freeform aplanatic systems", Optics express **25**, 10710–10715 (2017).

[108] P. Benitez, M. Nikolic, and J. C. Miñano, "Analytical solution of an afocal two freeform mirror design problem", Optics Express **25**, 4155–4161 (2017).

[109] M. C. Hetirick, "Aplanatic grazing incidence diffraction grating: a new optical element", Applied optics **25**, 3269–3282 (1986).

[110] F. Aieta, P. Genevet, M. Kats, and F. Capasso, "Aberrations of flat lenses and aplanatic metasurfaces", Optics express **21**, 31530–31539 (2013).

[111] I. Kitano, "Current status of aplanatic gradient-index lens systems", Applied optics **29**, 3992–3997 (1990).

[112] B. R. Masters, *Abbe theory of image formation and diffraction of light in transmitted light microscopes* (International Society for Optics and Photonics, 2006).

[113] J. H. Burge, C. Zhao, and M. B. Dubin, "Use of the abbe sine condition to quantify alignment aberrations in optical imaging systems", in International optical design conference (Optical Society of America, 2010), ITuD5.

[115] H. Gross, F. Blechinger, and B. Achtner, *Survey of optical instruments* (Wiley-VCH Verlag GmbH & Company KGaA, 2008).

[116] M. Born and E. Wolf, *Principles of optics: electromagnetic theory of propagation, interference and diffraction of light* (Elsevier, 2013).

[117] A. Ernst, "On the estimation of aperture in the microscope", JR Microsc. Soc **1**, 388–423 (1881).

[118] Z. OpticStudio, "19.4", Zemax LLC, Seattle, WA (2019).

[119] I. Malitson, "Interspecimen comparison of the refractive index of fused silica", Josa **55**, 1205–1209 (1965).

[120] N. P. Bansal and R. H. Doremus, *Chapter 2 - vitreous silica* (Academic Press, 1986), pp. 7–30.

[121] R. J. Noll, "Zernike polynomials and atmospheric turbulence", JOsA **66**, 207–211 (1976).

[122] A. V. Goncharov, N. Devaney, and C. Dainty, "Atmospheric dispersion compensation for extremely large telescopes", Optics express **15**, 1534–1542 (2007).

[123] O. Iwert, D. Ouellette, M. Lesser, and B. Delabre, "First results from a novel curving process for large area scientific imagers", in High energy, optical, and infrared detectors for astronomy v, Vol. 8453 (International Society for Optics and Photonics, 2012), 84531W.

[124] J. Braat and P. Török, *Imaging optics* (Cambridge University Press, 2019).